THERANOSTIC IMAGING IN CANCER PRECISION MEDICINE

EDITED BY: Marie-France Penet and Zaver Bhujwalla
PUBLISHED IN: Frontiers in Oncology

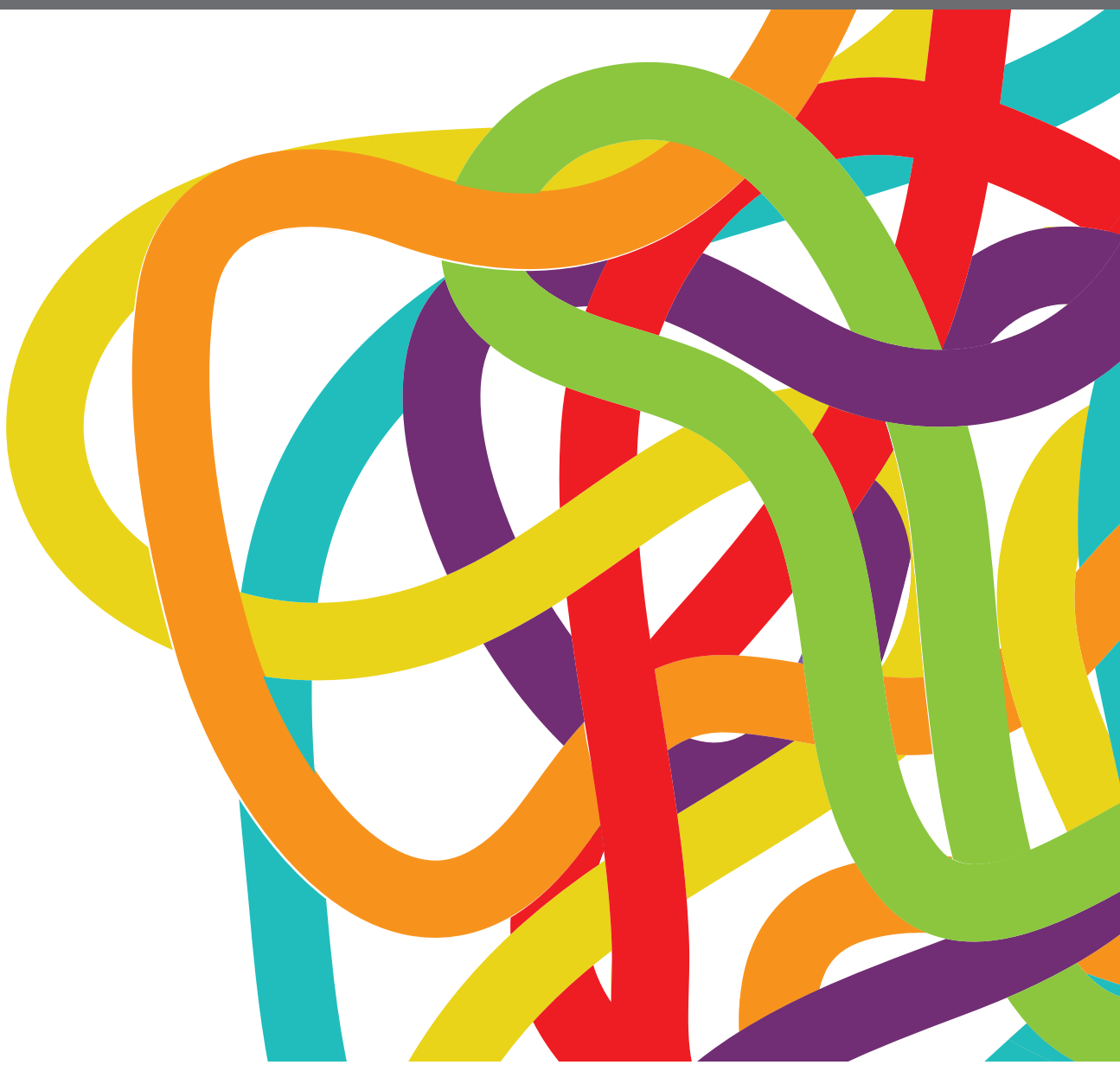

frontiers Research Topics

ISSN 1664-8714
ISBN 978-2-88974-472-5
DOI 10.3389/978-2-88974-472-5

About Frontiers

Frontiers is more than just an open-access publisher of scholarly articles: it is a pioneering approach to the world of academia, radically improving the way scholarly research is managed. The grand vision of Frontiers is a world where all people have an equal opportunity to seek, share and generate knowledge. Frontiers provides immediate and permanent online open access to all its publications, but this alone is not enough to realize our grand goals.

Frontiers Journal Series

The Frontiers Journal Series is a multi-tier and interdisciplinary set of open-access, online journals, promising a paradigm shift from the current review, selection and dissemination processes in academic publishing. All Frontiers journals are driven by researchers for researchers; therefore, they constitute a service to the scholarly community. At the same time, the Frontiers Journal Series operates on a revolutionary invention, the tiered publishing system, initially addressing specific communities of scholars, and gradually climbing up to broader public understanding, thus serving the interests of the lay society, too.

Dedication to Quality

Each Frontiers article is a landmark of the highest quality, thanks to genuinely collaborative interactions between authors and review editors, who include some of the world's best academicians. Research must be certified by peers before entering a stream of knowledge that may eventually reach the public - and shape society; therefore, Frontiers only applies the most rigorous and unbiased reviews.
Frontiers revolutionizes research publishing by freely delivering the most outstanding research, evaluated with no bias from both the academic and social point of view. By applying the most advanced information technologies, Frontiers is catapulting scholarly publishing into a new generation.

What are Frontiers Research Topics?

Frontiers Research Topics are very popular trademarks of the Frontiers Journals Series: they are collections of at least ten articles, all centered on a particular subject. With their unique mix of varied contributions from Original Research to Review Articles, Frontiers Research Topics unify the most influential researchers, the latest key findings and historical advances in a hot research area! Find out more on how to host your own Frontiers Research Topic or contribute to one as an author by contacting the Frontiers Editorial Office: frontiersin.org/about/contact

THERANOSTIC IMAGING IN CANCER PRECISION MEDICINE

Topic Editors:
Marie-France Penet, School of Medicine, Johns Hopkins Medicine, United States
Zaver Bhujwalla, School of Medicine, Johns Hopkins Medicine, United States

Citation: Penet, M.-F., Bhujwalla, Z., eds. (2022). Theranostic Imaging in Cancer Precision Medicine. Lausanne: Frontiers Media SA.
doi: 10.3389/978-2-88974-472-5

Table of Contents

frontiers in Oncology

REVIEW
published: 12 December 2017
doi: 10.3389/fonc.2017.00310

Guidelines for Rational Cancer Therapeutics

*Byunghee Yoo[1], Ann-Marie Billig[2] and Zdravka Medarova[1]**

[1] MGH/MIT/HMS Athinoula A. Martinos Center for Biomedical Imaging, Massachusetts General Hospital and Harvard Medical School, Boston, MA, United States, [2] Bouvé College of Health Sciences, Northeastern University, Boston, MA, United States

Traditionally, cancer therapy has relied on surgery, radiation therapy, and chemotherapy. In recent years, these interventions have become increasingly replaced or complemented by more targeted approaches that are informed by a deeper understanding of the underlying biology. Still, the implementation of fully rational patient-specific drug design appears to be years away. Here, we present a vision of rational drug design for cancer that is defined by two major components: modularity and image guidance. We suggest that modularity can be achieved by combining a nanocarrier and an oligonucleotide component into the therapeutic. Image guidance can be incorporated into the nanocarrier component by labeling with a specific imaging reporter, such as a radionuclide or contrast agent for magnetic resonance imaging. While limited by the need for additional technological advancement in the areas of cancer biology, nanotechnology, and imaging, this vision for the future of cancer therapy can be used as a guide to future research endeavors.

Keywords: imaging, cancer, therapy, rational, nanomedicine

OPEN ACCESS

Edited by:
Zaver Bhujwalla, Johns Hopkins University, United States

Reviewed by:
Aslam Khan, University of Missouri, United States
Rossella Canese, Istituto Superiore di Sanità, Italy

****Correspondence:***
Zdravka Medarova
zmedarova@partners.org

Specialty section:
This article was submitted to Cancer Imaging and Diagnosis, a section of the journal Frontiers in Oncology

Received: *04 October 2017*
Accepted: *29 November 2017*
Published: *12 December 2017*

Citation:
Yoo B, Billig A-M and Medarova Z (2017) Guidelines for Rational Cancer Therapeutics. Front. Oncol. 7:310. doi: 10.3389/fonc.2017.00310

INTRODUCTION

The recent past has seen an impetus to develop more personalized therapies for cancer, as part of the general concept of precision medicine. In this review, we look at a component of precision medicine focused on the specific design of the therapeutic. We suggest that it is possible to design therapeutics that are fully rational. Namely, we envision rational therapeutics as therapeutics based entirely on predesigned components. This strategy is different than strategies that we have seen in the past or are seeing currently. Traditional approaches are largely reliant on trial-and-error discovery. A prime example is penicillin, which was discovered by pure chance. Even more rational modern approaches such as combinatorial screening, have a large element of trial-and-error in their discovery. The approach we are talking about has no trial-and-error components. It is entirely predesigned, meaning that that each patient will be given a treatment plan that would have been determined as nearly 100% effective because of their genetic makeup, anatomy, and physiology. Because of that, this approach fits perfectly into the concept of precision medicine—if an approach is truly rational, it can tell us whether a patient is going to respond to treatment before that patient has even been injected with the drug.

Key components of rational therapeutics are modularity and image guidance. Modularity allows us to synthesize libraries of therapeutic agents that are optimized for a given indication or a given patient in terms of size, surface coating and charge, hydrophilicity/hydrophobicity; antigen-targeting through incorporation of targeting peptides, and therapeutic moiety. Image guidance answers questions about the individual biology of a given patient or indication. It is necessary

because we know that each organ and each patient are highly variable in terms of vascularity, fat content, vascular permeability, inflammatory profile, etc. Because of these differences, we need to vary features such as physicochemical drug design, injection dose, schedule, and even route, in order to provide the best and most effective treatment possible for every individual patient. Imaging is the only modality that can provide answers to these questions.

In our experience, an ideal candidate for rational drug design has three components: a DNA/RNA therapeutic component, a nanoparticle carrier, and an imaging reporter. DNA/RNA-targeted methods could be an integral part of rational therapeutics. This essential component takes advantage of the "coded" nature of the genome and transcriptome. Because of that, DNA/RNA-targeted methods provide an ideal platform for completely rational design of diagnostic and therapeutic agents based on the phenomenon of complementarity. This approach can be used while relying on recent advances in genome sequencing like antisense oligonucleotides [locked nucleic acid (LNA) oligos, antagomirs, miRNA sponges], small interfering RNA (siRNA) duplexes, or ribozymes. These molecules can be synthesized to target portions of the code that are aberrant in disease and thus the unique genome of the patient would in turn direct us to an equally unique cocktail of therapeutic agents. This constitutes a prime example of achievable individualized medicine.

Nanotechnology is another component of the envisioned rational therapeutic. Specifically, nanoparticles are carriers that can incorporate all three components of the drugs that we envision. They can easily be functionalized with oligonucleotides (antisense, siRNA, etc.) without interfering with the functionality of the oligos. Their design can be fine-tuned using standard synthetic chemistry, e.g., liposomes, iron oxide nanoparticles, etc. Finally, they can be labeled with an imaging reporter, e.g., radionuclide. An example is presented by polymer-coated iron oxide nanoparticles. By varying the ratios of coating to iron, the size of the nanoparticles can be adjusted. In addition, fairly standardized chemistry can be used to incorporate different coats onto the nanoparticles, e.g., dextran, carboxydextran, starch, polyethylene glycol (PEG), etc. These changes in size and surface coating result in very diverse biological fates, related to the agents' pharmacokinetics and pharmacodynamics.

Image guidance is the third component of the envisioned drug design. By labeling the drug with an imaging reporter, we can monitor the delivery of the therapeutic agent to the tissue of interest. Image-guided delivery can be instrumental to assess and control delivery to the target tissues. Imaging can be used to determine the optimal drug design, delivery schedule, route, and therapeutic dose on an individual basis and to suggest alternatives should therapy fail in a given patient. In our view, dual-modality approaches, such as PET-MR or PET-CT would be optimal. PET-MR specifically could obtain near perfect spatial registration of molecular/functional positron emission tomography (PET) and anatomic/functional magnetic resonance imaging (MRI). This combination allows highly detailed anatomical images (MR) to be co-registered with PET images that have greater sensitivity and the capability for precise quantitation of local drug concentration.

OLIGONUCLEOTIDE DESIGN

Of the three elements of rational therapeutics, oligonucleotide development is by far the most advanced. Partly, the reason for this investment in the development of oligonucleotide therapeutics stems from the vast potential to address therapeutic challenges, including undruggable targets. Synthetic oligonucleotides include, among others, antisense oligonucleotides, mRNA oligos, siRNA, microRNA inhibitors or mimics, and more recently, long non-coding RNA modulators. Unlike biologics or small molecules, the listed synthetic oligonucleotides have the advantage of generally binding their targets through direct Watson–Crick complementarity. This fundamentally straightforward property provides an opportunity for rational, computational design of therapeutics, based on the simple knowledge of the target and its sequence.

Nevertheless, there is a list of challenges related to the design of synthetic oligonucleotides for therapy. These challenges relate to the fact that the chemical architecture of the oligonucleotide needs to be fine-tuned according to the requirements for favorable pharmacokinetics. This includes ADME, long-term stability, safety, and immunogenicity, and capacity to engage the target with high affinity and specificity without off-target effects. The latter is especially important when the oligonucleotide functions in the context of a multi-enzyme complex, as is the case for siRNA.

On the level of oligonucleotide architecture, these issues are addressed by rationally designed chemical modifications. Backbone and sugar modifications are two general strategies that have found application. The most commonly encountered backbone modification is the phosphorothioate linkage. The phosphorothioate (PS) linkage imparts significant resistance to nuclease degradation. However, in addition to this role, the PS linkage also has a major impact on oligonucleotide trafficking and uptake. Specifically, phosphorothioates can promote oligonucleotide binding to serum albumin (1) and effectively alter the pharmacokinetics and circulation half-life of the oligos. Phosphorothioate linkages also enhance the cellular uptake of oligos without a carrier for transfection (2). Finally, phosphorothioate linkages can have a reduced binding affinity for the target (3), necessitating further optimization to offset this effect and increase potency.

Such a level of flexibility can be achieved through sugar modifications. These include, among others: incorporation of 2′-*O*-Me units to increase affinity and nuclease stability (4, 5); the incorporation of LNA analogs (6, 7) to dramatically increase binding affinity, improve nuclease stability, and reduce immunogenicity; and the incorporation of a 2′-*O*-MOE [2′-*O*-(2-methoxyethyl)] modification to increase affinity and nuclease stability (8). A thorough review on the subject can be found in Ref. (8, 9).

Iterative computational methods are available to arrive at a candidate that has the required properties for a given target. Still, an element of empiricism can be involved, for example, when designing siRNA oligos to an mRNA of interest due to variability in the properties of the specific binding site on the mRNA oligo. Oftentimes, this is addressed by utilizing a cocktail of siRNAs.

Nevertheless, compared to methodologies for the design and selection of small molecule drugs or biologics, the degree

of empiricism is somewhat limited, and originates from the fact that even short oligos have unique structures that impact their biophysical properties. In this context, we would like to highlight a recent publication, which reported on the development of an automated methodology for the prediction of the pharmacological properties of short DNA/LNA oligonucleotides. Namely, the authors apply quantum mechanical calculations to predict structures and electrostatic surface potentials for the oligos, which are primary determinants of interaction between molecules (10).

As an example, the authors studied the effects of changed internucleoside linkages from a phosphodiester (PO) to a phosphorothioate (PS). LNA-PO-AAG (**Figure 1A**) was compared with LNA-PS-AAG (with the PSs in the RS configuration) (**Figure 1B**). The LNA-PS-AAG (RS) modification resulted in a large potential change and exhibited a more scattered topology compared to LNA-PO-AAG, with a shift of the electrostatic potential toward the 5′ end. PS modification also induced changes in the localization of the frontier orbitals. The highest occupied molecular orbitals/lowest unoccupied molecular orbitals are split between adenine and guanine for LNA-PO-AAG (**Figure 1A**) but the LUMO resides on the central adenines for PS (**Figure 1B**) (10). The study illustrates the application of quantum mechanical modeling that can be used to understand antisense oligonucleotide properties and to explain the observation that small structural changes in oligonucleotide composition may lead to dramatic shifts in phenotypes, i.e., toxicity, protein binding, and tissue and cell uptake. This type of analysis could be applied in future oligonucleotide drug discovery and would allow the production improved antisense drugs.

NANOCARRIER DESIGN

Despite the advancements in oligonucleotide design for therapy, rapid entry into the clinic is hampered partly by obstacles related to oligo delivery *in vivo*. After intravascular administration, oligos get aggregated by serum proteins in the plasma, and/or are rapidly eliminated by the kidneys, resulting in very short intravascular circulating half-lives in the range of minutes (11). Additional obstacles to delivery include passage across the vascular endothelium, diffusion through the extracellular matrix, and translocation across the cell membrane. Finally, oligonucleotides are associated with immune activation, further limiting their clinical application (12, 13).

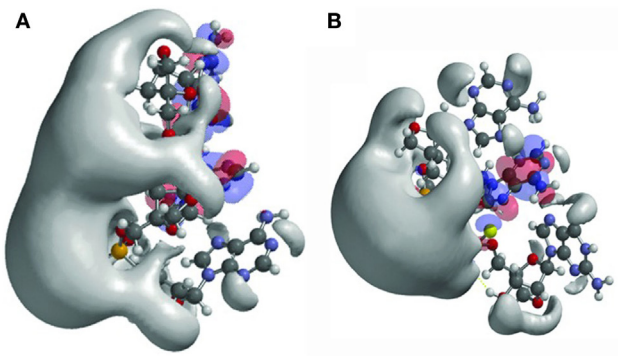

FIGURE 1 | Structures and frontier orbitals (red/blue) for **(A)** locked nucleic acid (LNA) with the sequence 5′-AAG-3′ (5′ end at *bottom* of structure) and **(B)** LNA with sequence 5′-AAG-3′, chemically modified by phosphorothioate internucleoside linkages (PS). The electrostatic potential (negative) is shown in gray and represented by an *Iso*-potential value of −83 kJ/mol. Reproduced from Ref. (10) with kind permission by Mary Ann Liebert, Inc.

These issues could be addressed by conjugating, complexing, or encapsulating the oligos to nanocarriers. These can be classified into three types: lipid-based, polymer-based, and inorganic nanoparticles. Nanocarrier design is optimized in terms of physicochemical properties (surface coating and particle size) in order to achieve optimal biodistribution and pharmacokinetics, to shield the oligo from degradation, to facilitate cellular uptake, and release the oligo in the proper intracellular compartment, and to satisfy requirements related to their physiological safety, including lack of immunogenicity, non-coagulation with serum proteins, and low non-specific uptake by normal tissues or cells.

As stated in Ref. (14), a major prerequisite for successful oligo delivery is the presence of positive charges on the surface of the nanoparticles that would facilitate uptake across cell membranes. However, cationic surface charges increase the chances of aggregate formation with plasma proteins. This can be overcome by the introduction of PEG on the surface of the nanocarrier. This can neutralize the surface charge and avoid interaction with plasma proteins, resulting in longer circulation half-life and faster diffusion across the extracellular matrix (15). However, this modification interferes with cellular uptake and necessitates an additional moiety for receptor-mediated endocytosis, which significantly limits the modular potential of the construct.

With respect to nanoparticle size, we are limited by the requirement that the size of the nanocarrier–oligo construct should be larger than the pore size of the glomerular filtering system (>7 nm) to avoid renal clearance but small enough (<100 nm) to avoid rapid phagocytosis by cells of the reticuloendothelial system (16–19). Typically, nanocarriers in the range of 10–100 nm in diameter are optimal to allow delivery to tissues through the enhanced permeation and retention effect. This is particularly relevant for solid tumors that are characterized by leaky vasculature (16, 20, 21). Even in poorly permeable tumors, nanocarriers smaller than 50 nm can penetrate the capillary endothelium, whereas micellar nanoparticles of 70 nm are retained in the vasculature (22). Based on these observations, the optimal size of nanocarriers for cancer treatment can be narrowed to 10–50 nm.

These requirements, as well as detailed descriptions of polymeric nanoparticles, lipid-based nanoparticles, and inorganic nanoparticles for oligo delivery can be found in Ref. (14). Here, we will highlight a few investigations that relate to the advancement of modularity in nanocarrier design. An ingenious new method was described earlier this year (23) that would permit the high throughput *in vivo* discovery of targeted nucleic acid nanotherapeutics. This methodology directly addresses the fact that nucleic acid therapeutics are limited by inefficient delivery to target tissues and by an incomplete understanding of how nanoparticle structure affects biodistribution. The authors developed a method to simultaneously measure the biodistribution of many chemically distinct nanoparticles by formulating the nanoparticles to carry specific DNA barcode oligonucleotides. These barcoded

nanoparticles were then administered to mice *in vivo*. After a pre-selected time, nanoparticle biodistribution was quantified by deep sequencing the barcodes (**Figure 2**). This method permitted the accurate measurement of relative quantities of nucleic acid delivered to tissues and identified chemical properties promoting nanoparticle delivery to specific tissues (23). Using this system, it should be possible to rapidly select nanoparticles targeting specific organs following *in vivo* administration. The approach would also facilitate a deeper understanding of how the chemical structure of nanoparticles affects their delivery *in vivo*.

To illustrate the modular potential of nanotechnology, we focus on a recent publication by Robert Siegwart's group at the University of Texas Southwestern Medical Center (24). In their study, the authors synthesized more than 1,500 siRNA-incorporating modular dendrimers using sequential, orthogonal reactions where ester degradability was systematically integrated with chemically diversified cores, peripheries, and generations (**Figure 3**). They then screened these dendrimers in cell lines and in mice to identify candidates that achieve high potency to tumors and low hepatotoxicity and provide a pronounced survival benefit in an aggressive liver cancer model (24). This study is just an example of the power of nanotechnology for modularity. However, multiple nanocarriers, beyond dendrimers, could be synthesized using a modular approach. These include soft/hollow-core nanoparticles, such as lipid nanoparticles, polymeric nanoparticles, carbon nanotubes, and porous silica nanoparticles, as well as hard-core nanoparticles, such as quantum dots, gold nanoparticles, and iron oxide nanoparticles. Also, modular building blocks can be utilized for the optimization of nanocarrier structure in terms of size, surface charge, spacer length, and functional groups to ensure long-term stability, the enhanced interaction with target transcriptomes, and optimal circulation half-life/biodistribution.

IMAGING

The role of imaging in cancer therapy is well established. As part of their routine work-up, patients are imaged by ultrasonography, computerized tomography (CT), MRI, or positron emission tomography (PET) to both diagnose and stage the disease, and to monitor the progress of treatment. The value and necessity for this type of analysis is indisputable. In addition to imaging, a wide variety of circulating biomarkers, such as circulating tumor cells, exosomes, and circulating cell-free DNA/RNA, are finding application in recent years. Finally, more invasive *in situ* diagnostic methods that involve biopsy are widely used and largely considered as the gold standard diagnostic approach.

In this review, we focus on imaging not for the diagnosis, staging, and monitoring of cancer, but rather for the specific measurement of drug delivery to the target tissue and/or the overall pharmacokinetics of the drug. Even though this kind of studies are routinely involved in the process of drug development, they are not part of patient care. Since the overall goal is the modular development of strictly personalized therapeutic agents, in the treatment paradigm that we illustrate here, knowledge about pharmacokinetics and drug delivery need to be obtained for each patient. Hopefully, this could be accomplished concurrently with the assessment of therapeutic response.

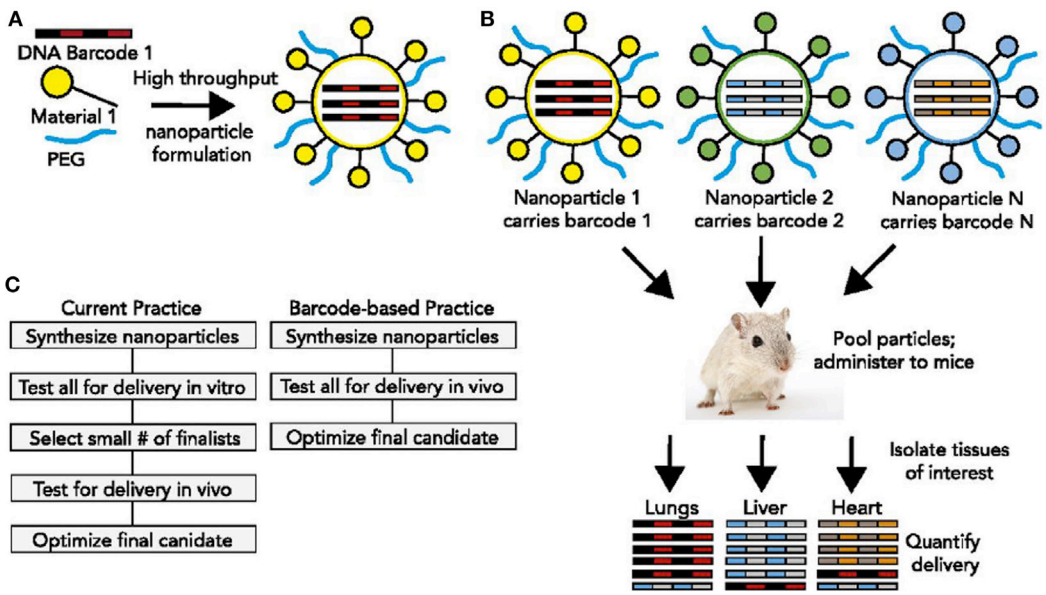

FIGURE 2 | DNA barcoded nanoparticles for high-throughput *in vivo* nanoparticle delivery. **(A)** Using high-throughput fluidic mixing, nanoparticles are formulated to carry a DNA barcode. **(B)** Many nanoparticles can be formulated in a single day; each nanoparticle chemical structure carries a distinct barcode. Particles are then combined and administered simultaneously to mice. Tissues are then isolated, and delivery is quantified by sequencing the barcodes. In this example, nanoparticle 1 delivers to the lungs, nanoparticle 2 delivers to the liver, and nanoparticle *N* delivers to the heart. **(C)** This DNA barcode system enables multiplexed nanoparticle-targeting studies *in vivo*, improving upon the current practice, which relies on *in vitro* nanoparticle screening to identify lead candidates. Reproduced from Ref. (23) with kind permission by the National Academy of Sciences.

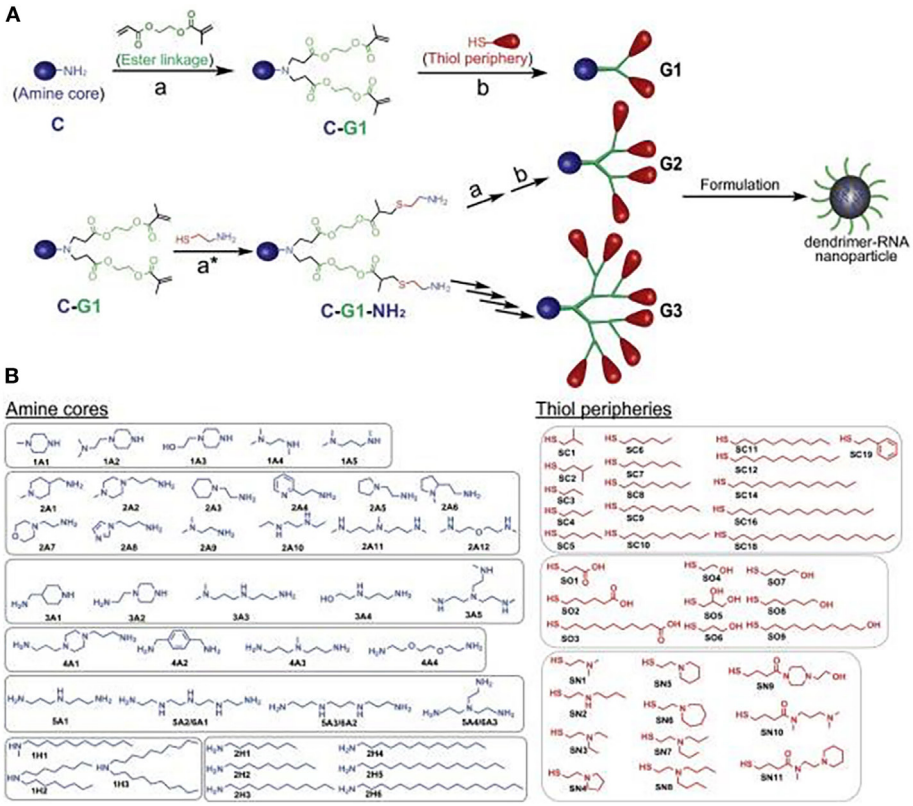

FIGURE 3 | A modular strategy for diversifying the chemical functionality and size of ester-based dendrimers allowed discovery of potent and nontoxic dendrimers for *in vivo* small-RNA delivery to tumor cells. **(A)** Orthogonal reactions accelerated the synthesis of >1,500 modular degradable dendrimers by combination of 42 cores (C) and 36 peripheries (P) through degradable linkages (L) and generations. The library was established *via* sequential reactions. First, amines (C) with a series of N–H bonds reacted quantitatively and selectively with the less steric acrylate groups of AEMA (L). The products (C–L) then quantitatively reacted with various thiols (P) under optimized DMPP-catalyzed conditions. **(B)** Dendrimers were independently modulated with chemically diverse amines and thiols. Selected amines were divided into two categories: ionizable amines (1A–6A) to tune RNA binding from C that generated one to six branched dendrimers, and alkyl amines (1H–2H) to tune NP C stabilization. Alkyl thiols (SC1–SC19) and alcohol/carboxylic acid terminated thiols (SO1–SO9) were selected to tune NP P stabilization. Aminothiols (SN1–SN11) were selected to tune P RNA binding. G2–G4 higher generation dendrimers with multiple branches were also synthesized using generation expansion reactions. Reproduced from Ref. (24) with kind permission by the National Academy of Sciences.

One study that illustrates this vision comes from Zaver Bhujwalla's group at Johns Hopkins University (25). The authors developed a PSMA-targeted nanoplex platform for theranostic imaging of prostate cancer. The therapeutic nanoplex was designed to deliver siRNA against choline kinase (Chk) along with a prodrug (5-fluorocytosine; 5-FC). Importantly, the nanoplex contained multimodal imaging reporters that permitted the assessment of its accumulation in tumors and its therapeutic effect manifested as siRNA-mediated down-regulation of Chk and the conversion of the prodrug 5-FC to the cytotoxic drug 5-FU. Specifically, SPECT/CT of mice bearing PC3-PIP and PC3-Flu tumors revealed a significantly higher uptake of the targeted nanoplex in PSMA-overexpressing PC3-PIP tumors compared to PC3-Flu tumors (**Figure 4A**). To assess the efficacy of siRNA-Chk to downregulate Chk, the authors acquired *in vivo* 1H MRSI of PC3-PIP tumors 48 h after administration of the nanoplex. As shown in **Figure 4B**, there was a significant decrease of the total choline signal that consists of free choline, PC, and glycerophosphocholine. Moreover, by performing 19F MRS, the authors observed the activity of the prodrug enzyme bCD, as it converted the prodrug 5-FC to 5-FU (**Figure 4C**) (25).

In our own work, we have strived to incorporate imaging of drug delivery as an indispensable companion to drug development. We have extensively used dextran coated iron oxide nanoparticles as delivery vehicles for siRNA or antagomir therapeutics to tumors (26–31).

Since these nanoparticles are easily detected by MRI, we have utilized this modality to measure drug bioavailability *in vivo*.

A specific application is illustrated in Ref. (29). The study described the testing of an imaging-capable nanodrug that was designed to inhibit the pro-metastatic miRNA-10b. The nanodrug's physicochemistry was specifically optimized to reach primary and metastatic tumor cells. Therapy was delivered to a mouse model of metastatic breast cancer. During the course of treatment, the animals were imaged by MRI in an attempt to fine-tune the administration schedule and design of the nanodrug. MRI revealed that the nanodrug was successfully delivered to the tumors, as shown by the decrease in transverse relaxation time

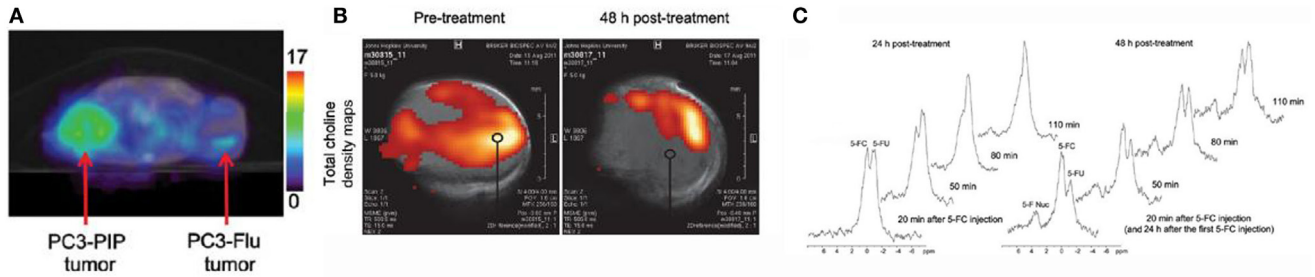

FIGURE 4 | A multimodal approach for the non-invasive assessment of drug bioavailability and therapeutic effect in a model of prostate cancer. **(A)** Representative SPECT images of a SCID mouse bearing PC3-PIP and PC3-Flu tumors. **(B)** *In vivo* total choline density maps from 2D CSI datasets acquired from a representative PC3-PIPtumor (~400 mm^3) before and 48 h after i.v. injection of the PSMA-targeted nanoplex 1 (150 mg/kg). **(C)** *In vivo* ^{19}FMR spectra acquired from a PC3-PIP tumor (~400 mm^3) at 24 and 48 h after i.v. injection of the PSMA-targeted nanoplex (150 mg/kg) carrying bCD and siRNA-Chk. Reproduced from Ref. (25) with kind permission by the American Chemical Society.

(**Figure 5A**). Quantitative analysis suggested a tendency toward nanodrug build-up in the tissue after the second treatment session (**Figure 5B**). These results illustrate a potentially useful application of imaging, especially when the delivery vehicle is innately imaging capable, as is the case for iron oxide nanoparticles. Such capabilities could be essential when optimizing a modular nanocarrier of this kind (29).

When the nanocarrier is not innately imaging-capable, it is highly beneficial to apply protocols for modular labeling of the nanocarrier with a radionuclide for nuclear imaging. This approach is illustrated in a study by Thomas Reiner's group at Memorial Sloan-Kettering Cancer Center (32). The authors developed an ^{89}Zr-based labeling strategy for liposomal nanoparticles that accumulate in tumors *via* passive targeting mechanisms. Labeling was accomplished either by click labeling (CLL) or surface chelation (SCL), illustrating the versatility of the labeling process. PET/CT imaging of the radiolabeled nanoparticles was performed on a mouse model of breast cancer. **Figure 6A** shows a comparative ^{89}Zr activity biodistribution in selected tissues after intravenous administration of the liposomes in mice bearing breast cancer xenografts. PET/CT imaging with ^{89}Zr-CLL at 2 h after injection showed predominantly liver and spleen uptake. In contrast, ^{89}Zr-SCL PET images at first showed high blood-pool activity and strong signals from liver and spleen. At 24 h, the blood-pool signal was moderate but tumor accumulation was higher (**Figure 6B**) (32).

The highlighted papers represent just a first step in the direction of integrating imaging more closely with the process of drug development and treatment planning. Given the need to obtain concurrent information of therapeutic response and drug delivery, it is likely that such approaches would involve a dual-modality capability, most likely PET-MR or PET-CT. The combination of these modalities is uniquely poised to obtain quantitative co-registered information about tumor dynamics, as a function of drug accumulation and could provide clues about the failure of some therapies in a given patient from the standpoint of drug delivery. On a broader scale, the introduction of this methodology would greatly enrich the process of drug development, which is currently hampered by a limited understanding of patient-to-patient variability in terms of drug delivery.

FUTURE OUTLOOK

While exciting, the vision we outline may be criticized for being unrealistic. A major impediment to the fulfillment of this vision would likely be cost. It does not seem cost-effective to completely elucidate the genetic profile of a given patient's tumor, identify causative therapeutic targets, and design oligonucleotide probes that would normalize the tumor cell phenotype. It would also not be cost-effective to diagnose and monitor each patient using sophisticated imaging modalities at multiple time points during therapy. Finally, the cost of synthesizing individualized drugs may seem overwhelming. However, given the high degree of trial-and-error empiricism that defines the current approaches, it is likely that the cost of multiple ineffective treatments is equally great not only in terms of money but, more importantly, in terms of patient distress and treatment failure.

An additional important point is the clear need for technological advancement before the vision of fully rational therapeutics could be fulfilled. Areas that need development include the following:

1. Complete elucidation of the genetic/epigenetic regulatory pathways that lead to cancer, so that we functionally understand the transcriptome of the cancer cell. This will allow us to predict the complete array of phenotypic effects of targeting a given gene/mRNA/or miRNA;
2. Design and validation of oligonucleotide probes that have the highest specificity and no off-target effects using non-empirical computational approaches;
3. Design and optimization of delivery vehicles for these oligonucleotide probes based on target organ, desired circulation half-life, need for no systemic toxicity, etc;
4. Development of standardized labeling protocols for image guidance and the implementation of optimal imaging protocols and instrumentation for a given modality.

Despite these issues, the vision of fully rational cancer therapy inspires hope defined mostly by the promise of better outcomes. Cancer is still largely an unaddressed health issue.

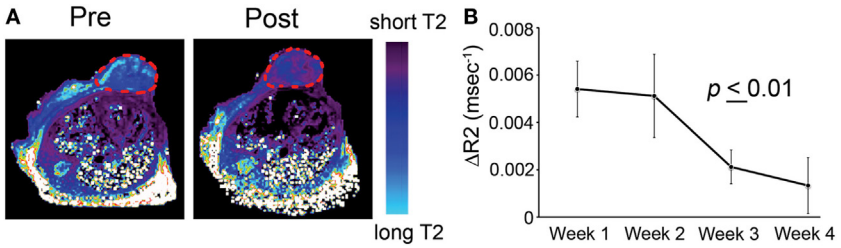

FIGURE 5 | T2-weighted magnetic resonance imaging of MN-anti-miR10b accumulation in orthotopic MDA-MB-231-luc-D3H2LN tumors. **(A)** Representative color-coded T2 maps before (left) and 24 h after (right) MN-anti-miR10b injection demonstrating a shortening of the T2 relaxation times of the tumors (outlined) consistent with nanodrug accumulation. **(B)** Quantitative analysis of ΔR2 relaxation rates (1/T2 pre − 1/T2 post, ms) of the tumors, suggesting a tendency toward build-up of the MN-anti-miR10b ($p \leq 0.01$, $n = 12$). Data are represented as mean ± SD. Reproduced from Ref. (29) with kind permission by Nature Publishing Group.

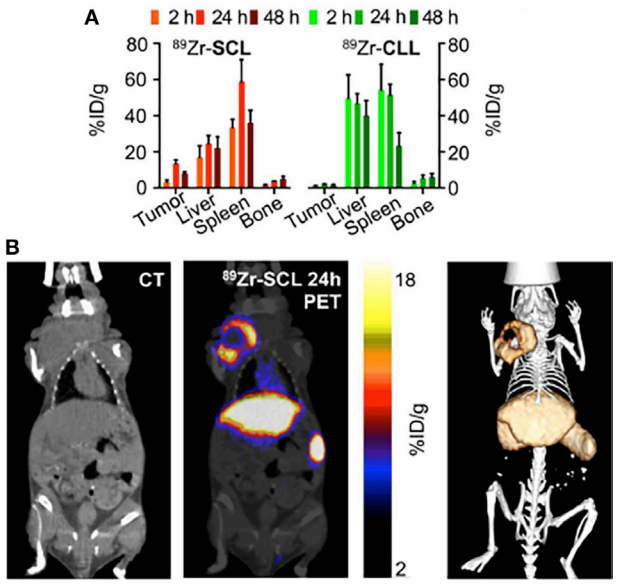

FIGURE 6 | Modular labeling for *in vivo* positron emission tomography (PET) imaging of tumor-homing nanoparticles. **(A)** Radioactivity distribution in selected tissues of ^{89}Zr-SCL and ^{89}Zr-CLL. **(B)** PET/computerized tomography (CT) imaging of ^{89}Zr-SCL: CT only (left), PET/CT fusion (middle), and 3-dimensional rendering of PET/CT fusion (right) at 24 h after injection. Reproduced from Ref. (32) with kind permission by the Society of Nuclear Medicine and Molecular Imaging.

It remains the second most common cause of death in the US, accounting for nearly one of every four deaths. As an example, pancreatic cancer is a devastating diagnosis defined by a mere 2% 5-year survival when diagnosed at an advanced inoperable stage, which defines 80% of the cases. Despite overall progress in research, the prognosis for people with pancreatic cancer has not improved in over 40 years. In light of the tremendous suffering caused by this disease and the modest progress achieved using standard treatments, it is clear that we need to explore radical, transformative approaches for therapy. The vision of fully rational drug design represents a hopeful step in that direction.

AUTHOR CONTRIBUTIONS

ZM conceived of the ideas presented and drafted the review. BY and A-MB drafted the sections detailing the highlighted research papers and provided feedback on the discussion.

FUNDING

The study was supported under grant R01CA16346101A1 from the National Cancer Institute to ZM. A-MB was supported by the CaNCURE program. CaNCURE is a partnership between Northeastern University and Dana-Farber/Harvard Cancer Center funded by the National Cancer Institute.

REFERENCES

1. Bennett CF, Swayze EE. RNA targeting therapeutics: molecular mechanisms of antisense oligonucleotides as a therapeutic platform. *Annu Rev Pharmacol Toxicol* (2010) 50:259–93. doi:10.1146/annurev.pharmtox.010909.105654
2. Stein CA, Hansen JB, Lai J, Wu S, Voskresenskiy A, Hog A, et al. Efficient gene silencing by delivery of locked nucleic acid antisense oligonucleotides, unassisted by transfection reagents. *Nucleic Acids Res* (2010) 38(1):e3. doi:10.1093/nar/gkp841
3. Kibler-Herzog L, Zon G, Uznanski B, Whittier G, Wilson WD. Duplex stabilities of phosphorothioate, methylphosphonate, and RNA analogs of two DNA 14-mers. *Nucleic Acids Res* (1991) 19(11):2979–86. doi:10.1093/nar/19.11.2979
4. Majlessi M, Nelson NC, Becker MM. Advantages of 2'-O-methyl oligoribonucleotide probes for detecting RNA targets. *Nucleic Acids Res* (1998) 26(9):2224–9. doi:10.1093/nar/26.9.2224
5. Rettig GR, Behlke MA. Progress toward in vivo use of siRNAs-II. *Mol Ther* (2012) 20(3):483–512. doi:10.1038/mt.2011.263
6. Koshkin AA, Wengel J. Synthesis of novel 2',3'-linked bicyclic thymine ribonucleosides. *J Org Chem* (1998) 63(8):2778–81. doi:10.1021/jo972239c
7. Fontenete S, Barros J, Madureira P, Figueiredo C, Wengel J, Azevedo NF. Mismatch discrimination in fluorescent in situ hybridization using different types of nucleic acids. *Appl Microbiol Biotechnol* (2015) 99(9):3961–9. doi:10.1007/s00253-015-6389-4
8. Deleavey GF, Damha MJ. Designing chemically modified oligonucleotides for targeted gene silencing. *Chem Biol* (2012) 19(8):937–54. doi:10.1016/j.chembiol.2012.07.011

9. Khvorova A, Watts JK. The chemical evolution of oligonucleotide therapies of clinical utility. *Nat Biotechnol* (2017) 35(3):238–48. doi:10.1038/nbt.3765
10. Koch T, Shim I, Lindow M, Orum H, Bohr HG. Quantum mechanical studies of DNA and LNA. *Nucleic Acid Ther* (2014) 24(2):139–48. doi:10.1089/nat.2013.0465
11. Soutschek J, Akinc A, Bramlage B, Charisse K, Constien R, Donoghue M, et al. Therapeutic silencing of an endogenous gene by systemic administration of modified siRNAs. *Nature* (2004) 432(7014):173–8. doi:10.1038/nature03121
12. Judge AD, Sood V, Shaw JR, Fang D, McClintock K, MacLachlan I. Sequence-dependent stimulation of the mammalian innate immune response by synthetic siRNA. *Nat Biotechnol* (2005) 23(4):457–62. doi:10.1038/nbt1081
13. Hornung V, Guenthner-Biller M, Bourquin C, Ablasser A, Schlee M, Uematsu S, et al. Sequence-specific potent induction of IFN-α by short interfering RNA in plasmacytoid dendritic cells through TLR7. *Nat Med* (2005) 11(3):263–70. doi:10.1038/nm1191
14. Yoo B, Medarova Z. Nanoformulations for pharmacological siRNA delivery in cancer. In: Bulte J, Modo M, editors. *Design and Applications of Nanoparticles in Biomedical Imaging*. Switzerland: Springer International Publishing (2017). p. 171–86.
15. Stylianopoulos T, Poh M-Z, Insin N, Bawendi MG, Fukumura D, Munn LL, et al. Diffusion of particles in the extracellular matrix: the effect of repulsive electrostatic interactions. *Biophys J* (2010) 99(5):1342–9. doi:10.1016/j.bpj.2010.06.016
16. Lin Q, Chen J, Zhang Z, Zheng G. Lipid-based nanoparticles in the systemic delivery of siRNA. *Nanomedicine* (2014) 9(1):105–20. doi:10.2217/nnm.13.192
17. Kanasty RL, Whitehead KA, Vegas AJ, Anderson DG. Action and reaction: the biological response to siRNA and its delivery vehicles. *Mol Ther* (2012) 20(3):513–24. doi:10.1038/mt.2011.294
18. Aird WC. Phenotypic heterogeneity of the endothelium I. Structure, function, and mechanisms. *Circ Res* (2007) 100(2):158–73. doi:10.1161/01.RES.0000255691.76142.4a
19. Wisse E, Jacobs F, Topal B, Frederik P, De Geest B. The size of endothelial fenestrae in human liver sinusoids: implications for hepatocyte-directed gene transfer. *Gene Ther* (2008) 15(17):1193–9. doi:10.1038/gt.2008.60
20. Choi HS, Liu W, Misra P, Tanaka E, Zimmer JP, Ipe BI, et al. Renal clearance of quantum dots. *Nat Biotechnol* (2007) 25(10):1165–70. doi:10.1038/nbt1340
21. Singh S, Sharma A, Robertson GP. Realizing the clinical potential of cancer nanotechnology by minimizing toxicologic and targeted delivery concerns. *Cancer Res* (2012) 72(22):5663–8. doi:10.1158/0008-5472.CAN-12-1527
22. Cabral H, Matsumoto Y, Mizuno K, Chen Q, Murakami M, Kimura M, et al. Accumulation of sub-100 nm polymeric micelles in poorly permeable tumours depends on size. *Nat Nanotechnol* (2011) 6(12):815–23. doi:10.1038/nnano.2011.166
23. Dahlman JE, Kauffman KJ, Xing Y, Shaw TE, Mir FF, Dlott CC, et al. Barcoded nanoparticles for high throughput in vivo discovery of targeted therapeutics. *Proc Natl Acad Sci U S A* (2017) 114(8):2060–5. doi:10.1073/pnas.1620874114
24. Zhou K, Nguyen LH, Miller JB, Yan Y, Kos P, Xiong H, et al. Modular degradable dendrimers enable small RNAs to extend survival in an aggressive liver cancer model. *Proc Natl Acad Sci U S A* (2016) 113(3):520–5. doi:10.1073/pnas.1520756113
25. Chen Z, Penet MF, Nimmagadda S, Li C, Banerjee SR, Winnard PT Jr, et al. PSMA-targeted theranostic nanoplex for prostate cancer therapy. *ACS Nano* (2012) 6(9):7752–62. doi:10.1021/nn301725w
26. Ghosh SK, Yigit MV, Uchida M, Ross AW, Barteneva N, Moore A, et al. Sequence-dependent combination therapy with doxorubicin and a survivin-specific small interfering RNA nanodrug demonstrates efficacy in models of adenocarcinoma. *Int J Cancer* (2014) 134(7):1758–66. doi:10.1002/ijc.28499
27. Medarova Z, Pham W, Farrar C, Petkova V, Moore A. In vivo imaging of siRNA delivery and silencing in tumors. *Nat Med* (2007) 13(3):372–7. doi:10.1038/nm1486
28. Kumar M, Yigit M, Dai G, Moore A, Medarova Z. Image-guided breast tumor therapy using a small interfering RNA nanodrug. *Cancer Res* (2010) 70(19):7553–61. doi:10.1158/0008-5472.CAN-10-2070
29. Yigit MV, Ghosh SK, Kumar M, Petkova V, Kavishwar A, Moore A, et al. Context-dependent differences in miR-10b breast oncogenesis can be targeted for the prevention and arrest of lymph node metastasis. *Oncogene* (2013) 32(12):1530–8. doi:10.1038/onc.2012.173
30. Yoo B, Kavishwar A, Ross A, Wang P, Tabassum DP, Polyak K, et al. Combining miR-10b-targeted nanotherapy with low-dose doxorubicin elicits durable regressions of metastatic breast cancer. *Cancer Res* (2015) 75(20):4407–15. doi:10.1158/0008-5472.CAN-15-0888
31. Yoo B, Kavishwar A, Wang P, Ross A, Pantazopoulos P, Dudley M, et al. Therapy targeted to the metastatic niche is effective in a model of stage IV breast cancer. *Sci Rep* (2017) 7:45060. doi:10.1038/srep45060
32. Perez-Medina C, Abdel-Atti D, Zhang Y, Longo VA, Irwin CP, Binderup T, et al. A modular labeling strategy for in vivo PET and near-infrared fluorescence imaging of nanoparticle tumor targeting. *J Nucl Med* (2014) 55(10):1706–11. doi:10.2967/jnumed.114.141861

Conflict of Interest Statement: ZM is Founder, Director, and Scientific Advisory Board Member of TransCode Therapeutics, Inc.

frontiers in Oncology

REVIEW
published: 22 December 2017
doi: 10.3389/fonc.2017.00314

Fluorescence-Guided Surgery

*Tadanobu Nagaya, Yu A. Nakamura, Peter L. Choyke and Hisataka Kobayashi**

Molecular Imaging Program, Center for Cancer Research, National Cancer Institute, National Institutes of Health, Bethesda, MD, United States

Surgical resection of cancer remains an important treatment modality. Despite advances in preoperative imaging, surgery itself is primarily guided by the surgeon's ability to locate pathology with conventional white light imaging. Fluorescence-guided surgery (FGS) can be used to define tumor location and margins during the procedure. Intraoperative visualization of tumors may not only allow more complete resections but also improve safety by avoiding unnecessary damage to normal tissue which can also reduce operative time and decrease the need for second-look surgeries. A number of new FGS imaging probes have recently been developed, complementing a small but useful number of existing probes. In this review, we describe current and new fluorescent probes that may assist FGS.

OPEN ACCESS

Edited by:
Marie-France Penet, Johns Hopkins University, United States

Reviewed by:
Luigi Aloj, Cambridge University Hospitals NHS Foundation Trust, United Kingdom
Laurence Gluch, The Strathfield Breast Centre, Australia

***Correspondence:**
Hisataka Kobayashi
kobayash@mail.nih.gov

Specialty section:
This article was submitted to Cancer Imaging and Diagnosis, a section of the journal Frontiers in Oncology

Received: *27 October 2017*
Accepted: *05 December 2017*
Published: *22 December 2017*

Citation:
Nagaya T, Nakamura YA, Choyke PL and Kobayashi H (2017) Fluorescence-Guided Surgery. Front. Oncol. 7:314. doi: 10.3389/fonc.2017.00314

Keywords: fluorescence-guided surgery, activatable probe, monoclonal antibodies, molecular imaging, always-on probe

INTRODUCTION

Surgery is a primary mode of treatment for many malignancies. For example, 63–98% of patients with lung, breast, bladder, and colorectal cancer will undergo surgery (1). The goal of surgery is to safely remove as much cancer as possible. The degree to which cancer is removed relates closely to prognosis. However, the ability to resect tumor currently relies on the visual localization of the tumor and/or the ability to palpate it. The former is limited by the low contrast between tumors and background tissue and many small tumors may be missed. Moreover, the determination of tumor margins must often be done blindly followed by frozen section pathologic analysis.

The presence of residual tumor cells after resection is considered a strong predictor of tumor recurrence and, therefore, survival. Many studies show that positive margins, defined as the identification of tumor cells at the cut edge of a surgical specimen, are associated with increased local recurrence and indicate a poor prognosis in most cancer types including head and neck cancers (2), breast cancer (3, 4), non-small-cell lung cancer (5), colorectal cancer (6), bladder cancer (7), and prostate cancer (8). Despite advances in preoperative imaging such as computerized tomography (CT), magnetic resonance imaging (MRI), and positron emission tomography, surgical margin positivity rate has not changed significantly over the past several decades (9), with margin positivity rates of 15–60% across all cancers (10–16). Currently, the standard of care for achieving negative

Abbreviations: AAA, abdominal aortic aneurysm; ALA, aminolevulinic acid; ADC, antibody-drug-conjugate; APC, antibody-photo-absorber conjugate; CA, carbohydrate antigen; CABG, coronary artery bypass grafting; CEA, carcinoembryonic antigen; CT, computerized tomography; epidermal growth factor receptor; FDA, Food and Drug Administration; FGS, fluorescence-guided surgery; FITC, fluorescein isothiocyanate; FLARE, fluorescence-assisted resection and exploration; FRET, Föster (fluorescence) resonance energy transfer; gGlu, γ-glutamyl; GGT, γ-glutamyltransferase; H-dimer, homo-dimers; HLA, hexaminolevulinate; HMRG, hydroxymethyl rhodamine green; ICG, indocyanine green; mAb, monoclonal antibodies; MB, methylene blue; MMP, matrix metalloproteinase; MRI, magnetic resonance imaging; NDA, New Drug Application, NIR, near-infrared; PET, positron emission tomography; PeT, photon induced electron transfer; PIT, photoimmunotherapy; Pp, protoporphyrin; PSMA, prostate-specific membrane antigen; SLN, sentinel lymph node; TBR, target-to-background ratio; VEGF, vascular endothelial growth factor.

margins rests on visual inspection, palpation, and intraoperative histopathological analysis of frozen tumor margins all of which have severe limitations. The naked eye is limited in its ability to detect small tumors. Palpation is limited in sensitivity and is increasingly not used due to the increased utilization of robotic laparoscopic surgery. Intraoperative frozen section analysis is limited to certain tissue types, is time-consuming, and is prone to sampling error. Frozen section analysis is discrepant with permanent pathology in 5–15% of cases (17).

A number of non-optical imaging methods have been proposed during surgery. Typically, these methods are not targeted to the tumor *per se* but rely on anatomic abnormalities to define the tumor. For instance, intraoperative CT and MRI have played a significant role in the field of neurosurgical image guidance (18–20). However, intraoperative systems are costly, complex and require space. Moreover, their use interrupts the normal workflow of the surgical procedure lengthening operative/anesthesia times. These methods are, mainly used for neurosurgery at major medical centers.

Therefore, practical methods for augmenting the surgeon's ability to resect tumors are needed. One such method is fluorescence-guided surgery (FGS). The first use of fluorescence imaging in surgery dates back to 1948 when surgeons used intravenous fluorescein to enhance intracranial neoplasms during neurosurgery (21). Since then, additional fluorescent agents have been used for a variety of surgical applications (22–24). Intraoperative fluorescence imaging offers the benefits of high contrast and sensitivity, low cost, absence of ionizing radiation, ease of use, safety, and high specificity (25, 26). Compared with standard unaided vision using white light imaging, real-time fluorescence imaging is helpful in identifying cancerous tissue and delineating tumor margins. Moreover, improved visualization of the cancer can reduce damage to important normal structures such as nerves, blood vessels, ureters, and bile ducts.

In this review article, we focus on the currently used Food and Drug Administration (FDA)-approved fluorescent probes and new types of fluorescence imaging probes for FGS that are under development.

CURRENT FGS

The exponential growth in the field of FGS is demonstrated by the number of published articles in the field, which has grown from under 50/year in 1995, to nearly 500/year in 2015 (27). Furthermore, FGS has enjoyed a number of preliminary successes (23, 28) and some FGS techniques have already achieved clinical success (29). FGS may improve tumor resection rates while minimizing normal tissue resection (9, 30, 31). This can translate into improved clinical outcomes.

Compared to expensive traditional imaging methods, optical methods are less costly and require less space. One cost estimate of the fluorescence-assisted resection and exploration (FLARE) system is 120,000 USD and 40,000 USD for the mini-FLARE (32, 33). Of course, this does not include the cost of the optical probe itself but the overall costs are much lower than with conventional imaging. Moreover, because it is portable a single instrument could be shared among multiple operating rooms.

Fluorescence-guided surgery has been currently used for multiple surgical situations, including sentinel lymph node (SLN) mapping, identification of solid tumors, lymphography, angiography, and anatomical imaging during surgery. Importantly, FGS can be used seamlessly during the procedure without interrupting the surgeon's workflow. This integrates FGS into the surgery creating numerous opportunities for its use. We summarize current clinical and preclinical FGS techniques in **Table 1**.

TABLE 1 | Current clinical and preclinical fluorescence-guided surgery techniques.

Application	Types	Contrast agent	Status
Sentinel lymph node mapping	Breast cancer	Indocyanine green (ICG) (34–37)	Clinical
		Methylene blue (MB) (38, 39)	Clinical
	Melanoma	ICG (40, 41)	Clinical
	Head and neck cancer	ICG (42)	Clinical
	Lung cancer	ICG (43)	Clinical
	Esophagus cancer	ICG (44, 45)	Clinical
	Gastric cancer	ICG (46, 47)	Clinical
	Colorectal cancer	ICG (48)	Clinical
	Anal cancer	ICG (49)	Clinical
	Prostate cancer	ICG (50–52)	Clinical
	Penile cancer	ICG (51, 52)	Clinical
Lymphography	Lymph flow	ICG (53–55)	Clinical
Angiography	Cerebral aneurysm	Fluorescein sodium (56–58)	Clinical
	Coronary artery bypass grafting	ICG (59, 60)	Clinical
	Abdominal aortic aneurysm	ICG (61)	Clinical
	Abdominal surgery	ICG (62, 63)	Clinical
	Reconstructive surgery	ICG (64–70)	Clinical
Anatomic imaging	Cholangiography	ICG (71, 72)	Clinical
	Pancreas	MB (73)	Preclinical
		T700-F (74)	Preclinical
	Ureters	MB (75)	Preclinical
	Nerves	Various fluorescently labeled peptide (NP) (76, 77)	Preclinical
	Parathyroid and thyroid grands	T700 and T800 fluorophores (78)	Preclinical
	Endocrine grands	Various near-infrared fluorophores (79–81)	Preclinical
Tumor imaging	Malignant glioma	5-ALA (82–86)	Clinical
		Fluorescein sodium (87–89)	Clinical
		BLZ-100 (90)	Clinical
		GB119 (91)	Preclinical
	Brain metastases	Fluorescein sodium (92, 93)	Clinical
	Head and neck cancer	IRDye800CW conjugate (94, 95)	Clinical
		IRDye700DX conjugate (96)	Clinical
	Hepatocellular carcinoma	ICG (97–100)	Clinical
	Liver metastases	ICG (99)	Clinical
	Breast cancer	MB (101)	Clinical
		EC17 (102)	Clinical
		IRDye800CW conjugate (102)	Clinical
		LUM015 (103)	Clinical
		AVB-620 (104)	Clinical

(*Continued*)

TABLE 1 | Continued

Application	Types	Contrast agent	Status
	Lung and chest masses	ICG (105)	Clinical
		Folate-fluorescein isothiocyanate (FITC) (106)	Clinical
		EC17 (107)	Clinical
		OTL38 (108)	Clinical
	Ovarian cancer	ICG (109)	Clinical
		Folate-FITC (28)	Clinical
		EC17 (110)	Clinical
		OTL38 (111)	Clinical
		gGlu-HMRG (112)	Preclinical
	Pancreatic cancer	Green fluorophore conjugate (113, 114)	Preclinical
		IRDye800CW conjugate (102)	Preclinical
	Insulinoma	MB (73)	Preclinical
	Solitary fibrous tumor (pancreas)	MB (115)	Preclinical
	Renal cell carcinoma	EC17 (116)	Clinical
		OTL38 (102)	Clinical
	Bladder cancer	5-ALA/HAL (117–120)	Clinical
	Prostate cancer	ICG conjugate (121)	Preclinical
		5-ALA (122)	Clinical
	Gastric cancer	ICG (123–125)	Clinical
	Colorectal cancer	Green fluorophore conjugate (113)	Preclinical
		IRDye800CW conjugate (126)	Clinical
		gGlu-HMRG (127)	Preclinical
	Basal cell carcinoma	5-ALA (128)	Clinical
		GB119 (129)	Preclinical
	Sarcoma	LUM015 (103)	Clinical
	Parathyroid adenoma	MB (130)	Clinical
Laparoscopic- and robotic-assisted surgeries	Nephrectomy	ICG (131)	Clinical
	Cholecystectomy	ICG (72, 132)	Clinical
	Esophagectomy	ICG (133)	Clinical
	Gastrectomy	ICG (134)	Clinical
	Adrenalectomy	ICG (135, 136)	Clinical
Fluorescence endoscopy	Brain aneurysm	ICG (137–139)	Clinical
	Endonasal surgery	ICG (140–142)	Clinical
	Angiography	ICG (142, 143)	Clinical
	Brain tumor	ICG (140, 144, 145)	Clinical
	Head and Neck tumor	ICG (146)	Clinical
	Gastric cancer	ICG (123–125)	Clinical
Marking tumor	Colonic tattooing	ICG (147–149)	Clinical

CLINICALLY AVAILABLE FLUORESCENCE IMAGING

There has been an explosion of interest in FGS, which has led to a steady demand for new fluorescence imaging devices and probes. Currently, most FGS imaging has been performed with the Novadaq SPY system which was the first to be approved by FDA in 2005; however, several new fluorescence imaging systems have subsequently been approved by the FDA as shown in **Table 2**. These systems are approved for a variety of procedures including imaging blood flow, tissue perfusion, and circulation in free flaps, plastic surgery, and reconstructive surgery. These systems are portable making their positioning within a room completely customizeable to the situation. Hand-held cameras of PDE and Fluobeam, for instance, possess the advantage of being compact and convenient for real-time fluorescence imaging. Other cameras such as Quest Spectrum and VS3 Iridium simultaneously show the white light image and the fluorescent probe image overlay which reduces distractions for the surgeon (150, 151). In the field of breast oncology, the SPY system has been applied to monitor skin perfusion in nipple-sparing mastectomies using ICG as the imaging probe. This method can guide the location of mastectomy incisions and minimize ischemic complications (152).

A successful device should be able to display RGB white light imaging, fluorescence imaging, and overlay imaging. The device should be capable of quantitating the light intensity to the extent possible. Quantitation permits FGS to be used in multicenter trials and allows comparison at different time points in the same patient. Further investigations are needed to establish reliable quantitative analyses of fluorescent imaging.

CURRENT CLINICAL USE OF FLUORESCENCE IMAGING PROBES

Biomedical fluorescence imaging operates in wavelengths in the visible spectrum (400–700 nm), extending into the near infrared (NIR) spectrum (700–900 nm). A large number of commercially available fluorophores are available; however, few are clinically approved. While the majority of fluorescent probes emit light in the visible range, this is probably the least desirable part of the spectrum due to overlap with tissue autofluorescence and high absorbance of light in tissue in the visible spectrum. NIR fluorophores are better suited for *in vivo* imaging. While, wavelengths below 700 nm are strongly absorbed in tissue by

TABLE 2 | Clinically available Food and Drug Administration-approved fluorescence imaging systems.

Imaging system	Company	Excitation wavelength(s) (nm)	Light source	Working distance (cm)	Field of view (cm)	Real-time overlay
SPY	Novadaq Technologies	805	Laser	~30	19 × 14	No
PDE	Hamamatsu Photonics	760	LED	~20	5 × 5 to 10 × 6.7	No
Fluobeam 700 (800)	Fluoptics Minatec	680 (750)	Laser	15 ~ 25	2.2 × 1.5 to 20 × 14	No
Quest Spectrum	Quest Medical Imaging	400–1,000	Laser	5~	2.25 × 2.25 (5 cm distance)	Yes
VS3 Iridium system	VisionSense	805	Laser	~30	19 × 14	Yes

endogenous molecules, such as hemoglobin and myoglobin, wavelengths above 900 nm are limited by water and lipid absorption wavelengths (153–155). Fluorophores emitting light <700 or >900 nm are, therefore, limited in their ability to penetrate tissue (156). The "NIR window" from 700 to 900 nm arises from less absorbance in tissues, allowing for deeper imaging and detection (153, 154). Thus, fluorophores in the NIR range have excellent potential for FGS. Fluorescence imaging using NIR fluorophores enhances cancer surgery navigation and offers higher sensitivity when compared to preoperative imaging, visual inspection, and palpation during surgery (157). Next, we will focus on the currently used fluorescence imaging probes in surgical oncology (**Table 3**).

Indocyanine Green (ICG)

Currently, ICG is one of the most frequently employed NIR fluorophores used for FGS. ICG is a water-soluble, anionic, amphiphilic tricarbocyanine probe with a molecular weight of 776 Da (158, 159), which rapidly binds to plasma proteins in the body. The excitation peak is 780 nm and the emission peak is at 820 nm, which places outside the range of most tissue autofluorescence. ICG was first produced in 1955 by the Kodak Research Laboratories, and in 1959 it was approved by the FDA for retinal angiography. Historically, it has been clinically used to measure cardiac output (160), hepatic function (161), and retinal angiography (162).

Throughout its history, ICG has maintained a high safety index (25, 163, 164), as the number of allergic reactions is very low (1:10,000, as reported by manufacturer) (165). ICG also allows multiple repeated uses due to its short half-life of 150 to 180 s and is cleared exclusively by the liver (166).

Near infrared ICG-guided SNL mapping has been performed in various cancers as shown in **Table 1**. ICG has also been used for lymphography (167), angiography (61, 168), reconstructive surgery (65, 67), cholangiography (71) and tumor imaging (99), and so on. The use of ICG for delineating tumors has been a success. For instance, ICG fluorescence imaging identified 100% of primary hepatocellular carcinomas (HCCs) and in 40% of the cases also identified additional, small (3–6 mm) HCCs that would otherwise have gone undetected (98).

TABLE 3 | Currently used Food and Drug Administration-approved fluorescence probes.

Fluorescence probe	Excitation	Emission	Fluorescence type
Indocyanine green	780 nm	820 nm	Indocyanin green
Methylene blue (MB)	670 nm	690 nm	MB
5-Aminolevulinic acid (5-ALA)	380–440 nm	620 nm (alkaline pH) 634 nm (acid pH)	Porphyrin
Fluorescein sodium	494 nm	512 nm	Fluorescein
Folate	495 nm (folate-FITC)	520 nm (folate-FITC)	Fluorescein isothiocyanate (FITC)
IRDye800CW conjugate	775 nm	796 nm	IRDye800
IRDye700DX conjugate	680 nm	687 nm	IRDye700
Activatable probes	Various	Various	Various

Methylene Blue (MB)

Methylene blue is a heterocyclic aromatic compound with a molecular weight of 320 Da (51). It is a FDA-approved visible (dark blue) contrast agent. When sufficiently diluted, MB acts as a near-infrared fluorescent dye that operates within the NIR optical window with an absorption peak at 670 nm and an emission peak at 690 nm and is naturally excreted through the urine (51). MB was the first entirely synthetic drug used in medicine and was used in the treatment of malaria as early as 1891 by Guttmann and Ehrlich (169). MB continues to be applied and investigated as treatment for a variety of medical applications in the clinical setting, including methemoglobinemias and ifosfamide-induced encephalopathy (170, 171). MB has also been used to identify breast cancer (101) and neuroendocrine tumors (73), and is commonly used for SLN mapping (38, 39), as well as the identification of urologic tumors (51, 52) and tumors in the parathyroid glands (130).

Methylene blue is known to be relatively safe; however, the use of MB can potentially lead to cardiac arrhythmias, coronary vasoconstriction, decreased cardiac output, decreased renal blood flow and mesenteric blood flow, and increased pulmonary vascular pressure (172). Although MB accumulates in most tumors, the amount of accumulation varies with tumor type. Therefore, dye concentration appropriately matched to each tumor type is required (38).

5-Aminolevulinic Acid (5-ALA)

5-ALA is the major substrate for protoporphyrin synthesis, and has been used clinically for tumor detection and tumor treatment (photodynamic therapy; PDT), as a FDA-approved substance. 5-ALA, typically administered in a topical or oral form, induces synthesis and accumulation of the fluorescent molecule protoporphyrin IX (PpIX) in epithelia and neoplastic tissues (83, 85, 86). 5-ALA-induced PpIX exhibits multiple physiochemical states depending on the microenvironment. One of the most important parameters affecting the state of PpIX is pH. In the pH range 3 to 11.5, there are two distinct states: emission peaks at 620 nm in alkaline environments and emission peaks at 634 nm in acidic environments after excitation with visible blue light of 380–440 nm (173, 174).

Cancer specific FGS with 5-ALA has been successfully implemented for resection of malignant gliomas in Europe after studies clearly demonstrated clinical benefits with regards to completeness of tumor removal (65% complete resection with 5-ALA compared to 36% in the white light group) and progression-free survival with its use (83). 5-ALA and derivatives have also been described in bladder cancer (117, 118, 120) and prostate cancer (122).

The use of 5-ALA has been limited by its relatively high costs, and an inconvenient method of administration (it is administered orally some hours before it is to be used). The high risk of skin sensitization within 24 h after the operation (the patient should not be exposed to sunlight or strong artificial light) also presents a challenge to its use (175).

Fluorescein Sodium

Fluorescein sodium is a fluorescent drug that can be used intravenously to improve visualization of brain tumor tissue based

primarily on non-specific vascular leakage. It is also used for retinal angiography (56–58). Fluorescein sodium is a sodium salt and an organic fluorescent dye with peak excitation at 494 nm and peak emission at 512 nm. It has been safely used in humans for many years, predominantly in ophthalmology for retinal angiography, and the cost of fluorescein sodium is relatively low when compared with the cost of 5-ALA (176). Fluorescein sodium is usually visible to the naked eye at high dosages (20 mg/kg body weight), and is observable through the yellow 560 nm filter at lower doses, allowing better tissue discrimination with more natural colors (177, 178).

The use of fluorescein sodium for the identification of intracranial tumors has been known since 1947 (179). As an FGS agent, fluorescein sodium has been commonly used for identifying glioblastoma (88) and metastatic brain tumors (92, 93). It has also been used for intracranial angiography (56–58).

NEW FLUORESCENCE IMAGING PROBES

The ideal fluorescence imaging probe must provide excellent contrast between the tumor or affected lymph node and healthy tissue (180). Therefore, a current challenge is to design fluorescent imaging probes with high selectivity for tumors, high tumor to background ratios, and minimal toxicity (155).

Current clinical studies are based on contrast agents that have already been approved. The most often used fluorophores are blood pool agents (including ICG) that have no inherent specificity for tumor or normal tissues, and thus are not ideal fluorophores for FGS. A number of new agents are currently being investigated, including several dyes from the cyanine family, such as Cy5.5, Cy7, Cy7.5, IR-dyes, nanoparticle formulations, and visible spectrum dyes (181). Most research focuses on increasing the availability of novel, fluorescently labeled agents to identify crucial landmarks, such as tumor margins, lymph nodes, and vital structures of interest to surgeons. A new generation of agents that target-specific antigens have been based on antibodies (113, 182, 183), nanobodies (184), aptamers, and peptides (77). Other approaches make use of enzymes for fluorescence activation (185–189).

In the following sections, we summarize progress made in several specific targeted optical imaging agents for FGS.

Folate-Targeted FGS

The Folate receptor is commonly upregulated on tumor cells and, therefore, is a good candidate for a general-purpose fluorescently labeled, targeted agent. An example is folate fluorescein isothiocyanate (folate-FITC) that excites at a wavelength of 495 nm and emits at 520 nm (190). Folate and these folate analogs are internalized in the cell *via* receptor-mediated endocytosis within 2 h (191). Once inside the endosome, the conjugate remains intact and can, therefore, remain fluorescent after internalization (191, 192). This stability led to the development of a broad variety of folate-targeted conjugates. van Dam et al. used a folate fluorescein isothiocyanate to identify tumor implants in ovarian cancer patients who were undergoing abdominal surgery (28). Lung adenocarcinoma is also known to express high levels of folate receptor α (193, 194). This was exploited by Okusanya et al. who demonstrated that lung adenocarcinomas demonstrated fluorescence in 92% (46/50) of patients with folate-FITC (106). Another folate analog, EC17, was also used for imaging renal cell carcinoma, although only two of four cancers were detected (116). In another study using EC17 for intraoperative detection of ovarian cancer, Tummers et al. showed that the addition of FGS resulted in a16% increase in the resection of malignant tumors when compared to visual inspection and palpation (110). Of course, the clinical significance of this increase is still uncertain. Another folate analog, OTL38, has been used to delineate renal cell carcinoma margins during partial nephrectomy (102), and to identify ovarian cancer (111). Hoogstins et al. also reported that OTL38 accumulated in folate receptor α-positive tumors and metastases in 12 patients with ovarian cancer, enabling the surgeon to resect an additional 29% of malignant lesions that were not identified by inspection and/or palpation (111). Recently, both EC17 and OTL38 were also used for intraoperative lung tumor imaging (107, 108). Like all targeted agents, folate-FITC is restricted to use only in tumors over expressing folate receptor and, by virtue of the visible light emitted by FITC, the agent has a limited depth penetration.

Monoclonal Antibody-Based Fluorescent Probes

Perhaps the most generalizable FGS probes are based on monoclonal antibodies (mAb) conjugated to a fluorescent dye. There are at least two scenarios in which mAb-based fluorescent probes could become clinically useful. One is in fluorescence-guided navigation to aid surgeons in detecting tiny lesions and determining the margin between cancer and normal tissue. Another is in selecting patients whose cancer cells express a sufficient amount of target to enable molecularly targeted therapies such as antibody–drug conjugates or antibody-photo-absorber conjugates.

Promising preclinical examples of targeted fluorescently labeled probes include anti carcinoembryonic antigen in pancreatic cancer and colorectal cancer conjugated to a green fluorophore (113), anti carbohydrate antigen 19-9 in pancreatic cancer conjugated to a green fluorophore (114), epidermal growth factor receptor (EGFR) and EGFR type2 (HER2) in breast cancer (195–197) and prostate-specific membrane antigen (PSMA) in prostate cancer conjugated to ICG (121). Most mAb-based fluorescent probes are designed for systemic administration. Compared to other routes of administration, such as oral or intra-tumoral injection, systemic administration allows for more homogeneous microdistribution. Moreover, systemic administration allows for sufficient washout time to elapse, to allow for the elimination of non-specific fluorescence from the blood and the urinary tract (22). In contrast to intra-tumoral injection, systemic administration also allows the detection of previously unrecognized tumor foci or metastases.

Few of these mAb-based fluorescent probes have progressed into clinical testing. One that did, a first-in-human clinical trial of fluorescence-guided navigation to aid surgery in head and neck cancers is currently underway. This trial utilizes the anti-EGFR antibody conjugate, cetuximab-IRDye800CW for use in head and neck cancers (94, 95). In this trial, Rosenthal et al. demonstrated

that the EGFR mAb-fluorophore conjugate was both safe and effective. The target-to-background ratio (TBR) achieved in this study (mean TBR of 5.2 in the highest dose range) improved the accuracy of surgical decision-making (95). Recently, cetuximab-IRDye800CW or bevacizumab-IRDye800CW (targeting vascular endothelial growth factor)-have also been in clinical trials targeting pancreatic adenocarcinoma, colon cancer, and breast cancer (102, 126). It was noted that the conjugation of the IRDye800CW significantly shortened the circulating half-life of cetuximab despite a low antibody-to-dye conjugation ratio (approximately 1) (95). Rapid clearance of mAb–dye conjugates can help lower the background signal; however, it can simultaneously compromise tumor accumulation. Taken together, these alterations could lower the overall performance of the agent.

Another exciting advancement with potential implications for FGS is a technique called "near infrared photoimmunotherapy" (NIR-PIT) (96). NIR-PIT is based on an antibody that targets a cell-surface antigen but is conjugated to a photoabsorbing dye (IRDye700DX) that has both fluorescent characteristics and the ability to damage cells to which it has conjugated. Thus, NIR-PIT has the dual ability to localize tumors and as well as selectively eliminate cancer cells. The cytotoxic effects of NIR-PIT are observed only when the mAb-IR700 conjugate is bound to receptors on the cell membrane; no phototoxicity is observed when the conjugate is present but not yet bound (96). Therefore, NIR-PIT achieves highly selected targeted cancer cell killing. NIR-PIT has been shown to be effective in a variety of different cancer cell types exhibiting a range of surface antigens such as EGFR, CD20, mesothelin, and PSMA (198–202). Furthermore, a first-in-human phase 2 trial of NIR-PIT in patients with inoperable head and neck cancer was recently completed and the agent is being commercialized. NIR-PIT has great potential as a new cancer treatment for many tumor types when combined with FGS.

These fluorescence imaging probes, including IRDye700DX and IRDye800CW, typically result in an "always-on" type of fluorescence signal. Therefore, fluorescence in the cancer tissues is roughly related to the amount of conjugated mAb bound to the tumor. By showing sufficient expression of target molecules, activatable fluorescent probes would be useful for selecting eligible patients who could be efficiently treated with FGS.

Activatable Fluorescent Probes

Based on pharmacokinetics, the "perfect" *in vivo* targeting agent has not yet been developed. The fundamental disadvantage of "always-on" probes is that they emit signal regardless of their proximity or interaction with the target tissues. As a result, there is considerable background signal to contend with. In order to design superior molecular imaging probes, one seeks to either (1) maximize signal from the target, (2) minimize signal from the background, or (3) do both. All lead to improved TBR, which, in turn, improves the sensitivity and specificity for detecting tumors with imaging (203).

Activatable fluorescent probes ("smart probes") target tumor cells by taking advantage of the physiologic differences between cancerous and normal cells, thus enhancing tumor margin detection (204). Because activatable probes do not emit signals before engaging the target, unbound probes do not yield a signal. Therefore, there is less background signal to compromise the sensitivity and specificity, yielding an absolute increase in TBR (205). Consequently, compared with "always-on" fluorescent probes, activatable fluorescent probes have a higher TBR (203). Preclinical studies have shown the merits of this approach (206–208). For example, when employing the antibody as a platform for activatable imaging probes, IgG-based activatable probes typically yield both the highest signal (due to high binding) as well as highest TBR (due to absent background signal) compared with "always-on" probes (203, 209, 210) (**Figure 1**).

There are two basic types of activatable fluorescent probes (**Figure 2**) (203, 207, 211). One type is enzyme reactive activatable fluorescent probe, which exist in the quenched state until they are activated by enzymatic cleavage mostly outside of the cells (212, 213) (**Figure 2**). Well known targeted enzymes are cathepsin, matrix metalloproteinases (MMP), γ-glutamyltransferase (GGT), and beta-galactosidases. Some of enzyme reactive activatable fluorescent probes can be topically or locally applied.

Another type of activatable fluorescent probe is molecular-binding activatable fluorescent probes, which are quenched until activated in targeted cells by endolysosomal processing (**Figure 2**). Within the lysosome, catabolism can occur under conditions such as low pH, protease activity, or oxidation, which

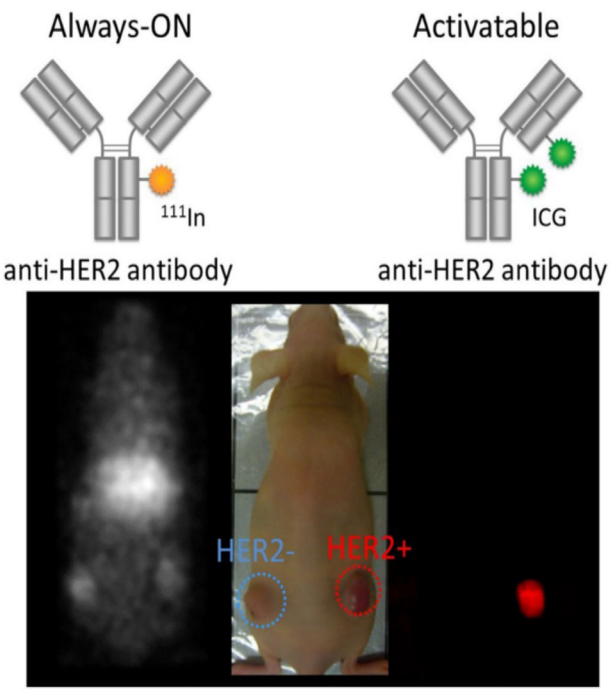

FIGURE 1 | Comparison of molecularly targeted fluorescent probes using always-on and activatable fluorescence strategies. Radiolabeled trastuzumab targeting HER2 with always-on fluorophores depicts both bound and unbound agents (left and right tumors) resulting in poor target-to-background ratio (TBR). In contrast, the activatable fluorescent probe, indocyanine green (ICG)-labeled trastuzumab, depicts only HER2-expressing tumors (right tumor) without incurring background signal resulting in superior TBR. Reprinted from publication (210) with permission from Elsevier.

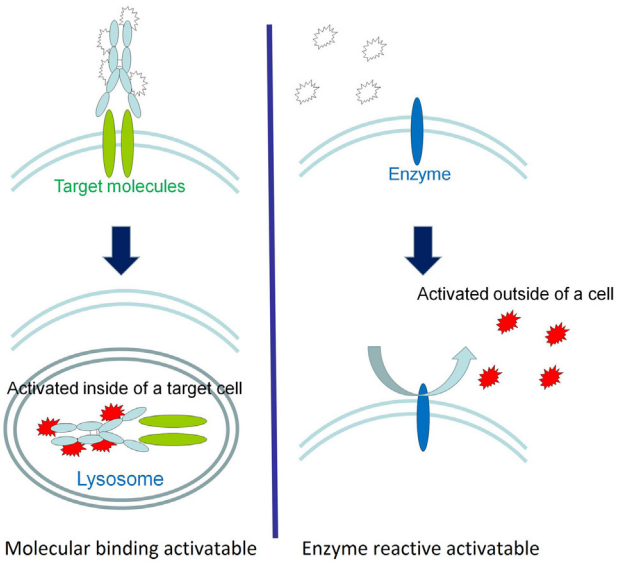

FIGURE 2 | A schematic explanation of the two types of activatable fluorescence probes. The fluorescence activation of molecularly targeted activatable probes occurs intracellularly (left), whereas enzyme reactive activation typically occurs in the extracellular environment (right). Reprinted with permission from Ref. (203). Copyright 2011 American Chemical Society.

can release the fluorophore from its quenched state. For example, a pH-activatable fluorescent probe produces light only in tumors due to their acidic microenvironment, resulting in high TBR whereas control "always-on" probes produce lower TBR due to higher background signal (**Figure 3**) (155, 214). This type of activatable fluorescent probe is administered systematically *via* intravenous injection.

There are advantages and disadvantages to both methods. In enzymatic activation, a single target enzyme can activate many different fluorescent molecules, thus amplifying the signal from the target tissue. However, a disadvantage of enzymatic activation is that the activation occurs in the extracellular space and the enzyme may diffuse away from the target contributing to background signal. Furthermore, this type of probe lacks specificity because none of the currently utilized enzymes for fluorescence activation are specific for carcinogenesis. In contrast, probes that are activated by endolysosomal processing, are highly specific for cancer and generally remain localized to the target as activation relies upon the probe binding specific cell-surface receptors and being internalized. However, molecular-binding of specific activatable fluorescent probes requires a biological and catabolic process to gain sufficient TBR. Targeted activatable fluorescent probes need to first leak from the vasculature, bind target cells, and then internalize within the target cell to activate the probe. The activation process often requires days, which decreases their practicality for routine clinical use (214). Novel activatable fluorescent probes targeting additional physiologic characteristics of cancer cells, such as degradation of the micelle, thiol concentration, surface lectins, and antibody binding, are also currently in development (159, 207, 211, 215–218). Translating these activatable fluorescent probes into clinical studies could significantly increase the number and quality of intraoperative imaging tools available during cancer excision.

Activatable fluorescent probes vary greatly by the mechanism by which fluorescence is quenched. The best known quenching mechanism is Föster (fluorescence) resonance energy transfer (FRET), wherein energy from one fluorophore is transferred to another molecule when the two molecules are in close (<10 nm) proximity. The FRET pair can consist of two fluorophores (self-quenching) or a fluorophore and a quencher molecule (203, 219). Homo-dimer (H or J-dimer) formation is other method of quenching. For instance, xanthene derivatives are known to form H-dimers at higher concentrations (~mM) which induces shifts of absorbance spectra, completely quenching fluorescence (195, 203). Fundamental to both FRET and H-dimer formation is the inter-fluorophore processing that occurs when the two molecules are in proximity to each other.

Another quenching mechanism, photon induced electron transfer (PeT) occurs when an electron is transfered from the PeT donor to the excited fluorophore diminishing the fluorescence signal. When the PeT donor is cleaved from the fluorophore or inactivated, activation occurs. Unlike FRET and H-dimer formation, PeT occurs within a single fluorophore molecule and does not require the presence of a second fluorophore (203, 220). The PeT mechanism has a particularly high dequench:quench light ratio.

Yet another mechanism of dequenching is to hold two fluorophores in close proximity to each other using a peptide backbone. In the presence of an enzyme the peptide backbone is cleaved releasing and activating the fluorophores.

The first activatable fluorescent probe to be tested in clinical trials was LUM015. The activation of LUM015 relied on cleavage by a cathepsin protease, an enzyme commonly overexpressed by tumors (221). LUM015 is optically inactive under normal conditions, but upon proteolytic cleavage, a covalently attached quencher molecule is released and fluorescence signal greatly intensifies (103). It was first evaluated by Whitley et al. in a cohort of 15 patients with breast cancer or soft-tissue sarcoma (103). Intravenous injection of this protease-activated fluorescent imaging probe before surgery was well tolerated, and imaging of resected human tissues showed that fluorescence from the tumor was significantly higher than fluorescence from normal tissues (103).

Recently, several other mechanisms have been tested. A quenched activatable cell-penetrating peptide, AVB-620 was tested in a first-in-human clinical trial in which 27 breast cancer patients received the infusion followed by surgical excision. Infusion of AVB-620 was safe and improved intraoperative cancer detection (104). Another new approach is to use peptide conjugated to ICG. In this case the agent, BLZ-100, uses chlorotoxin (36-amino acid peptide) as the targeting moiety and conjugates it to ICG. This agent has been used for glioma imaging (90).

Sprayable Activatable Fluorescent Probes

In many cases, the dequenching process takes hours to days making it problematic for integration into surgical workflows.

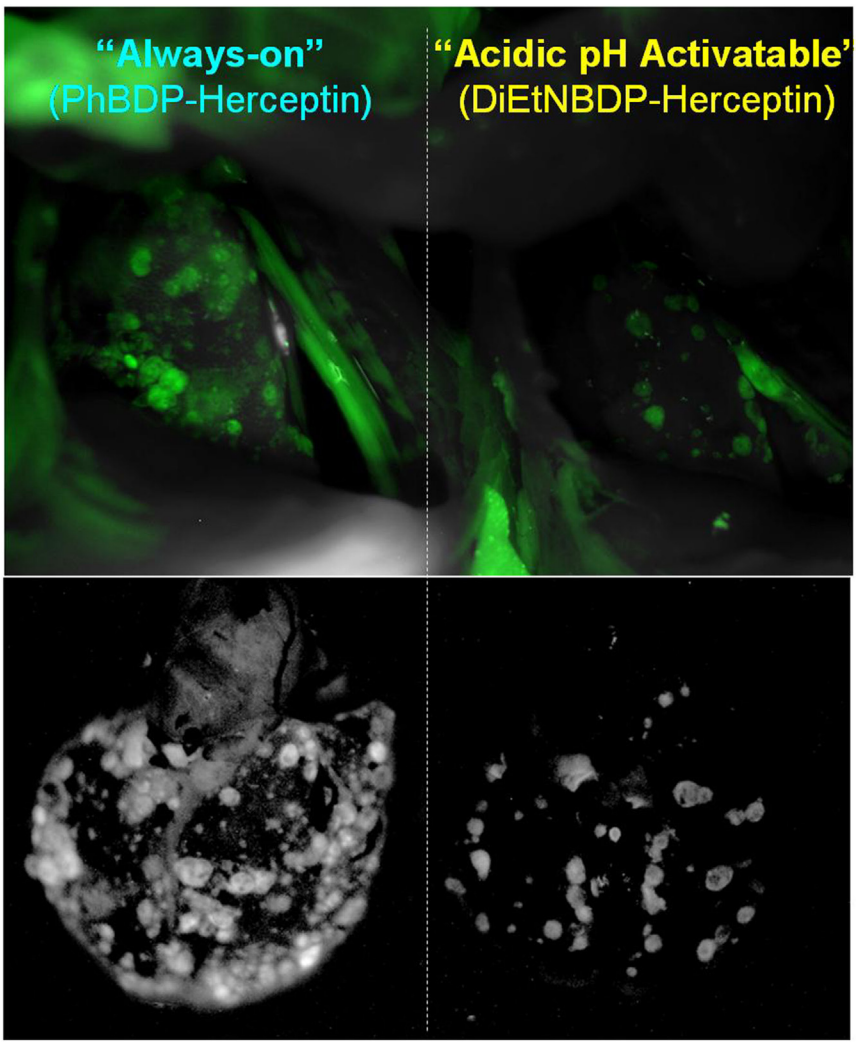

FIGURE 3 | *In vivo* tumor detection with targeted activatable fluorescent probes in a HER2-positive lung metastasis model mice. The pH-activatable fluorescent probe produces light only in tumors in the lung. However, the control "always-on" probe produces fluorescent signal from both tumors and normal lung and heart reducing the tumor to background ratio. Reprinted with permission from Ref. (155). Copyright 2010 American Chemical Society.

For instance, activatable probes using cathepsin D and MMP2/9 (222, 223), should be systemically injected at least a day before the surgery to be delivered to cancer and fully activated because of multiple cleavage sites. However, the kinetics of some other enzyme reactive probes is much faster especially when activated by a single cleavage. Therefore, such enzymatically activatable fluorescent probes can be so fast as to be used as needed during a surgical procedure. For instance, Urano et al. developed the activatable fluorescent probe, γ-glutamyl hydroxymethyl rhodamine green (gGlu-HMRG). The gGlu-HMRG is completely quenched by spirocyclic caging, but is activated rapidly with a one-step enzymatic reaction in the presence of GGT which is often present on cell membranes of cervical and ovarian cancer cells. As a result, this probe activates within 10 min of it being sprayed on. In a mouse model of human ovarian cancer, Urano et al. sprayed the abdominal cavity with the gGlu-HMRG probe and demonstrated that small tumor nodules could be visualized within 10 min after administration and remained labeled for at least 1 h (**Figure 4**) (112). Mitsunaga et al. used gGlu-HMRG during colonoscopy to differentiate long-term colitis from early colitis-associated cancer in a mouse colon cancer mouse model. They were able to visualize cancers and dysplasia 5–30 min after spraying gGlu-HMRG on the colon surface. Moreover, signal from cancer/dysplasia was 10 times higher than background fluorescence despite the presence of colitis (127). gGlu-HMRG probe has recently been tested in fresh human surgical specimens of colorectal tumor (224) and breast cancer (225) for detecting tumor borders and metastatic lymph nodes as a precursor to it being introduced in clinical trials. Similarly, these probes revealed that topical administration of the agent on aspirated specimens from patients with pancreatic tumors resulted in tumor-specific enhancement (226).

Other sprayable activatable probes are in development. These are activated by enzymes by a single cleavage such as cathepsin

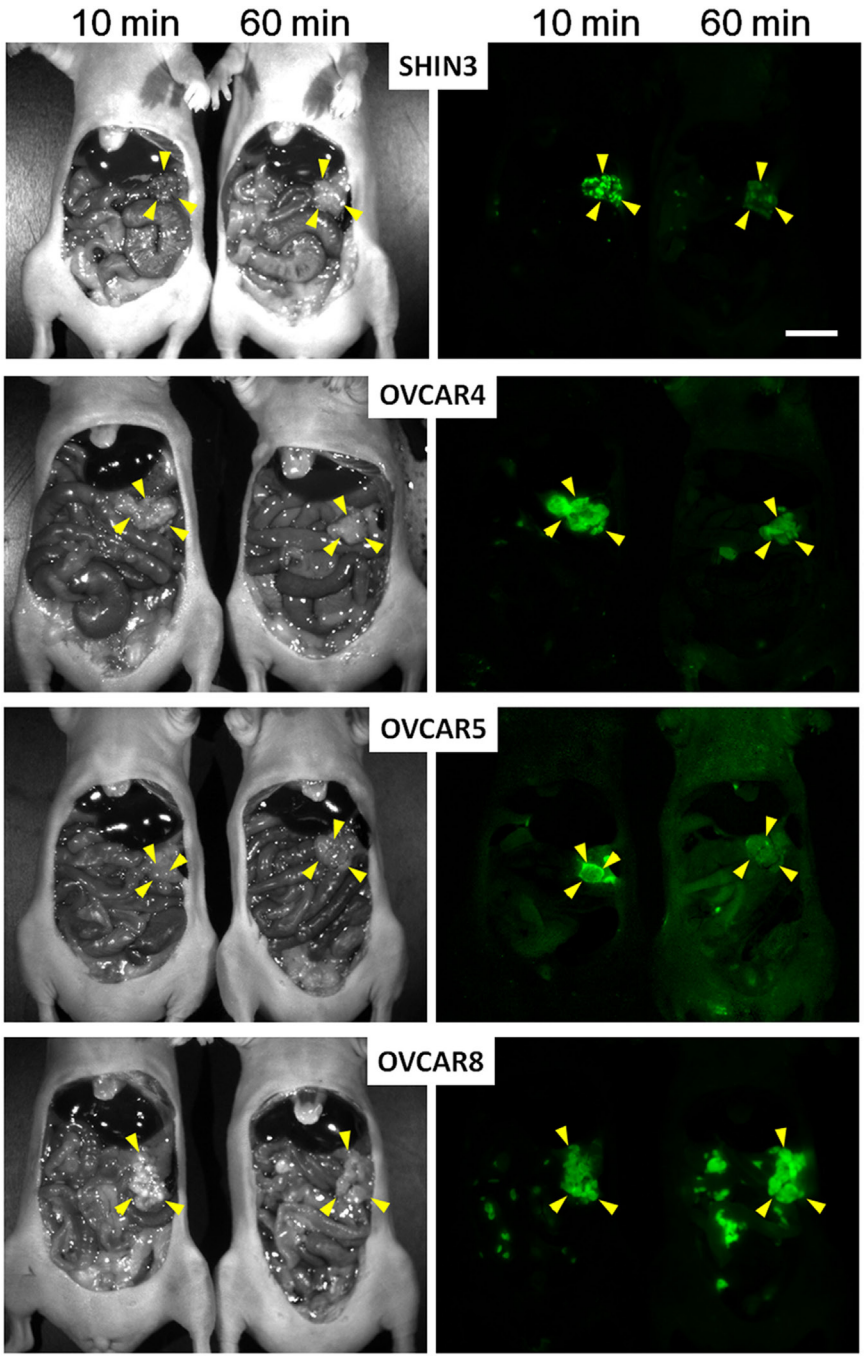

FIGURE 4 | Spectral fluorescence images of four peritoneal ovarian cancers using gGlu-HMRG. *In vivo* fluorescence intensity of a sprayable probe. By 10 and 60 min after intraperitoneal gGlu-HMRG administration each of four peritoneal ovarian tumor models: SHIN3, OVCAR4, OVCAR5, and OVCAR8 were evaluated. Yellow arrowheads indicate tumor location. Scale bar, 1 cm. Reprinted from publication (112) with permission from AAAS.

(91, 129), beta-galactosidase (227), endo-aminopeptidases (228), and NADPH (229).

The various types of recently developed activatable fluorescent probes tend to be superior to always-on probes; however, their safety in patients is yet to be determined. Given the relatively small market, bringing such agents thru the approval process to a New Drug Application will be challenging.

SUMMARY

The limits of white light imaging during surgical and endoscopic procedures are well known. It is acknowledged that current optical methods tend to have insufficient sensitivity for small tumors and do poorly at determining tumor margins. Targeted fluorescence imaging can provide additional information that

augments the ability of the operator to see and treat pathology, thus lowering the rate of persistent or recurrent disease. FGS, because of its high sensitivity, low cost, portability and real-time capabilities, has great potential to improve surgical outcomes. Not only can this approach direct intraoperative image guidance for surgical margin assessments but can also help surgeons detect microscopic tumors or residual lesions that may have otherwise been missed. In addition, anatomical fluorescence imaging techniques can aid in avoiding complications in various surgical situations. Despite the availability of these technologies, most surgeons still rely largely on visual and tactile cues combined with presurgical radiologic imaging to guide tissue resection.

As techniques continue to improve, FGS will move toward the concept of "precision surgical therapy." It is possible that FGS will be personally designed for each patient's specific disease process. Although much more work is necessary to reach this goal, in the meantime there is a rapidly expanding number of targeted fluorescence imaging probes that offer great potential for the future. Hopefully, these advances will enable FGS to become more widely available for a broad range of cancer types.

AUTHOR CONTRIBUTIONS

All authors listed have made a substantial, direct, and intellectual contribution to the work and approved it for publication.

ACKNOWLEDGMENTS

This review was supported by the Intramural Research Program of the NIH, National Cancer Institute, Center for Cancer Research (ZIA BC 011512).

REFERENCES

1. DeSantis CE, Lin CC, Mariotto AB, Siegel RL, Stein KD, Kramer JL, et al. Cancer treatment and survivorship statistics, 2014. *CA Cancer J Clin* (2014) 64(4):252–71. doi:10.3322/caac.21235
2. Haque R, Contreras R, McNicoll MP, Eckberg EC, Petitti DB. Surgical margins and survival after head and neck cancer surgery. *BMC Ear Nose Throat Disord* (2006) 6:2. doi:10.1186/1472-6815-6-2
3. Singletary SE. Surgical margins in patients with early-stage breast cancer treated with breast conservation therapy. *Am J Surg* (2002) 184(5):383–93. doi:10.1016/S0002-9610(02)01012-7
4. Meric F, Mirza NQ, Vlastos G, Buchholz TA, Kuerer HM, Babiera GV, et al. Positive surgical margins and ipsilateral breast tumor recurrence predict disease-specific survival after breast-conserving therapy. *Cancer* (2003) 97(4):926–33. doi:10.1002/cncr.11222
5. Snijder RJ, Brutel de la Riviere A, Elbers HJ, van den Bosch JM. Survival in resected stage I lung cancer with residual tumor at the bronchial resection margin. *Ann Thorac Surg* (1998) 65(1):212–6. doi:10.1016/S0003-4975(97)01114-4
6. Nagtegaal ID, Quirke P. What is the role for the circumferential margin in the modern treatment of rectal cancer? *J Clin Oncol* (2008) 26(2):303–12. doi:10.1200/jco.2007.12.7027
7. Dotan ZA, Kavanagh K, Yossepowitch O, Kaag M, Olgac S, Donat M, et al. Positive surgical margins in soft tissue following radical cystectomy for bladder cancer and cancer specific survival. *J Urol* (2007) 178(6):2308–12; discussion 2313. doi:10.1016/j.juro.2007.08.023
8. Wieder JA, Soloway MS. Incidence, etiology, location, prevention and treatment of positive surgical margins after radical prostatectomy for prostate cancer. *J Urol* (1998) 160(2):299–315. doi:10.1097/00005392-199808000-00003
9. Rosenthal EL, Warram JM, Bland KI, Zinn KR. The status of contemporary image-guided modalities in oncologic surgery. *Ann Surg* (2015) 261(1):46–55. doi:10.1097/sla.0000000000000622
10. Ravasz LA, Slootweg PJ, Hordijk GJ, Smit F, van der Tweel I. The status of the resection margin as a prognostic factor in the treatment of head and neck carcinoma. *J Craniomaxillofac Surg* (1991) 19(7):314–8. doi:10.1016/S1010-5182(05)80339-7
11. Choti MA, Sitzmann JV, Tiburi MF, Sumetchotimetha W, Rangsin R, Schulick RD, et al. Trends in long-term survival following liver resection for hepatic colorectal metastases. *Ann Surg* (2002) 235(6):759–66. doi:10.1097/00000658-200206000-00002
12. McMahon J, O'Brien CJ, Pathak I, Hamill R, McNeil E, Hammersley N, et al. Influence of condition of surgical margins on local recurrence and disease-specific survival in oral and oropharyngeal cancer. *Br J Oral Maxillofac Surg* (2003) 41(4):224–31. doi:10.1016/S0266-4356(03)00119-0
13. Woolgar JA, Triantafyllou A. A histopathological appraisal of surgical margins in oral and oropharyngeal cancer resection specimens. *Oral Oncol* (2005) 41(10):1034–43. doi:10.1016/j.oraloncology.2005.06.008
14. Iczkowski KA, Lucia MS. Frequency of positive surgical margin at prostatectomy and its effect on patient outcome. *Prostate Cancer* (2011) 2011:673021. doi:10.1155/2011/673021
15. Atkins J, Al Mushawah F, Appleton CM, Cyr AE, Gillanders WE, Aft RL, et al. Positive margin rates following breast-conserving surgery for stage I-III breast cancer: palpable versus nonpalpable tumors. *J Surg Res* (2012) 177(1):109–15. doi:10.1016/j.jss.2012.03.045
16. Chagpar AB. Cavity shave margins in breast cancer. *N Engl J Med* (2015) 373(22):2187–8. doi:10.1056/NEJMc1511344
17. Rosenthal EL, Warram JM, de Boer E, Basilion JP, Biel MA, Bogyo M, et al. Successful translation of fluorescence navigation during oncologic surgery: a consensus report. *J Nucl Med* (2016) 57(1):144–50. doi:10.2967/jnumed.115.158915
18. Kubben PL, ter Meulen KJ, Schijns OE, ter Laak-Poort MP, van Overbeeke JJ, van Santbrink H. Intraoperative MRI-guided resection of glioblastoma multiforme: a systematic review. *Lancet Oncol* (2011) 12(11):1062–70. doi:10.1016/s1470-2045(11)70130-9
19. Li L, Wang P, Chen L, Ma X, Bu B, Yu X. Individualized treatment of craniovertebral junction malformation guided by intraoperative computed tomography. *J Spinal Disord Tech* (2012) 25(2):77–84. doi:10.1097/BSD.0b013e31820f8afb
20. Singh H, Rote S, Jada A, Bander ED, Almodovar-Mercado GJ, Essayed WI, et al. Endoscopic endonasal odontoid resection with real-time intraoperative image-guided computed tomography: report of 4 cases. *J Neurosurg* (2017):1–6. doi:10.3171/2017.1.jns162601
21. Moore GE, Peyton WT. The clinical use of fluorescein in neurosurgery; the localization of brain tumors. *J Neurosurg* (1948) 5(4):392–8. doi:10.3171/jns.1948.5.4.0392
22. Nguyen QT, Tsien RY. Fluorescence-guided surgery with live molecular navigation – a new cutting edge. *Nat Rev Cancer* (2013) 13(9):653–62. doi:10.1038/nrc3566
23. Vahrmeijer AL, Hutteman M, van der Vorst JR, van de Velde CJ, Frangioni JV. Image-guided cancer surgery using near-infrared fluorescence. *Nat Rev Clin Oncol* (2013) 10(9):507–18. doi:10.1038/nrclinonc.2013.123
24. DeLong JC, Hoffman RM, Bouvet M. Current status and future perspectives of fluorescence-guided surgery for cancer. *Expert Rev Anticancer Ther* (2016) 16(1):71–81. doi:10.1586/14737140.2016.1121109
25. Alander JT, Kaartinen I, Laakso A, Patila T, Spillmann T, Tuchin VV, et al. A review of indocyanine green fluorescent imaging in surgery. *Int J Biomed Imaging* (2012) 2012:940585. doi:10.1155/2012/940585
26. Xi L, Jiang H. Image-guided surgery using multimodality strategy and molecular probes. *Wiley Interdiscip Rev Nanomed Nanobiotechnol* (2016) 8(1):46–60. doi:10.1002/wnan.1352
27. AV DS, Lin H, Henderson ER, Samkoe KS, Pogue BW. Review of fluorescence guided surgery systems: identification of key performance capabilities beyond indocyanine green imaging. *J Biomed Opt* (2016) 21(8):80901. doi:10.1117/1.jbo.21.8.080901

28. van Dam GM, Themelis G, Crane LM, Harlaar NJ, Pleijhuis RG, Kelder W, et al. Intraoperative tumor-specific fluorescence imaging in ovarian cancer by folate receptor-alpha targeting: first in-human results. *Nat Med* (2011) 17(10):1315–9. doi:10.1038/nm.2472
29. Aldave G, Tejada S, Pay E, Marigil M, Bejarano B, Idoate MA, et al. Prognostic value of residual fluorescent tissue in glioblastoma patients after gross total resection in 5-aminolevulinic acid-guided surgery. *Neurosurgery* (2013) 72(6):915–20; discussion 920–1. doi:10.1227/NEU.0b013e31828c3974
30. Hussain T, Nguyen QT. Molecular imaging for cancer diagnosis and surgery. *Adv Drug Deliv Rev* (2014) 66:90–100. doi:10.1016/j.addr.2013.09.007
31. de Boer E, Harlaar NJ, Taruttis A, Nagengast WB, Rosenthal EL, Ntziachristos V, et al. Optical innovations in surgery. *Br J Surg* (2015) 102(2):e56–72. doi:10.1002/bjs.9713
32. Lee BT, Hutteman M, Gioux S, Stockdale A, Lin SJ, Ngo LH, et al. The FLARE intraoperative near-infrared fluorescence imaging system: a first-in-human clinical trial in perforator flap breast reconstruction. *Plast Reconstr Surg* (2010) 126(5):1472–81. doi:10.1097/PRS.0b013e3181f059c7
33. Hill TK, Mohs AM. Image-guided tumor surgery: will there be a role for fluorescent nanoparticles? *Wiley Interdiscip Rev Nanomed Nanobiotechnol* (2016) 8(4):498–511. doi:10.1002/wnan.1381
34. Motomura K, Inaji H, Komoike Y, Kasugai T, Noguchi S, Koyama H. Sentinel node biopsy guided by indocyanine green dye in breast cancer patients. *Jpn J Clin Oncol* (1999) 29(12):604–7. doi:10.1093/jjco/29.12.604
35. Kitai T, Inomoto T, Miwa M, Shikayama T. Fluorescence navigation with indocyanine green for detecting sentinel lymph nodes in breast cancer. *Breast Cancer* (2005) 12(3):211–5. doi:10.2325/jbcs.12.211
36. Tagaya N, Yamazaki R, Nakagawa A, Abe A, Hamada K, Kubota K, et al. Intraoperative identification of sentinel lymph nodes by near-infrared fluorescence imaging in patients with breast cancer. *Am J Surg* (2008) 195(6):850–3. doi:10.1016/j.amjsurg.2007.02.032
37. Murawa D, Hirche C, Dresel S, Hunerbein M. Sentinel lymph node biopsy in breast cancer guided by indocyanine green fluorescence. *Br J Surg* (2009) 96(11):1289–94. doi:10.1002/bjs.6721
38. Zakaria S, Hoskin TL, Degnim AC. Safety and technical success of methylene blue dye for lymphatic mapping in breast cancer. *Am J Surg* (2008) 196(2):228–33. doi:10.1016/j.amjsurg.2007.08.060
39. Peek MC, Charalampoudis P, Anninga B, Baker R, Douek M. Blue dye for identification of sentinel nodes in breast cancer and malignant melanoma: a systematic review and meta-analysis. *Future Oncol* (2017) 13(5):455–67. doi:10.2217/fon-2016-0255
40. Fujiwara M, Mizukami T, Suzuki A, Fukamizu H. Sentinel lymph node detection in skin cancer patients using real-time fluorescence navigation with indocyanine green: preliminary experience. *J Plast Reconstr Aesthet Surg* (2009) 62(10):e373–8. doi:10.1016/j.bjps.2007.12.074
41. Tanaka R, Nakashima K, Fujimoto W. Sentinel lymph node detection in skin cancer using fluorescence navigation with indocyanine green. *J Dermatol* (2009) 36(8):468–70. doi:10.1111/j.1346-8138.2009.00679.x
42. Bredell MG. Sentinel lymph node mapping by indocyanin green fluorescence imaging in oropharyngeal cancer – preliminary experience. *Head Neck Oncol* (2010) 2:31. doi:10.1186/1758-3284-2-31
43. Yamashita S, Tokuishi K, Anami K, Miyawaki M, Moroga T, Kamei M, et al. Video-assisted thoracoscopic indocyanine green fluorescence imaging system shows sentinel lymph nodes in non-small-cell lung cancer. *J Thorac Cardiovasc Surg* (2011) 141(1):141–4. doi:10.1016/j.jtcvs.2010.01.028
44. Yuasa Y, Seike J, Yoshida T, Takechi H, Yamai H, Yamamoto Y, et al. Sentinel lymph node biopsy using intraoperative indocyanine green fluorescence imaging navigated with preoperative CT lymphography for superficial esophageal cancer. *Ann Surg Oncol* (2012) 19(2):486–93. doi:10.1245/s10434-011-1922-x
45. Kubota K, Yoshida M, Kuroda J, Okada A, Ohta K, Kitajima M. Application of the HyperEye Medical System for esophageal cancer surgery: a preliminary report. *Surg Today* (2013) 43(2):215–20. doi:10.1007/s00595-012-0251-4
46. Nimura H, Narimiya N, Mitsumori N, Yamazaki Y, Yanaga K, Urashima M. Infrared ray electronic endoscopy combined with indocyanine green injection for detection of sentinel nodes of patients with gastric cancer. *Br J Surg* (2004) 91(5):575–9. doi:10.1002/bjs.4470
47. Kusano M, Tajima Y, Yamazaki K, Kato M, Watanabe M, Miwa M. Sentinel node mapping guided by indocyanine green fluorescence imaging: a new method for sentinel node navigation surgery in gastrointestinal cancer. *Dig Surg* (2008) 25(2):103–8. doi:10.1159/000121905
48. Noura S, Ohue M, Seki Y, Tanaka K, Motoori M, Kishi K, et al. Feasibility of a lateral region sentinel node biopsy of lower rectal cancer guided by indocyanine green using a near-infrared camera system. *Ann Surg Oncol* (2010) 17(1):144–51. doi:10.1245/s10434-009-0711-2
49. Hirche C, Dresel S, Krempien R, Hunerbein M. Sentinel node biopsy by indocyanine green retention fluorescence detection for inguinal lymph node staging of anal cancer: preliminary experience. *Ann Surg Oncol* (2010) 17(9):2357–62. doi:10.1245/s10434-010-1010-7
50. Jeschke S, Lusuardi L, Myatt A, Hruby S, Pirich C, Janetschek G. Visualisation of the lymph node pathway in real time by laparoscopic radioisotope- and fluorescence-guided sentinel lymph node dissection in prostate cancer staging. *Urology* (2012) 80(5):1080–6. doi:10.1016/j.urology.2012.05.050
51. Polom W, Markuszewski M, Rho YS, Matuszewski M. Usage of invisible near infrared light (NIR) fluorescence with indocyanine green (ICG) and methylene blue (MB) in urological oncology. Part 1. *Cent European J Urol* (2014) 67(2):142–8. doi:10.5173/ceju.2014.02.art5
52. Polom W, Markuszewski M, Rho YS, Matuszewski M. Use of invisible near infrared light fluorescence with indocyanine green and methylene blue in urology. Part 2. *Cent European J Urol* (2014) 67(3):310–3. doi:10.5173/ceju.2014.03.art19
53. Ogata F, Narushima M, Mihara M, Azuma R, Morimoto Y, Koshima I. Intraoperative lymphography using indocyanine green dye for near-infrared fluorescence labeling in lymphedema. *Ann Plast Surg* (2007) 59(2):180–4. doi:10.1097/01.sap.0000253341.70866.54
54. Unno N, Inuzuka K, Suzuki M, Yamamoto N, Sagara D, Nishiyama M, et al. Preliminary experience with a novel fluorescence lymphography using indocyanine green in patients with secondary lymphedema. *J Vasc Surg* (2007) 45(5):1016–21. doi:10.1016/j.jvs.2007.01.023
55. Chang DW, Suami H, Skoracki R. A prospective analysis of 100 consecutive lymphovenous bypass cases for treatment of extremity lymphedema. *Plast Reconstr Surg* (2013) 132(5):1305–14. doi:10.1097/PRS.0b013e3182a4d626
56. Kuroda K, Kinouchi H, Kanemaru K, Nishiyama Y, Ogiwara M, Yoshioka H, et al. Intra-arterial injection fluorescein videoangiography in aneurysm surgery. *Neurosurgery* (2013) 72(2 Suppl Operative):ons141–50; discussion ons150. doi:10.1227/NEU.0b013e3182752f32
57. Ichikawa T, Suzuki K, Watanabe Y. Intra-arterial fluorescence angiography with injection of fluorescein sodium from the superficial temporal artery during aneurysm surgery: technical notes. *Neurol Med Chir (Tokyo)* (2014) 54(6):490–6. doi:10.2176/nmc.tn.2013-0232
58. Ichikawa T, Suzuki K, Watanabe Y, Sato T, Sakuma J, Saito K. Development of and clinical experience with a simple device for performing intraoperative fluorescein fluorescence cerebral angiography: technical notes. *Neurol Med Chir (Tokyo)* (2016) 56(3):141–9. doi:10.2176/nmc.tn.2015-0188
59. Yamamoto M, Sasaguri S, Sato T. Assessing intraoperative blood flow in cardiovascular surgery. *Surg Today* (2011) 41(11):1467–74. doi:10.1007/s00595-010-4553-0
60. Yamamoto M, Orihashi K, Nishimori H, Handa T, Kondo N, Fukutomi T, et al. Efficacy of intraoperative HyperEye Medical System angiography for coronary artery bypass grafting. *Surg Today* (2015) 45(8):966–72. doi:10.1007/s00595-014-1015-0
61. Yamamoto M, Orihashi K, Nishimori H, Wariishi S, Fukutomi T, Kondo N, et al. Indocyanine green angiography for intra-operative assessment in vascular surgery. *Eur J Vasc Endovasc Surg* (2012) 43(4):426–32. doi:10.1016/j.ejvs.2011.12.030
62. Jafari MD, Lee KH, Halabi WJ, Mills SD, Carmichael JC, Stamos MJ, et al. The use of indocyanine green fluorescence to assess anastomotic perfusion during robotic assisted laparoscopic rectal surgery. *Surg Endosc* (2013) 27(8):3003–8. doi:10.1007/s00464-013-2832-8
63. Pacheco PE, Hill SM, Henriques SM, Paulsen JK, Anderson RC. The novel use of intraoperative laser-induced fluorescence of indocyanine green tissue angiography for evaluation of the gastric conduit in esophageal reconstructive surgery. *Am J Surg* (2013) 205(3):349–52; discussion 352–3. doi:10.1016/j.amjsurg.2012.11.005
64. Yamaguchi S, De Lorenzi F, Petit JY, Rietjens M, Garusi C, Giraldo A, et al. The "perfusion map" of the unipedicled TRAM flap to reduce postoperative

partial necrosis. *Ann Plast Surg* (2004) 53(3):205–9. doi:10.1097/01.sap.0000116284.51679.ea
65. Giunta RE, Holzbach T, Taskov C, Holm PS, Brill T, Busch R, et al. Prediction of flap necrosis with laser induced indocyanine green fluorescence in a rat model. *Br J Plast Surg* (2005) 58(5):695–701. doi:10.1016/j.bjps.2005.02.018
66. Holm C, Mayr M, Hofter E, Raab N, Ninkovic M. Interindividual variability of the SIEA angiosome: effects on operative strategies in breast reconstruction. *Plast Reconstr Surg* (2008) 122(6):1612–20. doi:10.1097/PRS.0b013e31818a9a3f
67. Lamby P, Prantl L, Gais S, Walter M, Bachthaler M, Nerlich M, et al. Evaluation of the vascular integrity of free flaps based on microcirculation imaging techniques. *Clin Hemorheol Microcirc* (2008) 39(1–4):253–63. doi:10.3233/CH-2008-1094
68. Newman MI, Samson MC. The application of laser-assisted indocyanine green fluorescent dye angiography in microsurgical breast reconstruction. *J Reconstr Microsurg* (2009) 25(1):21–6. doi:10.1055/s-0028-1090617
69. Pestana IA, Coan B, Erdmann D, Marcus J, Levin LS, Zenn MR. Early experience with fluorescent angiography in free-tissue transfer reconstruction. *Plast Reconstr Surg* (2009) 123(4):1239–44. doi:10.1097/PRS.0b013e31819e67c1
70. Komorowska-Timek E, Gurtner GC. Intraoperative perfusion mapping with laser-assisted indocyanine green imaging can predict and prevent complications in immediate breast reconstruction. *Plast Reconstr Surg* (2010) 125(4):1065–73. doi:10.1097/PRS.0b013e3181d17f80
71. Ishizawa T, Bandai Y, Ijichi M, Kaneko J, Hasegawa K, Kokudo N. Fluorescent cholangiography illuminating the biliary tree during laparoscopic cholecystectomy. *Br J Surg* (2010) 97(9):1369–77. doi:10.1002/bjs.7125
72. Boni L, David G, Mangano A, Dionigi G, Rausei S, Spampatti S, et al. Clinical applications of indocyanine green (ICG) enhanced fluorescence in laparoscopic surgery. *Surg Endosc* (2015) 29(7):2046–55. doi:10.1007/s00464-014-3895-x
73. Winer JH, Choi HS, Gibbs-Strauss SL, Ashitate Y, Colson YL, Frangioni JV. Intraoperative localization of insulinoma and normal pancreas using invisible near-infrared fluorescent light. *Ann Surg Oncol* (2010) 17(4):1094–100. doi:10.1245/s10434-009-0868-8
74. Wada H, Hyun H, Vargas C, Gravier J, Park G, Gioux S, et al. Pancreas-targeted NIR fluorophores for dual-channel image-guided abdominal surgery. *Theranostics* (2015) 5(1):1–11. doi:10.7150/thno.10259
75. Verbeek FP, van der Vorst JR, Schaafsma BE, Swijnenburg RJ, Gaarenstroom KN, Elzevier HW, et al. Intraoperative near infrared fluorescence guided identification of the ureters using low dose methylene blue: a first in human experience. *J Urol* (2013) 190(2):574–9. doi:10.1016/j.juro.2013.02.3187
76. Whitney MA, Crisp JL, Nguyen LT, Friedman B, Gross LA, Steinbach P, et al. Fluorescent peptides highlight peripheral nerves during surgery in mice. *Nat Biotechnol* (2011) 29(4):352–6. doi:10.1038/nbt.1764
77. Wu AP, Whitney MA, Crisp JL, Friedman B, Tsien RY, Nguyen QT. Improved facial nerve identification with novel fluorescently labeled probe. *Laryngoscope* (2011) 121(4):805–10. doi:10.1002/lary.21411
78. Hyun H, Park MH, Owens EA, Wada H, Henary M, Handgraaf HJ. Structure-inherent targeting of near-infrared fluorophores for parathyroid and thyroid gland imaging. *Nat Med* (2015) 21(2):192–7. doi:10.1038/nm.3728
79. Owens EA, Hyun H, Tawney JG, Choi HS, Henary M. Correlating molecular character of NIR imaging agents with tissue-specific uptake. *J Med Chem* (2015) 58(10):4348–56. doi:10.1021/acs.jmedchem.5b00475
80. Ashitate Y, Levitz A, Park MH, Hyun H, Venugopal V, Park G, et al. Endocrine-specific NIR fluorophores for adrenal gland targeting. *Chem Commun (Camb)* (2016) 52(67):10305–8. doi:10.1039/c6cc03845j
81. Owens EA, Hyun H, Dost TL, Lee JH, Park G, Pham DH, et al. Near-infrared illumination of native tissues for image-guided surgery. *J Med Chem* (2016) 59(11):5311–23. doi:10.1021/acs.jmedchem.6b00038
82. Stummer W, Stocker S, Wagner S, Stepp H, Fritsch C, Goetz C, et al. Intraoperative detection of malignant gliomas by 5-aminolevulinic acid-induced porphyrin fluorescence. *Neurosurgery* (1998) 42(3):518–25; discussion 525–6. doi:10.1097/00006123-199803000-00017
83. Stummer W, Pichlmeier U, Meinel T, Wiestler OD, Zanella F, Reulen HJ. Fluorescence-guided surgery with 5-aminolevulinic acid for resection of malignant glioma: a randomised controlled multicentre phase III trial. *Lancet Oncol* (2006) 7(5):392–401. doi:10.1016/s1470-2045(06)70665-9
84. Roberts DW, Valdes PA, Harris BT, Fontaine KM, Hartov A, Fan X, et al. Coregistered fluorescence-enhanced tumor resection of malignant glioma: relationships between delta-aminolevulinic acid-induced protoporphyrin IX fluorescence, magnetic resonance imaging enhancement, and neuropathological parameters. Clinical article. *J Neurosurg* (2011) 114(3):595–603. doi:10.3171/2010.2.jns091322
85. Colditz MJ, Jeffree RL. Aminolevulinic acid (ALA)-protoporphyrin IX fluorescence guided tumour resection. Part 1: clinical, radiological and pathological studies. *J Clin Neurosci* (2012) 19(11):1471–4. doi:10.1016/j.jocn.2012.03.009
86. Colditz MJ, Leyen K, Jeffree RL. Aminolevulinic acid (ALA)-protoporphyrin IX fluorescence guided tumour resection. Part 2: theoretical, biochemical and practical aspects. *J Clin Neurosci* (2012) 19(12):1611–6. doi:10.1016/j.jocn.2012.03.013
87. Kuroiwa T, Kajimoto Y, Ohta T. Development of a fluorescein operative microscope for use during malignant glioma surgery: a technical note and preliminary report. *Surg Neurol* (1998) 50(1):41–8; discussion 48–49. doi:10.1016/S0090-3019(98)00055-X
88. Shinoda J, Yano H, Yoshimura S, Okumura A, Kaku Y, Iwama T, et al. Fluorescence-guided resection of glioblastoma multiforme by using high-dose fluorescein sodium. Technical note. *J Neurosurg* (2003) 99(3):597–603. doi:10.3171/jns.2003.99.3.0597
89. Okuda T, Yoshioka H, Kato A. Fluorescence-guided surgery for glioblastoma multiforme using high-dose fluorescein sodium with excitation and barrier filters. *J Clin Neurosci* (2012) 19(12):1719–22. doi:10.1016/j.jocn.2011.12.034
90. Butte PV, Mamelak A, Parrish-Novak J, Drazin D, Shweikeh F, Gangalum PR, et al. Near-infrared imaging of brain tumors using the Tumor Paint BLZ-100 to achieve near-complete resection of brain tumors. *Neurosurg Focus* (2014) 36(2):E1. doi:10.3171/2013.11.focus13497
91. Cutter JL, Cohen NT, Wang J, Sloan AE, Cohen AR, Panneerselvam A, et al. Topical application of activity-based probes for visualization of brain tumor tissue. *PLoS One* (2012) 7(3):e33060. doi:10.1371/journal.pone.0033060
92. Okuda T, Kataoka K, Taneda M. Metastatic brain tumor surgery using fluorescein sodium: technical note. *Minim Invasive Neurosurg* (2007) 50(6):382–4. doi:10.1055/s-2007-993200
93. Okuda T, Kataoka K, Yabuuchi T, Yugami H, Kato A. Fluorescence-guided surgery of metastatic brain tumors using fluorescein sodium. *J Clin Neurosci* (2010) 17(1):118–21. doi:10.1016/j.jocn.2009.06.033
94. de Boer E, Warram JM, Tucker MD, Hartman YE, Moore LS, de Jong JS, et al. In vivo fluorescence immunohistochemistry: localization of fluorescently labeled cetuximab in squamous cell carcinomas. *Sci Rep* (2015) 5:10169. doi:10.1038/srep10169
95. Rosenthal EL, Warram JM, de Boer E, Chung TK, Korb ML, Brandwein-Gensler M, et al. Safety and tumor specificity of cetuximab-IRDye800 for surgical navigation in head and neck cancer. *Clin Cancer Res* (2015) 21(16):3658–66. doi:10.1158/1078-0432.ccr-14-3284
96. Mitsunaga M, Ogawa M, Kosaka N, Rosenblum LT, Choyke PL, Kobayashi H. Cancer cell-selective in vivo near infrared photoimmunotherapy targeting specific membrane molecules. *Nat Med* (2011) 17(12):1685–91. doi:10.1038/nm.2554
97. Cherrick GR, Stein SW, Leevy CM, Davidson CS. Indocyanine green: observations on its physical properties, plasma decay, and hepatic extraction. *J Clin Invest* (1960) 39:592–600. doi:10.1172/jci104072
98. Gotoh K, Yamada T, Ishikawa O, Takahashi H, Eguchi H, Yano M, et al. A novel image-guided surgery of hepatocellular carcinoma by indocyanine green fluorescence imaging navigation. *J Surg Oncol* (2009) 100(1):75–9. doi:10.1002/jso.21272
99. Ishizawa T, Fukushima N, Shibahara J, Masuda K, Tamura S, Aoki T, et al. Real-time identification of liver cancers by using indocyanine green fluorescent imaging. *Cancer* (2009) 115(11):2491–504. doi:10.1002/cncr.24291
100. Uchiyama K, Ueno M, Ozawa S, Kiriyama S, Shigekawa Y, Yamaue H. Combined use of contrast-enhanced intraoperative ultrasonography and a fluorescence navigation system for identifying hepatic metastases. *World J Surg* (2010) 34(12):2953–9. doi:10.1007/s00268-010-0764-1
101. Tummers QR, Verbeek FP, Schaafsma BE, Boonstra MC, van der Vorst JR, Liefers GJ, et al. Real-time intraoperative detection of breast cancer using

near-infrared fluorescence imaging and methylene blue. *Eur J Surg Oncol* (2014) 40(7):850–8. doi:10.1016/j.ejso.2014.02.225
102. Tipirneni KE, Warram JM, Moore LS, Prince AC, de Boer E, Jani AH, et al. Oncologic procedures amenable to fluorescence-guided surgery. *Ann Surg* (2017) 266(1):36–47. doi:10.1097/sla.0000000000002127
103. Whitley MJ, Cardona DM, Lazarides AL, Spasojevic I, Ferrer JM, Cahill J, et al. A mouse-human phase 1 co-clinical trial of a protease-activated fluorescent probe for imaging cancer. *Sci Transl Med* (2016) 8(320):320ra324. doi:10.1126/scitranslmed.aad0293
104. Unkart JT, Chen SL, Wapnir IL, Gonzalez JE, Harootunian A, Wallace AM. Intraoperative tumor detection using a ratiometric activatable fluorescent peptide: a first-in-human phase 1 study. *Ann Surg Oncol* (2017) 24(11): 3167–73. doi:10.1245/s10434-017-5991-3
105. Holt D, Okusanya O, Judy R, Venegas O, Jiang J, DeJesus E, et al. Intraoperative near-infrared imaging can distinguish cancer from normal tissue but not inflammation. *PLoS One* (2014) 9(7):e103342. doi:10.1371/journal.pone.0103342
106. Okusanya OT, DeJesus EM, Jiang JX, Judy RP, Venegas OG, Deshpande CG, et al. Intraoperative molecular imaging can identify lung adenocarcinomas during pulmonary resection. *J Thorac Cardiovasc Surg* (2015) 150(1):28–35. e1. doi:10.1016/j.jtcvs.2015.05.014
107. Predina JD, Okusanya O, D Newton A, Low P, Singhal S. Standardization and optimization of intraoperative molecular imaging for identifying primary pulmonary adenocarcinomas. *Mol Imaging Biol* (2017). doi:10.1007/s11307-017-1076-8
108. Predina JD, Newton AD, Keating J, Barbosa EM Jr, Okusanya O, Xia L, et al. Intraoperative molecular imaging combined with positron emission tomography improves surgical management of peripheral malignant pulmonary nodules. *Ann Surg* (2017) 266(3):479–88. doi:10.1097/sla.0000000000002382
109. Tummers QR, Hoogstins CE, Peters AA, de Kroon CD, Trimbos JB, van de Velde CJ, et al. The value of intraoperative near-infrared fluorescence imaging based on enhanced permeability and retention of indocyanine green: feasibility and false-positives in ovarian cancer. *PLoS One* (2015) 10(6):e0129766. doi:10.1371/journal.pone.0129766
110. Tummers QR, Hoogstins CE, Gaarenstroom KN, de Kroon CD, van Poelgeest MI, Vuyk J, et al. Intraoperative imaging of folate receptor alpha positive ovarian and breast cancer using the tumor specific agent EC17. *Oncotarget* (2016) 7(22):32144–55. doi:10.18632/oncotarget.8282
111. Hoogstins CE, Tummers QR, Gaarenstroom KN, de Kroon CD, Trimbos JB, Bosse T, et al. A novel tumor-specific agent for intraoperative near-infrared fluorescence imaging: a translational study in healthy volunteers and patients with ovarian cancer. *Clin Cancer Res* (2016) 22(12):2929–38. doi:10.1158/1078-0432.ccr-15-2640
112. Urano Y, Sakabe M, Kosaka N, Ogawa M, Mitsunaga M, Asanuma D, et al. Rapid cancer detection by topically spraying a gamma-glutamyltranspeptidase-activated fluorescent probe. *Sci Transl Med* (2011) 3 (110):110ra119. doi:10.1126/scitranslmed.3002823
113. Kaushal S, McElroy MK, Luiken GA, Talamini MA, Moossa AR, Hoffman RM, et al. Fluorophore-conjugated anti-CEA antibody for the intraoperative imaging of pancreatic and colorectal cancer. *J Gastrointest Surg* (2008) 12(11): 1938–50. doi:10.1007/s11605-008-0581-0
114. McElroy M, Kaushal S, Luiken GA, Talamini MA, Moossa AR, Hoffman RM, et al. Imaging of primary and metastatic pancreatic cancer using a fluorophore-conjugated anti-CA19-9 antibody for surgical navigation. *World J Surg* (2008) 32(6):1057–66. doi:10.1007/s00268-007-9452-1
115. van der Vorst JR, Vahrmeijer AL, Hutteman M, Bosse T, Smit VT, van de Velde CJ, et al. Near-infrared fluorescence imaging of a solitary fibrous tumor of the pancreas using methylene blue. *World J Gastrointest Surg* (2012) 4(7):180–4. doi:10.4240/wjgs.v4.i7.180
116. Guzzo TJ, Jiang J, Keating J, DeJesus E, Judy R, Nie S, et al. Intraoperative molecular diagnostic imaging can identify renal cell carcinoma. *J Urol* (2016) 195(3):748–55. doi:10.1016/j.juro.2015.09.093
117. Jichlinski P, Forrer M, Mizeret J, Glanzmann T, Braichotte D, Wagnieres G, et al. Clinical evaluation of a method for detecting superficial surgical transitional cell carcinoma of the bladder by light-induced fluorescence of protoporphyrin IX following the topical application of 5-aminolevulinic acid: preliminary results. *Lasers Surg Med* (1997) 20(4):402–8. doi:10.1002/(SICI)1096-9101(1997)20:4<402::AID-LSM5>3.0.CO;2-U
118. Jichlinski P, Guillou L, Karlsen SJ, Malmstrom PU, Jocham D, Brennhovd B, et al. Hexyl aminolevulinate fluorescence cystoscopy: new diagnostic tool for photodiagnosis of superficial bladder cancer – a multicenter study. *J Urol* (2003) 170(1):226–9. doi:10.1097/01.ju.0000060782.52358.04
119. Stenzl A, Burger M, Fradet Y, Mynderse LA, Soloway MS, Witjes JA, et al. Hexaminolevulinate guided fluorescence cystoscopy reduces recurrence in patients with nonmuscle invasive bladder cancer. *J Urol* (2010) 184(5):1907–13. doi:10.1016/j.juro.2010.06.148
120. Rink M, Babjuk M, Catto JW, Jichlinski P, Shariat SF, Stenzl A, et al. Hexyl aminolevulinate-guided fluorescence cystoscopy in the diagnosis and follow-up of patients with non-muscle-invasive bladder cancer: a critical review of the current literature. *Eur Urol* (2013) 64(4):624–38. doi:10.1016/j.eururo.2013.07.007
121. Nakajima T, Mitsunaga M, Bander NH, Heston WD, Choyke PL, Kobayashi H. Targeted, activatable, in vivo fluorescence imaging of prostate-specific membrane antigen (PSMA) positive tumors using the quenched humanized J591 antibody-indocyanine green (ICG) conjugate. *Bioconjug Chem* (2011) 22(8):1700–5. doi:10.1021/bc2002715
122. Fukuhara H, Inoue K, Kurabayashi A, Furihata M, Shuin T. Performance of 5-aminolevulinic-acid-based photodynamic diagnosis for radical prostatectomy. *BMC Urol* (2015) 15:78. doi:10.1186/s12894-015-0073-y
123. Iseki K, Tatsuta M, Iishi H, Sakai N, Yano H, Ishiguro S. Effectiveness of the near-infrared electronic endoscope for diagnosis of the depth of involvement of gastric cancers. *Gastrointest Endosc* (2000) 52(6):755–62. doi:10.1067/mge.2000.110455
124. Mataki N, Nagao S, Kawaguchi A, Matsuzaki K, Miyazaki J, Kitagawa Y, et al. Clinical usefulness of a new infrared videoendoscope system for diagnosis of early stage gastric cancer. *Gastrointest Endosc* (2003) 57(3): 336–42. doi:10.1067/mge.2003.133
125. Kimura T, Muguruma N, Ito S, Okamura S, Imoto Y, Miyamoto H, et al. Infrared fluorescence endoscopy for the diagnosis of superficial gastric tumors. *Gastrointest Endosc* (2007) 66(1):37–43. doi:10.1016/j.gie.2007.01.009
126. Gong L, Ding H, Long NE, Sullivan BJ, Martin EW Jr, Magliery TJ, et al. A 3E8.scFv.Cys-IR800 conjugate targeting TAG-72 in an orthotopic colorectal cancer model. *Mol Imaging Biol* (2017). doi:10.1007/s11307-017-1096-4
127. Mitsunaga M, Kosaka N, Choyke PL, Young MR, Dextras CR, Saud SM, et al. Fluorescence endoscopic detection of murine colitis-associated colon cancer by topically applied enzymatically rapid-activatable probe. *Gut* (2013) 62(8):1179–86. doi:10.1136/gutjnl-2011-301795
128. Alkalay R, Alcalay J, Maly A, Ingber A, Fritsch C, Ruzicka T, et al. Fluorescence imaging for the demarcation of basal cell carcinoma tumor borders. *J Drugs Dermatol* (2008) 7(11):1033–7.
129. Walker E, Mann M, Honda K, Vidimos A, Schluchter MD, Straight B, et al. Rapid visualization of nonmelanoma skin cancer. *J Am Acad Dermatol* (2017) 76(2): 209–216.e9. doi:10.1016/j.jaad.2016.09.008
130. van der Vorst JR, Schaafsma BE, Verbeek FP, Swijnenburg RJ, Tummers QR, Hutteman M, et al. Intraoperative near-infrared fluorescence imaging of parathyroid adenomas with use of low-dose methylene blue. *Head Neck* (2014) 36(6):853–8. doi:10.1002/hed.23384
131. Tobis S, Knopf J, Silvers C, Yao J, Rashid H, Wu G, et al. Near infrared fluorescence imaging with robotic assisted laparoscopic partial nephrectomy: initial clinical experience for renal cortical tumors. *J Urol* (2011) 186(1):47–52. doi:10.1016/j.juro.2011.02.2701
132. Morita K, Ishizawa T, Tani K, Harada N, Shimizu A, Yamamoto S, et al. Application of indocyanine green-fluorescence imaging to full-thickness cholecystectomy. *Asian J Endosc Surg* (2014) 7(2):193–5. doi:10.1111/ases.12083
133. Schlottmann F, Patti MG. Evaluation of gastric conduit perfusion during esophagectomy with indocyanine green fluorescence imaging. *J Laparoendosc Adv Surg Tech A* (2017) 27(12):1305–8. doi:10.1089/lap.2017.0359
134. Kim M, Son SY. Real-time vessel navigation using indocyanine green fluorescence during robotic or laparoscopic gastrectomy for gastric cancer. *J Gastric Cancer* (2017) 17(2):145–53. doi:10.5230/jgc.2017.17.e17
135. Manny TB, Pompeo AS, Hemal AK. Robotic partial adrenalectomy using indocyanine green dye with near-infrared imaging: the initial clinical experience. *Urology* (2013) 82(3):738–42. doi:10.1016/j.urology.2013.03.074

136. Colvin J, Zaidi N, Berber E. The utility of indocyanine green fluorescence imaging during robotic adrenalectomy. *J Surg Oncol* (2016) 114(2):153–6. doi:10.1002/jso.24296
137. Nishiyama Y, Kinouchi H, Senbokuya N, Kato T, Kanemaru K, Yoshioka H, et al. Endoscopic indocyanine green video angiography in aneurysm surgery: an innovative method for intraoperative assessment of blood flow in vasculature hidden from microscopic view. *J Neurosurg* (2012) 117(2):302–8. doi:10.3171/2012.5.jns112300
138. Bruneau M, Appelboom G, Rynkowski M, Van Cutsem N, Mine B, De Witte O. Endoscope-integrated ICG technology: first application during intracranial aneurysm surgery. *Neurosurg Rev* (2013) 36(1):77–84; discussion 84–5. doi:10.1007/s10143-012-0419-9
139. Mielke D, Malinova V, Rohde V. Comparison of intraoperative microscopic and endoscopic ICG angiography in aneurysm surgery. *Neurosurgery* (2014) 10(Suppl 3):418–25; discussion 425. doi:10.1227/neu.0000000000000345
140. Litvack ZN, Zada G, Laws ER Jr. Indocyanine green fluorescence endoscopy for visual differentiation of pituitary tumor from surrounding structures. *J Neurosurg* (2012) 116(5):935–41. doi:10.3171/2012.1.jns11601
141. Hide T, Yano S, Shinojima N, Kuratsu J. Usefulness of the indocyanine green fluorescence endoscope in endonasal transsphenoidal surgery. *J Neurosurg* (2015) 122(5):1185–92. doi:10.3171/2014.9.jns14599
142. Simal Julian JA, Sanroman Alvarez P, Miranda Lloret P, Botella Asuncion C. Endo ICG videoangiography: localizing the carotid artery in skull-base endonasal approaches. *Acta Neurochir (Wien)* (2016) 158(7):1351–3. doi:10.1007/s00701-016-2830-4
143. Wachter D, Behm T, von Eckardstein K, Rohde V. Indocyanine green angiography in endoscopic third ventriculostomy. *Neurosurgery* (2013) 73 (1 Suppl Operative):ons67–72. doi:10.1227/NEU.0b013e318285b846
144. Foersch S, Heimann A, Ayyad A, Spoden GA, Florin L, Mpoukouvalas K, et al. Confocal laser endomicroscopy for diagnosis and histomorphologic imaging of brain tumors in vivo. *PLoS One* (2012) 7(7):e41760. doi:10.1371/journal.pone.0041760
145. Tsuzuki S, Aihara Y, Eguchi S, Amano K, Kawamata T, Okada Y. Application of indocyanine green (ICG) fluorescence for endoscopic biopsy of intraventricular tumors. *Childs Nerv Syst* (2014) 30(4):723–6. doi:10.1007/s00381-013-2266-6
146. Schmidt F, Dittberner A, Koscielny S, Petersen I, Guntinas-Lichius O. Feasibility of real-time near-infrared indocyanine green fluorescence endoscopy for the evaluation of mucosal head and neck lesions. *Head Neck* (2017) 39(2):234–40. doi:10.1002/hed.24570
147. Lee JG, Low AH, Leung JW. Randomized comparative study of indocyanine green and India ink for colonic tattooing: an animal survival study. *J Clin Gastroenterol* (2000) 31(3):233–6. doi:10.1097/00004836-200010000-00010
148. Miyoshi N, Ohue M, Noura S, Yano M, Sasaki Y, Kishi K, et al. Surgical usefulness of indocyanine green as an alternative to India ink for endoscopic marking. *Surg Endosc* (2009) 23(2):347–51. doi:10.1007/s00464-008-9938-4
149. Watanabe M, Tsunoda A, Narita K, Kusano M, Miwa M. Colonic tattooing using fluorescence imaging with light-emitting diode-activated indocyanine green: a feasibility study. *Surg Today* (2009) 39(3):214–8. doi:10.1007/s00595-008-3849-9
150. Gray D, Kim E, Cotero V, Staudinger P, Yazdanfar S, Hehir CT. Compact fluorescence and white light imaging system for intraoperative visualization of nerves. *Proc SPIE Int Soc Opt Eng* (2012) 8207. doi:10.1117/12.905354
151. Keereweer S, Mol IM, Vahrmeijer AL, Van Driel PB, Baatenburg de Jong RJ, Kerrebijn JD, et al. Dual wavelength tumor targeting for detection of hypopharyngeal cancer using near-infrared optical imaging in an animal model. *Int J Cancer* (2012) 131(7):1633–40. doi:10.1002/ijc.27430
152. Wapnir I, Dua M, Kieryn A, Paro J, Morrison D, Kahn D, et al. Intraoperative imaging of nipple perfusion patterns and ischemic complications in nipple-sparing mastectomies. *Ann Surg Oncol* (2014) 21(1):100–6. doi:10.1245/s10434-013-3214-0
153. Richards-Kortum R, Sevick-Muraca E. Quantitative optical spectroscopy for tissue diagnosis. *Annu Rev Phys Chem* (1996) 47:555–606. doi:10.1146/annurev.physchem.47.1.555
154. Hilderbrand SA, Weissleder R. Near-infrared fluorescence: application to in vivo molecular imaging. *Curr Opin Chem Biol* (2010) 14(1):71–9. doi:10.1016/j.cbpa.2009.09.029
155. Kobayashi H, Ogawa M, Alford R, Choyke PL, Urano Y. New strategies for fluorescent probe design in medical diagnostic imaging. *Chem Rev* (2010) 110(5):2620–40. doi:10.1021/cr900263j
156. Chance B. Near-infrared images using continuous, phase-modulated, and pulsed light with quantitation of blood and blood oxygenation. *Ann N Y Acad Sci* (1998) 838:29–45. doi:10.1111/j.1749-6632.1998.tb08185.x
157. Bouvet M, Hoffman RM. Glowing tumors make for better detection and resection. *Sci Transl Med* (2011) 3(110):110fs110. doi:10.1126/scitranslmed.3003375
158. Moody ED, Viskari PJ, Colyer CL. Non-covalent labeling of human serum albumin with indocyanine green: a study by capillary electrophoresis with diode laser-induced fluorescence detection. *J Chromatogr B Biomed Sci Appl* (1999) 729(1–2):55–64. doi:10.1016/S0378-4347(99)00121-8
159. Ogawa M, Kosaka N, Choyke PL, Kobayashi H. In vivo molecular imaging of cancer with a quenching near-infrared fluorescent probe using conjugates of monoclonal antibodies and indocyanine green. *Cancer Res* (2009) 69(4):1268–72. doi:10.1158/0008-5472.can-08-3116
160. Tanaka E, Chen FY, Flaumenhaft R, Graham GJ, Laurence RG, Frangioni JV. Real-time assessment of cardiac perfusion, coronary angiography, and acute intravascular thrombi using dual-channel near-infrared fluorescence imaging. *J Thorac Cardiovasc Surg* (2009) 138(1):133–40. doi:10.1016/j.jtcvs.2008.09.082
161. Deja M, Ahlers O, Macguill M, Wust P, Hildebrandt B, Riess H, et al. Changes in hepatic blood flow during whole body hyperthermia. *Int J Hyperthermia* (2010) 26(2):95–100. doi:10.3109/02656730903250574
162. Kang SW, Chung SE, Shin WJ, Lee JH. Polypoidal choroidal vasculopathy and late geographic hyperfluorescence on indocyanine green angiography. *Br J Ophthalmol* (2009) 93(6):759–64. doi:10.1136/bjo.2008.145862
163. Alford R, Simpson HM, Duberman J, Hill GC, Ogawa M, Regino C, et al. Toxicity of organic fluorophores used in molecular imaging: literature review. *Mol Imaging* (2009) 8(6):341–54. doi:10.2310/7290.2009.00031
164. Kudszus S, Roesel C, Schachtrupp A, Hoer JJ. Intraoperative laser fluorescence angiography in colorectal surgery: a noninvasive analysis to reduce the rate of anastomotic leakage. *Langenbecks Arch Surg* (2010) 395(8):1025–30. doi:10.1007/s00423-010-0699-x
165. Schaafsma BE, Mieog JS, Hutteman M, van der Vorst JR, Kuppen PJ, Lowik CW, et al. The clinical use of indocyanine green as a near-infrared fluorescent contrast agent for image-guided oncologic surgery. *J Surg Oncol* (2011) 104(3):323–32. doi:10.1002/jso.21943
166. Shimizu S, Kamiike W, Hatanaka N, Yoshida Y, Tagawa K, Miyata M, et al. New method for measuring ICG Rmax with a clearance meter. *World J Surg* (1995) 19(1):113–8; discussion 118. doi:10.1007/BF00316992
167. Kung TA, Champaneria MC, Maki JH, Neligan PC. Current concepts in the surgical management of lymphedema. *Plast Reconstr Surg* (2017) 139(4):1003e–13e. doi:10.1097/prs.0000000000003218
168. Champagne BJ, Darling RC III, Daneshmand M, Kreienberg PB, Lee EC, Mehta M, et al. Outcome of aggressive surveillance colonoscopy in ruptured abdominal aortic aneurysm. *J Vasc Surg* (2004) 39(4):792–6. doi:10.1016/j.jvs.2003.12.002
169. Schirmer RH, Adler H, Pickhardt M, Mandelkow E. Lest we forget you – methylene blue…. *Neurobiol Aging* (2011) 32(12): 2325.e7–16. doi:10.1016/j.neurobiolaging.2010.12.012
170. Ashurst J, Wasson M. Methemoglobinemia: a systematic review of the pathophysiology, detection, and treatment. *Del Med J* (2011) 83(7):203–8.
171. Richards A, Marshall H, McQuary A. Evaluation of methylene blue, thiamine, and/or albumin in the prevention of ifosfamide-related neurotoxicity. *J Oncol Pharm Pract* (2011) 17(4):372–80. doi:10.1177/1078155210385159
172. Ginimuge PR, Jyothi SD. Methylene blue: revisited. *J Anaesthesiol Clin Pharmacol* (2010) 26(4):517–20.
173. Melo TB, Reisaeter G. The physicochemical state of protoporphyrin IX in aqueous solution investigated by fluorescence and light scattering. *Biophys Chem* (1986) 25(1):99–104. doi:10.1016/0301-4622(86)85070-0
174. Montcel B, Mahieu-Williame L, Armoiry X, Meyronet D, Guyotat J. Two-peaked 5-ALA-induced PpIX fluorescence emission spectrum distinguishes glioblastomas from low grade gliomas and infiltrative component of glioblastomas. *Biomed Opt Express* (2013) 4(4):548–58. doi:10.1364/boe.4.000548
175. Acerbi F, Broggi M, Eoli M, Anghileri E, Cuppini L, Pollo B, et al. Fluorescein-guided surgery for grade IV gliomas with a dedicated filter on the surgical

microscope: preliminary results in 12 cases. *Acta Neurochir (Wien)* (2013) 155(7):1277–86. doi:10.1007/s00701-013-1734-9
176. Acerbi F, Broggi M, Eoli M, Anghileri E, Cavallo C, Boffano C, et al. Is fluorescein-guided technique able to help in resection of high-grade gliomas? *Neurosurg Focus* (2014) 36(2):E5. doi:10.3171/2013.11.focus13487
177. Diaz RJ, Dios RR, Hattab EM, Burrell K, Rakopoulos P, Sabha N, et al. Study of the biodistribution of fluorescein in glioma-infiltrated mouse brain and histopathological correlation of intraoperative findings in high-grade gliomas resected under fluorescein fluorescence guidance. *J Neurosurg* (2015) 122(6):1360–9. doi:10.3171/2015.2.jns132507
178. Schwake M, Stummer W, Suero Molina EJ, Wolfer J. Simultaneous fluorescein sodium and 5-ALA in fluorescence-guided glioma surgery. *Acta Neurochir (Wien)* (2015) 157(5):877–9. doi:10.1007/s00701-015-2401-0
179. Moore GE. Fluorescein as an agent in the differentiation of normal and malignant tissues. *Science* (1947) 106(2745):130–1. doi:10.1126/science.106.2745.130-a
180. Te Velde EA, Veerman T, Subramaniam V, Ruers T. The use of fluorescent dyes and probes in surgical oncology. *Eur J Surg Oncol* (2010) 36(1):6–15. doi:10.1016/j.ejso.2009.10.014
181. Gioux S, Choi HS, Frangioni JV. Image-guided surgery using invisible near-infrared light: fundamentals of clinical translation. *Mol Imaging* (2010) 9(5):237–55.
182. Terwisscha van Scheltinga AG, van Dam GM, Nagengast WB, Ntziachristos V, Hollema H, Herek JL, et al. Intraoperative near-infrared fluorescence tumor imaging with vascular endothelial growth factor and human epidermal growth factor receptor 2 targeting antibodies. *J Nucl Med* (2011) 52(11):1778–85. doi:10.2967/jnumed.111.092833
183. Sano K, Mitsunaga M, Nakajima T, Choyke PL, Kobayashi H. In vivo breast cancer characterization imaging using two monoclonal antibodies activatably labeled with near infrared fluorophores. *Breast Cancer Res* (2012) 14(2):R61. doi:10.1186/bcr3167
184. Oliveira S, van Dongen GA, Stigter-van Walsum M, Roovers RC, Stam JC, Mali W, et al. Rapid visualization of human tumor xenografts through optical imaging with a near-infrared fluorescent anti-epidermal growth factor receptor nanobody. *Mol Imaging* (2012) 11(1):33–46. doi:10.2310/7290.2011.00025
185. Blum G, von Degenfeld G, Merchant MJ, Blau HM, Bogyo M. Noninvasive optical imaging of cysteine protease activity using fluorescently quenched activity-based probes. *Nat Chem Biol* (2007) 3(10):668–77. doi:10.1038/nchembio.2007.26
186. Blum G, Weimer RM, Edgington LE, Adams W, Bogyo M. Comparative assessment of substrates and activity based probes as tools for non-invasive optical imaging of cysteine protease activity. *PLoS One* (2009) 4(7):e6374. doi:10.1371/journal.pone.0006374
187. Olson ES, Jiang T, Aguilera TA, Nguyen QT, Ellies LG, Scadeng M, et al. Activatable cell penetrating peptides linked to nanoparticles as dual probes for in vivo fluorescence and MR imaging of proteases. *Proc Natl Acad Sci U S A* (2010) 107(9):4311–6. doi:10.1073/pnas.0910283107
188. Deu E, Verdoes M, Bogyo M. New approaches for dissecting protease functions to improve probe development and drug discovery. *Nat Struct Mol Biol* (2012) 19(1):9–16. doi:10.1038/nsmb.2203
189. Olson ES, Whitney MA, Friedman B, Aguilera TA, Crisp JL, Baik FM, et al. In vivo fluorescence imaging of atherosclerotic plaques with activatable cell-penetrating peptides targeting thrombin activity. *Integr Biol (Camb)* (2012) 4(6):595–605. doi:10.1039/c2ib00161f
190. Lu Y, Low PS. Folate targeting of haptens to cancer cell surfaces mediates immunotherapy of syngeneic murine tumors. *Cancer Immunol Immunother* (2002) 51(3):153–62. doi:10.1007/s00262-002-0266-6
191. Leamon CP, Low PS. Delivery of macromolecules into living cells: a method that exploits folate receptor endocytosis. *Proc Natl Acad Sci U S A* (1991) 88(13):5572–6. doi:10.1073/pnas.88.13.5572
192. Low PS, Henne WA, Doorneweerd DD. Discovery and development of folic-acid-based receptor targeting for imaging and therapy of cancer and inflammatory diseases. *Acc Chem Res* (2008) 41(1):120–9. doi:10.1021/ar7000815
193. Weitman SD, Lark RH, Coney LR, Fort DW, Frasca V, Zurawski VR Jr, et al. Distribution of the folate receptor GP38 in normal and malignant cell lines and tissues. *Cancer Res* (1992) 52(12):3396–401.
194. O'Shannessy DJ, Yu G, Smale R, Fu YS, Singhal S, Thiel RP, et al. Folate receptor alpha expression in lung cancer: diagnostic and prognostic significance. *Oncotarget* (2012) 3(4):414–25. doi:10.18632/oncotarget.489
195. Ogawa M, Kosaka N, Choyke PL, Kobayashi H. H-type dimer formation of fluorophores: a mechanism for activatable, in vivo optical molecular imaging. *ACS Chem Biol* (2009) 4(7):535–46. doi:10.1021/cb900089j
196. Ogawa M, Kosaka N, Longmire MR, Urano Y, Choyke PL, Kobayashi H. Fluorophore-quencher based activatable targeted optical probes for detecting in vivo cancer metastases. *Mol Pharm* (2009) 6(2):386–95. doi:10.1021/mp800115t
197. Ogawa M, Regino CA, Choyke PL, Kobayashi H. In vivo target-specific activatable near-infrared optical labeling of humanized monoclonal antibodies. *Mol Cancer Ther* (2009) 8(1):232–9. doi:10.1158/1535-7163.mct-08-0862
198. Hanaoka H, Nagaya T, Sato K, Nakamura Y, Watanabe R, Harada T, et al. Glypican-3 targeted human heavy chain antibody as a drug carrier for hepatocellular carcinoma therapy. *Mol Pharm* (2015) 12(6):2151–7. doi:10.1021/acs.molpharmaceut.5b00132
199. Sato K, Nagaya T, Choyke PL, Kobayashi H. Near infrared photoimmunotherapy in the treatment of pleural disseminated NSCLC: preclinical experience. *Theranostics* (2015) 5(7):698–709. doi:10.7150/thno.11559
200. Nagaya T, Nakamura Y, Sato K, Harada T, Choyke PL, Kobayashi H. Near infrared photoimmunotherapy of B-cell lymphoma. *Mol Oncol* (2016) 10(9):1404–14. doi:10.1016/j.molonc.2016.07.010
201. Nagaya T, Nakamura Y, Sato K, Zhang YF, Ni M, Choyke PL, et al. Near infrared photoimmunotherapy with an anti-mesothelin antibody. *Oncotarget* (2016) 7(17):23361–9. doi:10.18632/oncotarget.8025
202. Nagaya T, Nakamura Y, Okuyama S, Ogata F, Maruoka Y, Choyke PL, et al. Near-infrared photoimmunotherapy targeting prostate cancer with prostate-specific membrane antigen (PSMA) antibody. *Mol Cancer Res* (2017) 15(9):1153–62. doi:10.1158/1541-7786.mcr-17-0164
203. Kobayashi H, Choyke PL. Target-cancer-cell-specific activatable fluorescence imaging probes: rational design and in vivo applications. *Acc Chem Res* (2011) 44(2):83–90. doi:10.1021/ar1000633
204. Chi C, Zhang Q, Mao Y, Kou D, Qiu J, Ye J, et al. Increased precision of orthotopic and metastatic breast cancer surgery guided by matrix metalloproteinase-activatable near-infrared fluorescence probes. *Sci Rep* (2015) 5:14197. doi:10.1038/srep14197
205. Weissleder R. A clearer vision for in vivo imaging. *Nat Biotechnol* (2001) 19(4):316–7. doi:10.1038/86684
206. Sheth RA, Upadhyay R, Stangenberg L, Sheth R, Weissleder R, Mahmood U. Improved detection of ovarian cancer metastases by intraoperative quantitative fluorescence protease imaging in a pre-clinical model. *Gynecol Oncol* (2009) 112(3):616–22. doi:10.1016/j.ygyno.2008.11.018
207. Urano Y, Asanuma D, Hama Y, Koyama Y, Barrett T, Kamiya M, et al. Selective molecular imaging of viable cancer cells with pH-activatable fluorescence probes. *Nat Med* (2009) 15(1):104–9. doi:10.1038/nm.1854
208. Mieog JS, Hutteman M, van der Vorst JR, Kuppen PJ, Que I, Dijkstra J, et al. Image-guided tumor resection using real-time near-infrared fluorescence in a syngeneic rat model of primary breast cancer. *Breast Cancer Res Treat* (2011) 128(3):679–89. doi:10.1007/s10549-010-1130-6
209. Ogawa M, Regino CA, Seidel J, Green MV, Xi W, Williams M, et al. Dual-modality molecular imaging using antibodies labeled with activatable fluorescence and a radionuclide for specific and quantitative targeted cancer detection. *Bioconjug Chem* (2009) 20(11):2177–84. doi:10.1021/bc900362k
210. Kobayashi H, Choyke PL, Ogawa M. Monoclonal antibody-based optical molecular imaging probes; considerations and caveats in chemistry, biology and pharmacology. *Curr Opin Chem Biol* (2016) 33:32–8. doi:10.1016/j.cbpa.2016.05.015
211. Hama Y, Urano Y, Koyama Y, Kamiya M, Bernardo M, Paik RS, et al. A target cell-specific activatable fluorescence probe for in vivo molecular imaging of cancer based on a self-quenched avidin-rhodamine conjugate. *Cancer Res* (2007) 67(6):2791–9. doi:10.1158/0008-5472.can-06-3315
212. Mahmood U, Tung CH, Bogdanov A Jr, Weissleder R. Near-infrared optical imaging of protease activity for tumor detection. *Radiology* (1999) 213(3):866–70. doi:10.1148/radiology.213.3.r99dc14866
213. Tung CH, Bredow S, Mahmood U, Weissleder R. Preparation of a cathepsin D sensitive near-infrared fluorescence probe for imaging. *Bioconjug Chem* (1999) 10(5):892–6. doi:10.1021/bc990052h

214. Urano Y. Novel live imaging techniques of cellular functions and in vivo tumors based on precise design of small molecule-based 'activatable' fluorescence probes. *Curr Opin Chem Biol* (2012) 16(5–6):602–8. doi:10.1016/j.cbpa.2012.10.023
215. Lotan R, Raz A. Lectins in cancer cells. *Ann N Y Acad Sci* (1988) 551:385–96; discussion 396–8. doi:10.1111/j.1749-6632.1988.tb22372.x
216. Ang CY, Tan SY, Lu Y, Bai L, Li M, Li P, et al. "Turn-on" fluorescence probe integrated polymer nanoparticles for sensing biological thiol molecules. *Sci Rep* (2014) 4:7057. doi:10.1038/srep07057
217. Shimizu Y, Temma T, Hara I, Makino A, Yamahara R, Ozeki E, et al. Micelle-based activatable probe for in vivo near-infrared optical imaging of cancer biomolecules. *Nanomedicine* (2014) 10(1):187–95. doi:10.1016/j.nano.2013.06.009
218. Feng T, Ai X, Ong H, Zhao Y. Dual-responsive carbon dots for tumor extracellular microenvironment triggered targeting and enhanced anticancer drug delivery. *ACS Appl Mater Interfaces* (2016) 8(29):18732–40. doi:10.1021/acsami.6b06695
219. Johansson MK, Cook RM. Intramolecular dimers: a new design strategy for fluorescence-quenched probes. *Chemistry* (2003) 9(15):3466–71. doi:10.1002/chem.200304941
220. Urano Y, Kamiya M, Kanda K, Ueno T, Hirose K, Nagano T. Evolution of fluorescein as a platform for finely tunable fluorescence probes. *J Am Chem Soc* (2005) 127(13):4888–94. doi:10.1021/ja043919h
221. Mohamed MM, Sloane BF. Cysteine cathepsins: multifunctional enzymes in cancer. *Nat Rev Cancer* (2006) 6(10):764–75. doi:10.1038/nrc1949
222. Tung CH, Mahmood U, Bredow S, Weissleder R. In vivo imaging of proteolytic enzyme activity using a novel molecular reporter. *Cancer Res* (2000) 60(17):4953–8.
223. Chen J, Tung CH, Allport JR, Chen S, Weissleder R, Huang PL. Near-infrared fluorescent imaging of matrix metalloproteinase activity after myocardial infarction. *Circulation* (2005) 111(14):1800–5. doi:10.1161/01.cir.0000160936.91849.9f
224. Sato C, Abe S, Saito Y, So Tsuruki E, Takamaru H, Makazu M, et al. A pilot study of fluorescent imaging of colorectal tumors using a gamma-glutamyl-transpeptidase-activatable fluorescent probe. *Digestion* (2015) 91(1):70–6. doi:10.1159/000369367
225. Ueo H, Shinden Y, Tobo T, Gamachi A, Udo M, Komatsu H, et al. Rapid intraoperative visualization of breast lesions with gamma-glutamyl hydroxymethyl rhodamine green. *Sci Rep* (2015) 5:12080. doi:10.1038/srep12080
226. Kawakubo K, Ohnishi S, Hatanaka Y, Hatanaka KC, Hosono H, Kubota Y, et al. Feasibility of using an enzymatically activatable fluorescence probe for the rapid evaluation of pancreatic tissue obtained using endoscopic ultrasound-guided fine needle aspiration: a pilot study. *Mol Imaging Biol* (2016) 18(3):463–71. doi:10.1007/s11307-015-0898-5
227. Asanuma D, Sakabe M, Kamiya M, Yamamoto K, Hiratake J, Ogawa M, et al. Sensitive beta-galactosidase-targeting fluorescence probe for visualizing small peritoneal metastatic tumours in vivo. *Nat Commun* (2015) 6:6463. doi:10.1038/ncomms7463
228. Sakabe M, Asanuma D, Kamiya M, Iwatate RJ, Hanaoka K, Terai T, et al. Rational design of highly sensitive fluorescence probes for protease and glycosidase based on precisely controlled spirocyclization. *J Am Chem Soc* (2013) 135(1):409–14. doi:10.1021/ja309688m
229. Shen Z, Prasai B, Nakamura Y, Kobayashi H, Jackson MS, McCarley RL. A near-infrared, wavelength-shiftable, turn-on fluorescent probe for the detection and imaging of cancer tumor cells. *ACS Chem Biol* (2017) 12(4):1121–32. doi:10.1021/acschembio.6b01094

Conflict of Interest Statement: The authors declare that the research was conducted in the absence of any commercial or financial relationships that could be construed as a potential conflict of interest.

frontiers in Oncology

REVIEW
published: 03 July 2018
doi: 10.3389/fonc.2018.00240

Prospects for Theranostics in Neurosurgical Imaging: Empowering Confocal Laser Endomicroscopy Diagnostics *via* Deep Learning

Mohammadhassan Izadyyazdanabadi[1,2†], Evgenii Belykh[2,3†], Michael A. Mooney[2], Jennifer M. Eschbacher[2], Peter Nakaji[2], Yezhou Yang[1] and Mark C. Preul[2]*

[1] Active Perception Group, School of Computing, Informatics, and Decision Systems Engineering, Arizona State University, Tempe, AZ, United States, [2] Neurosurgery Research Laboratory, Department of Neurosurgery, Barrow Neurological Institute, St. Joseph's Hospital and Medical Center, Phoenix, AZ, United States, [3] Department of Neurosurgery, Irkutsk State Medical University, Irkutsk, Russia

OPEN ACCESS

Edited by:
Zaver Bhujwalla,
Johns Hopkins University,
United States

Reviewed by:
Sandro M. Krieg,
Technische Universität München, Germany
Aslam Khan,
University of Missouri,
United States
Samata Kakkad,
Johns Hopkins University,
United States

***Correspondence:**
Mark C. Preul
mark.preul@dignityhealth.org

[†]These authors share first authorship.

Specialty section:
This article was submitted to Cancer Imaging and Diagnosis, a section of the journal Frontiers in Oncology

Received: 16 February 2018
Accepted: 18 June 2018
Published: 03 July 2018

Citation:
Izadyyazdanabadi M, Belykh E, Mooney MA, Eschbacher JM, Nakaji P, Yang Y and Preul MC (2018) Prospects for Theranostics in Neurosurgical Imaging: Empowering Confocal Laser Endomicroscopy Diagnostics via Deep Learning. Front. Oncol. 8:240. doi: 10.3389/fonc.2018.00240

Confocal laser endomicroscopy (CLE) is an advanced optical fluorescence imaging technology that has potential to increase intraoperative precision, extend resection, and tailor surgery for malignant invasive brain tumors because of its subcellular dimension resolution. Despite its promising diagnostic potential, interpreting the gray tone fluorescence images can be difficult for untrained users. CLE images can be distorted by motion artifacts, fluorescence signals out of detector dynamic range, or may be obscured by red blood cells, and thus interpreted as nondiagnostic (ND). However, just a single CLE image with a detectable pathognomonic histological tissue signature can suffice for intraoperative diagnosis. Dealing with the abundance of images from CLE is not unlike sifting through a myriad of genes, proteins, or other structural or metabolic markers to find something of commonality or uniqueness in cancer that might indicate a potential treatment scheme or target. In this review, we provide a detailed description of bioinformatical analysis methodology of CLE images that begins to assist the neurosurgeon and pathologist to rapidly connect on-the-fly intraoperative imaging, pathology, and surgical observation into a conclusionary system within the concept of theranostics. We present an overview and discuss deep learning models for automatic detection of the diagnostic CLE images and discuss various training regimes and ensemble modeling effect on power of deep learning predictive models. Two major approaches reviewed in this paper include the models that can automatically classify CLE images into diagnostic/ND, glioma/nonglioma, tumor/injury/normal categories, and models that can localize histological features on the CLE images using weakly supervised methods. We also briefly review advances in the deep learning approaches used for CLE image analysis in other organs. Significant advances in speed and precision of automated diagnostic frame selection would augment the diagnostic potential of CLE, improve operative workflow, and integration into brain tumor surgery. Such technology and bioinformatics analytics lend themselves to improved precision, personalization, and theranostics in brain tumor treatment.

Keywords: brain neoplasm, brain tumor imaging, cancer, confocal laser endomicroscopy, convolutional neural networks, deep learning, fluorescence, theranostics

INTRODUCTION

According to the American Cancer Society (1), in 2018 nearly 24,000 patients will be diagnosed with brain or other nervous system cancer and about 17,000 patients will die of the disease. Gliomas represent about 25% of all primary brain tumors and about 80% of all malignant tumors of the central nervous system (2). Over half of gliomas are glioblastoma multiforme (GBM), which is the most malignant primary brain tumor. GBMs are infiltrative and normally lack a clear margin making complete resection nearly impossible. Maximal resection of gliomas has been associated with improved prognosis (3, 4), although invasion and the bounds of functional cortex often limit extensive removal. Currently, technology for extending the limits of the tumor resection relies on intraoperative image-guided surgical navigation platforms, intraoperative magnetic resonance imaging (MRI), and intraoperative ultrasound (5). Wide-field fluorescence illumination through the operative microscope has been utilized more recently in an attempt identify the margins of infiltrating tumors (6).

Regardless of the means for identifying the tumor margin, examining tissue samples during surgery is paramount, especially for neurosurgery. Rapid intraoperative assessment of tumor tissue remains key for planning the treatment and for guiding the surgeon to areas of suspected tumor tissue during the operation, or planning adjunct intraoperative or post-operative therapy. The standard for the preliminary intraoperative histopathological interpretation is frozen section biopsy. However, the frozen section biopsy method has inherent complications such as sampling error, tissue freezing and cutting artifacts, lack of immediate pathologist interactivity with the surgeon, time spent for tissue delivery, processing, and analysis reporting back to the operating room (7, 8).

Handheld (i.e., size of a pen), portable confocal laser endomicroscopy (CLE) is undergoing exploration in brain tumor surgery because of its ability to produce precise histopathological information of tissue with subcellular resolution *in vivo* in real-time during tumor resection (8–13). CLE is a fluorescence imaging technology that is used with a combination with fluorescent drugs or probes. While a wide range of fluorophores have been used for CLE in gastroenterology and other medical specialties, fluorophore options are limited for *in vivo* human brain use due to potential toxicity (8, 9, 11, 14). Fluorescent dyes currently approved for use *in vivo* in the human brain include fluorescein sodium (FNa), indocyanine green, and 5-aminolevulinic acid (5-ALA) (9, 15, 16). Other fluorescent dyes, such as acridine orange, acriflavine (AF), and cresyl violet, can be used on human brain tissue *ex vivo* (12, 17). In neurosurgical oncology, CLE has been used to rapidly obtain optical cellular and cytoarchitectural information about tumor tissue as the resection progresses and to interrogate the resection cavity (12, 13). The details of system operation have been previously described in detail (8, 12, 13, 18). Briefly, the neurosurgeon may hold the CLE probe by the hand, fixate it with a flexible instrument holder in place, or may glide the probe across the tissue surface to obtain an "optical biopsy" with an image acquisition speed ranging between 0.8 and 20 frames per second dependent on operation of the particular CLE system. The surgeon may place the probe in a resting position at any time and proceed with the tumor resection, then take up the probe conveniently as desired. CLE imaging is believed to be potentially advantageous for appraisal of tumor margin regions or to examine suspected invasion into functional cortex near the final phases of tumor resection. The images display on a touchscreen monitor attached to the system. The neurosurgeon uses a foot pedal module to control depth of scanning and image acquisition. An assistant can also control the acquisition of images using a touchscreen. CLE images can be processed and presented as still images, digital video loops showing motion, or three-dimensional digital imaging volumes. CLE is a promising technology with the strategy to optimize or maximally increase the resection of malignant infiltrating brain tumors and/or to increase the positive yield of tissue biopsy. CLE may be of especial value during surgery when interrogating tissue at the tumor border regions or within the surgical resection bed that may harbor remnant malignant or spreading tumor.

Cancer is the subject of intense investigation into how theranostics may improve care and survival. As oncology is continually refined in its quest to understand and treat malignant brain tumors, such as GBMs, with which it has had very little success, utilization of precision and personalized surgical techniques would seem to be a logical step forward, especially as tumor resection is usually the first definitive treatment step. Dealing with the abundance of images from CLE is not unlike sifting through a myriad of genes, proteins, or other structural or metabolic markers to find something of commonality or uniqueness in cancer that might indicate a potential treatment scheme or target. CLE data acquisition is vast, burdened with a near-overwhelming number of images, many of which appear not useful at first inspection, although they may have unrecognized informative image subregions or characteristics. Mathematical algorithms and computer-based technology may rapidly assist making decisions upon an incredible number of images, such as CLE produces, that has never been encountered in neurosurgery.

Critical success in theranostics relies on the analytical method. Finding meaning can be elusive, and what may seem at first meaningful may only be superficial or even a spurious result, thus the analytical methodology is critical. In this review, we provide a detailed description of bioinformatical analysis methodology of CLE images that begins to assist the neurosurgeon and pathologist to rapidly connect on-the-fly intraoperative imaging, pathology, and surgical observation into a conclusionary system within the concept of theranostics. We describe methodology of deep convolutional neural networks (DCNNs) applied to CLE imaging focusing on neurosurgical application and review current modeling outcomes, elaborating and discussing studies aiming to suggest a more precise and tailored surgical approach and workflow for brain tumor surgery.

DEMANDING IMAGING INFORMATION LOAD OF CLE

Although the number of non-diagnostic CLE images has been shown to be high, the first diagnostic frames were acquired at

an average after the 14th frame (about 17 s) *in vivo* (12). This is certainly faster than for an intraoperative frozen section biopsy preparation and diagnostic interpretation. Nevertheless, the high number of non-diagnostic images imposed a significant time requirement and image storage load for subsequent image reviews, leading us and other groups to employ deep learning algorithms and neural networks that could potentially sort out non-diagnostic frames, while retaining only the diagnostic ones (19, 20). Attempts to use advanced feature coding schemes to classify cellular CLE images of brain tumor samples stained *ex vivo* with AF have been reported (21). Advantageously, acquired CLE images may be exchanged and translated for off-site digital histopathology review. However, large amounts of data may create an information overload that requires novel solutions for data CLE management and storage.

While CLE has obvious benefits of rapid on-the-fly digital imaging of tissue that can obviate long wait times for tissue interpretation and be quickly communicated between surgeons and pathologists, there are challenges to manage the amount of information provided. Current CLE systems can generate hundreds to thousands of images over the course of examination of the tumor or resection cavity which may take only a few minutes. It has been estimated that since CLE technology was put into use in 2011 for gastrointestinal (GI) diagnosis, over 100 million images have been created, with 30 million images created in the past year (22). The number of images may become rapidly overwhelming for the neurosurgeon and neuropathologist when trying to review and select a diagnostic or meaningful image or group of images as the surgical inspection progresses. CLE is designed to be used in real-time while the surgeon operates on the brain, but overcoming the barriers of image selection for diagnosis is a key component for making CLE a practical and advantageous technology for the neurosurgical operating room.

Other barriers for revealing underlying meaningful histology are motion and blood artifacts (especially) that are present in some of the CLE images, especially for CLE systems functioning in the blue laser range versus near-infrared (8, 9, 12, 23, 24). In addition, the neuropathologist must begin to work in a world of fluorescence images showing shades of gray, black, and white or artificial colorization, where before natural colored stains existed. The display of suboptimal nondiagnostic (ND) frames interferes with the selection of and focuses upon diagnostic images by the neurosurgeon and pathologist throughout the surgery to make a correct intraoperative interpretation. A previous study of CLE in human brain tumor surgeries found that about half of the acquired images were interpreted as nonuseful (i.e., ND) due to an inherent nature of the handheld microscopic probe with a narrow field of view that is subject to motion and blood artifacts or lack of discernible or characteristic features of the tissue itself (12). These artifacts or inherent aspects of operation of the probe include unsteady hand movements, moving the probe while in imaging mode across the tissue surface, and irregularities of the tissue surface such as a tumor resection bed in the cortex that includes tissue crevices, surface irregularities, bleeding, movement of the cortex with arterial pressure and respiration, etc.

Thus, although imaging is acquired on-the-fly, an image discrimination system to optimally sift out and identify useful images would substantially improve the performance of the CLE. Manually filtering out the ND images before making an intraoperative decision is challenging due to the large number of images acquired, the novel and frequently unfamiliar appearance of fluorescent stained tissue features compared with conventional histology. Interpretation of fluorescence CLE images for routine clinical pathology has only recently been trained and studied. Great variability among images from the same tumor type, and potential similarity between images from other tumor types for the untrained interpreter (**Figure 1**) make simple image filters and thresholding unreliable, thus requiring advanced computational methods.

THERANOSTICS AND CLE

Investigations into cancer genetics have produced treatment pathways by the application of bioinformatics methods leading to the concept of theranostics. As advances in molecular science have enabled "fingerprinting" of individual tumor with genomic and proteomic profiling, personalized theranostic agents can be developed to target-specific tumor microenvironment compartments (26). Although theranostic imaging provides new opportunities for personalized cancer treatment through the interface of chemistry, molecular biology, and imaging, quantitative image analysis remains as one of its challenges (27). More sophisticated image analysis methods are required to visualize and target every aspect of the tumor microenvironment in combination with molecular agents (28). CLE technology potentially allows a more personalized, precise, or tailored approach to the surgical procedure to remove an invasive brain tumor because of its capability to image at cell resolution intraoperatively on-the-fly. Fluorescent stains or markers allow the imaging and potential targeting of cells—nearly we are at the surgery of the "cell" as specific stains or fluorescent markers are developed. Whether this technology has practicality or yields survival benefit for malignant invasive brain tumors awaits the results of the first substantial *in vivo* explorations.

DEEP LEARNING APPLICATION IN CLE BRAIN TUMOR DIAGNOSTICS

Deep convolutional neural networks are a subset of "deep learning" technology, a machine learning subfield that has achieved immense recognition in the field of medical image analysis. Advances in computer-aided detection and diagnosis (CADx) systems in ultrasound, MRI, and computed tomography have been reviewed previously (29). There have been only a few studies that investigated deep learning application to enhance the diagnostic utility of CLE imaging in brain tumors. The utilization of deep learning approaches is mainly focused around three goals: diagnostic image detection, tumor classification, and feature localization originating from image segmentation. Here, we provide an overview of the basics of a deep learning methodology applicable to CLE images, summarize current results of brain tumor CLE image analysis using DCNNs, and juxtapose these with related works in other cancers.

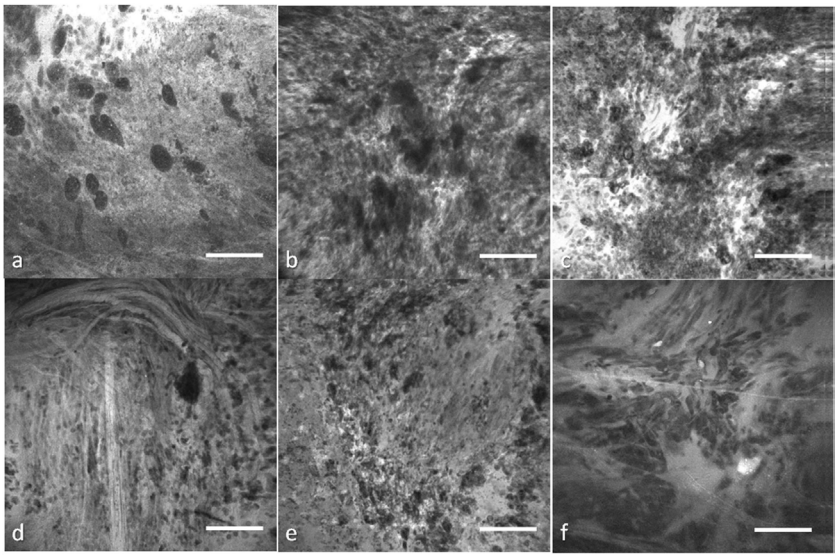

FIGURE 1 | Representative confocal laser endomicroscopy (CLE) images from glioma and meningioma acquired with Optiscan 5.1, Optiscan Pty., Ltd. **(A)** anaplastic oligodendroglioma, **(B)** recurrent astrocytoma, **(C)** glioblastoma multiforme, **(D)** fibrous meningioma (grade I), **(E)** chordoid meningioma (grade II), and **(F)** atypical meningioma (grade II). Field of view = 475 μm × 475 μm, resolution = 1,024 pixels × 1,024 pixels, bar = 100 μm. [Glioblastomas are a brain malignancy of astrocytic cell origin, show wild pleomorphism, proliferation of abnormal tumor-associated vasculature, necrosis, and vast brain invasion. Meningiomas arise from meningothelial cells and are usually attached to the dura. Although of a common origin, meningiomas have histological pattern subtypes and more aggressive types show atypical or anaplastic features. They do not display malignant brain infiltration (25)].

A DCNN consists of several layers, each having multiple units called feature maps (30). The first layer includes the input images that will be analyzed. To produce the second layer's feature maps, each pixel of layer 2 is connected to a local patch of pixels in layer 1 through a filter bank followed by an activation function, which is usually a rectified linear unit because of its fast-to-compute property compared with other functions (31). Model parameters are learned by minimizing the loss (the error between model prediction and the ground truth) using an optimization algorithm in two steps: forward and backward propagations (32, 33). To adjust the weights of filter banks, after each iteration of forward propagating the network, the derivatives of the loss function with respect to different weights are calculated to update the weights in a backward propagation (33). A pooling layer accumulates the features in a smaller region by replacing windows of a feature map with their maximum or the average value. By stacking several convolutional, pooling, and fully connected layers, a DCNN can learn a hierarchy of visual representations to recognize class-specific features in images (30). **Figure 2** shows an example network architecture and how the feature maps are calculated to perform diagnostic brain tumor image classification.

The validity of recommendations resulted from the DCNN analysis greatly depends upon the ground truth established by the expert professional. Unlike other conventional surgical tissue examination modalities like hematoxylin and eosin (H&E)-stained histopathological slides, the CLE images are novel to neuropathologists and neurosurgeons. Since the beginning of CLE investigation in brain tumor surgery, the ground truth was established by surgical biopsy and subsequent standard histopathology analysis acquired from the same location as the CLE "optical biopsy" and correlating the features on CLE images to the histopathological sections. Neuropathologists and neurosurgeons at a few select centers are correlating CLE features to histopathology in order to establish an expertise in reading CLE images, and such investigations are ongoing (10, 12, 18). The experience in CLE image interpretation is imperative for meaningful DCNN analysis. However, as described later, delving deeper into the DCNN analysis of the CLE while using ground truth established by the standard histopathology, results in identification of novel CLE features and allows many more images that may be termed suboptimal to in fact become useful. The improvement in workflow and diagnostics, and thus theranostics in CLE, will be dependent on robust computer learning architecture.

Tumor Classification

One of the first deep learning approaches for making a diagnosis of a brain tumor type based on the CLE images was a cascaded deep decision network (DDN), a type of DCNN (35). A network was trained for classification of glioma and meningioma images using their previously proposed multistage DDN architecture (36) for developing the model. The training process was as follows: LeNet, a relatively shallow CNN architecture initially proposed by LeCun et al. (37) for handwritten digit recognition, was trained on the training dataset until it produced descent classification results on validation images. Then, the images were divided into two categories: *easy images* (classified correctly by the model with high confidence) and *challenging images* (classified either wrongly or even correctly yet with a low confidence). The challenging images were passed to the next stage for retraining. In the second stage, a convolutional stage and two fully connected

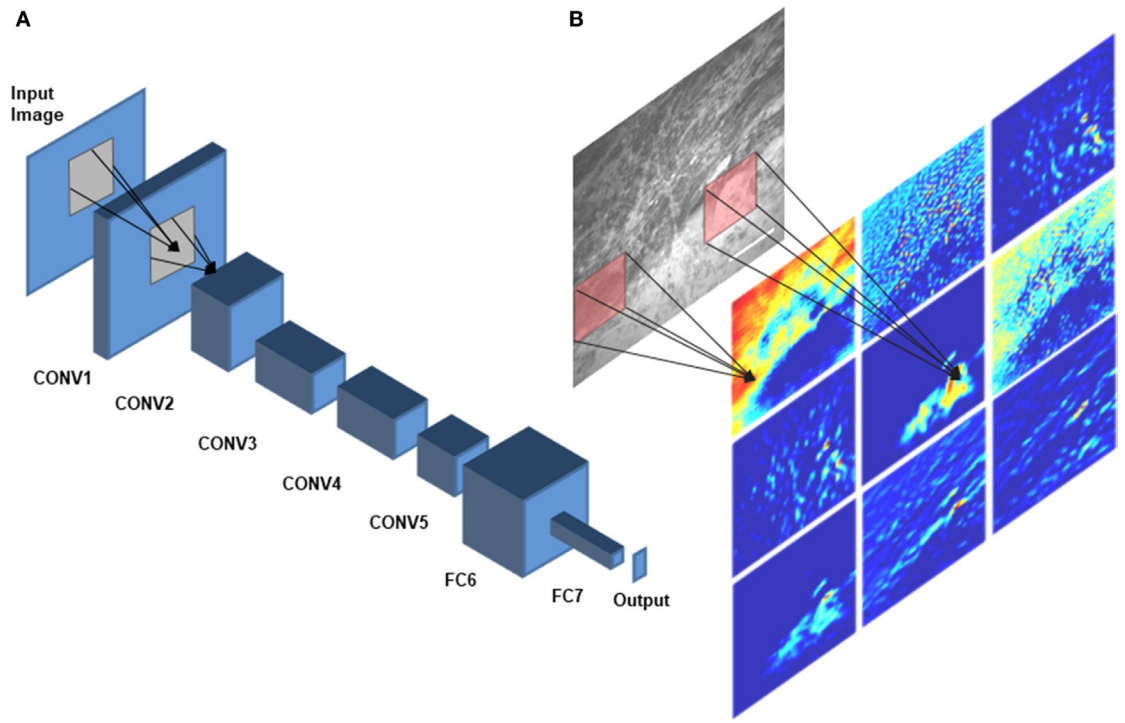

FIGURE 2 | Deep convolutional neural network (DCNN) architecture. A schematic diagram of AlexNet (34), a DCNN architecture that was trained on CLE images for diagnostic classification by Izadyyazdanabadi et al. (20), is shown in panel **(A)**. CONV1—CONV5 are the first five convolutional layers and FC6 and FC7 are the fully connected layers 6 and 7. Different feature maps of the first convolutional layer (color images) were calculated by convolving different filters (red squares) with the corresponding regions of the input image [illustrated in panel **(B)**].

layers and a softmax layer were stacked to the previous network and trained, while freezing the previous layers' parameters. After training the second stage on the challenging images from stage 1, the same process was repeated (finding confidence threshold, filtering the easy images, passing the challenging images to next stage, stacking the new layers to the previous network) until the model fails to improve on the validation dataset. After removing uninformative images using image entropy, a dataset was created of about 14,000 GBM and 12,000 meningioma images. The final proposed DDN could classify the GBM images with 86% accuracy while outperforming other methods such as SVM classifier applied on manual feature extraction, pretrained networks, and shallow CNNs (36).

We have previously developed an architecture to classify CLE images from experimental brain gliomas into three classes: tumor tissue, injured brain cortex tissue (no tumor), and normal brain cortical tissue (38). This study was undertaken to examine the ability of CLE image analysis to discriminate between tumor tissue, tissue subjected to the minor tissue trauma that surgical resection produces, and normal brain tissue. FNa may extravasate in the first two situations potentially causing surgeon confusion. This classification model was inspired by Inception, which is a DCNN for classifying generic images (39). Due to the small size of our training dataset (663 diagnostic images selected from 1,130 images acquired), we used fine-tuning to train the model with a learning rate of 0.001. We used a nested left-out validation method to estimate the model performance on images from new biopsies. Images were divided into three data sets based on biopsy level: training ($n = 446$), validation ($n = 217$), and test set ($n = 40$). Model performance increased to 88% when images were classified using two classes only (tumor tissue or non-tumor tissue) which was only slightly lower than the neuropathologists' mean accuracy (90%). The sensitivity and specificity of the model in discriminating a tumor region from non-tumor tissue were 78 and 100%, respectively. The area under the ROC curve (AUC) value for tumor/non-tumor tissue classification was 93%. Subgroup analysis showed that the model could discriminate CLE images from tumor and injury with 85% accuracy (mean of accuracy for neuropathologists was 88%), 78% sensitivity, and 100% specificity. We expect that performance of the model will be improved in terms of accuracy and speed by going forth from a small experimental data set to operation on large clinical data sets.

Diagnostic Image Classification

Entropy-based filtering is one of the simplest ways to filter out non-diagnostic CLE images. In a study by Kamen et al. (21), CLE images obtained from brain tumors were classified automatically. An entropy-based approach was used to remove the noninformative images from their dataset and two common brain tumors (meningioma and glioma) were differentiated using bag of words (BoW) and other sparse coding methods. However, entropy might not be an ideal method since many ND images have nearly as high entropy as diagnostic ones, as shown in **Figure 3**. Due to the large number of CLE images produced during surgery,

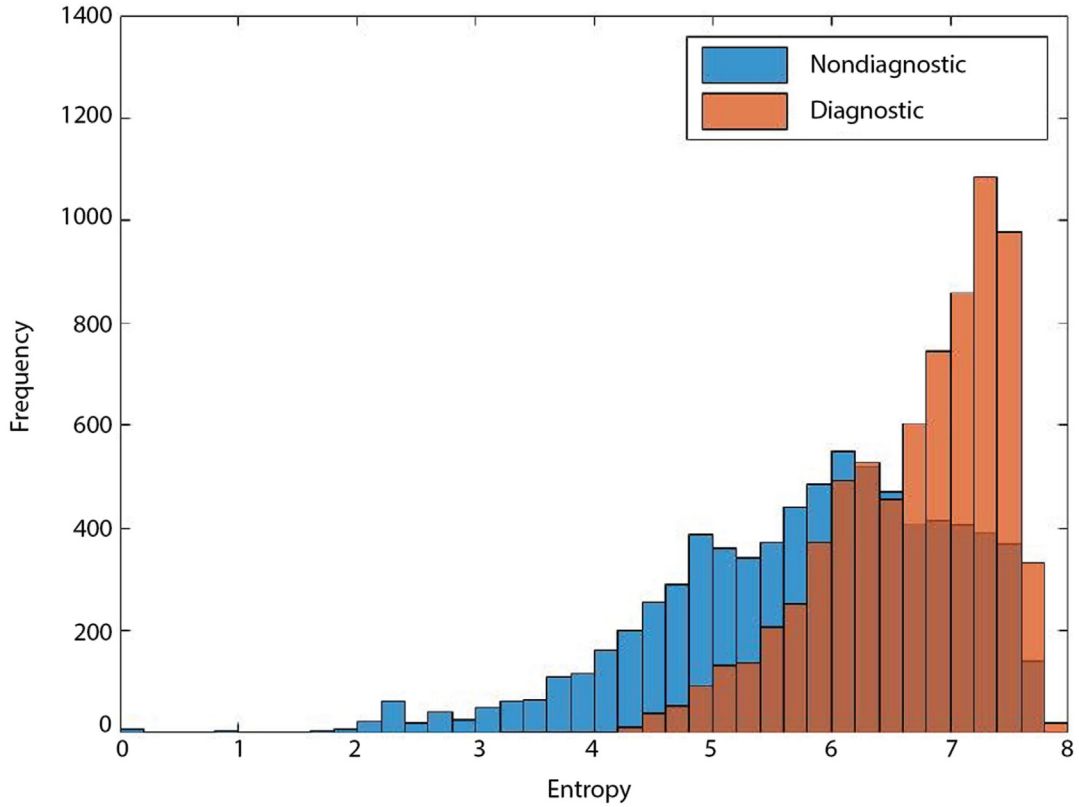

FIGURE 3 | Entropy of diagnostic (orange) and nondiagnostic (ND) (blue) images. The overlap between the entropy of diagnostic and ND CLE frames limits its feasibility for precise discrimination between the two classes (19).

importance of data pruning, as has been shown in our previous study (38), and the incompetency of entropy method, we developed a deep learning model for reliable classification of images into diagnostic and non-diagnostic categories (20). A blinded neuropathologist and two neurosurgeons proficient with CLE image interpretation individually annotated all the images in our dataset. For each patient, the histopathological features of corresponding CLE images and H&E-stained frozen and permanent sections were reviewed and the diagnostic value of each image was examined. When a CLE image revealed any clear identifiable histopathological feature, it was labeled as diagnostic; otherwise, it was labeled as ND (12). **Table 1** provides the composition of our dataset. We tested the developed diagnostic frame detection models on 4,171 CLE images chosen from various patients isolated during training.

Aiming to improve the diagnostic image classification method, we then developed 42 new models, which included 30 single and 12 ensemble models using 2 network architectures, 3 training regimes, and 2 ensemble methods (20). During training of each single model, different sections of the dataset were used to reflect the diversity of training data in the developed models' knowledge. We exercised various training regimes to investigate how "deep" the training should be for CNNs applied to a CLE image classification problem to produce optimal (i.e., diagnostically useful) results. Depending on which layers of the network are being learned through training, we had three regimes. In the deep training (DT) regime, the whole model parameters were initialized randomly (training from scratch) and were updated through training. In the shallow fine-tuning (SFT) regime, the whole model weights, except the last fully connected layer, were initialized with the corresponding values from the pretrained model and their values were fixed during training. The last fully connected layer was initialized randomly and was tuned during training. In the deep fine-tuning (DFT) regime, all model weights were initialized with the corresponding values from the pretrained model and were tuned with nonzero learning rates. Our cross validation showed SFT and DFT experiments required 10 times smaller initial learning rates (0.001) compared with the DT regime (0.01). We also used a dropout layer (ratio = 0.5) and L2 regularization ($\lambda = 0.005$).

For this interobserver study, we created a validation review dataset consisting of 540 images randomly chosen from the test dataset in the second review. Two new neurosurgeons reviewed

TABLE 1 | The composition of our dataset in the diagnostic image classification (20).

	Development	Test	Total
No. of patients	59	15	74
No. of images	16,366	4,171	20,537
No. of diagnostic images	8,023	2,071	10,094
No. of nondiagnostic images	8,343	2,100	10,443

Number of patients and images used for model development and testing is provided.

the validation review dataset without having access to the corresponding H&E-stained slides and labeled them as diagnostic or ND. The ensemble of DCNN models for detecting diagnostic CLE images achieved 85% agreement with the gold standard defined by the trained expert with subsequent confirmation by another independent observer (**Figure 4**), without considering or comparison to the H&E slide images. In comparison, the two trained neurosurgeons achieved 75 and 67% agreement with the gold standard using only CLE images. These results indicated that when only CLE images were provided, the model could detect the diagnostic CLE images with better agreement to the H&E-aided annotation. The example CLE images assessed with our diagnostic analysis model are presented on **Figure 5**. In order to compare the power of deep learning models with filtering approaches used in other related studies, we used entropy as a baseline (21, 35). Subsequent evaluation of our test dataset of CLE images suggested that DCNN-based diagnostic evaluation has a higher agreement with the ground truth compared with the entropy-based quality assessment (**Table 2**).

Feature Localization and Image Segmentation

Most of the current object localization studies in medical imaging use supervised learning that requires an annotated dataset for the training process. Physicians need to review the images and mark the location of interesting areas for each image, thus making it a costly and time-consuming process. Weakly supervised localization (WSL) methods have been proposed in computer vision to localize features using a weaker annotation, i.e., image-level labels instead of pixel-level labels.

We have previously investigated feature localization on brain tumor CLE images (20). Following the training and testing of the DCNN model for diagnostic image classification, 8 of 384 reviewed colored neuron activation maps from the first layer of the model were selected for 4 diagnostic CLE images representative for glioma. Selected activation maps highlighted diagnostic tissue architecture patterns in warm colors. Particularly, selected maps emphasized regions of optimal image contrast, where hypercellular and abnormal nuclear features could be identified, and could serve as diagnostic features for image classification (**Figure 5**, bottom row). In addition, a sliding window method was successfully applied to highlight diagnostic aggregates of abnormally large malignant glioma cells and atypically hypercellular areas (20) (**Figure 5**). Such feature localization from the hidden layers makes the interpretation of the model results more illustrative and objective, especially from a clinical point of view where diagnosis cannot be made without sufficient evidence. In addition, model-based feature localization can be performed considerably faster than human inspection and interpretation.

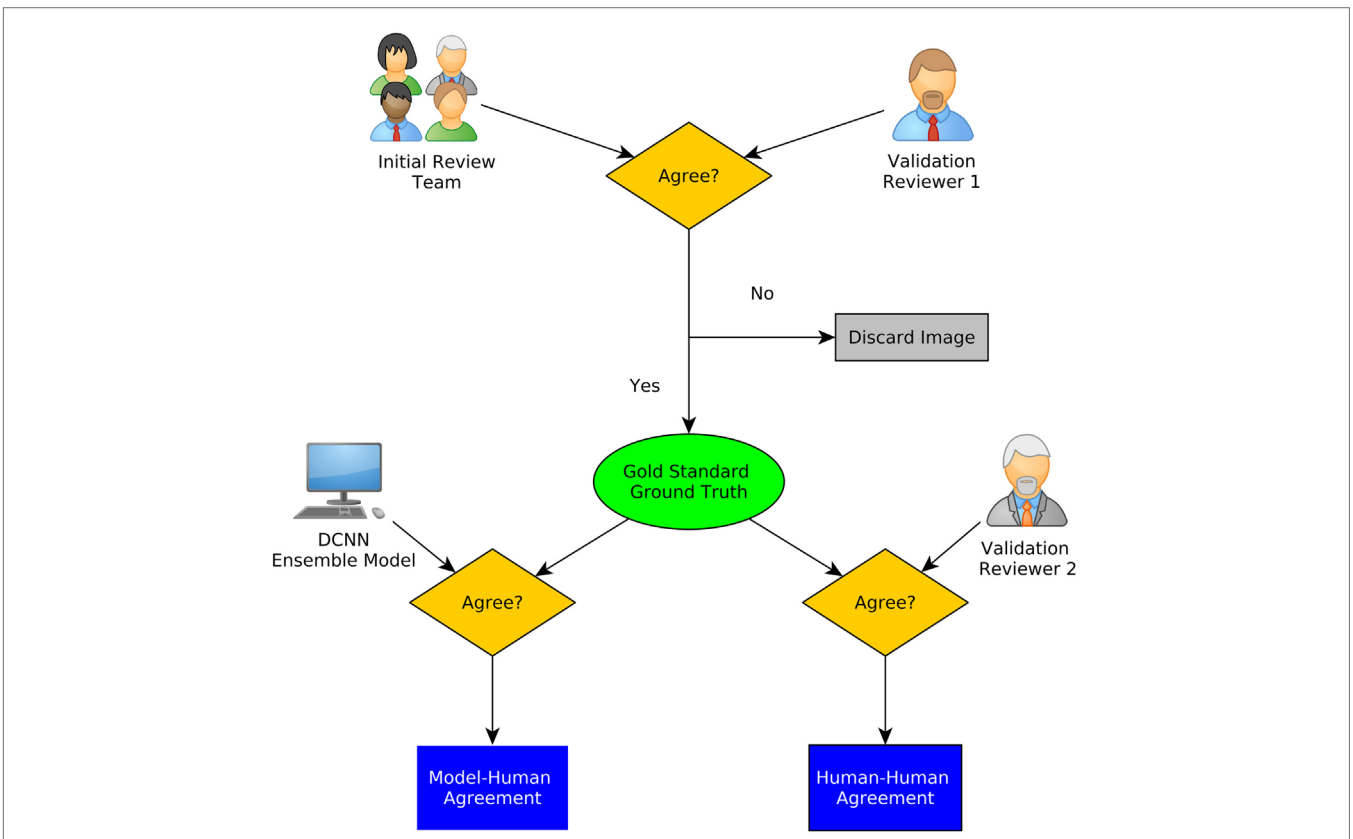

FIGURE 4 | A schematic diagram of interobserver study. Gold standard was defined using the initial review and one of the secondary raters. The agreement of the ensemble model as well as the other rater with the gold standard is calculated (20).

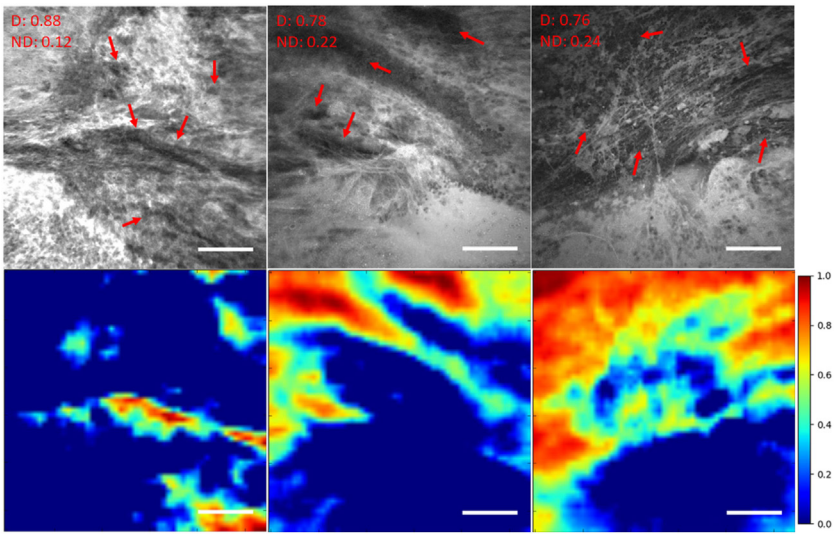

FIGURE 5 | Unsupervised semantic localization of the CLE histopathological features (20). First row displays the original CLE images, along with the probability of each image being diagnostic (D) and nondiagnostic (ND), estimated by the model. Red arrows mark the cellular regions recognized by a neurosurgeon. Second row shows the corresponding activation of neurons from the first layer (conv1, neuron 24) (shallow features learned by the model); it highlights some of the cellular areas (in warm colors) present in the images which were identified as diagnostic regions by the neurosurgeon reviewer. The color bars show the relative diagnostic value for each color: red marks the most diagnostic regions (1.0) and blue marks the ND regions (0.0). Field of view = 475 μm × 475 μm, resolution = 1,024 pixels × 1,024 pixels, bar = 100 μm.

TABLE 2 | Deep convolutional neural network (DCNN) and entropy-based performance in diagnostic image classification (20).

Model	Accuracy (%)	Area under the ROC curve
DCNN 1	78.8	0.87
DCNN 2	81.8	0.89
Entropy-based	57.20	0.71

DCNN methods showed higher agreement with the neurosurgeons' evaluation. DCNN2 (39) has a deeper architecture with fewer parameters than DCNN1 (34).

In another study, we applied a state-of-the-art WSL approach (40) to localize glioma tumor features in CLE images (41). In this method, a global average pooling layer was stacked to the convolutional layers of the network to create diagnostic feature maps. Representative localization and segmentation results are shown in **Figures 6** and **7**. A neurosurgeon with expertise in CLE imaging identified and highlighted the cellular areas in each CLE image (first column of both figures). By inserting the images and their labels (i.e., overall diagnostic quality: diagnostic and ND) to the network, the model automatically learns the primary diagnostic features of gliomas (e.g., cellular areas). In **Figure 6**, the first column shows three CLE images along with the annotated diagnostic areas (red arrows) by a neurosurgeon, while the second column presents the diagnostic areas that the model highlighted with warm colors. The color bar near to each intensity map shows the relative diagnostic value for each color—red marks the most diagnostic regions and blue marks the ND regions. In **Figure 7**, after producing the diagnostic feature maps, each image was then segmented into diagnostic and ND regions by thresholding (highlighted in green and purple); the recognized diagnostic regions correlated well with the neurosurgeon's annotation. This method has two potential benefits: (1) improvement of the efficiency of glioma CLE imaging by recognizing the present diagnostic features and guiding the surgeon in tumor resection and (2) further investigation of the detected diagnostic regions may extend the physician's perceptions about the glioma appearance and its phenotypes in CLE images.

DEEP LEARNING-EMPOWERED CLE DIAGNOSTICS IN OTHER CANCERS

Oral Squamous Cell Carcinoma (OSCC)

Oral squamous cell carcinoma is a common cancer affecting 1.3 million cases worldwide annually (42). Because of the insufficient precision in current screening methods, most OSCC cases are unfortunately diagnosed at advanced stages leading to poor clinical outcome. CLE has allowed *in vivo* examination of OSCC which may lead to earlier and more effective therapeutic outcomes during examination (43). In a study by Aubreville et al. (44), a CNN was trained to classify normal and carcinogenic CLE image patches. A dataset of 11,000 CLE images was evenly distributed between the two classes. The images were acquired from 12 patients and images with artifact (motion, noise, mucus, or blood) were excluded, leading to 7,894 good quality images. Consequently, each image was divided into 21 overlapping patches, all of which were labeled the same as the whole image. The artifact patches were removed from images and the remaining ones were normalized to have zero mean and unit SD. Image rotation was used to augment the image dataset size.

LeNet was used to train the model for patch classification. This network has only two convolutional and one fully connected

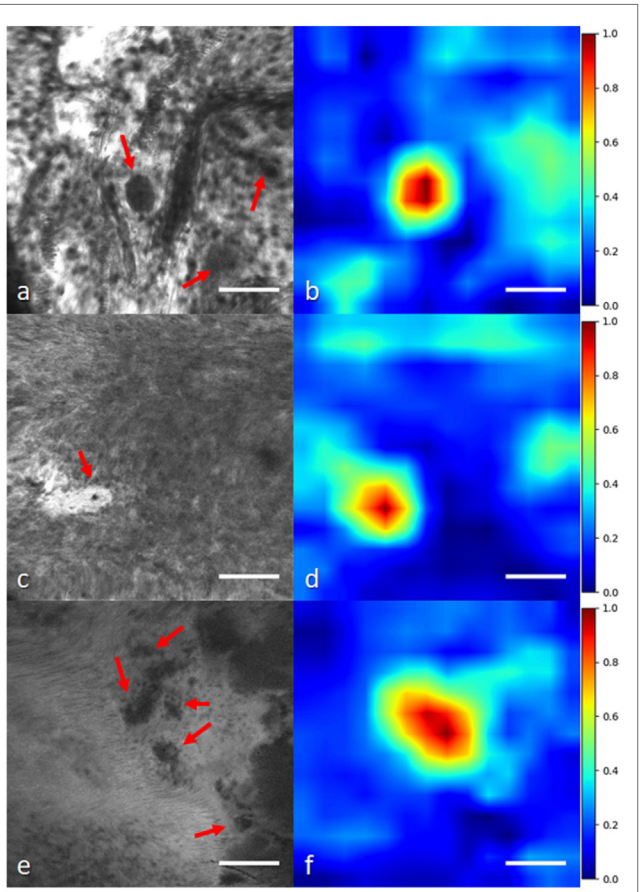

FIGURE 6 | Histological glioma feature localization with a weakly supervised approach: global average pooling (41). **(A,C,E)** Left column shows CLE images from glioma cases [**(A,C)** recurrent infiltrating astrocytoma **(E)** oligodendroglioma]. Red arrows mark the cellular regions recognized by a neurosurgeon. **(B,D,F)** Second column shows the important regions detected with the model (highlighted in warm colors). The color bars show the relative diagnostic value for each color: red marks the most diagnostic regions (1.0) and blue marks the nondiagnostic regions (0.0). Field of view = 475 μm × 475 μm, resolution = 1,024 pixels × 1,024 pixels, bar = 100 μm.

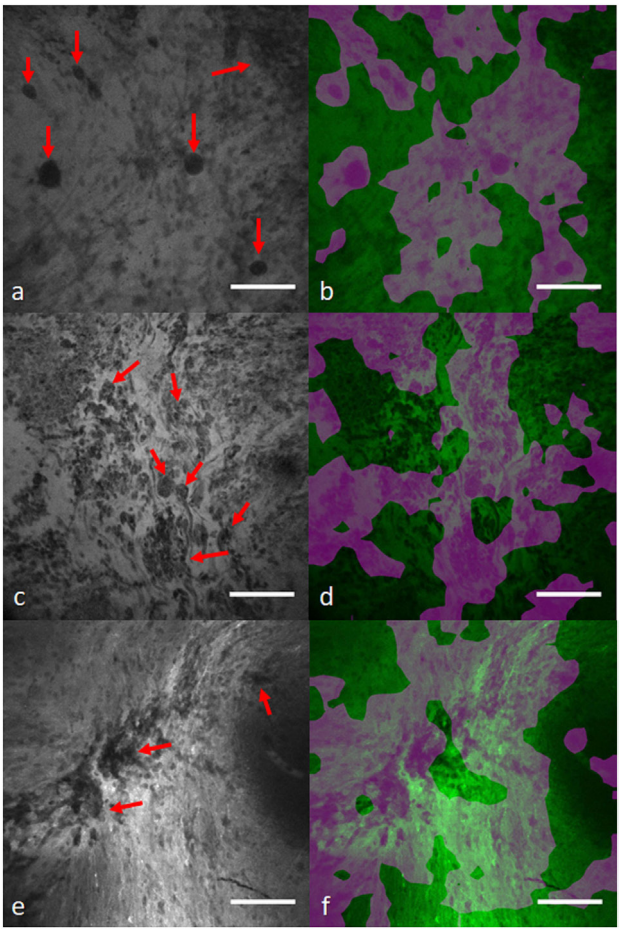

FIGURE 7 | Diagnostic image segmentation in CLE images of gliomas with global average pooling approach (41). First column **(A,C,E)** shows the original diagnostic images from glioma cases [**(A)** recurrent glioblastoma multiforme, **(C)** recurrent infiltrating astrocytoma, and **(E)** anaplastic oligodendroglioma]. Red arrows mark the cellular regions recognized by a neurosurgeon. **(B,D,F)** Second column shows the segmented key features highlighted in purple. Field of view = 475 μm × 475 μm, resolution = 1,024 pixels × 1,024 pixels, bar = 100 μm.

layers with drop out. The model combined the probability scores from each constituent patch as being carcinogenic to arrive at the final prediction for the whole image. The network was trained from scratch with initial learning rate of 0.001 and Adam optimizer to minimize the cross-entropy.

To compare the proposed method with conventional textural feature-based classification approaches, two feature extraction methods [gray-level co-occurrence matrix (GLCM) and local binary patterns (LBP)] and a classification approach [random forest (RF)] methods were combined to discriminate images at two scales (1.0× and 0.5×). Furthermore, CNN transfer learning was explored by SFT the last fully connected layer of the pretrained Inception-v3 network (45), using the original dataset. For cross validation, a leave-one-patient-out cross validation was followed, meaning images were used from one patient for testing the model and the remaining cases for training the model.

Both the patch-based and whole image CNN approaches outperformed the textural feature extraction and classification methods. The proposed CNN method could differentiate the normal and carcinogenic CLE images with 88% accuracy, 87% sensitivity, and 90% specificity when applied at 0.5× scale (the 1× scale produced suboptimal results). The shallow fine-tuned Inception-v3 model could also achieve 87% accuracy, 91% sensitivity, and 84% specificity. The AUC values for the two methods (the proposed CNN and Inception-v3) were roughly similar (95%). The AUC values for feature extraction methods and RF classifier was significantly lower than CNN methods (RF-GLCM = 81%, RF-LBP = 89%). Interestingly, the trained model on OSCC CLE images was successfully applied for classification of CLE images from a different organ site, vocal cord squamous cell carcinoma.

In transfer learning with pretrained Inception-v3, the authors only modified the weights of the last layer, while keeping the previous layers parameters stationary. However, studies (20, 46)

have shown that deeply fine-tuning the pretrained networks may help the network adapt better to the new dataset by upgrading the feature extraction layers as well. However, SFT only allows updating the classification layer, which might not be sufficient for optimal performance.

Vocal Cord Cancer

To differentiate between healthy and cancerous tissue of vocal cords, Vo et al. (47) developed a BoW based on textural and CNN features using a dataset of 1,767 healthy and 2,657 carcinogenic images from five patients. Small patches with 105 pixel × 105 pixel size were extracted and augmented (with rotation), leading to 374,972 patches. For the textural feature-based classification, each image was represented by the concatenation of all its constituent patch-driven feature descriptors. For the CNN features, a LeNet shallow CNN was trained on the patch dataset for a binary classification (with SGD optimizer; momentum = 0.9 and learning rate = 0.0005). To create the visual vocabulary, two feature encoding [Fisher vector (48) and Vector of Locally Aggregated Descriptors (VLAD) (49)] and two classification methods (SVM and RF) were tested for comparing their classification performance.

A Leave-One-Sequence-Out cross validation was used to evaluate these methods. The CNN features combined with VLAD encoder and RF classifier achieved an accuracy of 82% and sensitivity of 82% on the test images that surpassed other approaches. However, despite its promising accuracy, the proposed multistage approach (patch creation, feature extraction, feature encoding, clustering, and classification) is much more complicated than the current end-to-end DCNN architectures, which have all these procedures embedded in their stacked layers. However, even with this approach, the CNN features could outperform textural features extracted manually (47).

Lung Cancer

Gil et al. (50) investigated visual patterns in bronchoscopic CLE images for discriminating benign and malignant lesions and aiding lung cancer diagnosis. A pretrained network developed by the visual geometry group (VGG) (51) on a large generic image dataset was used for feature extraction and reduced the resulting feature vector dimension from 4,096 to 100, while preserving roughly 90% of the original feature vector energy for computational efficiency. Three different methods [k-means, k-Nearest Neighbor (kNN), and their proposed topology-based approach] were applied on the feature codes to group images with similar features together and intrinsically discriminate images from benign and malignant tissue. Model predictive power was compared with the final diagnosis on 162 images from 12 cases (6 with malignant and 6 with benign lesions) and achieved 85% accuracy, 88% sensitivity, and 81% specificity.

Interobserver studies were performed with three observers to compare the subjective visual assessment of images with the model performance (the observers were blinded to the final diagnosis). Interestingly, the three observers could make a correct diagnosis only for 60% of the selected CLE images (sensitivity: 73% for malignant and 36% for benign images) on average. In the second experiment, two observers made a final diagnosis after examining all the images from each case. The model was also supplied with all the images from each of the 12 cases and rendered a final decision for each case. While the model could differentiate malignant and benign cases with 100% accuracy (12/12), the two observers could confirmatively make the correct diagnosis only in 67% (8/12) of cases.

Although the observers' knowledge in the domain might have affected their performance, the objective results suggest that the bronchoscopic CLE images contain enough visual information for determining the malignancy of the tumor and the VGG network is an excellent candidate for extracting these discriminative features. The proposed topology-based clustering method could outperform common clustering and classification methods (k-means and kNN) in differentiating the two classes of images.

Despite its advantages, the proposed method had two major limitations. First, even though it can differentiate images from the two classes, it cannot predict the label for each cluster. The method can separate the images into two groups, but it is not able to give information about their labels. Second, it is unclear if there was independent development (for determining model parameters) and test datasets to avoid bias in model development.

GI Tract Cancer

Hong et al. (52) proposed a CNN architecture for classifying CLE images from three subcategories of Barret's esophagus: intestinal metaplasia (IM), gastric metaplasia (GM), and neoplasia (NPL). The network was composed of four convolutional layers and two max-pooling and fully connected layers. The size of convolutional kernels was 3 × 3 and zero padding was also used. Stride of max-pooling was 2 × 2 which was applied in layers two and four. Fully connected layers followed the fourth convolutional layer, and each had 1,024 neurons. The output label was determined by a softmax layer which produced three probabilities for each subcategory.

The network was trained on the augmented CLE images of Barret's esophagus (155 IM, 26 GM, and 55 NPL) for 15,000 iterations with the batch size of 20 images. Cross-entropy was used as a cost function in their experiment. The trained model was then tested on 26 independent images (17 IM, 4 GM, and 5 NPL) for validation. The imbalance in size of different subcategories caused the model to observe more frequent instances of IM and NPL compared with GM during training. This created a bias in the model prediction which can be seen in the high accuracy for predicting IM and NPL instances (100 and 80%) and very low accuracy for predicting GM instances (0%). However, CLE is being used with increasing frequency for detecting precancerous and cancerous lesions in the GI tract. The highest numbers of CLE images have been acquired from the GI tract where such imaging technology has been approved for use clinically for a few years.

CONCLUSION

Precision, personalization, and improved therapeutics in medicine can only progress with improved technology, analysis, and

logic. The science and philosophy of theranostics is the nexus of these. Several studies have emphasized the importance of theranostic imaging in personalized treatment of cancer (26–28). Medical data acquired on patients has become more voluminous, and it will continue in such manner. The amount of data available and necessary for analysis has already eclipsed human capabilities. For example, the new technology of handheld surgical tools that can rapidly image at the cellular resolution on-the-fly produces more images than a pathologist can possibly examine. As CLE technology develops, there will not be one fluorophore, but multiple fluorophores applied directly to the tumor or administered to the patient varying from nonspecific to specifically identifying cell structures or processes used simultaneously and presented in a myriad of image combinations for greatly varying histopathology. Analytic methods for selection and interpretation of the CLE images is already being explored to be incorporated into CLE operating systems, so that the unit display can differentiate tissue and label the image as well with near-on-the-fly capabilities. Computational hardware power and effective analytic model infrastructure are the only two limits. CLE systems and other related systems are being produced by several imaging technology companies and groups and are close to approval with European and American medical device regulatory agencies. However, it seems prudent given the enormous numbers of images already produced and those projected with adoption of such technology, that there is immediate exploration into such image analysis methods to allow the pathologist and neurosurgeon to make optimal decisions based on the CLE imaging and to take advantage of the on-the-fly technology proposition.

Success or meaningful diagnostic and therapeutic indication in the burgeoning field of theranostics is only as good as the data incorporated and the methodology employed for analysis and to extract meaning, including its validation. In many cases, relatively simple statistics have been used for analysis, while pattern recognition or neural network techniques may be used in more complicated scenarios. For images such as from CLE, the whole image may be important, or perhaps only certain subregions, or crucial data may lie in regions on cursory inspection deemed to be nonuseful, such as in areas of motion artifact. Complicating this situation are the overwhelming numbers of images yielded from the CLE application. Clinical decision environments currently require assistance to not only access and categorize the collection of images but to also draw conclusions and inferences that have critical diagnostic and treatment consequences. A pathologist and neurosurgeon will not have time to inspect a thousand images per case, especially in the midst of CLE use intraoperatively. Therefore, a theranostics approach, i.e., the nexus of biological data, rapid informatics scrutiny and evaluation, and tailored human decision, must be employed as we venture into realms of ever increasing information in neurosurgery in search of personalization and precision, especially as we have encountered it first in the surgery and treatment of malignant invasive brain tumors. In addition, pathologists and neurosurgeons will need to become versed in the methodology of the CLE decision making processes to have confidence in diagnostic labels and to base treatment decisions upon them, thus the reason for presenting details of analytical architectures in this review.

Two DCNN-based approaches are reviewed in this paper: models that can automatically classify CLE images [classifications of images that are diagnostic/ND (20), glioma/nonglioma (19), tumor/injury/normal (38)] and models that can localize histological features from diagnostic images using weakly supervised methods (41). Manually annotated in-house datasets were used to train and test these approaches in most of the studies. For the tumor classification purpose, data pruning could enhance the results for both DCNN models and outperformed manual feature extraction and classification (21). Fine-tuning and ensemble modeling could enhance the model performance in the diagnostic image classification. The ensemble effect was stronger in DT and DFT than SFT developed models.

Despite extensive research on CLE clinical application in neurosurgery (9–14, 18), there have been few attempts in the automatic analysis of these images to enhance CLE clinical utility. Deep learning could be beneficial in filtering the ND images with higher speed and reasonable accuracy compared with subjective assessment (19). Our inter-rater agreement evaluation (20) showed that the proposed model could achieve promising agreement with the gold standard defined by a majority assessment by neurosurgeon reviewers. Overall, results suggest that DCNN-based diagnostic evaluation has a higher agreement with the ground truth than the entropy-based quality assessment used in other studies (21, 35). Furthermore, such methods suggest that semantic histological features may be highlighted in CLE images as confirmed by a neurosurgeon reviewer. This shows that the DCNN structure could learn semantic concepts like tumor type or diagnostic value of CLE images through different levels of feature representation. Early results show that WSL-based glioma feature localization was able to precisely mark the cells in the images. DCNNs are also much faster than handcrafted methods at deployment phase. Our deeply trained models could classify about 40 new images in a second, while the handcrafted method takes 5.4 s to process single image (21).

Other confocal imaging techniques may be aided by such deep learning models. Confocal reflectance microscopy (CRM) has been studied (53, 54) for rapid, fluorophore-free evaluation of brain biopsy specimen *ex vivo*. CRM allows preserving the biopsy tissue for future permanent analysis, immunohistochemical studies, and molecular studies. Proposed DCNN classification and localization approaches are well suited for analysis and interpretation of CRM images as well as CLE. Further studies on application of DCNN on CRM images are needed to further validate their utility for intraoperative diagnosis.

Continued use of unsupervised image segmentation methods to detect meaningful histological features from confocal brain tumor images will likely allow for more rapid and detailed diagnosis. With the large rate of images produced, a technology-free and unassisted approach to analyze the CLE images would impede the exploitation of maximal pathological information during surgery. Accessible databases of CLE images would allow various image analysis methods to be tried on large numbers of images. Such image collection strategies are part of the platform of the relatively new International Society for Endomicroscopy.

DCNNs can enhance extraction and recognition of CLE diagnostic features that may be integrated into the standard brain tumor classification protocols similarly to the current research flow in the whole-slide digital image analysis for personalized cancer care (55, 56). This may refine current diagnostic criteria and potentially aid the discovery of novel-related features. With such technology, neurosurgery truly enters the realm of theranostics in the operating room itself—we are on the verge of highly tailored and precise surgery at the cellular level. Such an approach is critical for neurosurgery because surgery and treatment for an invasive brain tumor frequently deals with spread into eloquent cortex—the areas that make us "human." In fact, even before entering the operating room the neurosurgeon can begin to discuss strategy with the patient if tumor is located or not located in eloquent cortex based on a CLE "optical biopsy." Thus, theranostics also involves treatment strategies and decisions of when to "stop," especially true when the CLE system intraoperatively reveals cells invading, for example, primary motor or language cortex. With analytical pathologists uniting different clinical and morphological information for an integrated diagnosis, such a computer-aided CLE analysis workflow would improve imaging (diagnostics) and achieve maximal, more precise removal of tumor mass (therapy) as the initial treatment goals toward greater precision, personalization and success in the surgery and treatment of malignant invasive brain tumors (theranostics).

AUTHOR CONTRIBUTIONS

MI, EB, YY, and MP conceived and wrote article. MI and YY formulated computer learning systems. MM and PN acquired images from neurosurgical cases, reviewed, and edited manuscript. JE, EB, MP examined all pathology, reviewed, and edited manuscript. All the authors reviewed and approved manuscript.

FUNDING

We thank the Barrow Neurological Foundation and the Newsome Chair in Neurosurgery Research held by MP for funding. EB acknowledges stipend support SP-2240.2018.4. Part of this study involving Confocal Laser Endomicroscopy was supported by a materials grant from Carl Zeiss AG, Oberkochen, Germany. The grantor did not have any contribution or effect on study design, data collection, analysis, or paper preparation.

REFERENCES

1. American Cancer Society. *Cancer Facts and Statistics*. (2018). Available from: https://cancerstatisticscenter.cancer.org/ (accessed May 29, 2018).
2. Ostrom QT, Gittleman H, Fulop J, Liu M, Blanda R, Kromer C, et al. CBTRUS statistical report: primary brain and central nervous system tumors diagnosed in the United States in 2008–2012. *Neuro Oncol* (2015) 17:iv1–62. doi:10.1093/neuonc/nov189
3. Almeida JP, Chaichana KL, Rincon-Torroella J, Quinones-Hinojosa A. The value of extent of resection of glioblastomas: clinical evidence and current approach. *Curr Neurol Neurosci Rep* (2015) 15:517. doi:10.1007/s11910-014-0517-x
4. Sanai N, Polley M-Y, McDermott MW, Parsa AT, Berger MS. An extent of resection threshold for newly diagnosed glioblastomas: clinical article. *J Neurosurg* (2011) 115:3–8. doi:10.3171/2011.2.JNS10998
5. Sanai N, Berger MS. Surgical oncology for gliomas: the state of the art. *Nat Rev Clin Oncol* (2018) 15:112. doi:10.1038/nrclinonc.2017.171
6. Maugeri R, Villa A, Pino M, Imperato A, Giammalva GR, Costantino G, et al. With a little help from my friends: the role of intraoperative fluorescent dyes in the surgical management of high-grade gliomas. *Brain Sci* (2018) 8:31. doi:10.3390/brainsci8020031
7. Tofte K, Berger C, Torp SH, Solheim O. The diagnostic properties of frozen sections in suspected intracranial tumors: a study of 578 consecutive cases. *Surg Neurol Int* (2014) 5:170. doi:10.4103/2152-7806.146153
8. Martirosyan NL, Georges J, Eschbacher JM, Cavalcanti DD, Elhadi AM, Abdelwahab MG, et al. Potential application of a handheld confocal endomicroscope imaging system using a variety of fluorophores in experimental gliomas and normal brain. *Neurosurg Focus* (2014) 36:E16. doi:10.3171/2013.11.FOCUS13486
9. Belykh E, Martirosyan NL, Yagmurlu K, Miller EJ, Eschbacher JM, Izadyyazdanabadi M, et al. Intraoperative fluorescence imaging for personalized brain tumor resection: current state and future directions. *Front Surg* (2016) 3:55. doi:10.3389/fsurg.2016.00055
10. Charalampaki P, Javed M, Daali S, Heiroth HJ, Igressa A, Weber F. Confocal laser endomicroscopy for real-time histomorphological diagnosis: our clinical experience with 150 brain and spinal tumor cases. *Neurosurgery* (2015) 62:171–6. doi:10.1227/NEU.0000000000000805
11. Foersch S, Heimann A, Ayyad A, Spoden GA, Florin L, Mpoukouvalas K, et al. Confocal laser endomicroscopy for diagnosis and histomorphologic imaging of brain tumors in vivo. *PLoS One* (2012) 7:e41760. doi:10.1371/journal.pone.0041760
12. Martirosyan NL, Eschbacher JM, Kalani MY, Turner JD, Belykh E, Spetzler RF, et al. Prospective evaluation of the utility of intraoperative confocal laser endomicroscopy in patients with brain neoplasms using fluorescein sodium: experience with 74 cases. *Neurosurg Focus* (2016) 40:E11. doi:10.3171/2016.1.FOCUS15559
13. Sanai N, Eschbacher J, Hattendorf G, Coons SW, Preul MC, Smith KA, et al. Intraoperative confocal microscopy for brain tumors: a feasibility analysis in humans. *Neurosurgery* (2011) 68:282–90; discussion 290. doi:10.1227/NEU.0b013e318212464e
14. Zehri AH, Ramey W, Georges JF, Mooney MA, Martirosyan NL, Preul MC, et al. Neurosurgical confocal endomicroscopy: a review of contrast agents, confocal systems, and future imaging modalities. *Surg Neurol Int* (2014) 5:60. doi:10.4103/2152-7806.131638
15. Mooney MA, Zehri AH, Georges JF, Nakaji P. Laser scanning confocal endomicroscopy in the neurosurgical operating room: a review and discussion of future applications. *Neurosurg Focus* (2014) 36:E9. doi:10.3171/2013.11.FOCUS13484
16. Liu JTC, Meza D, Sanai N. Trends in fluorescence image-guided surgery for gliomas. *Neurosurgery* (2014) 75:61–71. doi:10.1227/NEU.0000000000000344
17. Martirosyan NL, Georges J, Eschbacher JM, Belykh E, Carotenuto A, Spetzler RF, et al. Confocal scanning microscopy provides rapid, detailed intraoperative histological assessment of brain neoplasms: experience with 106 cases. *Clin Neurol Neurosurg* (2018) 169:21–8. doi:10.1016/j.clineuro.2018.03.015
18. Eschbacher J, Martirosyan NL, Nakaji P, Sanai N, Preul MC, Smith KA, et al. In vivo intraoperative confocal microscopy for real-time histopathological imaging of brain tumors: clinical article. *J Neurosurg* (2012) 116:854–60. doi:10.3171/2011.12.JNS11696
19. Izadyyazdanabadi M, Belykh E, Martirosyan N, Eschbacher J, Nakaji P, Yang Y, et al. Improving utility of brain tumor confocal laser endomicroscopy: objective value assessment and diagnostic frame detection with convolutional neural networks. *Progress in Biomedical Optics and Imaging – Proceedings of SPIE 10134*. Orlando, FL (2017).
20. Izadyyazdanabadi M, Belykh E, Mooney M, Martirosyan N, Eschbacher J, Nakaji P, et al. Convolutional neural networks: ensemble modeling, fine-tuning and unsupervised semantic localization for neurosurgical CLE images. *J Vis Commun Image Represent* (2018) 54:10–20. doi:10.1016/j.jvcir.2018.04.004

21. Kamen A, Sun S, Wan S, Kluckner S, Chen T, Gigler AM, et al. Automatic tissue differentiation based on confocal endomicroscopic images for intraoperative guidance in neurosurgery. *Biomed Res Int* (2016) 2016:8. doi:10.1155/2016/6183218
22. Loiseau S. *Presentation at International Society for Endomicroscopy*. Paris, France (2017).
23. Sankar T, Delaney PM, Ryan RW, Eschbacher J, Abdelwahab M, Nakaji P, et al. Miniaturized handheld confocal microscopy for neurosurgery: results in an experimental glioblastoma model. *Neurosurgery* (2010) 66:410–7. doi:10.1227/01.NEU.0000365772.66324.6F
24. Martirosyan NL, Cavalcanti DD, Eschbacher JM, Delaney PM, Scheck AC, Abdelwahab MG, et al. Use of in vivo near-infrared laser confocal endomicroscopy with indocyanine green to detect the boundary of infiltrative tumor. *J Neurosurg* (2011) 115:1131–8. doi:10.3171/2011.8.JNS11559
25. Louis DN, Ohgaki H, Wiestler OD, Cavenee WK, Burger PC, Jouvet A, et al. The 2007 WHO classification of tumours of the central nervous system. *Acta Neuropathol* (2007) 114:97–109. doi:10.1007/s00401-007-0278-6
26. Stasinopoulos I, Penet MF, Chen Z, Kakkad S, Glunde K, Bhujwalla ZM. Exploiting the tumor microenvironment for theranostic imaging. *NMR Biomed* (2011) 24:636–47. doi:10.1002/nbm.1664
27. Penet MF, Chen Z, Kakkad S, Pomper MG, Bhujwalla ZM. Theranostic imaging of cancer. *Eur J Radiol* (2012) 81:S124–6. doi:10.1016/S0720-048X(12)70051-7
28. Penet M-F, Krishnamachary B, Chen Z, Jin J, Bhujwalla ZM. Molecular imaging of the tumor microenvironment for precision medicine and theranostics. *Adv Cancer Res* (2014) 124:235–56. doi:10.1016/B978-0-12-411638-2.00007-0
29. Greenspan H, van Ginneken B, Summers RM. Guest editorial deep learning in medical imaging: overview and future promise of an exciting new technique. *IEEE Trans Med Imaging* (2016) 35:1153–9. doi:10.1109/TMI.2016.2553401
30. LeCun Y, Bengio Y, Hinton G. Deep learning. *Nature* (2015) 521:436–44. doi:10.1038/nature14539
31. Glorot X, Bordes A, Bengio Y. Deep sparse rectifier neural networks. *AISTATS '11 Proc 14th Int Conf Artif Intell Stat*, Ft. Lauderdale, FL, (Vol. 15) (2011). p. 315–23.
32. Rumelhart DE, Hinton GE, Williams RJ. Learning representations by back-propagating errors. *Nature* (1986) 323:533–6. doi:10.1038/323533a0
33. Le Cun Y, Boser B, Denker JS, Henderson D, Howard RE, Hubbard W, et al. Handwritten digit recognition with a back-propagation network. *Adv. Neural Inf. Process. Syst*, Denver, CO (1990). p. 396–404.
34. Krizhevsky A, Sutskever I, Hinton GE. ImageNet classification with deep convolutional neural networks. *Advances in Neural Information Processing Systems*, Lake Tahoe, NV (2012). p. 1097–105.
35. Murthy VN, Singh V, Sun S, Bhattacharya S, Chen T, Comaniciu D. Cascaded deep decision networks for classification of endoscopic images. In: Styner MA, Angelini ED, editors. *Proc. SPIE 10133, Medical Imaging 2017: Image Processing, 101332B*. Orlando, FL (2017).
36. Murthy VN, Singh V, Chen T, Manmatha R, Comaniciu D. Deep decision network for multi-class image classification. *2016 IEEE Conference on Computer Vision and Pattern Recognition (CVPR)*, Las Vegas, NV (2016). p. 2240–8.
37. LeCun Y, Jackel LD, Eduard HA, Bottou N, Cartes C, Denker JS, et al. Learning algorithms for classification: a comparison on handwritten digit recognition. *Neural Networks: The Statistical Mechanics Perspective*, Pohang (1995). p. 261–76.
38. Belykh E, Miller EJ, Patel AA, Yazdanabadi MI, Martirosyan NL, Yağmurlu K, et al. Diagnostic accuracy of the confocal laser endomicroscope for in vivo differentiation between normal and tumor tissue during fluorescein-guided glioma resection: laboratory investigation. *World Neurosurg* (2018) 115:e337–48. doi:10.1016/j.wneu.2018.04.048
39. Szegedy C, Liu W, Jia Y, Sermanet P, Reed S, Anguelov D, et al. Going deeper with convolutions. *Proceedings of the IEEE Conference on Computer Vision and Pattern Recognition*, Boston, MA (2015). p. 1–9.
40. Zhou B, Khosla A, Lapedriza A, Oliva A, Torralba A. Learning deep features for discriminative localization. *Proceedings of the IEEE Conference on Computer Vision and Pattern Recognition*, Las Vegas, NV (2016). p. 2921–9.
41. Izadyyazdanabadi M, Belykh E, Cavallo C, Zhao X, Gandhi S, Moreira LB, et al. Weakly-supervised learning-based feature localization in confocal laser endomicroscopy glioma images. *arXiv Prepr. arXiv1804.09428* (2018).
42. Ferlay J, Soerjomataram I, Dikshit R, Eser S, Mathers C, Rebelo M, et al. Cancer incidence and mortality worldwide: sources, methods and major patterns in GLOBOCAN 2012. *Int J Cancer* (2015) 136:E359–86. doi:10.1002/ijc.29210
43. Thong PS, Olivo M, Kho KW, Zheng W, Mancer K, Harris M, et al. Laser confocal endomicroscopy as a novel technique for fluorescence diagnostic imaging of the oral cavity. *J Biomed Opt* (2007) 12:14007. doi:10.1117/1.2710193
44. Aubreville M, Knipfer C, Oetter N, Jaremenko C, Rodner E, Denzler J, et al. Automatic classification of cancerous tissue in laserendomicroscopy images of the oral cavity using deep learning. *Sci Rep* (2017) 7:11979. doi:10.1038/s41598-017-12320-8
45. Szegedy C, Vanhoucke V, Ioffe S, Shlens J, Wojna Z. Rethinking the inception architecture for computer vision. *2016 IEEE Conference on Computer Vision and Pattern Recognition (CVPR)*, Las Vegas, NV: IEEE (2016). p. 2818–26.
46. Tajbakhsh N, Shin JY, Gurudu SR, Hurst RT, Kendall CB, Gotway MB, et al. Convolutional neural networks for medical image analysis: full training or fine tuning? *IEEE Trans Med Imaging* (2016) 35:1299–312. doi:10.1109/TMI.2016.2535302
47. Vo K, Jaremenko C, Bohr C, Neumann H, Maier A. Automatic classification and pathological staging of confocal laser endomicroscopic images of the vocal cords. *Bildverarbeitung für die Medizin 2017*, Heidelberg: Springer (2017). p. 312–7.
48. Sánchez J, Perronnin F, Mensink T, Verbeek J. Image classification with the fisher vector: theory and practice. *Int J Comput Vis* (2013) 105:222–45. doi:10.1007/s11263-013-0636-x
49. Jégou H, Douze M, Schmid C, Pérez P. Aggregating local descriptors into a compact image representation. *Proceedings of the IEEE Computer Society Conference on Computer Vision and Pattern Recognition*, San Francisco, CA: IEEE (2010). p. 3304–11.
50. Gil D, Ramos-Terrades O, Minchole E, Sanchez C, Cubero de Frutos N, Diez-Ferrer M, et al. Classification of confocal endomicroscopy patterns for diagnosis of lung cancer. In: Cardoso MJ, Arbel T, Luo X, Stefan Wesarg S, Reichl T, González Ballester MA, editors. *Computer Assisted and Robotic Endoscopy and Clinical Image-Based Procedures. CARE 2017, CLIP 2017. Lecture Notes in Computer Science, vol 10550*. Quebec: Springer (2017). p. 151–9.
51. Chatfield K, Simonyan K, Vedaldi A, Zisserman A. Return of the devil in the details: delving deep into convolutional nets. *BMVC*, Nottingham, UK (2014). p. 1–11.
52. Hong J, Park B, Park H. Convolutional neural network classifier for distinguishing Barrett's esophagus and neoplasia endomicroscopy images. *2017 39th Annual International Conference of the IEEE Engineering in Medicine and Biology Society (EMBC)*, Jeju: IEEE (2017). p. 2892–5.
53. Eschbacher JM, Georges JF, Belykh E, Yazdanabadi MI, Martirosyan NL, Szeto E, et al. Immediate label-free ex vivo evaluation of human brain tumor biopsies with confocal reflectance microscopy. *J Neuropathol Exp Neurol* (2017) 76:1008–22. doi:10.1093/jnen/nlx089
54. Mooney MA, Georges J, Yazdanabadi MI, Goehring KY, White WL, Little AS, et al. Immediate ex-vivo diagnosis of pituitary adenomas using confocal reflectance microscopy: a proof-of-principle study. *J Neurosurg* (2018) 128:1072–5. doi:10.3171/2016.11.JNS161651
55. Madabhushi A, Lee G. Image analysis and machine learning in digital pathology: challenges and opportunities. *Med Image Anal* (2016) 33:170–5. doi:10.1016/j.media.2016.06.037
56. Djuric U, Zadeh G, Aldape K, Diamandis P. Precision histology: how deep learning is poised to revitalize histomorphology for personalized cancer care. *NPJ Precis Oncol* (2017) 1:22. doi:10.1038/s41698-017-0022-1

Conflict of Interest Statement: The authors declare that the research was conducted in the absence of any commercial or financial relationships that could be construed as a potential conflict of interest.

The reviewer SKa and handling Editor declared their shared affiliation.

frontiers in Oncology

ORIGINAL RESEARCH
published: 14 August 2019
doi: 10.3389/fonc.2019.00770

CXCR4-Directed Imaging in Solid Tumors

Rudolf A. Werner[1,2,3], Stefan Kircher[4], Takahiro Higuchi[1,2,5], Malte Kircher[1,2], Andreas Schirbel[1], Hans-Jürgen Wester[6], Andreas K. Buck[1,2], Martin G. Pomper[7,8], Steven P. Rowe[7,8†] and Constantin Lapa[1,2*†]*

[1] Department of Nuclear Medicine, University of Wuerzburg, Wuerzburg, Germany, [2] Comprehensive Heart Failure Center, University of Wuerzburg, Wuerzburg, Germany, [3] Department of Nuclear Medicine, Hanover Medical School, Hanover, Germany, [4] Institute for Pathology, University of Wuerzburg, Wuerzburg, Germany, [5] Graduate School of Medicine, Dentistry and Pharmaceutical Sciences, Okayama University, Okayama, Japan, [6] Pharmaceutical Radiochemistry, Technische Universität München, Munich, Germany, [7] Division of Nuclear Medicine and Molecular Imaging, The Russell H. Morgan Department of Radiology and Radiological Science, Johns Hopkins University School of Medicine, Baltimore, MD, United States, [8] Department of Urology, The James Buchanan Brady Urological Institute, Johns Hopkins University School of Medicine, Baltimore, MD, United States

OPEN ACCESS

Edited by:
Bo Gao,
Affiliated Hospital of Guizhou Medical University, China

Reviewed by:
Jiang He,
University of Virginia, United States
Xiu Juan Li,
Tai'an City Central Hospital, China

***Correspondence:**
Steven P. Rowe
srowe8@jhmi.edu
Constantin Lapa
lapa_c@ukw.de

† These authors have contributed equally to this work

Specialty section:
This article was submitted to Cancer Imaging and Image-directed Interventions, a section of the journal Frontiers in Oncology

Received: *28 April 2019*
Accepted: *30 July 2019*
Published: *14 August 2019*

Citation:
Werner RA, Kircher S, Higuchi T, Kircher M, Schirbel A, Wester H-J, Buck AK, Pomper MG, Rowe SP and Lapa C (2019) CXCR4-Directed Imaging in Solid Tumors. Front. Oncol. 9:770. doi: 10.3389/fonc.2019.00770

Despite histological evidence in various solid tumor entities, available experience with CXCR4-directed diagnostics and endoradiotherapy mainly focuses on hematologic diseases. With the goal of expanding the application of CXCR4 theranostics to solid tumors, we aimed to elucidate the feasibility of CXCR4-targeted imaging in a variety of such neoplasms.

Methods: Nineteen patients with newly diagnosed, treatment-naïve solid tumors including pancreatic adenocarcinoma or neuroendocrine tumor, cholangiocarcinoma, hepatocellular carcinoma, renal cell carcinoma, ovarian cancer, and prostate cancer underwent [^{68}Ga]Pentixafor PET/CT. CXCR4-mediated uptake was assessed both visually and semi-quantitatively by evaluation of maximum standardized uptake values (SUV_{max}) of both primary tumors and metastases. With physiologic liver uptake as reference, tumor-to-background ratios (TBR) were calculated. [^{68}Ga]Pentixafor findings were further compared to immunohistochemistry and [^{18}F]FDG PET/CT.

Results: On [^{68}Ga]Pentixafor PET/CT, 10/19 (52.6%) primary tumors were visually detectable with a median SUV_{max} of 5.4 (range, 1.7–16.0) and a median TBR of 2.6 (range, 0.8–7.4), respectively. The highest level of radiotracer uptake was identified in a patient with cholangiocarcinoma (SUV_{max}, 16.0; TBR, 7.4). The relatively low uptake on [^{68}Ga]Pentixafor was also noted in metastases, exhibiting a median SUV_{max} of 4.5 (range, 2.3–8.8; TBR, 1.7; range, 1.0–4.1). A good correlation between uptake on [^{68}Ga]Pentixafor and histological derived CXCR4 expression was noted ($R = 0.62$, $P < 0.05$). In the 3 patients in whom [^{18}F]FDG PET/CT was available, [^{68}Ga]Pentixafor exhibited lower uptake in all lesions.

Conclusions: In this cohort of newly diagnosed, treatment-naïve patients with solid malignancies, CXCR4 expression as detected by [^{68}Ga]Pentixafor-PET/CT and immunohistochemistry was rather moderate. Thus, CXCR4-directed imaging may not play a major role in the management of solid tumors in the majority of patients.

Keywords: CXCR4, [^{68}Ga]Pentixafor, theranostics, solid tumors, chemokine receptor

INTRODUCTION

C-X-C motif chemokine receptor 4 (CXCR4) is overexpressed in more than 20 tumor types and plays a crucial role in tumor growth, tumor invasiveness, cancer cell-microenvironment interaction, and metastasis (1, 2). Notably, the presence of CXCR4 has been linked to unfavorable outcomes in multiple different tumor entities, including hematologic malignancies, breast cancer, renal cell carcinoma, gynecologic malignancies, pancreatic adenocarcinoma, and hepatocellular carcinoma (3).

[^{68}Ga]Pentixafor is a radiolabelled CXCR4 ligand that allows for sensitive and high-contrast visualization of the presence of the receptor *in vivo* (4, 5). Its use for non-invasive whole-body positron emission tomography (PET) imaging has been demonstrated in multiple (mainly hematologic) malignancies and also inflammatory disease conditions (6–14). Additionally, ^{90}Y- or ^{177}Lu-labeled Pentixather (15), the therapeutic partner of [^{68}Ga]Pentixafor, has successfully been introduced for the treatment of hematologic neoplasias such as multiple myeloma, diffuse large B cell lymphoma, and acute myeloid leukemia (16–20).

In solid malignancies, pilot studies have hinted at a role for CXCR4-directed imaging in various selected diseases, such as small cell lung cancer, esophageal adenocarcinoma, and poorly differentiated neuroendocrine neoplasms (21–23). Of note, Blümel et al. reported on the use of [^{68}Ga]Pentixafor in patients diagnosed with adrenocortical cancer, with 70% of the subjects being potentially suitable for a treatment with [^{177}Lu]/[^{90}Y]Pentixather (24).

On the other hand, Vag et al. could not detect relevant [^{68}Ga]Pentixafor uptake in a heterogenous subset of different solid cancers, including non-small cell lung cancer, malignant melanoma, sarcoma, cancer of unknown primary (CUP), or breast cancer (25). Our group reported on rather discouraging results in a small cohort of patients with malignant pleural mesothelioma (26).

Thus, given these contradictory findings among different solid tumor entities, we aimed to broaden the experience of CXCR4-targeted PET imaging in solid cancers by investigating a subset of different tumors, including cholangiocarcinoma (CCC), hepatocellular carcinoma (HCC), pancreatic adenocarcinoma or neuroendocrine tumor, and ovarian cancer.

MATERIALS AND METHODS

[^{68}Ga]Pentixafor was administered on a compassionate use basis in compliance with §37 of the Declaration of Helsinki and The German Medicinal Products Act, AMG §13.2b. All patients underwent imaging for clinical purposes and gave written and informed consent to the diagnostic procedures. The local institutional review board waived the requirement for additional approval because of the retrospective character of this study.

Patients

Between September, 2014 and August, 2015, 19 patients (11 males, 8 females; aged 71 ± 7 years; range, 60–81 y) with newly diagnosed, treatment-naive solid tumors underwent [^{68}Ga]Pentixafor-PET/computed tomography (CT) for assessment of CXCR4 expression. In 3/19 (15.8%) subjects, additional [^{18}F]FDG PET/CT was also performed for staging purposes within 2 weeks after [^{68}Ga]Pentixafor-PET (interval between both scans, median 8 days; range, 1–12 d).

Following imaging, 17/19 (89.5%) subjects underwent either tumor biopsy (8/17, 47.1%) or surgery (n = 9/17, 52.9%) after a median of 4.5 days (range, 1–55 d). **Table 1** gives an overview of the clinical information for this patient cohort.

Synthesis of [^{68}Ga]Pentixafor

[^{68}Ga]Pentixafor was synthesized as previously described using a fully GMP compliant automated synthesizer (GRP, Scintomics, Fürstenfeldbruck, Germany) (27).

PET Imaging

All PET/CT scans were performed on a dedicated PET/CT scanner (Siemens Biograph mCT 64; Siemens Healthineers, Erlangen, Germany). Before acquisition of [^{18}F]FDG PET, patients fasted for at least 6 h and blood glucose levels were <160 mg/dl. Prior to [^{68}Ga]Pentixafor, patients did not fast. Imaging was performed 60 min after administration of 64–166 MBq (median, 145 MBq) of [^{68}Ga]Pentixafor and 297 (n = 1) or 301 (n = 2) MBq of [^{18}F]FDG, respectively. Spiral CT with (dose modulation with a quality reference of 210 mAs) or without (80mAs) intravenous contrast (120 kV, 512 × 512 matrix, 5 mm slice thickness) including a field of view from the base of the skull to the proximal thighs was acquired. Consecutively, PET emission data were acquired in three-dimensional mode with a 200 × 200 matrix with 2–3 min emission time per bed position. After decay and scatter correction, PET data were reconstructed iteratively with attenuation correction using the algorithm implemented by the manufacturer (Siemens Esoft, Siemens Healthineers, Erlangen, Germany).

Image Analysis

All PET/CT studies were visually assessed by two experienced nuclear medicine physicians (RAW and CL). Lesions were rated as visually detectable if they could be identified by both reviewers on the PET images in a consensus setting.

For derivation of maximum standardized uptake values (SUV_{max}) of both primary tumors (all patients) and metastatic disease (if present, in n = 7/19, 36.8%), 3-dimensional volumes of interest (VOI) were drawn around the respective lesions. If patients displayed more than 5 metastases (all histologically proven or verified by imaging follow-up), the five lesions with the highest uptake were selected. For calculation of tumor-to-background ratios (TBR), VOIs with a diameter of 3 cm were placed in normal liver parenchyma and mean SUV were noted. The radiotracer concentration in the VOI was normalized to the injected dose per kilogram of patient's body weight to derive the SUVs (22).

For [^{18}F]FDG-PET/CT, an analogous procedure was carried out.

TABLE 1 | Overview of included subjects.

Patient no.	Tumor entity	Grading*	TNM*	Visually detectable lesions on PET	Primary on [^{68}Ga]Pentixafor PET			Metastases on [^{68}Ga]Pentixafor PET			IRS
					SUV_{max}	TBR	VD	SUV_{max}	TBR	VD	
1	CCC	G2	–	1	4.65	1.68	0	–	–	0/1	0
2	RCC	G2	pT1b pNX Mx	1	1.88	0.88	0	–	–	0/1	1
3	Pancreas (NET)	G1	–	3	5.77	2.68	1	2.92	1.36	2/3	9
4	Pancreas (NET)	G2	–	>5	4.83	1.74	1	–	–	0/5	3
5	PDAC	–	pT3 Nx Mx	1	7.13	2.57	0	–	–	0/1	4
6	CUP	–	–	3	–	–	0	2.33	0.96	3/3	0
7	CCC	–	Tx Nx M1	3	16	7.41	1	8.83	4.09	2/3	12
8	HCC	–	–	0	4.39	2.71	0	–	–	–	–
9	Ovarian (low-grade serous)	–	pT2b N1 Mx	2	9.41	4.22	1	3.84	1.72	1/2	6
10	Prostate	–	–	0	1.7	0.85	0	–	–	–	–
11	PDAC	–	–	0	7.58	3.72	1	–	–	–	9
12	CCC	G3	pT1 pNx Mx	2	12.09	5.02	1	6.67	2.77	1/2	2
13	HCC	G3	pT2 pNx Mx	1	4.97	3.88	1	–	–	0/1	0
14	PDAC	–	–	1	8.22	2.07	1	–	–	0/1	6
15	Ovarian (granulosa cell tumor)	–	pT1a pNx Mx	1	2.69	1.48	0	–	–	0/1	0
16	PDAC	G2	pT2 pN1 Mx	>5	9.22	3.35	1	4.45	1.62	1/5	2
17	HCC	G3	pT1 pN0 Mx	0	3.74	1.33	0	–	–	0/1	0
18	Ovarian (high-grade serous)	G3	pT3c Nx Mx	>5	2.26	1.06	0	–	–	0/5	3
19	CCC	–	–	4	6.48	3.54	1	7.84	4.11	4/4	2

*PET, positron emission tomography; IRS, immunoreactive score; SUV_{max}, maximum standardized uptake value; TBR, tumor to background ratio; VD, visual detectability; CCC, cholangiocellular carcinoma; RCC, renal cell carcinoma; NET, neuroendocrine tumor; PDAC, pancreatic ductal adenocarcinoma; CUP, cancer of unknown primary; HCC, hepatocellular carcinoma. All patients underwent [^{68}Ga]Pentixafor PET/CT, while in 3/19 subjects, additional [^{18}F]FDG PET/CT was performed. *prior to CXCR4-directed imaging.*

Histological Tumor Characterization

Immunohistochemistry was performed on 10% formalin fixed paraffin embedded tissue sections (3 μm) and scored as previously described (28). CXCR4-immunohistochemistry was conducted using an anti-CXCR4 rabbit polyclonal antibody (ab2074; Abcam, Cambridge, United Kingdom) followed by detection with the DAKO *en vision* system according to the manufacturer's protocol. All immunostained sections were counterstained for 3 min with hematoxylin. The analysis of the stained sections was done semi-quantitatively by light-microscopy according to the immunoreactive score (IRS) by Remmele and Stegner (29). The percentage of CXCR4-positive cells was scored as follows: 0 (no positive cells), 1 (<10% positive cells), 2 (10–50% positive cells), 3 (>50–80% positive cells), and 4 (>80% positive cells). Additionally, the intensity of staining was graded: 0 (no color reaction), 1 (mild reaction), 2 (moderate reaction), 3 (intense reaction). Multiplication of both scores for a given sample yields the IRS classification: 0–1 (negative), 2–3 (mild), 4–8 (moderate), 9–12 (strongly positive). For a more detailed description please refer to Werner et al. (22). IRS were correlated with imaging findings.

Statistical Analysis

Descriptive statistics were predominantly utilized. All results are displayed as mean ± SD or as median + range where appropriate. The two-tailed paired Student's *t*-test was used to check for a correlation between [^{68}Ga]Pentixafor SUV_{max} and histologic CXCR4 expression. A *P*-value of <0.05 was considered to be statistically significant.

RESULTS

Clinical Findings

All patients presented with newly diagnosed, treatment-naïve solid tumors. The following histologic entities were represented in the cohort: pancreatic ductal adenocarcinoma ($n = 4$), pancreatic neuroendocrine tumor ($n = 2$, initially suspected as adenocarcinoma), CCC ($n = 4$), HCC ($n = 3$), and ovarian cancer ($n = 3$, one low- and one high-grade serous carcinoma as well as one granulosa cell tumor of the ovary, respectively). The remaining three subjects had, renal cell carcinoma (RCC), prostate cancer, and CUP, respectively. Evidence of metastases was detected in 7/19 (36.8%) patients.

Patient details are provided in **Table 1**.

Imaging Results of [^{68}Ga]Pentixafor PET/CT

On a visual basis, 10/19 (52.6%) primary tumors and 14/49 (28.6%) metastases were detectable. In semi-quantitative analysis, the median SUV_{max} of the primary was 5.4 (range, 1.7–16.0) with a median TBR of 2.6 (range, 0.8–7.4). The highest SUV_{max} were identified in patients suffering from CCC (#7, SUV_{max}, 16.0; #12, SUV_{max}, 12.1; **Table 1**).

Metastases exhibited a median SUV_{max} of 4.5 (range, 2.3–8.8) with a TBR of 1.7 (range, 1.0–4.1).

Comparison of [^{68}Ga]Pentixafor PET/CT With [^{18}F]FDG PET/CT

In 3/19 (15.8%) patients (#3, #8, and #10), an additional [^{18}F]FDG PET/CT scan was conducted. The primary tumor was identified in all subjects, while it was not visualized in 2/3 by [^{68}Ga]Pentixafor (#8 and #10). In semi-quantitative assessment, both SUV_{max} and TBR were higher than on CXCR4-directed imaging: Median SUV_{max} of the primary was 14.3 (14.3, 18.0, 9.0; [^{68}Ga]Pentixafor, 4.4; 5.8, 4.4, 1.7, respectively) with a median TBR of 4.8 (range, 2.9–6.7; [^{68}Ga]Pentixafor, 2.7; 2.7, 2.7, 0.8, respectively).

[^{18}F]FDG PET/CT detected metastases in 2/3 (#3 and #8) patients with a median SUV_{max} of 13.3 (range, 11.5–16.6) and a median TBR of 4.7 (range, 3.9–5.6) whereas [^{68}Ga]Pentixafor visualized only 2 metastases in patient #3 (SUV_{max}, 3.9 and 2.0, respectively).

Immunohistochemical Assessment

A total of 17 samples could be investigated in a pathological assessment. 5/17 samples (29.4%) were rated as negative, 6/17 (35.4%) as "weakly" positive (IRS score 1–3), 3/17 (17.6%) as "moderately" positive (IRS scores 4–8), and 3/17 (17.6%) as "strongly" positive (IRS scores 9–12) (**Table 1**). Notably, both membranous as well as intra-cytoplasmatic staining for CXCR4 was confirmed.

In 16/17 (94.1%), imaging results (SUV_{max} of the primary) could be compared to immunohistological CXCR4 staining, while in 1/17 (5.9%) a SUV_{max} could not be derived as the primary could not be identified (#6, suffering from CUP). A significant correlation between IRS and [^{68}Ga]Pentixafor SUV_{max} of the primary among all tumor entities was detected ($R = 0.62$, $P < 0.05$, **Figure 1**). **Figure 2** shows concordant cases of immunohistochemistry and non-invasive imaging in patients suffering from CCC (patient #7) and HCC (patient #17), respectively. **Figure 3** demonstrates CXCR4-directed imaging in further selected tumor entities which (with the exception of patient #9 suffering from low-grade ovarian carcinoma) primarily demonstrated moderate to no uptake on CXCR4-directed imaging.

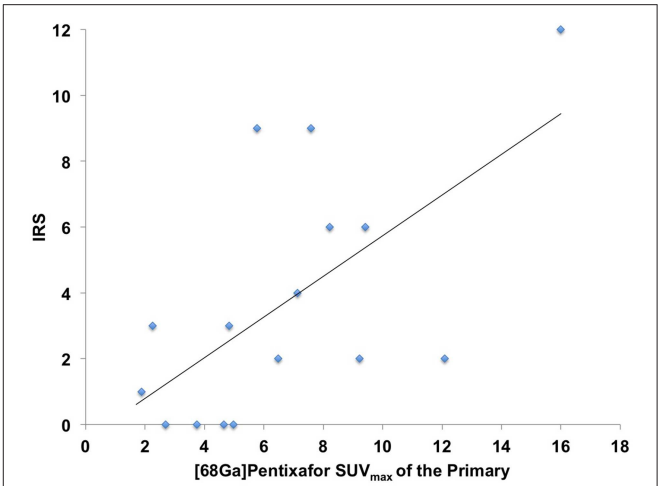

FIGURE 1 | Correlation between immunoreactive score (IRS) vs. [^{68}Ga]Pentixafor SUV_{max} of the primary among all tumor entities available for analysis $R = 0.62$.

DISCUSSION

An extensive body of literature has demonstrated that over-expression of CXCR4 is linked with increased aggressiveness and worse prognosis in solid cancers. Thus, this chemokine receptor is an interesting target in oncology and several therapeutic antagonists have been developed (30, 31). A recent phase I trial in women with advanced HER-2 negative metastatic breast cancer investigated a combination regimen of balixafortide (a peptidic CXCR4 antagonist) and eribulin and demonstrated favorable safety and tolerability as well as promising anti-tumor activity (32). Additionally, a first experience with chemokine receptor-directed radioligand therapy in heavily pre-treated hematologic disease has been reported (17–19).

As an important pre-requisite to CXCR4 directed therapy, [^{68}Ga]Pentixafor PET/CT enables the non-invasive evaluation of receptor expression of all tumor lesions. Marked inter- and intra-individual differences in CXCR4 expression have been noted (33). Further, the receptor presentation on the tumor cell surface seems to be highly dynamic and influenced by a variety of factors including previous therapy (34).

In this study, we aimed to expand the experience with non-invasive imaging of CXCR4 in solid cancers. Previous reports had hinted at a potential role of chemokine-directed imaging in selected entities such as small cell lung cancer, adrenocortical carcinoma, or glioblastoma (21, 24, 35), while another study by Vag et al. questioned its suitability in other tumors including sarcoma, pancreatic cancer, and breast cancer (25). In the present analysis, additional solid cancers in which CXCR4 expression had been linked to metastasis and inferior outcomes such as renal cell cancer (36), ovarian cancer (37), and CCC (38) were investigated. All patients presented with newly diagnosed, treatment-naïve disease. To exclude potential influence of concomitant therapy on receptor surface expression, biopsies, and/or surgery were performed shortly after PET imaging and prior to treatment

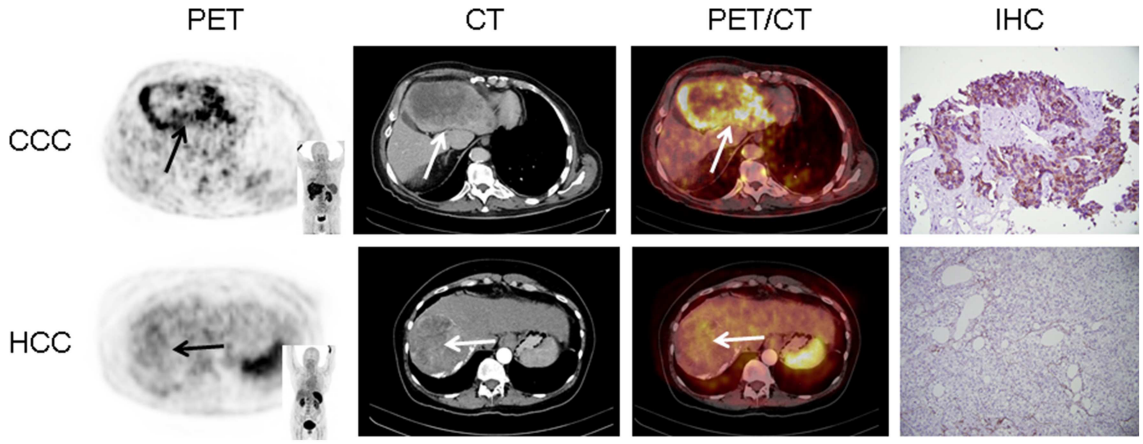

FIGURE 2 | Concordance of immunohistochemistry (IHC) and non-invasive CXCR4-directed positron emission tomography (PET) imaging in patients suffering from cholangiocellular carcinoma (CCC, upper row, patient #7) and hepatocellular carcinoma (HCC, lower row, patient #17). Upper row (patient #7): Display of transaxial PET (left), computed tomography (CT, second panel) and fused PET/CT (third panel) images of a left liver lesion. The lesion demonstrates high CXCR4 expression, which could be confirmed in the surgical specimen after tumor resection (IHC, fourth panel). The immunoreactive score (IRS) was 12 (**Table 1**). Lower row (patient #17): Display of transaxial PET (left), CT (second panel) and fused PET/CT (third panel) images of the primary. The lesions demonstrates no CXCR4 expression on PET. The patient presented with negative IHC for CXCR4 derived from a surgical specimen (IRS, 0, **Table 1**). Magnification of IHC: × 400.

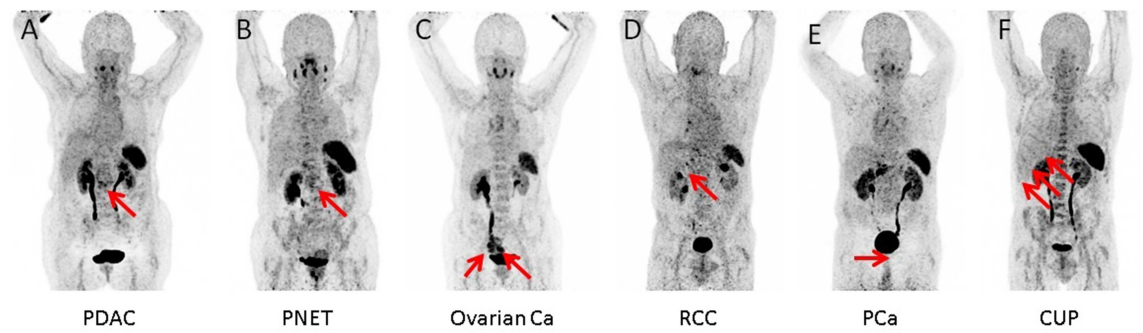

FIGURE 3 | Maximum intensity projections of CXCR4-directed positron emission tomography of other selected tumor entities, primarily demonstrating moderate to no uptake on CXCR4-directed imaging (arrows). Pancreatic ductal adenocarcinoma [PDCA; **(A)**], pancreatic neuroendocrine tumor [PNET; **(B)**], ovarian cancer **(C)**, renal cell carcinoma [RCC; **(D)**], prostate cancer [PCA; **(E)**], and cancer of unknown primary (CUP) with multiple liver metastases **(F)**. Only the tumor masses of the patient with low-grade ovarian carcinoma (patient #9) display relevant CXCR4 expression.

initiation. However, only weak to moderate [^{68}Ga]Pentixafor uptake was recorded in the vast majority of patients and almost 80% of lesions could not be visually detected. In addition, only two patients exhibited primary tumor $SUV_{max} > 10$. Interestingly, both patients suffered from CCC (#7, **Figure 2** and #12). These findings were paralleled by immunohistochemistry that also identified relevant CXCR4 expression in few tumor specimens and correlated well with non-invasive imaging results ($R = 0.62$, **Figure 1**).

Taken together, the current findings indicate that [^{68}Ga]Pentixafor is unlikely to play a major role in staging and re-staging of most solid tumors, in particular when compared to [^{18}F]FDG. Given the physiologic expression of CXCR4 on hematopoietic stem cells and thus the need for subsequent stem cell support (17, 18), endoradiotherapy with radiolabelled Pentixather might also be reserved to very selected cases.

Future efforts for potential applications of CXCR4-directed imaging might focus on the characterization of intra-/inter-lesional heterogeneity by performing dual-radiotracer studies (in conjunction with [^{18}F]FDG) to visualize different levels of tumor de-differentiation and predict lesions with prognostic relevance. For example, CXCR4-directed PET/CT might help to visualize receptor positive cancer stem cells (and their niche) which are considered to be especially resistant to radiation or chemotherapy (1, 39).

Several limitations of the present study have to be considered. It is retrospective and the number of patients is rather small. Further research including a higher number of subjects is

definitely warranted to confirm the preliminary findings of the present feasibility study. Histologic validation of imaging results was not available in all cases. Additionally, a variety of different tumor entities were included. However, all patients presented with newly diagnosed disease and were treatment-naïve at the time of imaging. Moreover, in only 3 patients, an additional [^{18}F]FDG PET/CT has been conducted and future studies should evaluate potential tumor heterogeneity in a higher number of subjects. Although the value of [^{68}Ga]Pentixafor PET/CT has been investigated before, our small series adds first experience with other tumor entities such as ovarian cancer and renal cell carcinoma, along with histopathologic proof in the majority of the cases.

CONCLUSIONS

In this cohort of various treatment-naïve solid malignancies, CXCR4 expression as detected by [^{68}Ga]Pentixafor-PET/CT and immunohistochemistry was rather moderate. Thus, CXCR4-directed imaging may not play a major role in the management of the majority of solid cancer patients.

DATA AVAILABILITY

The raw data supporting the conclusions of this manuscript will be made available by the authors, without undue reservation, to any qualified researcher.

ETHICS STATEMENT

The local institutional review board of University Würzburg waived the requirement for additional approval because of the retrospective character of this study. All subjects gave written informed consent in accordance with the Declaration of Helsinki.

AUTHOR CONTRIBUTIONS

RW, SK, CL, TH, MP, and SR designed the study, wrote the manuscript, and researched data. MK, AS, H-JW, and AB performed analysis. All authors aided in drafting the manuscript and revised it critically for important intellectual content. All authors read and approved the final manuscript.

FUNDING

This work was supported by the Competence Network of Heart Failure funded by the Integrated Research and Treatment Center (IFB) of the Federal Ministry of Education and Research (BMBF) and German Research Council (DFG grant HI 1789/3-3). This publication was funded by the German Research Foundation (DFG) and the University of Wuerzburg in the funding programme Open Access Publishing. This work was supported by Grants-in-Aid for Scientific Research (Kakenhi, 15K21774) from the Japan Society for the Promotion of Science (JSPS).

REFERENCES

1. Domanska UM, Kruizinga RC, Nagengast WB, Timmer-Bosscha H, Huls G, de Vries EG, et al. A review on CXCR4/CXCL12 axis in oncology: no place to hide. *Eur J Cancer*. (2013) 49:219–30. doi: 10.1016/j.ejca.2012.05.005
2. Walenkamp AME, Lapa C, Herrmann K, Wester HJ. CXCR4 ligands: the next big hit? *J Nucl Med*. (2017) 58:77S–82S. doi: 10.2967/jnumed.116.186874
3. Zhao H, Guo L, Zhao H, Zhao J, Weng H, Zhao B. CXCR4 over-expression and survival in cancer: a system review and meta-analysis. *Oncotarget*. (2015) 6:5022–40. doi: 10.18632/oncotarget.3217
4. Demmer O, Gourni E, Schumacher U, Kessler H, Wester HJ. PET imaging of CXCR4 receptors in cancer by a new optimized ligand. *ChemMedChem*. (2011) 6:1789–91. doi: 10.1002/cmdc.201100320
5. Gourni E, Demmer O, Schottelius M, D'Alessandria C, Schulz S, Dijkgraaf I, et al. PET of CXCR4 expression by a (68)Ga-labeled highly specific targeted contrast agent. *J Nucl Med*. (2011) 52:1803–10. doi: 10.2967/jnumed.111.098798
6. Wester HJ, Keller U, Schottelius M, Beer A, Philipp-Abbrederis K, Hoffmann F, et al. Disclosing the CXCR4 expression in lymphoproliferative diseases by targeted molecular imaging. *Theranostics*. (2015) 5:618–30. doi: 10.7150/thno.11251
7. Philipp-Abbrederis K, Herrmann K, Knop S, Schottelius M, Eiber M, Luckerath K, et al. *In vivo* molecular imaging of chemokine receptor CXCR4 expression in patients with advanced multiple myeloma. *EMBO Mol Med*. (2015) 7:477–87. doi: 10.15252/emmm.201404698
8. Kircher M, Herhaus P, Schottelius M, Buck AK, Werner RA, Wester HJ, et al. CXCR4-directed theranostics in oncology and inflammation. *Ann Nucl Med*. (2018) 32:503–11. doi: 10.1007/s12149-018-1290-8
9. Reiter T, Kircher M, Schirbel A, Werner RA, Kropf S, Ertl G, et al. Imaging of C-X-C motif chemokine receptor CXCR4 expression after myocardial infarction with [(68)Ga]Pentixafor-PET/CT in correlation with cardiac MRI. *JACC Cardiovasc Imaging*. (2018) 11:1541–3. doi: 10.1016/j.jcmg.2018.01.001
10. Lapa C, Reiter T, Werner RA, Ertl G, Wester HJ, Buck AK, et al. [(68)Ga]Pentixafor-PET/CT for imaging of chemokine receptor 4 expression after myocardial infarction. *JACC Cardiovasc Imaging*. (2015) 8:1466–8. doi: 10.1016/j.jcmg.2015.09.007
11. Derlin T, Sedding DG, Dutzmann J, Haghikia A, Konig T, Napp LC, et al. Imaging of chemokine receptor CXCR4 expression in culprit and nonculprit coronary atherosclerotic plaque using motion-corrected [(68)Ga]pentixafor PET/CT. *Eur J Nucl Med Mol Imaging*. (2018) 45:1934–44. doi: 10.1007/s00259-018-4076-2
12. Weiberg D, Thackeray JT, Daum G, Sohns JM, Kropf S, Wester HJ, et al. Clinical molecular imaging of chemokine receptor CXCR4 expression in atherosclerotic plaque using (68)Ga-Pentixafor PET: correlation with cardiovascular risk factors and calcified plaque burden. *J Nucl Med*. (2018) 59:266–72. doi: 10.2967/jnumed.117.196485
13. Thackeray JT, Derlin T, Haghikia A, Napp LC, Wang Y, Ross TL, et al. Molecular imaging of the chemokine receptor CXCR4 after acute myocardial infarction. *JACC Cardiovasc Imaging*. (2015) 8:1417–26. doi: 10.1016/j.jcmg.2015.09.008
14. Werner RA, Weich A, Schirbel A, Samnick S, Buck AK, Higuchi T, et al. Intraindividual tumor heterogeneity in NET - Further insight by C-X-C motif chemokine receptor 4-directed imaging. *Eur J Nucl Med Mol Imaging*. (2017) 44:553–4. doi: 10.1007/s00259-016-3566-3
15. Schottelius M, Osl T, Poschenrieder A, Hoffmann F, Beykan S, Hanscheid H, et al. [177Lu]pentixather: comprehensive preclinical characterization of a first CXCR4-directed endoradiotherapeutic agent. *Theranostics*. (2017) 7:2350–62. doi: 10.7150/thno.19119
16. Herrmann K, Schottelius M, Lapa C, Osl T, Poschenrieder A, Hanscheid H, et al. First-in-human experience of CXCR4-directed endoradiotherapy with 177Lu- and 90Y-labeled pentixather in advanced-stage multiple myeloma

with extensive intra- and extramedullary disease. *J Nucl Med*. (2016) 57:248–51. doi: 10.2967/jnumed.115.167361
17. Lapa C, Herrmann K, Schirbel A, Hanscheid H, Luckerath K, Schottelius M, et al. CXCR4-directed endoradiotherapy induces high response rates in extramedullary relapsed multiple myeloma. *Theranostics*. (2017) 7:1589–97. doi: 10.7150/thno.19050
18. Lapa C, Hanscheid H, Kircher M, Schirbel A, Wunderlich G, Werner R, et al. Feasibility of CXCR4-directed radioligand therapy in advanced diffuse large B cell lymphoma. *J Nucl Med*. (2018) 60:60–4. doi: 10.2967/jnumed.118.210997
19. Habringer S, Lapa C, Herhaus P, Schottelius M, Istvanffy R, Steiger K, et al. Dual targeting of acute leukemia and supporting niche by CXCR4-directed theranostics. *Theranostics*. (2018) 8:369–83. doi: 10.7150/thno.21397
20. Maurer S, Herhaus P, Lippenmeyer R, Hanscheid H, Kircher M, Schirbel A, et al. Side effects of CXC-chemokine receptor 4 - directed endoradiotherapy with pentixather prior to hematopoietic stem cell transplantation. *J Nucl Med*. (2019). doi: 10.2967/jnumed.118.223420. [Epub ahead of print].
21. Lapa C, Luckerath K, Rudelius M, Schmid JS, Schoene A, Schirbel A, et al. [68Ga]Pentixafor-PET/CT for imaging of chemokine receptor 4 expression in small cell lung cancer - initial experience. *Oncotarget*. (2016) 7:9288–95. doi: 10.18632/oncotarget.7063
22. Werner RA, Weich A, Higuchi T, Schmid JS, Schirbel A, Lassmann M, et al. Imaging of chemokine receptor 4 expression in neuroendocrine tumors - a triple tracer comparative approach. *Theranostics*. (2017) 7:1489–98. doi: 10.7150/thno.18754
23. Fang HY, Munch NS, Schottelius M, Ingermann J, Liu H, Schauer M, et al. CXCR4 is a potential target for diagnostic PET/CT imaging in Barrett's dysplasia and esophageal adenocarcinoma. *Clin Cancer Res*. (2018) 24:1048–61. doi: 10.1158/1078-0432.CCR-17-1756
24. Bluemel C, Hahner S, Heinze B, Fassnacht M, Kroiss M, Bley TA, et al. Investigating the chemokine receptor 4 as potential theranostic target in adrenocortical cancer patients. *Clin Nucl Med*. (2017) 42:e29–34. doi: 10.1097/RLU.0000000000001435
25. Vag T, Gerngross C, Herhaus P, Eiber M, Philipp-Abbrederis K, Graner FP, et al. First experience with chemokine receptor CXCR4-targeted PET imaging of patients with solid cancers. *J Nucl Med*. (2016) 57:741–6. doi: 10.2967/jnumed.115.161034
26. Lapa C, Kircher S, Schirbel A, Rosenwald A, Kropf S, Pelzer T, et al. Targeting CXCR4 with [(68)Ga]Pentixafor: a suitable theranostic approach in pleural mesothelioma? *Oncotarget*. (2017) 8:96732–7. doi: 10.18632/oncotarget.18235
27. Martin R, Juttler S, Muller M, Wester HJ. Cationic eluate pretreatment for automated synthesis of [(6)(8)Ga]CPCR4.2. *Nucl Med Biol*. (2014) 41:84–9. doi: 10.1016/j.nucmedbio.2013.09.002
28. Kaemmerer D, Peter L, Lupp A, Schulz S, Sanger J, Baum RP, et al. Comparing of IRS and Her2 as immunohistochemical scoring schemes in gastroenteropancreatic neuroendocrine tumors. *Int J Clin Exp Pathol*. (2012) 5:187–94.
29. Remmele W, Stegner HE. [Recommendation for uniform definition of an immunoreactive score (IRS) for immunohistochemical estrogenreceptor detection (ER-ICA) in breast cancer tissue]. *Pathologe*. (1987) 8:138–40.
30. Tamamura H, Fujii N. The therapeutic potential of CXCR4 antagonists in the treatment of HIV infection, cancer metastasis and rheumatoid arthritis. *Expert Opin Ther Targets*. (2005) 9:1267–82. doi: 10.1517/14728222.9.6.1267
31. Burger JA, Peled A. CXCR4 antagonists: targeting the microenvironment in leukemia and other cancers. *Leukemia*. (2009) 23:43–52. doi: 10.1038/leu.2008.299
32. Pernas S, Martin M, Kaufman PA, Gil-Martin M, Gomez Pardo P, Lopez-Tarruella S, et al. Balixafortide plus eribulin in HER2-negative metastatic breast cancer: a phase 1, single-arm, dose-escalation trial. *Lancet Oncol*. (2018) 19:812–24. doi: 10.1016/S1470-2045(18)30147-5
33. Buck AK, Stolzenburg A, Hänscheid H, Schirbel A, Lückerath K, Schottelius M, et al. Chemokine receptor - Directed imaging and therapy. *Methods*. (2017) 130:63–71. doi: 10.1016/j.ymeth.2017.09.002
34. Lapa C, Luckerath K, Kircher S, Hanscheid H, Grigoleit GU, Rosenwald A, et al. Potential influence of concomitant chemotherapy on CXCR4 expression in receptor directed endoradiotherapy. *Br J Haematol*. (2019) 184:440–3. doi: 10.1111/bjh.15096
35. Lapa C, Luckerath K, Kleinlein I, Monoranu CM, Linsenmann T, Kessler AF, et al. (68)Ga-Pentixafor-PET/CT for imaging of chemokine receptor 4 expression in glioblastoma. *Theranostics*. (2016) 6:428–34. doi: 10.7150/thno.13986
36. Staller P, Sulitkova J, Lisztwan J, Moch H, Oakeley EJ, Krek W. Chemokine receptor CXCR4 downregulated by von Hippel-Lindau tumour suppressor pVHL. *Nature*. (2003) 425:307–11. doi: 10.1038/nature01874
37. Scotton CJ, Wilson JL, Scott K, Stamp G, Wilbanks GD, Fricker S, et al. Multiple actions of the chemokine CXCL12 on epithelial tumor cells in human ovarian cancer. *Cancer Res*. (2002) 62:5930–8.
38. Kaemmerer D, Schindler R, Mussbach F, Dahmen U, Altendorf-Hofmann A, Dirsch O, et al. Somatostatin and CXCR4 chemokine receptor expression in hepatocellular and cholangiocellular carcinomas: tumor capillaries as promising targets. *BMC Cancer*. (2017) 17:896. doi: 10.1186/s12885-017-3911-3
39. Rosen JM, Jordan CT. The increasing complexity of the cancer stem cell paradigm. *Science*. (2009) 324:1670–3. doi: 10.1126/science.1171837

Conflict of Interest Statement: The authors declare that the research was conducted in the absence of any commercial or financial relationships that could be construed as a potential conflict of interest.

frontiers in Oncology

ORIGINAL RESEARCH
published: 03 December 2019
doi: 10.3389/fonc.2019.01351

Effective MR Molecular Imaging of Triple Negative Breast Cancer With an EDB-Fibronectin-Specific Contrast Agent at Reduced Doses

*Nadia R. Ayat[1], Amita Vaidya[1], Grace A. Yeung[1], Megan N. Buford[1], Ryan C. Hall[1], Peter L. Qiao[1], Xin Yu[1] and Zheng-Rong Lu[1,2]**

[1] Department of Biomedical Engineering, School of Engineering, Case Western Reserve University, Cleveland, OH, United States, [2] Case Comprehensive Cancer Center, Case Western Reserve University, Cleveland, OH, United States

MR molecular imaging (MRMI) of abundant oncogenic biomarkers in tumor microenvironment has the potential to provide precision cancer imaging in high resolution. Extradomain-B fibronectin (EDB-FN) is an oncogenic extracellular matrix protein, highly expressed in aggressive triple negative breast cancer. A targeted macrocyclic gadolinium-based contrast agent (GBCA) ZD2-N_3-Gd(HP-DO3A) (MT218), specific to EDB-FN, was developed for MRMI of aggressive breast cancer. The effectiveness of different doses of MT218 for MRMI was tested in MDA-MB-231 and Hs578T human triple negative breast cancer models. At clinical dose of 0.1 and subclinical dose of 0.04 mmol Gd/kg, MT218 rapidly bound to the extracellular matrix EDB-FN and produced robust tumor contrast enhancement in both the tumor models, as early as 1–30 min post-injection. Substantial tumor enhancement was also observed in both the models with MT218 at doses as low as 0.02 mmol Gd/kg, which was significantly better than the clinical agent Gd(HP-DO3A) at 0.1 mmol Gd/kg. Little non-specific enhancement was observed in the normal tissues including liver, spleen, and brain for MT218 at all the tested doses, with renal clearance at 30 min. These results demonstrate that MRMI with reduced doses of MT218 is safe and effective for sensitive and specific imaging of aggressive breast cancers.

Keywords: EDB-fibronectin, GBCAs, targeted MRI contrast agent, breast cancer, tumor microenvironment

OPEN ACCESS

Edited by:
Marie-France Penet, School of Medicine, Johns Hopkins University, United States

Reviewed by:
Zhuxian Zhou, Zhejiang University, China
Rossella Canese, National Institute of Health (ISS), Italy

***Correspondence:**
Zheng-Rong Lu
zxl125@case.edu

Specialty section:
This article was submitted to Cancer Imaging and Image-directed Interventions, a section of the journal Frontiers in Oncology

Received: *20 August 2019*
Accepted: *15 November 2019*
Published: *03 December 2019*

Citation:
Ayat NR, Vaidya A, Yeung GA, Buford MN, Hall RC, Qiao PL, Yu X and Lu Z-R (2019) Effective MR Molecular Imaging of Triple Negative Breast Cancer With an EDB-Fibronectin-Specific Contrast Agent at Reduced Doses. Front. Oncol. 9:1351. doi: 10.3389/fonc.2019.01351

INTRODUCTION

MRI is a powerful non-invasive imaging modality that provides high resolution, three-dimensional images of soft tissues, including cancerous lesions. Gadolinium (III)-based contrast agents (GBCAs) are routinely used to enhance the contrast between cancerous lesions and surrounding normal tissues for accurate cancer detection and diagnosis (1). However, the use of clinical GBCAs for diagnosis and therapeutic monitoring is limited due to the lack of disease-specific contrast agents, and concerns of potential Gd toxicity (2–4). Currently used clinical GBCAs are non-specific to tumor tissues and are unable to accurately detect and differentiate aggressive malignancies from benign lesions. Therefore, high dosages of GBCAs are often used for detectable contrast enhancement in tumors. Frequent use of GBCAs at high doses may lead to adverse side effects such as nephrogenic systemic fibrosis (NSF) caused by the retention of Gd in tissues in patients

with compromised renal function (2). In addition, GBCAs have been shown to deposit in human brains with intact blood brain barriers and in the absence of intracranial abnormalities (5). While no adverse pharmacological and pathological effects have been associated with the observed tissue deposition, it is clinically imperative to address this concern by developing tumor-specific targeted contrast agents that can be used at substantially reduced dosages (1). This would improve diagnostic imaging of cancer with MRI, and simultaneously minimize potential dose-dependent toxicity and non-specific organ accumulation to alleviate the safety concerns for clinical use of GBCAs.

While MRI is routinely used to obtain specific and high-resolution images of cancer tissues, developing clinically feasible targeted MRI contrast agents for MR molecular imaging (MRMI) of the biomarkers expressed on cancer cell surface is challenging, due to the low sensitivity of MRI and low concentration of the biomarkers. To address these challenges for clinical MRMI, we have explored a strategy to target abundant oncoproteins expressed in tumor extracellular matrix (ECM) for safe and effective MRMI of aggressive cancers (6, 7). Fibronectin (FN) is considered as a marker of epithelial-to-mesenchymal transition (EMT), which is a biological process responsible for invasion and metastasis of aggressive tumors, including breast cancer (8). We previously developed small molecular peptide-targeted MRI contrast agents specific to fibrin-fibronectin complexes for cancer MRMI. The targeted contrast agents produced robust contrast enhancement in aggressive tumors for effective cancer MRMI, and have shown the potential to detect micrometastases as small as 300 μm in size (9–11). Clinical evidence has demonstrated that the tumor-specific isoform of FN, extradomain-B fibronectin (EDB-FN) is specifically overexpressed in the ECM of aggressive tumors, including breast tumors, thereby making EDB-FN a promising target for early detection and differential diagnosis of breast cancer (12–14). Recently, we have designed a new generation of small peptide targeted MRI contrast agents to target EDB-FN, for precision MRMI of prostate and breast tumors (15–17). A small peptide specific to EDB-FN, named ZD2 (Thr-Val-Arg-Thr-Ser-Ala-As), was identified and used for the design of a targeted MRI contrast agent for MRMI of EDB-FN in cancer (8, 15, 18). MRMI of EDB-FN with the targeted contrast agents was effective for detection and risk-stratification of aggressive solid tumors, including breast and prostate cancer, in animal tumor models (15, 17).

We further optimized the ZD2 peptide targeted MRI contrast agent and developed ZD2-N3-Gd(HP-DO3A) (MT218) as a lead agent for cost-effective clinical translation (19). MT218 possessed higher T_1 relaxivity (5.44 mM^{-1} s^{-1}) than the previously reported ZD2-Gd(HP-DO3A) (r_1 = 4.12 mM^{-1} s^{-1}) (15, 19). At the clinical dose of 0.1 mmol Gd/kg, MT218 generated robust signal enhancement in aggressive solid tumors, allowing for effective MRMI for early detection and risk-stratification of prostate cancer. In this study, we investigated the dose-dependent effectiveness of MT218 for MRMI of two independent triple negative breast cancer (TNBC) xenografts in athymic mice. The expression of EDB-FN was assessed in triple negative MDA-MB-231 and Hs578T breast cancer cells and tumors. Specific tumor contrast enhancement with MRMI was tested using clinical and subclinical doses of MT218 (as low as 0.02 mmol Gd/kg) in these tumor models, in comparison with a clinical agent Gd(HP-DO3A). A minimally effective dose was identified for effective MRMI of TNBC and for minimizing potential dose-dependent side-effects associated with GBCAs. Non-specific tissue enhancement was also evaluated in normal organs and tissues in the animal models.

MATERIALS AND METHODS

Cell Lines and Reagents

MDA-MB-231 and Hs578T TNBC cells were purchased from ATCC (Manassas, VA). MDA-MB-231 cells were maintained in Dulbecco's Modified Eagle's Medium (DMEM, Gibco, Waltham, MA) supplemented with 10% fetal bovine serum (FBS, Sigma, St. Louis, MO) and 1% Penicillin/Streptomycin. Hs578T cells were cultured in DMEM supplemented with 10% FBS, 1% Penicillin/Streptomycin, and 0.01 mg/mL recombinant human insulin (Sigma). MCF7 cells were maintained in Eagle's Minimum Essential Medium (EMEM, Gibco) supplemented with 10% FBS (Sigma), 1% Penicillin/Streptomycin, and 0.01 mg/mL recombinant human insulin (Sigma). MDA-MB-231 and Hs578T cells were engineered to stably express firefly luciferase and GFP with a lentivirus encoding for CMV-Luciferase (Firefly)-2A-GFP (Neo) (Amsbio, Cambridge, MA) and selected using flow cytometry.

Semiquantitative Real-Time PCR Analyses

Quantitative real-time PCR was conducted as described previously (20). Briefly, total RNA was extracted from TNBC cells using an RNeasy Plus Mini Kit (Qiagen, Germantown, MD) as per manufacturer's instructions. Reverse transcription was performed using the miScript II RT Kit (Qiagen), followed by qPCR using miScript SYBR Green PCR kit (Qiagen). mRNA expression levels were normalized to 18S control. The following primers were purchased from Integrated DNA Technologies (Coralville, IA): 18S: Fwd 5′-TCAAGAAC GAAAGTCGGAGG-3′ and Rev 5′-GGACATCTAAGGGCATCACA-3′; EDB-FN: Fwd 5′- AGCCCTGTGACTGTGTAGTA-3′ and Rev 5′-AGCCCTGTGACTGTGTAGTA-3′.

In vitro EDB-FN Binding

An EDB-FN-specific fluorescent probe ZD2-Cy5.5 was synthesized as previously described (8). Approximately 300,000 breast cancer cells were plated onto iBidi glass bottom plates coated with Corning Matrigel Membrane Matrix (Corning, Corning, NY). Upon formation of tumor spheroids, ZD2-Cy5.5 (250 nM) along with 5 μg/mL Hoechst 33342 (Invitrogen, Carlsbad, California) were incubated with the spheroids for 1 h. Peptide binding was monitored using an Olympus FV1000 confocal microscope (Olympus Corporation, Tokyo, Japan).

Animal Models

Female nude mice (nu/nu Balb/c background, 4–6 weeks old) were purchased from Jackson Laboratories (Bar Harbor, Maine) and cared for in the Animal Core Facility at Case Western Reserve University (Cleveland, OH). All animal experiments

were conducted in accordance with an approved protocol by the IACUC of CWRU. Mammary fat pads were injected with 2 x 10^6 MDA-MB-231-GFP-Luc and 4 × 10^6 Hs578T-GFP-Luc cells suspended in a matrigel-PBS mixture (1:1). Tumor volumes were monitored weekly using a Vernier caliper. Once the average tumor volume reached 70–90 mm^3, mice were subjected to MR imaging ($n = 5$ for MT218 and $n = 5$ for Gd(HP-DO3A) (Bracco, Milan, Italy).

MR Molecular Imaging

MR molecular imaging was performed on a 3T MRS 3000 scanner (MR Solutions, Surrey, UK). T_1-weighted images were acquired pre- and post-injection of MT218 at doses of 0.1 mmol Gd/kg (clinical dose), 0.04 mmol Gd/kg and 0.02 mmol Gd/kg using a fast spin echo (FSE) axial sequence with respiratory gating ($T_R = 305$ ms, $T_E = 11$ ms, FOV = 40 × 40 mm, slice thickness = 1 mm, slice number = 15, $N_{av} = 2$, matrix = 256 × 256) using a mouse short quad coil (MR Solutions). Biodistribution studies were conducted using a FSE coronal sequence with respiratory gating ($T_R = 305$ ms, $T_E = 11$ ms, FOV = 90 × 90 mm, slice thickness = 1 mm, slice number = 20, $N_{av} = 2$, matrix = 248 × 512). A group of 5 tumor-bearing mice was imaged for each dose. Images were acquired before and at 10, 20, and 30 min post-injection. The imaging protocol was repeated with the clinical agent, Gd(HP-DO3A) as a control at 0.1 mmol Gd/kg.

The MRI data were exported into DICOM data and analyzed using FIJI (https://imagej.net/Fiji). The contrast-to-noise ratio (CNR) of tumors were calculated at 10, 20, and 30 min post-injection as the difference of the mean tumor intensity and the mean muscle intensity, divided by the standard deviation of the noise. Tumor signal to noise ratio (SNR) was obtained as the mean signal intensity of the tumor divided by the standard deviation of the noise at 20 min post-contrast injection.

Histological Analysis

Tissue fixation, sectioning, and H&E staining were performed at the tissue resource core at Case Western Reserve University (Cleveland, OH). Tumor sections were deparaffinized and rehydrated (Abcam, Cambridge, UK) and blocked in PBS-T containing goat serum (10%) for 1 h. Rabbit anti-EDB-FN antibody, G4, (Absolute Antibody, Boston, MA) diluted with PBS-T containing goat serum (1:500) was applied to the tissue and incubated at room temperature for 1 h. After 3 washes of 5 min each, AlexaFluor555-conjugated anti-rabbit IgG secondary antibody (1:2,000, Abcam) was incubated with tissue sections for 1 h. Tissue sections were counterstained with AbcamProlong Gold with DAPI (Abcam). Fluorescence images were obtained using an Olympus FV1000 confocal microscope. H&E images were acquired using an Olympus Bx61VS slide scanner (Olympus America, Center Valley, PA) and processed in OlyVIA software.

Immunoblotting

MDA-MB-231 and Hs578T tumors were collected and homogenized in 350 μL 1x RIPA buffer supplemented with protease inhibitor (Roche, Basel, Switzerland). Samples were subsequently mixed with 350 μL 1x Laemmli buffer solution and boiled for 10 min, vortexing every 5 min. Samples were centrifuged at 15,000 g for 15 min at 4°C to remove insoluble components. Protein concentrations were quantified using Lowry assay with bovine serum albumin as a standard. Protein extracts (40 μg) were loaded onto a 4–20% gradient gel (BioRad, Hercules, CA) for SDS-PAGE, and transferred onto a nitrocellulose membrane (Cell Signaling, Danvers, MA). The nitrocellulose membrane was incubated overnight with anti-EDB-FN antibody G4 (1:1,000) and loading control anti-β-actin (Cell Signaling; 1:1,000). Gels were visualized using a ChemiDoc XRS system (BioRad).

Statistical Analysis

All experiments were independently replicated at least three times unless otherwise stated. Statistical comparison of the different dosing groups was performed using Graphpad software. Statistical significance between two groups was calculated using an unpaired *t*-test. Data between three groups was compared using one-way ANOVA with $p < 0.05$ being statistically significant.

RESULTS

The triple negative MDA-MB-231 and Hs578T are highly invasive, mesenchymal breast cancer cell lines (21). Two independent mouse orthotopic xenografts were developed by inoculating the cancer cell lines into the mammary fat pads for assessing the effectiveness of MT218 at different doses. The expression of EDB-FN in the cell lines was first compared to a hormone receptor-positive epithelial breast cancer cell line MCF-7 as a less invasive control (17). As shown in **Figure 1A**, both MDA-MB-231and Hs578T cells had significantly higher EDB-FN mRNA expression (3.5- and 45-fold) when compared to MCF7 cells, respectively. Since EDB-FN is secreted into the tumor ECM, the expression of EDB-FN was also evaluated in 3D tumor spheroids of MDA-MB-231 and Hs578T cells incubated with ZD2-Cy5.5, a fluorescent peptide probe specific to EDB-FN. Both the 3D spheroids demonstrated strong ZD2-Cy5.5 binding, evidenced by the intense red fluorescence, indicating elevated expression and secretion of EDB-FN by the cancer cells (**Figure 1B**). Moreover, the Hs578T spheroids showed stronger ZD2-Cy5.5 staining and thus higher EDB-FN expression than the MDA-MB-231 spheroids, in consistence with the qRT-PCR results. The differential EDB-FN expression in the two cancer cell lines was also corroborated in their orthotopic tumor xenografts. **Figure 1C** shows histological sections of poorly differentiated H&E stained tumor tissues. Immunofluorescence staining of MDA-MB-231 and Hs578T tumor sections was performed using an EDB-FN specific G4 antibody. Strong EDB-FN expression was observed in Hs578T tumors when compared to the MDA-MB-231 tumor sections (**Figure 1D**). Western blot analysis also revealed abundant expression of EDB-FN in Hs578T tumors when compared to MDA-MB-231 tumors (**Figure 1E**, **Supplementary Datasheet 1**). These results demonstrate elevated expression of EDB-FN in both the triple negative breast cancers, more so in the Hs578T model.

Following the characterization of EDB-FN expression, tumor contrast enhancement of MT218 was evaluated in mice

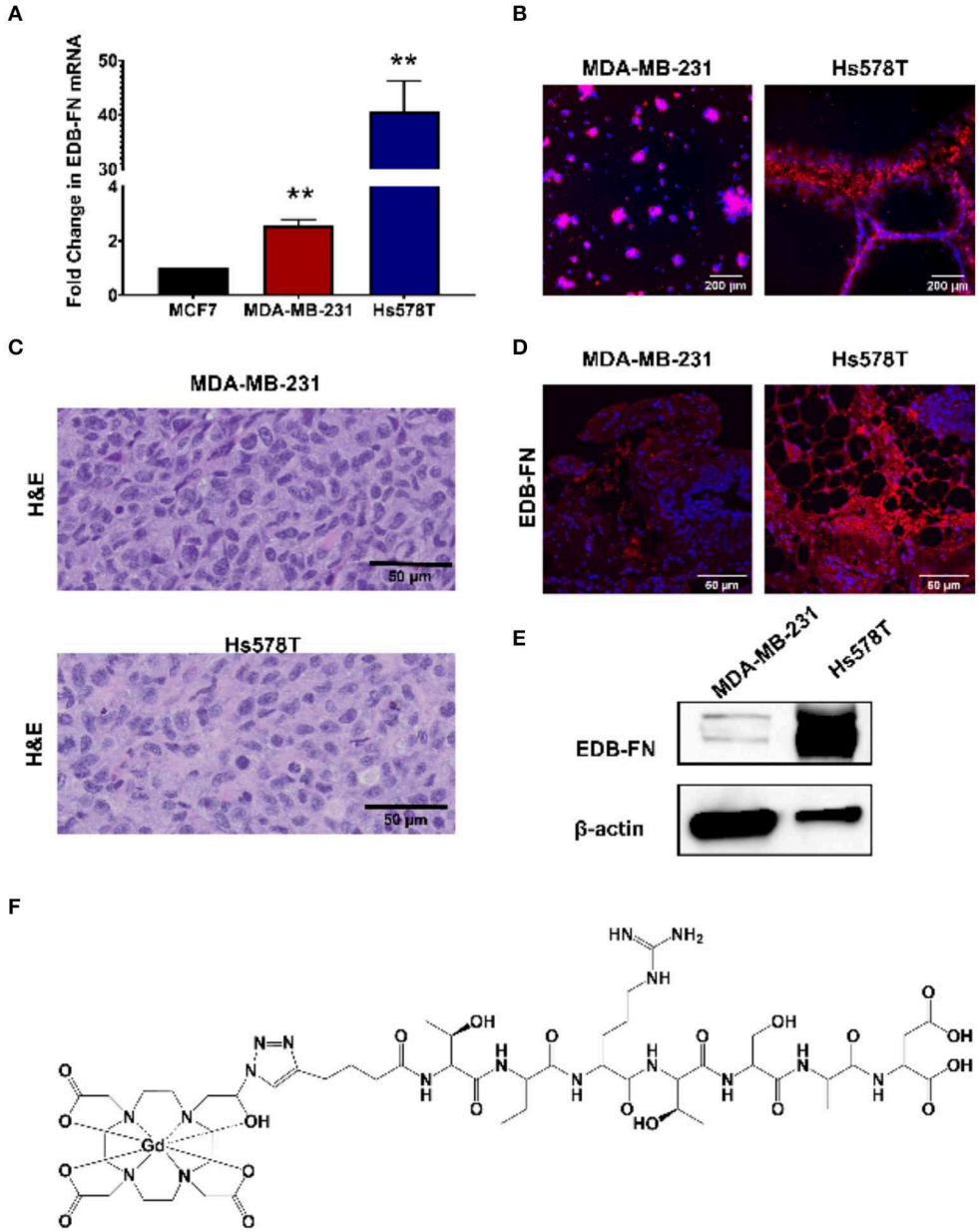

FIGURE 1 | EDB-FN is overexpressed in poorly differentiated, triple negative breast cancer. **(A)** Endogenous EDB-FN mRNA levels is significantly elevated in triple negative breast cancer cell lines MDA-MB-231 and Hs578T (claudin-low ER^-, PR^-, $HER2^-$) compared to MCF7 (luminal A; ER^+,$PR^{+/-}$, $HER2^-$) [$^{**}p < 0.01$, (22)]. mRNA was normalized to 18S mRNA control. **(B)** Representative fluorescence imaging reveals enhanced ZD2-Cy5.5 (red) binding in 3D cultures of MDA-MB-231 and Hs578T cells. **(C)** H&E staining of MDA-MB-231 and Hs578T tumor sections. Scale bar: 50 µm. **(D)** Analysis of EDB-FN expression in MDA-MB-231 and Hs578T tumor sections. Scale bar: 50 µm **(E)** Western blot analysis of EDB-FN expression in MDA-MB-231 and Hs578T tumors. β-actin was used as a loading control. **(F)** Chemical structure of ZD2-N3-Gd(HP-DO3A) (MT218).

bearing MDA-MB-231 and Hs578T xenografts before and after intravenous injection of MT218 at 0.1, 0.04, and 0.02 mmol Gd/kg. The chemical structure of MT218 is shown in **Figure 1F**. The tumor enhancement of the clinical control Gd(HP-DO3A) was also tested at the regular clinical dose of 0.1 mmol Gd/kg. Representative 2D T_1-weighted spin-echo MR images of the tumors were obtained before and at different time-points after injection of the contrast agents. While the non-targeted clinical agent Gd(HP-DO3A) resulted in little signal enhancement (**Figures 2**, **3**), MT218 exhibited dose-dependent tumor enhancement in both the tumors. Strong signal enhancement was observed in both MDA-MB-231 and Hs578T xenografts at clinical dose of 0.1 mmol Gd/kg of MT218. This signal brightness decreased slightly at a reduced dose of 0.04 mmol Gd/kg for the two tumors (**Figures 2**, **3**). The enhancement was then reduced substantially at 0.02 mmol

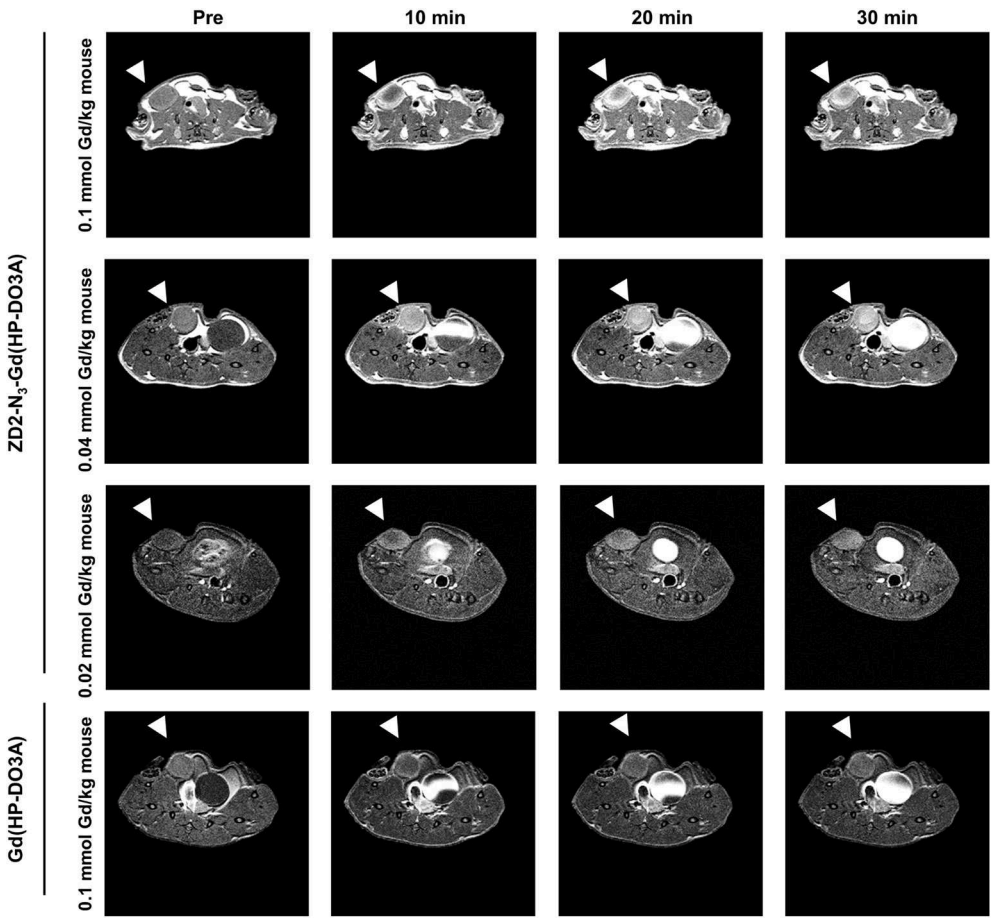

FIGURE 2 | MRMI with MT218 of MDA-MB-231 tumors in mice. Representative axial T_1-weighted 2D fast spin echo images taken before and at 10, 20, and 30 min post-injection of MT218 at doses of 0.1, 0.04, and 0.02 mmol Gd/kg mouse. Tumors are indicated by the white arrow heads. The clinical agent Gd(HP-DO3A) was used as a control at 0.1 mmol Gd/kg.

Gd/kg, but remained higher than that produced by clinical dose of Gd(HP-DO3A) (0.1 mmol Gd/kg) (**Figure 2**), demonstrating the superior tumor-targeting efficiency of MT218 over the clinical control. In addition, Hs578T tumors with higher EDB-FN expression exhibited brighter signal enhancement than MDA-MB-231 tumors at the same doses of MT218 (**Figure 3**). It appears that the background noise was low at the low doses for MT218. The tumor-specific contrast enhancement with MT218 in both the tumors lasted for at least 30 min for all the tested doses.

Quantitative analysis of the tumor signal enhancement revealed different dose-dependent signal enhancement pattern of MT218 in the tumor models. **Figure 4** shows the contrast-to-noise ratios (CNR) in the tumor models for up to 30 min post-injection of the agents. For the MDA-MB-231 model, MT218 produced comparable CNR at 0.1 and 0.04 mmol Gd/kg doses (**Figure 4A**), with ∼3 to 3.5-fold CNR increase over their respective pre-contrast images and those with Gd(HP-DO3A). At 0.02 mmol Gd/kg, MT218 produced, slightly higher (1.5-fold CNR) than that of clinical control agent. For the Hs578T tumor model, MT218 showed a dose-dependent trend of tumor CNR, although it was not statistically significant (**Figure 4B**). Specifically, MT218 produced up to 7-, 4-, and 3-fold CNR increase at the doses of 0.1, 0.04, and 0.02 mmol Gd/kg, respectively; while Gd(HP-DO3A) only produced 1.3-fold CNR increase in the tumor. The different dose-dependent enhancement pattern of MT218 in the tumor models could be attributed to their differential EDB-FN expression levels. MT218 might show saturated binding in MDA-MB-231 tumors at the high 0.1 mmol Gd/kg dose because of relatively low EDB-FN expression in the tumor. However, relatively consistent CNR was observed in the MDA-MB-231 tumors for at least 30 min. In contrast, the Hs578T tumors had higher EDB-FN expression and showed time-dependent tumor CNR changes at 0.1 mmol Gd/kg (**Figure 4B**). MT218 showed maximum signal enhancement at 0.1 mmol Gd/kg at 10 min post-injection and gradual reduction of tumor CNR over time. It produced relatively consistent CNR in the Hs578T tumors at the low doses for up to 30 min. MT218 produced substantial tumor CNR in the first minute post-injection in both the tumors, especially at the high doses.

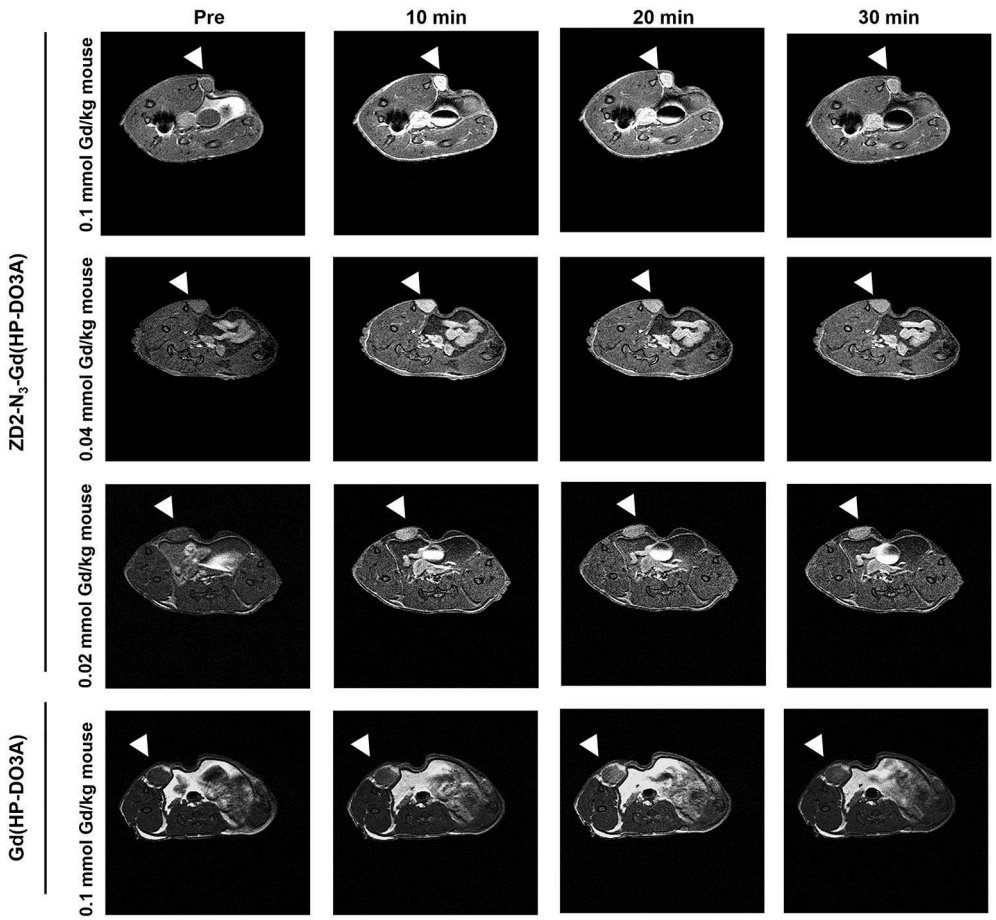

FIGURE 3 | MRMI with MT218 of Hs578T tumors in mice. Representative axial T_1-weighted 2D fast spin echo images taken before and at 10, 20, and 30 min post-injection of MT218 at doses of 0.1, 0.04, and 0.02 mmol Gd/kg mouse. Tumors are indicated by the white arrow heads. The clinical agent Gd(HP-DO3A) was used as a control at 0.1 mmol Gd/kg.

To determine if the uptake of MT218 is correlated with the endogenous EDB-FN expression in different tumor xenografts, we evaluated the changes in SNR in the MDA-MB-231 and Hs578T tumor models at 20 min post-injection of MT218 at 0.1, 0.04, and 0.02 mmol Gd/kg (**Figure 5**). At 0.1 mmol Gd/kg, the Hs578T tumors with high EDB-FN levels had 1.7-fold SNR over that of the MDA-MB-231 tumors with relatively lower EDB-FN (**Figure 5**). This tumor SNR decreased at the lower doses (0.04 and 0.02 mmol Gd/kg) in both the tumor models, with 1.7-fold higher SNR in Hs578T tumors than MDA-MB-231 tumors. On the other hand, no significant difference in SNR was observed for MT218 at different doses within the same tumor model. These results indicate that the uptake profile of MT218 is consistent with the tumor-specific expression profile of EDB-FN. Thus, MT218 has the promise to facilitate effective MRMI of aggressive tumors at doses as low as 0.02 mmol Gd/kg, a five-times reduction as compared to the clinical contrast agent.

In order to assess potential non-specific binding and enhancement of MT218, we analyzed the CNR in the brain and the key metabolic organs including the liver, kidney, and spleen. At all the tested doses of MT218, no significant changes in CNR were observed in the liver, spleen, or brain of all the tested mice for up to 30 min (**Figure 6**). Significant enhancement was observed in the kidneys as early as 10 min post-injection, but it steadily decreased at 30 min, indicating renal clearance of the agent. Taken together, these results exhibit the ability of MT218 to facilitate effective MRMI of aggressive tumors with minimal non-specific binding in normal tissues and organs at substantially reduced doses.

DISCUSSION

This work highlights the potential of the targeted contrast agent MT218 for effective MRMI of aggressive breast cancer at substantially reduced doses. MRMI is advantageous for precision cancer imaging if tumor-specific targeted contrast agents are available for risk-stratification of aggressive cancers (16, 23). MT218 targets the extracellular matrix oncoprotein EDB-FN, which is highly expressed in aggressive TNBC tumors. The ECM oncoprotein is more accessible for binding of the targeted

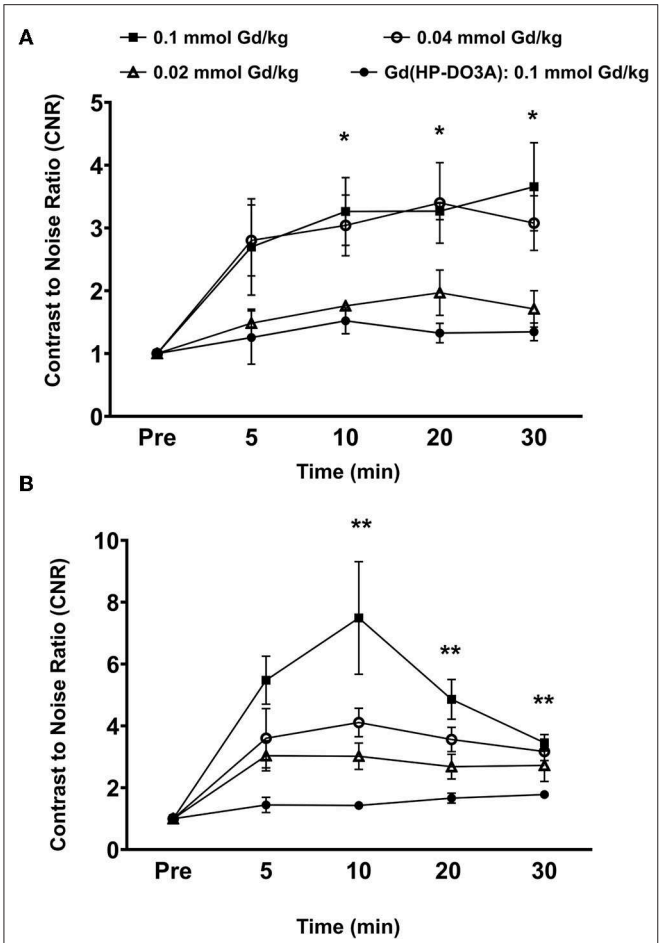

FIGURE 4 | Analysis of fold increase of tumor contrast-to-noise ratio (CNR) from images acquired as indicated in MDA-MB-231 **(A)** and Hs578T **(B)** tumors. Data is represented as mean ± s.e.m. $n = 5$ for MDA-MB-231 and Hs578T tumors. *$p < 0.05$ for comparison of increased CNR ratio of 0.1 and 0.04 mmol Gd/kg to control Gd(HP-DO3A). No statistical significance was observed between 0.02 mmol Gd/kg MT218 to control. **$p < 0.05$ for comparison of increased CNR ratio of 0.1, 0.04, and 0.02 mmol Gd/kg to control.

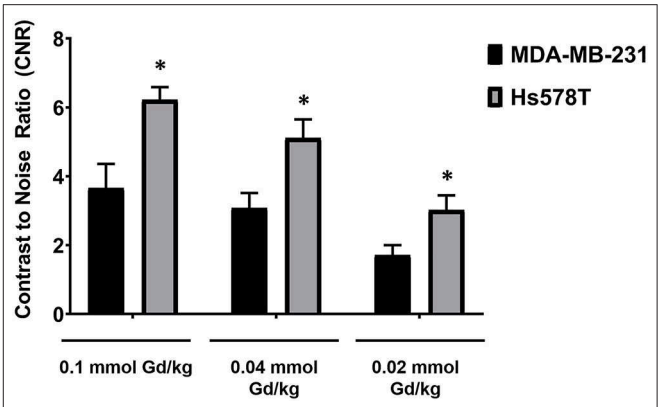

FIGURE 5 | Analysis of tumor signal-to-noise ratio (SNR) at 20 min post-injection of MT218 at doses of 0.1, 0.04, and 0.02 mmol Gd/kg mouse. Data is represented as mean ± s.e.m. $n = 5$ for MDA-MB-231 and Hs578T tumors. *$p < 0.05$ for comparison of increased SNR ratio.

contrast agent than cell surface biomarkers. Consequently, sufficient MT218 molecules bound to the abundant tumor-specific ECM protein produce robust enhancement throughout tumor tissues even at one fifth the clinical dose. Effective MRMI at such reduced doses has the promise to minimize the potential dose-dependent toxic side-effects of GBCAs in clinical practice, addressing the important safety concerns of their clinical use (2, 24).

MRMI with MT218 also exhibits several unique features for molecular imaging of TNBC tumors. MT218 produces significant tumor enhancement as early as 1 min post-injection at all the tested doses. High accessibility to EDB-FN in the tumor ECM allows rapid binding of MT218, resulting in effective tumor enhancement at the early time-point post-injection. MT218 produces relatively uniform contrast enhancement throughout the tumor tissues, especially at the later time-points post-injection. These observations indicate that EDB-FN is expressed throughout the ECM of the TNBC tumors, which enables specific binding of MT218 across the tumor tissues. The signal enhancement correlates well with the expression levels of EDB-FN in the tumors. EDB-FN is a marker of EMT and tumor angiogenesis (12). Clinical studies have shown that its expression is associated with poor survival of oral cancer patients (25, 26). Therefore, MRMI of EDB-FN with MT218 has the potential to differentiate tumor aggressiveness based on the EDB-FN expression (8, 15, 17).

GBCAs are FDA approved, and widely used for contrast-enhanced MRI for cancerous lesions (1). Although there have been observations of tissue accumulation and nephrogenic systemic fibrosis in patients with compromised renal functions for GBCAs, little clinical evidence exists to link their deposition to adverse effects. MRI contrast agents with other paramagnetic materials, such as iron and Mn, have been explored as alternative MRI contrast agents. Superparamagnetic iron oxide nanoparticles have been shown to provide excellent T_2-weighted MR signal enhancement. Ferumoxytol, a carboxymethyldextran-coated iron oxide nanoparticle has been used as a contrast agent in lieu of GBCAs (27). However, ferumoxytol is large, and has a blood elimination half-life of 14 h, requiring patients to be imaged the day post-injection to observe tumor enhancement. Mn complexes have also been explored as GBCA alternatives due to their strong paramagnetic properties, (24, 28). However, frequent use of Mn-based contrast agents can also be associated with toxicity concerns, limiting their use clinically (29, 30). Consequently, comprehensive safety assessments are still required for these non-GBCAs before any approval for clinical use by the regulatory agents. The FDA has concluded that there is little evidence that directly links gadolinium retention to adverse side-effects in healthy patients, suggesting that the benefits of GBCAs outweigh any potential risks (31). Nevertheless, the ability to substantially reduce the dose of GBCAs through tumor-specific contrast agents will further enhance the safety profile of GBCAs for clinical use.

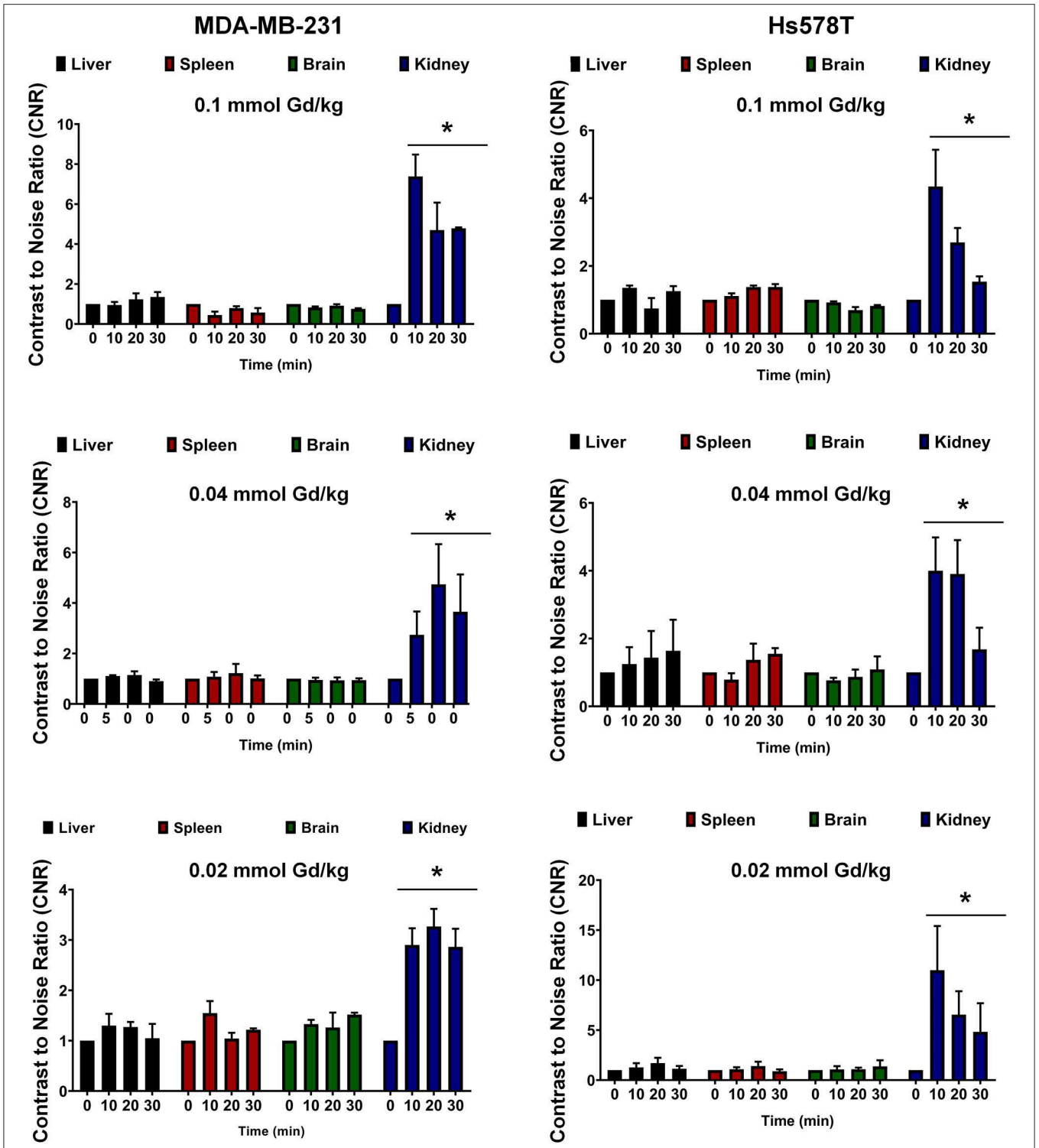

FIGURE 6 | Contrast-to-noise ratio at 10, 20, and 30 min post-injection of MT218 at doses of 0.1, 0.04, and 0.02 mmol Gd/kg. Analysis of fold increase of CNR of liver, spleen, brain, and kidney were acquired in groups as indicated. Post-contrast CNRs of kidneys are significantly increased over pre-contrast (*$p < 0.05$).

MT218 is a small peptide targeted macrocyclic contrast agent based on a clinical macrocyclic agent Gd(HP-DO3A), which has excellent thermodynamic and kinetic stability (19, 32, 33). Additionally, cyclic GBCAs have shown to have lower brain accumulation compared to linear contrast agents, indicating an excellent safety profile (34). It is expected that MT218 has

a similar safety profile as the clinical agent. Comprehensive preclinical pharmacological and toxicity studies of MT218 are currently on-going based on FDA guidelines for clinical translation. To our knowledge, MT218 is the only targeted small molecular MRI contrast agent specific to an oncoprotein for effective MRMI of cancer. The clinical translation of MT218 will enable precision MRMI for the detection and risk-stratification of aggressive breast cancer. High resolution MRMI by MT218 could provide early detection of aggressive breast cancer and metastatic disease (14). Importantly, the administration of MT218 at reduced doses would alleviate the safety concerns associated with the dose-dependent side effects of GBCAs.

CONCLUSIONS

EDB-FN is highly expressed by aggressive TNBC cells and tumors. The targeted MRI contrast agent MT218 specific to EDB-FN is effective for MRMI of TNBC tumors in mice at significantly reduced doses. MT218 rapidly binds to the extracellular matrix oncoprotein and produces robust tumor contrast enhancement at 1 min post-injection, lasting for 30 min. The effective MRMI with MT218 at low doses is an advantageous safety feature, and holds promise to minimize dose-dependent side effects of GBCAs. The clinical translation of MT218 has the potential to overcome the limitations of the existing clinical GBCAs for precision cancer MRMI and to provide accurate detection and risk-stratification of aggressive breast cancer.

DATA AVAILABILITY STATEMENT

The datasets generated for this study are available on request to the corresponding author.

ETHICS STATEMENT

The animal study was reviewed and approved by CWRU IACUC.

AUTHOR CONTRIBUTIONS

The conceptual design of the research was designed by NA and Z-RL. NA participated in execution of all aspects of the research work. NA and XY designed all MR sequences used in this study. GY and MB participated in data analysis of MR images. AV, RH, and PQ participated in fluorescence imaging and acquisition. The manuscript was written and edited by NA and Z-RL. AV assisted with critical comments and edits for the manuscript.

FUNDING

This research was supported in part by the National Institute of Health grants R01CA194518 and R01CA211762. Z-RL is a M. Frank Rudy and Margaret Domiter Rudy Professor of Biomedical Engineering.

ACKNOWLEDGMENTS

The authors acknowledge Dr. Zheng Han for providing the ZD2-Cy5.5 probe.

SUPPLEMENTARY MATERIAL

The Supplementary Material for this article can be found online at: https://www.frontiersin.org/articles/10.3389/fonc.2019.01351/full#supplementary-material

REFERENCES

1. Zhou Z, Lu ZR. Gadolinium-based contrast agents for magnetic resonance cancer imaging. *Wiley Interdiscip Rev Nanomed Nanobiotechnol.* (2013) 5:1–18. doi: 10.1002/wnan.1198
2. Kuo PH, Kanal E, Abu-Alfa AK, Cowper SE. Gadolinium-based MR contrast agents and nephrogenic systemic fibrosis. *Radiology.* (2007) 242:647–9. doi: 10.1148/radiol.2423061640
3. Lin K. Administration of gadolinium-based contrast agents in MR angiography. *AJR Am J Roentgenol.* (2009) 192:W193; author reply: W194. doi: 10.2214/AJR.08.1864
4. Berger F, Kubik-Huch RA, Niemann T, Schmid HR, Poetzsch M, Froehlich JM, et al. Gadolinium distribution in cerebrospinal fluid after administration of a gadolinium-based MR contrast agent in humans. *Radiology.* (2018) 288:703–9. doi: 10.1148/radiol.2018171829
5. McDonald RJ, McDonald JS, Kallmes DF, Jentoft ME, Paolini MA, Murray DL, et al. Gadolinium deposition in human brain tissues after contrast-enhanced MR imaging in adult patients without intracranial abnormalities. *Radiology.* (2017) 285:546–54. doi: 10.1148/radiol.2017161595
6. Ye F, Wu X, Jeong EK, Jia Z, Yang T, Parker D, et al. A peptide targeted contrast agent specific to fibrin-fibronectin complexes for cancer molecular imaging with MRI. *Bioconjug Chem.* (2008) 19:2300–3. doi: 10.1021/bc800211r
7. Zhou Z, Wu X, Kresak A, Griswold M, Lu ZR. Peptide targeted tripod macrocyclic Gd(III) chelates for cancer molecular MRI. *Biomaterials.* (2013) 34:7683–93. doi: 10.1016/j.biomaterials.2013.06.057
8. Han Z, Zhou Z, Shi X, Wang J, Wu X, Sun D, et al. EDB fibronectin specific peptide for prostate cancer targeting. *Bioconjug Chem.* (2015) 26:830–8. doi: 10.1021/acs.bioconjchem.5b00178
9. Wu X, Burden-Gulley SM, Yu GP, Tan M, Lindner D, Brady-Kalnay SM, et al. Synthesis and evaluation of a peptide targeted small molecular Gd-DOTA monoamide conjugate for MR molecular imaging of prostate cancer. *Bioconjug Chem.* (2012) 23:1548–56. doi: 10.1021/bc300009t
10. Wu X, Yu G, Lindner D, Brady-Kalnay SM, Zhang Q, Lu ZR. Peptide targeted high-resolution molecular imaging of prostate cancer with MRI. *Am J Nucl Med Mol Imaging.* (2014) 4:525–36.
11. Zhou Z, Qutaish M, Han Z, Schur RM, Liu Y, Wilson DL, et al. MRI detection of breast cancer micrometastases with a fibronectin-targeting contrast agent. *Nat Commun.* (2015) 6:7984. doi: 10.1038/ncomms8984
12. Khan ZA, Chan BM, Uniyal S, Barbin YP, Farhangkhoee H, Chen S, et al. EDB fibronectin and angiogenesis – a novel mechanistic pathway. *Angiogenesis.* (2005) 8:183–96. doi: 10.1007/s10456-005-9017-6
13. Gopal S, Veracini L, Grall D, Butori C, Schaub S, Audebert S, et al. Fibronectin-guided migration of carcinoma collectives. *Nat Commun.* (2017) 8:14105. doi: 10.1038/ncomms14105
14. Han Z, Cheng H, Parvani JG, Zhou Z, Lu ZR. Magnetic resonance molecular imaging of metastatic breast cancer by targeting extradomain-B fibronectin in the tumor microenvironment. *Magn Reson Med.* (2018) 79:3135–43. doi: 10.1002/mrm.26976
15. Han Z, Li Y, Roelle S, Zhou Z, Liu Y, Sabatelle R, et al. Targeted contrast agent specific to an oncoprotein in tumor microenvironment with the potential for

detection and risk stratification of prostate cancer with MRI. *Bioconjug Chem.* (2017) 28:1031–40. doi: 10.1021/acs.bioconjchem.6b00719
16. Han Z, Lu ZR. Targeting fibronectin for cancer imaging and therapy. *J Mater Chem B.* (2017) 5:639–54. doi: 10.1039/C6TB02008A
17. Han Z, Wu X, Roelle S, Chen C, Schiemann WP, Lu ZR. Author correction: targeted gadofullerene for sensitive magnetic resonance imaging and risk-stratification of breast cancer. *Nat Commun.* (2018) 9:153. doi: 10.1038/s41467-017-02302-9
18. Han Z, Wu X, Roelle S, Chen C, Schiemann WP, Lu ZR. Targeted gadofullerene for sensitive magnetic resonance imaging and risk-stratification of breast cancer. *Nat Commun.* (2017) 8:692. doi: 10.1038/s41467-017-00741-y
19. Ayat NR, Qin JC, Cheng H, Roelle S, Gao S, Li Y, et al. Optimization of ZD2 peptide targeted Gd(HP-DO3A) for detection and risk-stratification of prostate cancer with MRI. *ACS Med Chem Lett.* (2018) 9:730–5. doi: 10.1021/acsmedchemlett.8b00172
20. Vaidya AM, Sun Z, Ayat N, Schilb A, Liu X, Jiang H, et al. Systemic delivery of tumor-targeting siRNA nanoparticles against an oncogenic LncRNA facilitates effective triple-negative breast cancer therapy. *Bioconjug Chem.* (2019) 30:907–19. doi: 10.1021/acs.bioconjchem.9b00028
21. Chavez KJ, Garimella SV, Lipkowitz S. Triple negative breast cancer cell lines: one tool in the search for better treatment of triple negative breast cancer. *Breast Dis.* (2010) 32:35–48. doi: 10.3233/BD-2010-0307
22. Vaidya AM, Wang H, Qian V, Lu ZR. Extradomain-B fibronectin is a molecular marker of invasive breast cancer cells. *bioRxiv.* (2019) 743500. doi: 10.1101/743500
23. Stephen RM, Gillies RJ. Promise and progress for functional and molecular imaging of response to targeted therapies. *Pharm Res.* (2007) 24:1172–85. doi: 10.1007/s11095-007-9250-3
24. Pan D, Schmieder AH, Wickline SA, Lanza GM. Manganese-based MRI contrast agents: past, present and future. *Tetrahedron.* (2011) 67:8431–44. doi: 10.1016/j.tet.2011.07.076
25. Lyons AJ, Bateman AC, Spedding A, Primrose JN, Mandel U. Oncofetal fibronectin and oral squamous cell carcinoma. *Br J Oral Maxillofac Surg.* (2001) 39:471–7. doi: 10.1054/bjom.2001.0702
26. Mhawech P, Dulguerov P, Assaly M, Ares C, Allal AS. EB-D fibronectin expression in squamous cell carcinoma of the head and neck. *Oral Oncol.* (2005) 41:82–8. doi: 10.1016/j.oraloncology.2004.07.003
27. Gale EM, Caravan P. Gadolinium-free contrast agents for magnetic resonance imaging of the central nervous system. *ACS Chem Neurosci.* (2018) 9:395–7. doi: 10.1021/acschemneuro.8b00044
28. Massaad CA, Pautler RG. Manganese-enhanced magnetic resonance imaging (MEMRI). *Methods Mol Biol.* (2011) 711:145–74. doi: 10.1007/978-1-61737-992-5_7
29. Koretsky AP, Silva AC. Manganese-enhanced magnetic resonance imaging (MEMRI). *NMR Biomed.* (2004) 17:527–31. doi: 10.1002/nbm.940
30. Wendland MF. Applications of manganese-enhanced magnetic resonance imaging (MEMRI) to imaging of the heart. *NMR Biomed.* (2004) 17:581–94. doi: 10.1002/nbm.943
31. Gulani V, Calamante F, Shellock FG, Kanal E, Reeder SB, International Society for Magnetic Resonance in Medicine. Gadolinium deposition in the brain: summary of evidence and recommendations. *Lancet Neurol.* (2017) 16:564–70. doi: 10.1016/S1474-4422(17)30158-8
32. White GW, Gibby WA, Tweedle MF. Comparison of Gd(DTPA-BMA) (Omniscan) versus Gd(HP-DO3A) (ProHance) relative to gadolinium retention in human bone tissue by inductively coupled plasma mass spectroscopy. *Invest Radiol.* (2006) 41:272–8. doi: 10.1097/01.rli.0000186569.32408.95
33. Morcos SK. Extracellular gadolinium contrast agents: differences in stability. *Eur J Radiol.* (2008) 66:175–9. doi: 10.1016/j.ejrad.2008.01.025
34. Lohrke J, Frisk AL, Frenzel T, Schockel L, Rosenbruch M, Jost G, et al. Histology and gadolinium distribution in the rodent brain after the administration of cumulative high doses of linear and macrocyclic gadolinium-based contrast agents. *Invest Radiol.* (2017) 52:324–33. doi: 10.1097/RLI.0000000000000344

Conflict of Interest: Z-RL is a co-founder of Molecular Theranostics, LLC and has ownership interest in the company.

The remaining authors declare that the research was conducted in the absence of any commercial or financial relationships that could be construed as a potential conflict of interest.

frontiers in Oncology

PERSPECTIVE
published: 21 January 2020
doi: 10.3389/fonc.2019.01560

Biomimetic Nanoparticles Camouflaged in Cancer Cell Membranes and Their Applications in Cancer Theranostics

Jiefu Jin[1]* *and Zaver M. Bhujwalla*[1,2,3]*

[1] Division of Cancer Imaging Research, The Russell H. Morgan Department of Radiology and Radiological Science, Baltimore, MD, United States, [2] Sidney Kimmel Comprehensive Cancer Center, Baltimore, MD, United States, [3] Department of Radiation Oncology and Molecular Radiation Sciences, The Johns Hopkins University School of Medicine, Baltimore, MD, United States

Nanoparticles (NPs) camouflaged in cell membranes represent novel biomimetic platforms that can mimic some of the membrane functions of the cells from which these membranes are derived, in biological systems. Studies using cell membrane coated NPs cover a large repertoire of membranes derived from cells such as red blood cells, immune cells, macrophages, and cancer cells. Cancer cell membrane coated nanoparticles (CCMCNPs) typically consist of a NP core with a cancer cell plasma membrane coat that can carry tumor-specific receptors and antigens for cancer targeting. The NP core can serve as a vehicle to carry imaging and therapeutic moieties. As a result, these CCMCNPs are being investigated for multiple purposes including cancer theranostics. Here we have discussed the key steps and major issues in the synthesis and characterization of CCMCNPs. We have highlighted the homologous binding mechanisms of CCMCNPs that are being investigated for cancer targeting, and have presented our data that identify BT474 CCMCNPs as binding to multiple cancer cell lines. Current preclinical applications of CCMCNPs for cancer theranostics and their advantages and limitations are discussed.

Keywords: biomimetic nanoparticles, cancer cell membranes, theranostics, immune response, metastasis

OPEN ACCESS

Edited by:
Georgios S. Limouris, National and Kapodistrian University of Athens, Greece

Reviewed by:
Roberto Molinaro, University of Urbino Carlo Bo, Italy
Michael Evangelopoulos, Northwestern University, United States
Maria Prat, University of Eastern Piedmont, Italy

***Correspondence:**
Jiefu Jin
jjin@jhmi.edu
Zaver M. Bhujwalla
zbhujwa1@jhmi.edu

Specialty section:
This article was submitted to Cancer Imaging and Image-directed Interventions, a section of the journal Frontiers in Oncology

Received: *15 October 2019*
Accepted: *23 December 2019*
Published: *21 January 2020*

Citation:
Jin J and Bhujwalla ZM (2020) Biomimetic Nanoparticles Camouflaged in Cancer Cell Membranes and Their Applications in Cancer Theranostics. Front. Oncol. 9:1560. doi: 10.3389/fonc.2019.01560

INTRODUCTION

Biomimetic nanoparticles (NPs) are an emerging class of NPs that integrate the functionality of biological materials with the flexibility of synthetic materials to achieve effective navigation and interfacing in complex biological systems (1). Cell membrane coated NPs are biomimetic platforms that combine the functionality of cell membranes with the abilities of synthetic core structures to carry imaging reporters and therapeutic cargo (2).

Red blood cell (RBC) membrane-camouflaged poly(lactic-co-glycolic acid) (PLGA) NPs are one of the first reported cell membrane coated NPs. The RBC membrane was found to act as a nanosponge for toxins, and bestowed a longer circulation pharmacokinetic profile than uncoated NPs (3). Since this initial study, cell membrane coating technology has significantly expanded to the use of membranes from platelets (4–8) and from nucleated cells, such as macrophages (9–12), neutrophils (13), beta cells (14), and cancer cells (15–33). The use of cancer cell plasma membranes has attracted attention because these membranes carry tumor-specific receptors and antigens that play a role in cancer cell proliferation, invasion, and metastasis. While several comprehensive reviews have summarized the applications of cell membrane camouflaged NPs (34–46) from

various cell sources, to the best of our knowledge only one of these reviews is focused on advances with CCMCNPs (37).

Here, we have discussed the steps and issues in the manufacturing and characterization of CCMCNPs. We have highlighted the homologous binding ability of CCMCNPs with potential applications in cancer targeting, and summarized the current preclinical applications of CCMCNPs for cancer theranostics, and their advantages and limitations.

SYNTHESIS OF CCMCNPs

CCMCNPs are synthesized by coating NPs with a lipid bilayer of cancer cell plasma membranes. The nanoparticle cores are synthetic materials that feature the advantage of flexibility and reproducibility. These cores can be used to carry therapeutic or imaging moieties. The cancer cell plasma membrane coating is a natural entity possessing the complexity and functionality derived from the cell membranes of the source cancer cells. As a result, CCMCNPs combine the advantages of synthetic and biological materials within a single biomimetic platform. A schematic illustration of the steps involved in the preparation of CCMCNPs is shown in **Figure 1**. Typical applications of CCMCNPs for cancer theranostics are shown in the schematic in **Figure 2**.

CCMCNP Core Materials

The core of the CCMCNPs can be organic or inorganic. Organic nanoparticle cores include PLGA (15–17, 20, 31), semiconducting polymers (23), or poly(caprolactone) (PCL)-pluronic copolymers F68 (27). Polymeric NPs are usually biocompatible and biodegradable, and are used to encapsulate both hydrophilic and hydrophobic drugs for drug delivery. In particular, PLGA, an FDA approved polymer, has been widely investigated for pharmaceutical formulation applications (47). The polymer cores with their payloads are usually prepared via nano-precipitation followed by emulsion solvent evaporation, or self-assembly methods. Inorganic core materials used for CCMCNPs include silicon/silica (18, 30, 32), magnetic materials (22, 33), copper sulfide (CuS) (29), upconversion NPs (26), gold nanoshells (28), and metal–organic framework (MOF) (24, 25). Inorganic NP cores can exist in a porous structure to improve the drug loading efficiency and feature several unique electrical, magnetic, and optical properties adapted to meet to the specific need of the biomedical application. With recent advances in nanotechnology, inorganic NPs can be prepared with precise control of shape, size, and surface chemistry.

Cancer Cell Membranes

Unlike cancer cells that have a nucleus and organelles, RBCs do not have a nucleus and lack organelles. As a result, RBC membrane vesicles are relatively easily obtained by removing the hemoglobin content under hypotonic conditions. The isolation of cancer cell membranes is, however, a more complex process. Typically, cancer cells are first ruptured into cell fragments under hypotonic conditions and with the use of mechanical processes, such as homogenization or sonication. Unbroken cells and nuclei are pelleted under low-speed centrifugation. The supernatant contains the plasma membrane, the cytosol and other organelles, such as lysosomes, golgi, mitochondria, and endoplasmic reticulum. Based on the density difference between the plasma membrane and other cellular factions, differential centrifugation is mainly used for plasma membrane isolation. However, we found that gradient centrifugation was superior to differential centrifugation in terms of purity of isolated cell membrane fractions (19). Commonly used gradients include discontinuous sucrose, and self-generated Percoll or iodixanol gradients (48, 49). In our recent study (19), we employed sucrose gradient centrifugation and demonstrated a discernable separation of the plasma membrane portion at the top band that was clearly separated from two other discrete bands.

Plasma membrane protein isolation kits have also been used to isolate cancer cell plasma membranes (23), with various commercial available kits from different vendors. However, one major concern with these commercial kits is that they are designed to isolate plasma membrane proteins but not the intact phospholipid vesicles to which the membrane proteins are

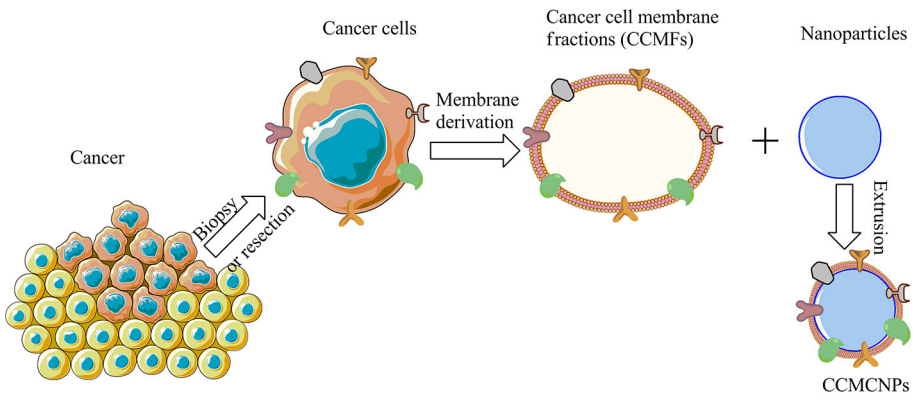

FIGURE 1 | Schematic illustration of the steps required in the synthesis of CCMCNPs. The schematic was produced, in part, by using the graphics from powerpoint, ChemBioDraw and Servier Medical Art image data bank (https://smart.servier.com).

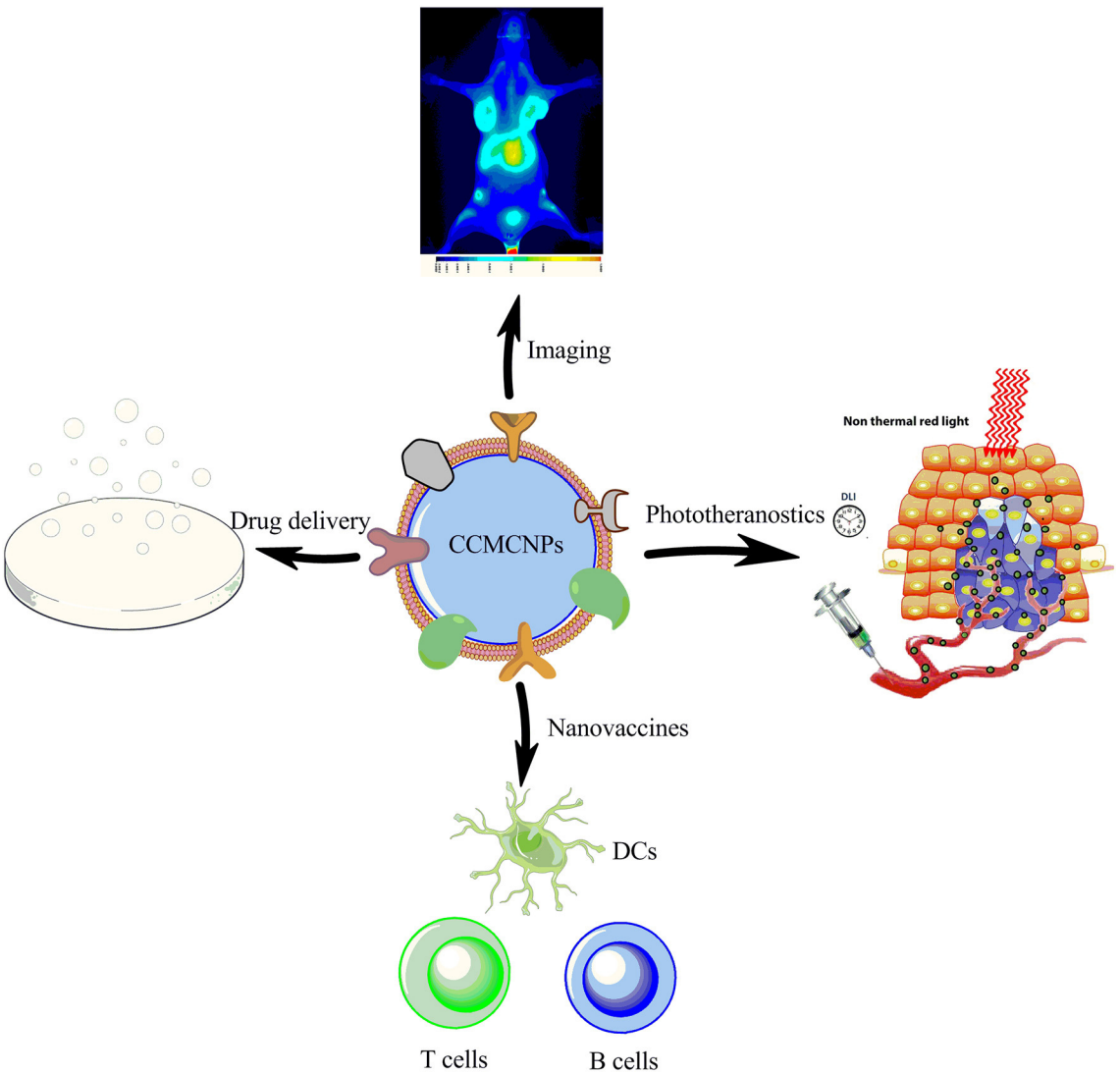

FIGURE 2 | Schematic illustration summarizing the current applications of CCMCNPs in preclinical cancer theranostics. The schematic was produced, in part, by using the graphics from powerpoint, ChemBioDraw and Servier Medical Art image data bank (https://smart.servier.com).

attached or embedded. As a result the plasma membrane vesicles are frequently too small (around 50 nm) and have a poor yield.

Cancer Cell Membrane Coating on NPs

Cancer cell membrane coating is commonly achieved though sonication and extrusion processes after mixing cancer cell membrane vesicles and NPs. Sonication is a pre-treatment process to break down and disperse cancer cell membrane vesicles. In an extrusion approach, a mini extruder used to make liposomes is connected to two air-tight syringes. Cancer cell membrane vesicles are mixed with NPs at a certain ratio and placed in the syringe on one side. Mechanical force is applied on the plunger of the syringe, and the mixture is extruded through a polycarbonate porous membrane located in the center of extruder. Cancer cell membrane coated NPs are collected after several passes through the polycarbonate membrane.

The mechanical force applied while the membrane vesicles and NPs are passing through the small pores of the polycarbonate membrane facilitates the fusion between vesicles and nanoparticle. This extrusion-based preparation method is adapted from liposome synthesis technology. However, this method suffers from several limitations when it is applied to fabricate CCMCNPs. Cancer cell membrane vesicles produced by mechanical rupture appear in a variety of sizes and shapes. Because they are much thicker and more rigid than liposomes, this hampers the curving of membrane vesicles for nanoparticle coating, and also results in pore obstruction of the polycarbonate membrane and loss of membrane vesicles. Due to these technical difficulties, the coating efficiency is largely compromised. The resulting product usually contains some NPs without membrane coating, and some membrane vesicles without an NP core. Unfortunately, because there is no efficient method

to remove the uncoated NPs or the membrane vesicles, the final product contains a small fraction of both these unwanted components. In addition, this laboratory-based small scale synthesis involves multiple manual steps that impede its clinical translation due to concerns such as synthesis variability and manufacturing scalability. Although the current extrusion-based coating method works for a variety of cell membranes and NPs, the coating mechanism and synthesis procedure require optimization. Such optimization should take into account the physicochemical properties of NPs, such as the size, shape, morphology, and surface chemistry that will impact coating efficiency.

Microfluidics provides a robust tool to produce nanomaterials in a controlled and reproducible manner. In a recent study, a microfluidic chip that incorporated electroporation was fabricated (50). Magnetic nanoparticles (MNs) and RBC membrane-derived vesicles (RBC-vesicles) were made to flow through the electroporation zone. Electric pulses between two electrodes promoted the entry of MNs into RBC-vesicles facilitating the synthesis of RBC-MNs. RBC-MNPs synthesized by the microfluidic electroporation approach exhibited significantly better treatment outcome than those prepared by conventional methods. Although not previously reported, such a microfluidic approach may provide a promising alternative to producing CCMCNPs.

Using cancer cell membranes to coat NPs is a top-down approach. Although it has the above-mentioned limitations in fabrication, it does recapitulate some of the biological complexities of the cell membrane on the carrier surface and provides a one-step solution to transferring some of the bioactive functions of the cell membrane to the carrier (51). Recently, a combined top down and bottom-up strategy was described that incorporated proteins derived from the leukocyte plasma membrane into lipid nanoparticles (51–53). The top-down strategy was used to obtain cell membrane proteins that were inserted into a lipid bilayer by a bottom-up approach. The resulting proteolipid vesicles, referred to as leukosomes, retained the versatility and physicochemical properties typical of liposomal formulations. This biomimetic approach provided better control of the final composition and formulation. However, it did not reproduce the complexity of the cellular membrane or maintain cell membrane protein conformation, surface density, or ratio.

CHARACTERIZATION OF CCMCNPs

Characterization of Physicochemical Properties

Transmission electron microscopy (TEM) is an effective way to characterize the size and morphology of CCMCNPs and their precursors. Cancer cell membrane vesicles exist in a coil-like shape with a broad size distribution. Core-shell structures observed in TEM images provide important evidence of successful coating. The thickness of the membrane coating ranges from 5 to 10 nm that is in agreement with the thickness of the phospholipid bilayer. Dynamic laser scattering (DLS) is another commonly used technique to detect the hydrodynamic size and zeta-potential of NPs. The hydrodynamic size of CCMCNPs is slightly higher than the size of the core NPs due to membrane coating, and much lower than cancer cell membrane vesicles. The zeta-potential of CCMCNPs is similar to that of membrane vesicles. Combined data from TEM and DLS can be used to confirm successful membrane coating. The stability of CCMCNPs can be evaluated by measuring the hydrodynamic size over a period of time in suspension in culture medium, serum or physiological buffers. The size fluctuation of CCMCNPs is minimal. Studies evaluating coagulation have not been reported so far.

Protein Profiling by SDS-PAGE

A major goal of cancer cell plasma membrane coating is to translocate membrane proteins in an intact state on to the core NPs. It is therefore important to confirm the preservation of membrane proteins and their associated structures and functions, once the membrane is coated on the NP. SDS-PAGE is usually used to demonstrate the preservation of membrane proteins by confirming the unchanged protein profiles of cancer cell membrane vesicles before and after coating. However, the protein staining after SDS-PAGE is non-specific and all the proteins are stained. The technique is a relatively coarse approach to profile proteins and is not sensitive to protein changes. We addressed this issue by using membranes from cells overexpressing the G protein-coupled receptor CXCR4 and the glycoprotein CD44 (19), and confirming the levels of these markers before and after cell membrane coating, using flow cytometry.

Purity, Integrity, and Sidedness

The purity of cancer cell plasma membrane vesicles is typically evaluated by western blot probing of a series of subcellular fractions along with purified membrane. We carefully examined the purity of the isolated membrane vesicles by probing a series of subcellular markers, Na^+/K^+-ATPase for plasma membrane, ATP5a for mitochondrial, GAPDH for cytosolic protein, and GRP78 for endoplasmic reticulum (19). We confirmed the successful enrichment of plasma membrane associated proteins and negligible contamination from subcellular organelle proteins. To check the purity of CCMCNPs, the core and shell are labeled with fluorescence dyes of different colors, and the overlapping of the two fluorescence signals is used to confirm that the cell membranes have coated the NPs. However, due to the limited spatial resolution of fluorescence microscopy, subtle mismatches at the nanoscale level can be missed by fluorescence microscopy.

To determine if CCMCNPs remain intact under physiological conditions, the most common approach is to label the NP core and the outer coat shell with different fluorescence dyes and check the fluorescence of CCMCNPs following internalization by cells. Although this approach is also subject to the limited spatial resolution of fluorescence microscopy, it is considered the simplest way to evaluate CCMCNP integrity.

As discussed earlier, sidedness or the orientation of the cancer cell plasma membrane is an important characteristic of CCMCNPs. The membrane coating on CCMCNPs has

to be in a "right-side-out" manner for applications that require the extracellular domains of membrane proteins to be exposed, such as for antigen binding and recognition. The sidedness of RBC membranes after coating has been evaluated by using immunogold labeling (54), where antigen markers located at extracellular and intracellular domains were separately stained with colloidal gold NPs labeled with respective specific antibodies. However, the sidedness of CCMCNPs has not been well-investigated, and immunogold labeling combined with electron microscopy will be useful techniques for evaluating CCMCNP sidedness. Although electron microscopy of immunogold labeling can determine membrane sidedness at high spatial resolution, flow cytometry is better adapted to quantify translocated membrane proteins (51).

TARGETING MECHANISMS OF CCMCNPs

Homologous Binding of CCMCNPs to Cancer Cells

Cell adhesion molecules, including cadherins, selectins, integrins, and Thomsen–Friedenreich (TF) antigens, have been identified as mediators of cell-cell and cell-extracellular matrix adhesion (55). These play a pivotal role in recurrence, invasion, and distant metastasis (55). Homotypic aggregation and metastatic cell heterotypic adhesion to the microvascular endothelium are thought to be mediated through similar molecular mechanisms, specifically the interactions of tumor-associated TF glycoantigen with the beta-galactoside-binding protein, galectin-3 (56, 57). The homologous targeting ability of CCMCNPs was first evaluated using PLGA NPs coated with the plasma membrane of human MDA-MB-435 cancer cells (17). In these studies, CCMCNPs had a much higher affinity toward MDA-MB-435 cells compared to RBC-camouflaged NPs and bare PLGA cores. When a heterotypic human foreskin fibroblast cell line was used as a negative control, MDA-MB-435 CCMCNPs exhibited little increased uptake compared to bare PLGA cores, indicating that the homologous binding effect was specific to the MDA-MB-435 cell membrane coating.

Following these pioneering studies, several published reports have observed homologous binding of CCMCNPs derived from a variety of cancer cells, such as mouse breast cancer 4T1 cells (24, 25, 27, 28), MDA-MB-435 cells (26), human breast cancer MDA-MB-231 (15), and MCF-7 (16) cells, human squamous carcinoma UM-SCC-7 cells (33), and human hepatocellular carcinoma SMMC-7721 cells (22). CCMCNPs derived from these cancer cells demonstrated homologous specificity in preclinical cancer imaging or therapy studies.

We performed a study in which membranes derived from five breast cancer cell lines (MDA-MB-231, SUM-159, MCF-7, BT-474, and 4T1) were evaluated for homologous binding toward their source cell lines. Cancer cell membrane fractions (CCMFs) were first fluorescently labeled with fluorescein isothiocyanate (FITC). FITC-labeled CCMFs were characterized by measuring the absorbance at 494 nm by UV spectroscopy. 1×10^6 live cells were dispersed in 100 μL of FACS buffer, after which 5 μL of FITC-labeled CCMF solution ($A_{494} = 0.4$) was added and the mixture was incubated at 4°C for 30 min. After washing, flow cytometry measurements were conducted on a FACS Calibur (BD Bioscience); ten thousand events were collected for each measurement and analyzed by FlowJo software (BD Bioscience). In a separate study, live cells were incubated with FITC-labeled CCMFs at 37°C for 1 h. After washing, the live cells were imaged by fluorescence microscopy. As shown in **Figure 3A** and **Table 1**, although we did not see homologous binding of the CCMFs investigated, we found that BT474 CCMFs had a higher affinity for all five cell lines, suggesting that BT474 cell membranes showed promiscuous binding to these five cancer cell lines. MDA-MB-231 cells had the highest binding affinity for all the CCMFs. SUM-159 CCMFs and SUM-159 cells had the lowest binding affinity. Representative fluorescence images shown in **Figure 3B** confirm that MDA-MB-231 cells had the highest level of CCMF binding among the five cell lines that was consistent with the flow cytometry results. The fluorescent images confirm the low binding affinity of SUM-159 CCMFs and cells. These results support further investigating the use of NPs coated with BT474 cancer cell membranes to detect cancers and to deliver therapeutic cargo.

Other studies have reported an absence of homologous binding *in vivo*. In one such study, semiconducting polymer nanoparticles (SPN) were coated with the plasma membrane derived from 4T1 cells to form 4T1 CC-SPN (23). The core SPN absorbed near-infrared (NIR) light that was converted to NIR fluorescence and photoacoustic signals. In addition, SPN can be also used for photodynamic therapy (PDT) and photothermal therapy (PTT). Homologous targeting of 4T1 CC-SPN was evaluated in 4T1 tumors. Compared to naked SPN, 4T1 CC-SPN did not show significant enhancement of fluorescence or photoacoustic intensities in 4T1 tumors, indicating that the accumulation of 4T1 CC-SPN in 4T1 tumors was not significantly different from naked SPN. Following phototherapy, the 4T1 CC-SPN group did not show significant difference of tumor growth control in comparison to the naked SPN group.

Many of the homologous targeting studies used uncoated NPs for comparison. If the homologous targeting of CCMCNPs originates from cell surface adhesion molecules, studies with specific inhibitors with competitive binding to these adhesion molecules will provide further insights into the mechanisms underlying the homotypic and heterotypic effects.

Several studies have suggested that the CD47 cell surface antigen may suppress the uptake of CCMCNPs by macrophages (27). On the other hand, neoantigens encoded by tumor-specific mutated genes can help elicit tumor-specific immune responses (58). We investigated the pharmacokinetic profiles of CCMF-PLGA NPs and uncoated PLGA NPs in immunodeficient mice and found that CCMF-PLGA NPs had even significantly shorter circulation time in the bloodstream, indicating that the membrane antigens present

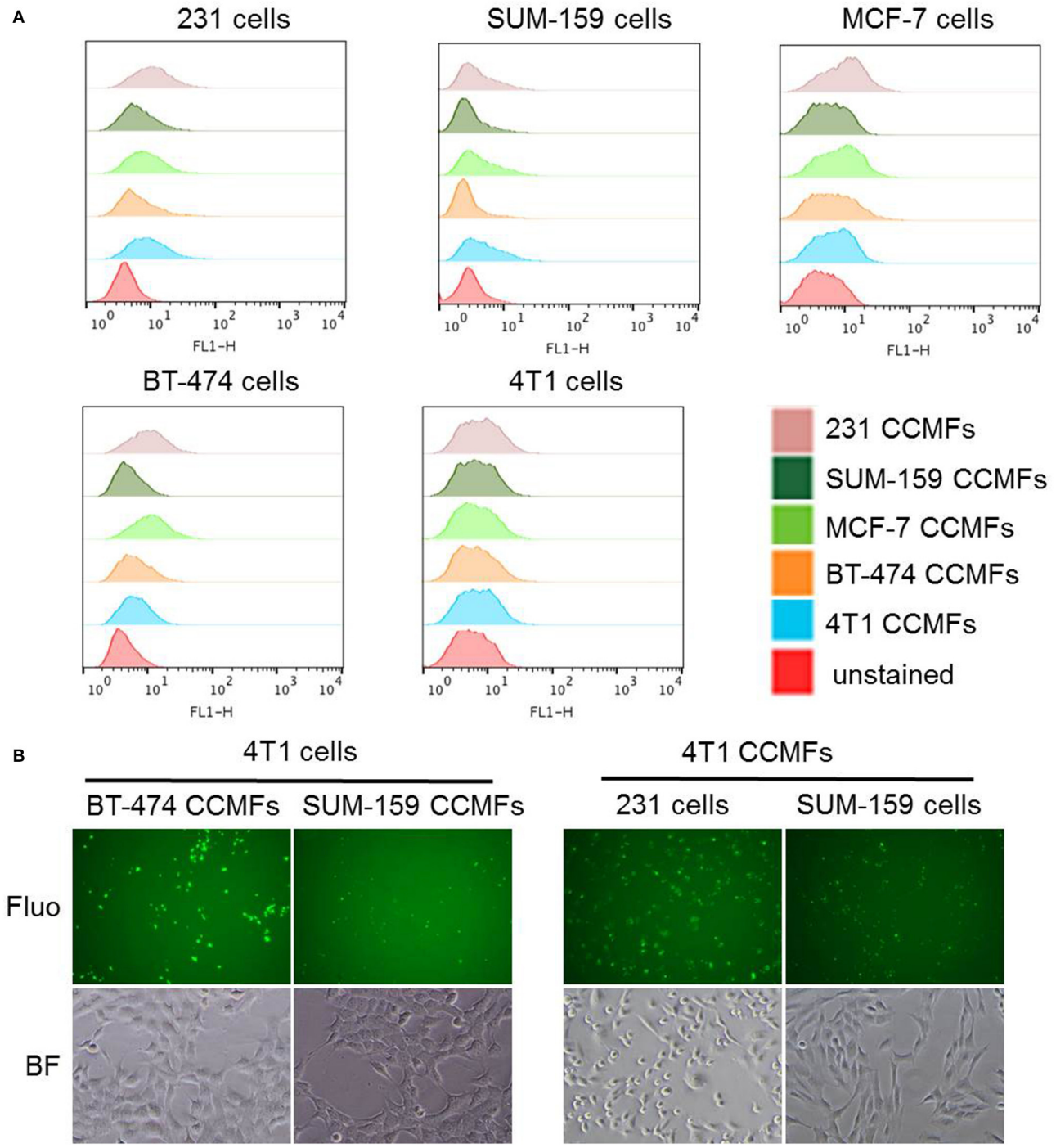

FIGURE 3 | Evaluation of homologous binding by flow cytometry and fluorescence imaging. **(A)** Flow cytometry profiles of five breast cancer cell lines, MDA-MB-231, SUM-159, MCF-7, BT-474, and 4T1 cells after CCMF-incubation. Live cells were individually stained with FITC-labeled CCMFs derived from these five cell lines at the same FITC concentration. **(B)** Representative fluorescence (Fluo) and bright field (BF) images of cancer cells after CCMF-incubation showing the high binding affinity of BT-474 CCMFs and MDA-MB-231 cells, compared to the low binding affinity of SUM-159 CCMFs and SUM-159 cells.

on CCMF-PLGA NPs may have accelerated clearance (19). These opposing effects require further investigation to clearly understand how CCMCNPs interface with mononuclear phagocytic system.

Disruption of Cancer Cell-Stromal Cell Interaction

Proteins present on the membranes of source cells are maintained on the surface of CCMCNPs. Some of these proteins play a

role in mediating cell-cell interaction. We therefore investigated the ability of CCMCNPs to misdirect cancer cell-stromal cell interaction (19). We found that the presence of CCMFs or CCMCNPs reduced the migration of cancer cells toward human mammary fibroblasts (HMFs) by ∼30%. Core PLGA NPs alone did not induce any inhibition of cancer cell migration. We established an experimental metastasis model by intravenously injecting MDA-MD-231 cells constitutively expressing luciferase (231-luc) into nude mice. We observed a significant reduction of metastasis in the group of mice injected with 231-luc cells pre-incubated with CCMCNPs. Our data collectively showed that CCMCNPs actively reduced the ability of fibroblasts to attract cancer cells, and confirmed the ability of CCMCNPs to significantly reduce metastasis. Fibroblasts have been observed to track to the premetastatic niche prior to the arrival of cancer cells. Therefore, NPs that disrupt the ability of fibroblasts to attract cancer cells may disrupt the metastatic cascade and the formation of metastasis. However, we have not as yet identified the specific membrane antigens responsible for the reduction of migration.

TABLE 1 | Flow cytometry analysis of mean fluorescence intensity (MFI) obtained following incubation of different CCMFs with different cancer cells.

CCMFs / cells	MDA-MB-231	SUM-159[c]	MCF-7	BT-474[a]	4T1
MDA-MB-231[b]	14.1	8.8	17.3	32.8	13.5
SUM-159[c]	6.4	4.2	7.3	7.8	7.8
MCF-7	14.2	7.1	12.0	22.3	10.7
BT-474	12.8	5.9	14.6	14.0	8.7
4T1	12.1	10.8	13.1	25.0	10.4

Values are obtained from two separate sets of experiments.
[a]BT474 CCMFs had a higher binding affinity than other CCMFs across the five cell lines as outlined by a vertical box.
[b]From the five cell lines, MDA-MB-231 cells had the highest binding affinity as outlined by a horizontal box.
[c]SUM-159 CCMFs and SUM-159 cells had the lowest binding affinity.

CANCER THERANOSTIC APPLICATIONS OF CCMCNPs

Since the NP cores are synthetic materials, these can be adapted for use as theranostic materials to serve as vehicles that carry imaging and therapeutic moieties. We have summarized the reported examples of CCMCNPs for cancer theranostics in **Table 2**.

Preclinical Cancer Imaging

Cloaking cancer cell membranes onto upconversion nanoparticles (UCNPs) to obtain CC-UCNPs have been reported (26). Four cancer cell lines including human melanoma, prostate, squamous cell, and colorectal cells were selected to synthesize the corresponding CC-UCNPs. The homologous binding of CC-UCNPs was investigated *in vitro* by flow cytometry and confocal microscopy. Significant binding was observed when the cell membrane of the CC-UCNPs matched the cancer cell type. Mismatch between the donor and host cells led to almost no targeting. By virtue of the UCNP core's ability to convert NIR radiation to visible light, CC-UCNPs possessed the ability for *in vivo* tumor imaging. Mice injected with CC-UCNPs derived from MDA-MB-435 cells exhibited the highest upconversion luminescence in MDA-MB-435 tumor xenografts, as well as much higher tumor accumulation than the CC-UCNPs from other cell lines. These homologous targeting abilities together with the NIR fluorescence of UCNPs indicate the potential use of CC-UCNPs for tumor specific *in vivo* imaging.

In another study, a brain metastatic breast cancer cell (MDA-MB-831) membrane-coated polymeric nanoparticle (mPEG-PLGA) platform was constructed (21). NIR dye IR780 was loaded into the mPEG-PLGA polymeric NPs for imaging. *In vivo* and *ex vivo* NIR imaging in mice showed

TABLE 2 | Summary of CCMCNPs and their components used for cancer theranostics.

Cancer cell line	Core	Size (nm)	Imaging/therapeutics	Applications	References
MDA-MB-435	UCNPs	100	UCNPs	NIR imaging	(26)
MDA-MB-831	mPEG-PLGA	70	IR780	NIR imaging	(21)
MCF-7	PLGA	200	ICG	NIR/PA imaging and PTT	(16)
SMCC-7721	SPIO	192	Ce6	MR/NIR imaging and PDT	(22)
4T1	PCN-224	228	GOx and catalase	Cancer starvation and PDT	(25)
4T1	PCN-224	154	TPZ	Bioreductive therapy and PDT	(24)
4T1	F68 copolymer	175	PTX	Drug delivery	(27)
UM-SCC-7	MNPs	103	DOX	Drug delivery	(33)
4T1	Gold nanocages	70	DOX	Drug delivery and PTT	(28)
B16-F10 & RBC	Copper sulfide	200	DOX	Drug delivery and PTT	(29)
MDA-MB-231	Porous Silicon	405	N/A	Cancer nanovaccines	(18)
B16-F10	PLGA	110	CpG	Cancer nanovaccines	(20)
B16-F10	PLGA	160	R837 and mannose	Cancer nanovaccines	(31)

UCNPs, upcoversion nanoparticles; NIR, near infrared; PLGA, poly(lactic-co-glycolic acid); SPIO, superparamagnetic iron oxide; MR, magnetic resonance; PA, photoacoustic; PDT, photodynamic therapy; PTT, photothermal therapy; MNPs, magnetic nanoparticles; PTX, paclitaxel; DOX, doxorubicin; GOx, glucose oxidase; PCN, porous coordination network, TPZ, tirapazamine.

extended circulation and retention of MDA-MB-831 CCMCNPs compared to uncoated mPEG-PLGA nanoparticles. These data demonstrated the ability of dye-loaded CCMCNPs to cross the blood-brain barrier (BBB) for imaging of metastatic breast cancers to the brain. These two examples represent applications of CCMCNPs for NIR tumor imaging, where the NIR light is able to penetrate deeper into the tissue than visible light. Although the penetration of NIR light makes superficial tumor imaging possible, it cannot be applied to deep-seated tissues. Magnetic nanoparticles are an alternative option as they allow detection of deep-seated tissues with MRI, and pave the way for translational applications. To be clinically translatable, cancer cell membranes can also be labeled with radiotracers for detection *in vivo* by PET/SPECT imaging.

Phototheranostics

A cancer cell membrane–cloaked NP as a phototheranostic nanoplatform has been previously reported (16). The NP core consisted of PLGA containing indocyanine green (ICG) that has excellent fluorescence/photoacoustic (FL/PA) properties for FL/PA dual-modal imaging and PTT effects for eradicating tumors using NIR light. The membranes of human breast cancer MCF-7 cells were used for coating. MCF-7 CCMCNPs not only demonstrated homologous targeting *in vitro* but also demonstrated specific targeting with *in vivo* MCF-7 tumors with high spatial resolution and good penetration. Due to the PTT effect, MCF-7 tumors were ablated with a single dose of MCF-7 CCMCNPs combined with laser treatment.

In another study, a cancer cell membrane coated magnetic NP platform for MR/NIR fluorescence dual-modal imaging and PDT of cancer was described (22), where the core consisted of styrene (St) and acrylic acid (AA)-crosslinked superparamagnetic iron oxide nanoparticles (SPION), loaded with a clinically used photosensitizer Ce6. The nanobead core was coated with the membranes from human hepatocellular carcinoma SMMC-7721 cells. Compared to nanobeads without coating, SMMC-7721 CCMCNPs demonstrated higher tumor accumulation as observed by MR/NIR fluorescence imaging, and enhanced PDT effects in SMMC-7721 tumor-bearing mice.

In two recent studies, cancer cell membrane camouflaged cascade bioreactors (designated as mCGP) were used for a synergistic combination of starvation and PDT (24, 25). The core consisted of porphyrin MOF loaded with glucose oxidase (GOx) and catalase. PCN (porous coordination network)-224 acted as a photosensitizer and also had photoluminescence suitable for NIR imaging. Coating the surface with 4T1 cancer cell membranes provided mCGP with biocompatibility, immune system-evasion and homotypic targeting. Once internalized by cancer cells, mCGP promoted microenvironmental oxygenation by catalyzing the endogenous H_2O_2 to produce O_2 that subsequently accelerate the decomposition of intracellular glucose and enhanced the production of cytotoxic singlet oxygen under light irradiation. This cancer targeted cascade bioreactor mCGP efficiently inhibited cancer growth after administration of a single dose.

As highlighted in the examples presented here, the integration of imaging with phototherapy enabled real-time *in vivo* monitoring of the distribution of CCMCNPs to identify the ideal time to trigger treatment for an optimal therapeutic effect.

Chemotherapy Drug Delivery

CCMCNPs can be effective drug delivery nanocarriers when the NP cores are loaded with chemotherapy payloads as demonstrated in published studies. In one study, a cancer cell biomimetic nano drug delivery system (NDDS) was developed for targeted chemotherapy of metastatic cancer (27). The NDDS was constructed from two distinct components. The NP coat derived from the membranes of 4T1 mammary breast cancer cells formed one component. The second component consisted of the paclitaxel (PTX)-loaded polymeric NP core prepared from poly(caprolactone) (PCL) and pluronic copolymer F68. The preservation of several membrane proteins associated with cell adhesion and recognition was confirmed. Among these were TF-antigen and E-cadherin, CD44 and CD326, and CD47. The 4T1 CCMCNPs could selectively enable high accumulation of PTX in primary tumors and metastatic pulmonary tissues as demonstrated in 4T1 orthotopic mammary tumors and experimental metastasis. The membrane proteins present on CCMCNPs were postulated to result in homotypic binding of CCMCNPs and in the reduction of internalization by macrophages. In addition, 4T1 CCMCNPs significantly inhibited the growth of primary and metastatic tumors.

Besides polymeric NP cores, several inorganic NPs have been used to encapsulate chemotherapy drugs. Examples are magnetic nanoparticles (33), gold nanocages (28), and CuS (29). As an example, a magnetic iron oxide based nanoplatform that was coated with cancer cell membranes from different cancer cells, such as UM-SCC-7, COS7, and HeLa cells was recently described (33). Clinically used doxorubicin hydrochloride (DOX·HCl) was incorporated as the model drug that electrostatically bound to the negatively charged Fe_3O_4 magnetic NPs. These CCMCNPs exhibited excellent "homing" ability to the homologous tumor *in vivo* even in the presence of a second heterologous tumor. Due to the targeted accumulation of DOX in UM-SCC-7 tumors, UM-SCC-7 CCMCNPs resulted in significant tumor growth control. The magnetic property of the NP core also allowed the use of a magnetic field to guide CCMCNPs toward the site of interest to increase accumulation. In another study, a biomimetic drug delivery system consisting of DOX-loaded gold nanocages as the inner core and 4T1 cancer cell membranes as the outer shell was used for homologous targeting to 4T1 tumors, with the gold nanocages providing both PTT effects and hyperthermia-triggered DOX release under NIR laser irradiation (28). The combination of chemo and PTT therapy achieved about 98% growth reduction of primary and metastatic 4T1 tumors. Hollow CuS NPs have also been used to load DOX (29). Similar to the gold nanocages, DOX-loaded CuS NPs provided PTT effects and NIR light-triggered DOX release. Instead of using cancer cell membrane alone, in these studies membranes derived from RBCs and melanoma cells (B16-F10 cells) were fused to create hybrid biomimetic membranes (RBC-B16) that were coated onto DOX-loaded CuS NPs to construct DCuS@[RBC-B16] NPs. The hybrid membrane coating provided functional advantages of homologous targeting from the B16-F10 cell membranes and prolonged circulation time from the RBC membranes. Compared to the bare CuS NPs, the DCuS@[RBC-B16] NPs exhibited specific self-recognition to the source cell line *in vitro* and achieved prolonged circulation

lifetime and enhanced homogeneous targeting abilities. The DOX-loaded [RBC-B16]-coated CuS NP platform exhibited synergistic PTT and chemotherapy to achieve significant tumor growth inhibition.

Cancer Nanovaccines

Because cancer cell membranes carry a repertoire of membrane proteins from their source cancer cells, CCMCNPs have been actively investigated as cancer nanovaccines to induce cancer-specific immune responses. Subunit vaccines, such as molecular adjuvants and cancer-associated antigens or cancer-specific neoantigens, have been demonstrated to elicit potent antitumor immunity (59). However, subunit vaccines have shown limited clinical benefit in cancer therapy, due in part to inefficient vaccine delivery. Nanovaccines possess several favorable characteristics for effective cancer immunotherapy, such as efficient co-delivery of antigens and adjuvants into lymphoid organs, controllable intracellular vaccine delivery and release, and antigen cross-presentation in antigen presenting cells (APCs). The earliest example of using CCMCNPs to induce anti-tumor immunity *in vivo* was reported by Kroll et al. (20). The anticancer nanovaccine contained a PLGA polymeric core loaded with CpG oligodeoxynucleotide 1826 (CpG), a nucleic acid-based immunological adjuvant, and a cancer cell membrane shell derived from B16-F10 mouse melanoma cells. The nanovaccine resulted in a potent antitumor immune response *in vivo* and exhibited substantial therapeutic effects when combined with additional immunotherapies such as immune checkpoint blockades.

In a similar study (31), with a nanovaccine containing a PLGA core and a B16-F10 cell membrane shell, the toll-like receptor 7 agonist imiquimod (R837) was used as an adjuvant instead of CpG. Additionally the surface was modified with mannose as an APC-recognition moiety. This modified nanovaccine demonstrated both prophylactic and therapeutic efficacy *in vivo,* and enhanced therapeutic effects when combined with anti-PD-1 immune checkpoint blockade therapy.

We performed a proof-of-principle study investigating the immune response induced by CCMCNPs (19). We used human glioblastoma cells (U87MG) and human breast cancer cells (MDA-MB-231 and BT-474) for the derivation of cell membranes. We observed the localization of CCMCNPs in proximal draining lymph nodes with NIR fluorescence imaging. Following immunization of Balb/c mice, we detected a higher percentage of $CD8^+$ and $CD4^+$ cytotoxic T-lymphocyte populations in spleens and lymph nodes of CCMCNPs-immunized mice. Since U87-CXCR4 cells are of human origin and the CCMCNPs were injected into immunocompetent mice, our study did not demonstrate a cancer-cell specific immune response, but identified the possibility of using such formulations together with immunogenic adjuvants in combination with checkpoint inhibitors for cancer treatment.

CCMCNPs-based nanovaccines provide several advantages for cancer immunotherapy. Although many intracellular housekeeping proteins are removed that can dilute the immune responses, the membrane-bound tumor antigens are retained creating the possibility of synthesizing personalized vaccines. Tumor antigens from CCMCNPs are multi-epitope and endogenously autologous that can potentially be derived from a patient's own tumor following surgical resection or biopsy. The core-shell structure of CCMCNPs allows the delivery of tumor antigens and adjuvant concurrently to maximize effective antigen presentation and activation of downstream immune processes (20).

However, such bioinspired nanovaccine platforms are still in their infancy. The prophylactic and therapeutic effects generated from CCMCNPs have to be optimized. Cancer cell membranes also contain housekeeping proteins that can result in immune response dilution. In addition, the antigens located in the cell membranes can be degraded or inactivated in the complex physiological environments of the host body. Finally, the potential adverse effects of immunomodulatory cocktails have to be considered.

CONCLUDING REMARKS AND FUTURE PERSPECTIVES

Homologous targeting to deliver imaging and therapeutic agents, disruption of cancer cell-stromal cell interactions, and induction of an immune response are the major cancer applications that are emerging with this class of NPs. Overall, this novel biomimetic nanoplatform allows the incorporation of personalized cancer receptors and antigens, which can, in the future, be derived from a patient's own tumor. Furthermore, the NP cores can be loaded with a variety of different cargoes, for precision medicine. The challenges that need to be addressed to enable translation to applications in humans are reproducible synthesis under good medical practice conditions that can be scaled up, and understanding the mechanisms underlying homologous targeting.

Current synthesis involves multiple manual steps that can introduce process variability. Some important characteristics, such as purity, integrity, and sidedness, in particular, need to be further investigated and elucidated. There are very few studies reporting the yield, loading capacity, or efficacy of CCMCNPs. Successfully addressing these challenges will allow the incorporation of this novel class of NPs for cancer theranostics to achieve personalized precision medicine.

AUTHOR CONTRIBUTIONS

JJ wrote the manuscript and performed the experiments. ZB wrote and edited the manuscript.

FUNDING

Support from NIH R35 CA209960, R01 CA82337, P41 EB024495, P30 CA006973, and a grant from the Emerson Collective Cancer Research Fund is gratefully acknowledged.

ACKNOWLEDGMENTS

We thank Dr. K. M. Horton for her support.

REFERENCES

1. Meyer RA, Sunshine JC, Green JJ. Biomimetic particles as therapeutics. *Trends Biotechnol.* (2015) 33:514–24. doi: 10.1016/j.tibtech.2015.07.001
2. Kroll AV, Fang RH, Zhang L. Biointerfacing and applications of cell membrane-coated nanoparticles. *Bioconjug Chem.* (2017) 28:23–32. doi: 10.1021/acs.bioconjchem.6b00569
3. Hu CM, Zhang L, Aryal S, Cheung C, Fang RH. Erythrocyte membrane-camouflaged polymeric nanoparticles as a biomimetic delivery platform. *Proc Natl Acad Sci USA.* (2011) 108:10980–5. doi: 10.1073/pnas.1106634108
4. Hu CM, Fang RH, Wang KC, Luk BT, Thamphiwatana S, Dehaini D, et al. Nanoparticle biointerfacing by platelet membrane cloaking. *Nature.* (2015) 526:118–21. doi: 10.1038/nature15373
5. Hu Q, Sun W, Qian C, Wang C, Bomba HN, Gu Z. Anticancer platelet-mimicking nanovehicles. *Adv Mater.* (2015) 27:7043–50. doi: 10.1002/adma.201503323
6. Hu Q, Qian C, Sun W, Wang J, Chen Z, Bomba HN, et al. Engineered nanoplatelets for enhanced treatment of multiple myeloma and thrombus. *Adv Mater.* (2016) 28:9573–80. doi: 10.1002/adma.201603463
7. Wei X, Gao J, Fang RH, Luk BT, Kroll AV, Dehaini D, et al. Nanoparticles camouflaged in platelet membrane coating as an antibody decoy for the treatment of immune thrombocytopenia. *Biomaterials.* (2016) 111:116–23. doi: 10.1016/j.biomaterials.2016.10.003
8. Dehaini D, Wei X, Fang RH, Masson S, Angsantikul P, Luk BT, et al. Erythrocyte-platelet hybrid membrane coating for enhanced nanoparticle functionalization. *Adv Mater.* (2017) 29:1606209. doi: 10.1002/adma.201606209
9. Xuan M, Shao J, Dai L, He Q, Li J. Macrophage cell membrane camouflaged mesoporous silica nanocapsules for in vivo cancer therapy. *Adv Healthc Mater.* (2015) 4:1645–52. doi: 10.1002/adhm.201500129
10. Xuan M, Shao J, Dai L, Li J, He Q. Macrophage cell membrane camouflaged au nanoshells for in vivo prolonged circulation life and enhanced cancer photothermal therapy. *ACS Appl Mater Interfaces.* (2016) 8:9610–8. doi: 10.1021/acsami.6b00853
11. Krishnamurthy S, Gnanasammandhan MK, Xie C, Huang K, Cui MY, Chan JM. Monocyte cell membrane-derived nanoghosts for targeted cancer therapy. *Nanoscale.* (2016) 8:6981–5. doi: 10.1039/C5NR07588B
12. Cao H, Dan Z, He X, Zhang Z, Yu H, Yin Q, et al. Liposomes coated with isolated macrophage membrane can target lung metastasis of breast cancer. *ACS Nano.* (2016) 10:7738–48. doi: 10.1021/acsnano.6b03148
13. Kang T, Zhu Q, Wei D, Feng J, Yao J, Jiang T, et al. Nanoparticles coated with neutrophil membranes can effectively treat cancer metastasis. *ACS Nano.* (2017) 11:1397–411. doi: 10.1021/acsnano.6b06477
14. Chen W, Zhang Q, Luk BT, Fang RH, Liu Y, Gao W, et al. Coating nanofiber scaffolds with beta cell membrane to promote cell proliferation and function. *Nanoscale.* (2016) 8:10364–70. doi: 10.1039/C6NR00535G
15. Chen M, Chen M, He J. Cancer cell membrane cloaking nanoparticles for targeted co-delivery of doxorubicin and PD-L1 siRNA. *Artif Cells Nanomed Biotechnol.* (2019) 47:1635–41. doi: 10.1080/21691401.2019.1608219
16. Chen Z, Zhao P, Luo Z, Zheng M, Tian H, Gong P, et al. Cancer cell membrane–biomimetic nanoparticles for homologous-targeting dual-modal imaging and photothermal therapy. *ACS Nano.* (2016) 10:10049–57. doi: 10.1021/acsnano.6b04695
17. Fang RH, Hu CM, Luk BT, Gao W, Copp JA, Tai Y, et al. Cancer cell membrane-coated nanoparticles for anticancer vaccination and drug delivery. *Nano Lett.* (2014) 14:2181–8. doi: 10.1021/nl500618u
18. Fontana F, Shahbazi M-A, Liu D, Zhang H, Mäkilä E, Salonen J, et al. Multistaged nanovaccines based on porous Silicon@Acetalated Dextran@Cancer cell membrane for cancer immunotherapy. *Adv Mater.* (2017) 29:1603239. doi: 10.1002/adma.201603239
19. Jin J, Krishnamachary B, Barnett JD, Chatterjee S, Chang D, Mironchik Y, et al. Human cancer cell membrane-coated biomimetic nanoparticles reduce fibroblast-mediated invasion and metastasis and induce T-cells. *ACS Appl Mater Interf.* (2019) 11:7850–61. doi: 10.1021/acsami.8b22309
20. Kroll AV, Fang RH, Jiang Y, Zhou J, Wei X, Yu CL, et al. Nanoparticulate delivery of cancer cell membrane elicits multiantigenic antitumor immunity. *Adv Mater.* (2017) 29:1703969. doi: 10.1002/adma.201703969
21. Kumar P, Treuren TV, Ranjan AP, Chaudhary P, Vishwanatha JK. *In vivo* imaging and biodistribution of near infrared dye loaded brain-metastatic-breast-cancer-cell-membrane coated polymeric nanoparticles. *Nanotechnology.* (2019) 30:1361–6528. doi: 10.1088/1361-6528/ab0f46
22. Li J, Wang X, Zheng D, Lin X, Wei Z, Zhang D, et al. Cancer cell membrane-coated magnetic nanoparticles for MR/NIR fluorescence dual-modal imaging and photodynamic therapy. *Biomater Sci.* (2018) 6:1834–45. doi: 10.1039/C8BM00343B
23. Li J, Zhen X, Lyu Y, Jiang Y, Huang J, Pu K. Cell membrane coated semiconducting polymer nanoparticles for enhanced multimodal cancer phototheranostics. *ACS Nano.* (2018) 12:8520–30. doi: 10.1021/acsnano.8b04066
24. Li S-Y, Cheng H, Qiu W-X, Zhang L, Wan S-S, Zeng J-Y, et al. Cancer cell membrane-coated biomimetic platform for tumor targeted photodynamic therapy and hypoxia-amplified bioreductive therapy. *Biomaterials.* (2017) 142:149–61. doi: 10.1016/j.biomaterials.2017.07.026
25. Li S-Y, Cheng H, Xie B-R, Qiu W-X, Zeng J-Y, Li C-X, et al. Cancer cell membrane camouflaged cascade bioreactor for cancer targeted starvation and photodynamic therapy. *ACS Nano.* (2017) 11:7006–18. doi: 10.1021/acsnano.7b02533
26. Rao L, Bu L-L, Cai B, Xu J-H, Li A, Zhang W-F, et al. Cancer cell membrane-coated upconversion nanoprobes for highly specific tumor imaging. *Adv Mater.* (2016) 28:3460–6. doi: 10.1002/adma.201506086
27. Sun H, Su J, Meng Q, Yin Q, Chen L, Gu W, et al. Cancer-cell-biomimetic nanoparticles for targeted therapy of homotypic tumors. *Adv Mater.* (2016) 28:9581–8. doi: 10.1002/adma.201602173
28. Sun H, Su J, Meng Q, Yin Q, Chen L, Gu W, et al. Cancer cell membrane-coated gold nanocages with hyperthermia-triggered drug release and homotypic target inhibit growth and metastasis of breast cancer. *Adv Funct Mater.* (2017) 27:1604300. doi: 10.1002/adfm.201604300
29. Wang D, Dong H, Li M, Cao Y, Yang F, Zhang K, et al. Erythrocyte–cancer hybrid membrane camouflaged hollow copper sulfide nanoparticles for prolonged circulation life and homotypic-targeting photothermal/chemotherapy of melanoma. *ACS Nano.* (2018) 12:5241–52. doi: 10.1021/acsnano.7b08355
30. Yang J, Teng Y, Fu Y, Zhang C. Chlorins e6 loaded silica nanoparticles coated with gastric cancer cell membrane for tumor specific photodynamic therapy of gastric cancer. *Int J Nanomed.* (2019) 14:5061–71. doi: 10.2147/IJN.S202910
31. Yang R, Xu J, Xu L, Sun X, Chen Q, Zhao Y, et al. Cancer cell membrane-coated adjuvant nanoparticles with mannose modification for effective anticancer vaccination. *ACS Nano.* (2018) 12:5121–9. doi: 10.1021/acsnano.7b09041
32. Zhang J, Miao Y, Ni W, Xiao H, Zhang J. Cancer cell membrane coated silica nanoparticles loaded with ICG for tumour specific photothermal therapy of osteosarcoma. *Artif Cells Nanomed Biotechnol.* (2019) 47:2298–305. doi: 10.1080/21691401.2019.1622554
33. Zhu JY, Zheng DW, Zhang MK, Yu WY, Qiu WX, Hu JJ, et al. Preferential cancer cell self-recognition and tumor self-targeting by coating nanoparticles with homotypic cancer cell membranes. *Nano Lett.* (2016) 16:5895–901. doi: 10.1021/acs.nanolett.6b02786
34. Angsantikul P, Fang RH, Zhang L. Toxoid vaccination against bacterial infection using cell membrane-coated nanoparticles. *Bioconjug Chem.* (2018) 29:604–12. doi: 10.1021/acs.bioconjchem.7b00692
35. Angsantikul P, Thamphiwatana S, Gao W, Zhang L. Cell membrane-coated nanoparticles as an emerging antibacterial vaccine platform. *Vaccines.* (2015) 3:814–28. doi: 10.3390/vaccines3040814
36. Bose RJ, Lee SH, Park H. Biofunctionalized nanoparticles: an emerging drug delivery platform for various disease treatments. *Drug Discov Today.* (2016) 21:1303–12. doi: 10.1016/j.drudis.2016.06.005
37. Bose RJ, Paulmurugan R, Moon J, Lee SH, Park H. Cell membrane-coated nanocarriers: the emerging targeted delivery system for cancer theranostics. *Drug Discov Today.* (2018) 23:891–9. doi: 10.1016/j.drudis.2018.02.001
38. Gao W, Zhang L. Coating nanoparticles with cell membranes for targeted drug delivery. *J Drug Target.* (2015) 23:619–26. doi: 10.3109/1061186X.2015.1052074
39. Hu C-MJ, Fang RH, Zhang L. Erythrocyte-inspired delivery systems. *Adv Healthcare Mater.* (2012) 1:537–47. doi: 10.1002/adhm.201200138

40. Li R, He Y, Zhang S, Qin J, Wang J. Cell membrane-based nanoparticles: a new biomimetic platform for tumor diagnosis and treatment. *Acta Pharmaceut Sinica B*. (2018) 8:14–22. doi: 10.1016/j.apsb.2017.11.009
41. Luk BT, Zhang L. Cell membrane-camouflaged nanoparticles for drug delivery. *J Control Release*. (2015) 220(Pt B):600–7. doi: 10.1016/j.jconrel.2015.07.019
42. Narain A, Asawa S, Chhabria V, Patil-Sen Y. Cell membrane coated nanoparticles: next-generation therapeutics. *Nanomedicine*. (2017) 12:2677–92. doi: 10.2217/nnm-2017-0225
43. Vijayan V, Uthaman S, Park IK. Cell membrane-camouflaged nanoparticles: a promising biomimetic strategy for cancer theragnostics. *Polymers*. (2018) 10:983. doi: 10.3390/polym10090983
44. Wu M, Le W, Mei T, Wang Y, Chen B, Liu Z, et al. Cell membrane camouflaged nanoparticles: a new biomimetic platform for cancer photothermal therapy. *Int J Nanomed*. (2019) 14:4431–48. doi: 10.2147/IJN.S200284
45. Zhai Y, Su J, Ran W, Zhang P, Yin Q, Zhang Z, et al. Preparation and application of cell membrane-camouflaged nanoparticles for cancer therapy. *Theranostics*. (2017) 7:2575–92. doi: 10.7150/thno.20118
46. Zhen X, Cheng P, Pu K. Recent advances in cell membrane-camouflaged nanoparticles for cancer phototherapy. *Small*. (2019) 15:20. doi: 10.1002/smll.201804105
47. Danhier F, Ansorena E, Silva JM, Coco R, Le Breton A, Preat V. PLGA-based nanoparticles: an overview of biomedical applications. *J Control Release*. (2012) 161:505–22. doi: 10.1016/j.jconrel.2012.01.043
48. Suski JM, Lebiedzinska M, Wojtala A, Duszynski J, Giorgi C, Pinton P, et al. Isolation of plasma membrane-associated membranes from rat liver. *Nat Protoc*. (2014) 9:312–22. doi: 10.1038/nprot.2014.016
49. Wieckowski MR, Giorgi C, Lebiedzinska M, Duszynski J, Pinton P. Isolation of mitochondria-associated membranes and mitochondria from animal tissues and cells. *Nat Protoc*. (2009) 4:1582–90. doi: 10.1038/nprot.2009.151
50. Rao L, Cai B, Bu LL, Liao QQ, Guo SS, Zhao XZ, et al. Microfluidic electroporation-facilitated synthesis of erythrocyte membrane-coated magnetic nanoparticles for enhanced imaging-guided cancer therapy. *ACS Nano*. (2017) 13:3496–505. doi: 10.1021/acsnano.7b00133
51. Molinaro R, Corbo C, Martinez JO, Taraballi F, Evangelopoulos M, Minardi S, et al. Biomimetic proteolipid vesicles for targeting inflamed tissues. *Nat Mater*. (2016) 15:1037–46. doi: 10.1038/nmat4644
52. Mohammadi MR, Corbo C, Molinaro R, Lakey JRT. Biohybrid nanoparticles to negotiate with biological barriers. *Small*. (2019) 15:1902333. doi: 10.1002/smll.201902333
53. Molinaro R, Evangelopoulos M, Hoffman JR, Corbo C, Taraballi F, Martinez JO, et al. Design and development of biomimetic nanovesicles using a microfluidic approach. *Adv Mater*. (2018) 30:7. doi: 10.1002/adma.201702749
54. Hu C-MJ, Fang RH, Luk BT, Chen KNH, Carpenter C, Gao W, et al. 'Marker-of-self' functionalization of nanoscale particles through a top-down cellular membrane coating approach. *Nanoscale*. (2013) 5:2664–8. doi: 10.1039/c3nr00015j
55. Okegawa T, Pong RC, Li Y, Hsieh JT. The role of cell adhesion molecule in cancer progression and its application in cancer therapy. *Acta Biochim Pol*. (2004) 51:445–57. doi: 10.18388/abp.2004_3583
56. Glinsky VV, Glinsky GV, Glinskii OV, Huxley VH, Turk JR, Mossine VV, et al. Intravascular metastatic cancer cell homotypic aggregation at the sites of primary attachment to the endothelium. *Cancer Res*. (2003) 63:3805–11.
57. Khaldoyanidi SK, Glinsky VV, Sikora L, Glinskii AB, Mossine VV, Quinn TP, et al. MDA-MB-435 human breast carcinoma cell homo- and heterotypic adhesion under flow conditions is mediated in part by Thomsen-Friedenreich antigen-galectin-3 interactions. *J Biol Chem*. (2003) 278:4127–34. doi: 10.1074/jbc.M209590200
58. Schumacher TN, Schreiber RD. Neoantigens in cancer immunotherapy. *Science*. (2015) 348:69–74. doi: 10.1126/science.aaa4971
59. Zhu G, Zhang F, Ni Q, Niu G, Chen X. Efficient nanovaccine delivery in cancer immunotherapy. *ACS Nano*. (2017) 11:2387–92. doi: 10.1021/acsnano.7b00978

Conflict of Interest: The authors declare that the research was conducted in the absence of any commercial or financial relationships that could be construed as a potential conflict of interest.

frontiers in Oncology

REVIEW
published: 21 January 2020
doi: 10.3389/fonc.2019.01537

Ovarian Cancer Targeted Theranostics

Sridhar Nimmagadda[1,2]* *and Marie-France Penet*[2,3]*

[1] *Division of Nuclear Medicine and Molecular Imaging, The Russell H. Morgan Department of Radiology and Radiological Science, The Johns Hopkins University School of Medicine, Baltimore, MD, United States,* [2] *Sidney Kimmel Comprehensive Cancer Center, The Johns Hopkins University School of Medicine, Baltimore, MD, United States,* [3] *Division of Cancer Imaging Research, The Russell H. Morgan Department of Radiology and Radiological Science, The Johns Hopkins University School of Medicine, Baltimore, MD, United States*

Ovarian cancer is a leading cause of death from gynecological malignancies. Although the prognosis is quite favorable if detected at an early stage, the vast majority of cases are diagnosed at an advanced stage, when 5-year survival rates are only 30–40%. Most recurrent ovarian tumors are resistant to traditional therapies underscoring the need for new therapeutic options. Theranostic agents, that combine diagnostic and therapeutic capabilities, are being explored to better detect, diagnose and treat ovarian cancer. To minimize morbidity, improve survival rates, and eventually cure patients, new strategies are needed for early detection and for delivering specifically anticancer therapies to tumor sites. In this review we will discuss various molecular imaging modalities and targets that can be used for imaging, therapeutic and theranostic agent development for improved diagnosis and treatment of ovarian cancer.

Keywords: ovarian cancer, diagnosis and therapy, molecular imaging, theranostic, targeted therapy

OPEN ACCESS

Edited by:
Tone Frost Bathen, Norwegian University of Science and Technology, Norway

Reviewed by:
Ingfrid Haldorsen, Haukeland University Hospital, Norway
Aslam Khan, University of Missouri, United States

***Correspondence:**
Sridhar Nimmagadda
snimmag1@jhmi.edu
Marie-France Penet
mpenet@mri.jhu.edu

Specialty section:
This article was submitted to Cancer Imaging and Image-directed Interventions, a section of the journal Frontiers in Oncology

Received: *04 October 2019*
Accepted: *19 December 2019*
Published: *21 January 2020*

Citation:
Nimmagadda S and Penet M-F (2020) Ovarian Cancer Targeted Theranostics. Front. Oncol. 9:1537. doi: 10.3389/fonc.2019.01537

INTRODUCTION

Ovarian cancer is the leading cause of death from gynecological malignancies and ranks fifth as a cause of cancer-related deaths among women. Nearly 14,240 deaths and 22,280 new cases of ovarian cancer are reported in the US every year (1). The majority of ovarian cancer related deaths, similar to other cancers, are due to metastatic disease. Nearly 90% of ovarian cancers are of epithelial origin and demonstrate various subtypes, serous, endometrioid, clear cell and mucinous, and have unique signature biomarkers for classification, some of which could be used for targeting. Vast majority (∼80%) of epithelial ovarian cancers are diagnosed at an advanced stage, with presentation of widely metastatic disease within the peritoneal cavity. The 5-year survival rate for extensive stage disease remains low at 30–40%, with limited therapeutic options.

Current first-line treatment of high-grade epithelial ovarian cancer involves a debulking surgery that is followed by combination chemotherapy consisting of carboplatin and paclitaxel. However, long-term results from those therapies have been disappointing (2). Cytoreductive surgery is used as therapeutic intervention, as well as for diagnosis and staging. The amount of residual disease following a debulking surgery is considered a prognostic factor of survival and the absence of macroscopic residual disease is associated with low recurrence. Overall survival of advanced stage ovarian cancer patients showed little improvement in the last 30 years despite progress made in surgery and therapy. New targeted strategies are urgently needed to minimize morbidity and mortality associated with ovarian cancer. Theranostic approaches that combine diagnostic imaging with therapy have been shown to improve patient survival in several difficult to treat advanced cancers, and could also be applied to ovarian cancer, a focus of this review (3–5).

Mainly due to the lack of effective biomarkers to detect an early stage disease, ovarian cancer is most frequently diagnosed at an advanced stage. In this review, we will focus on various molecular targets being used to develop imaging, therapeutic and theranostic agents. High and specific expression of a biologic target is paramount for cancer detection. Additionally, inter- and intra-tumoral target expression heterogeneity is one of the hallmarks of cancer and is poorly understood in the context of advanced stage disease. The theranostic concept relies on identifying appropriate molecular targets highly specific to the cancer cells and assessing their expression levels and distribution by imaging that can be subsequently used for guiding appropriate therapy. The effectiveness of the approach comes from using imaging to select the patient population who would most likely benefit from the therapeutic agent, thus minimizing any off target effects and toxicity. This process requires the development and optimization of ligands for use as imaging/contrast agents that bind to proteins overexpressed in ovarian cancers. Those molecularly-targeted imaging agents help determine the tumor location and heterogeneity in target expression. They also allow assessment of the dosage and timing of drug administration, and ultimately of tumor response to therapy. The imaging component can also act as a surrogate for the possible therapeutic agent that is likely to demonstrate similar chemical and *in vivo* pharmacokinetic properties. Imaging and therapeutic molecules that are chemically or biologically identical or agents that are not identical but have similar enough biodistribution can be used.

Currently, the most clinically used theranostic agents are primarily radiopharmaceuticals wherein a highly specific molecularly targeted and optimized ligand is used for chelating a radionuclide with imaging properties that can be readily swapped for a radionuclide with therapeutic properties (6). Radionuclide therapies also provide the benefits of bystander, crossfire and abscopal effects that could lead to sterilization of the tumor as a whole. With chemo- or targeted therapies only cells binding to the therapeutic agent are destroyed. In contrast, with therapeutic radionuclides, the emitted radiation particle path length is longer than several cell diameters, and cell death can be observed in multiple cells in the neighborhood of a cell with the accumulation of the targeted therapeutic radionuclide. Those effects provide an additional advantage to address the heterogeneity of the tumors over targeted therapies because cells and tissues not expressing the target and present in the particle path can still be impacted by the radiation. Bystander effects induced by radiation could also occur in cells that have not themselves been exposed to the radiation but have received a signal from a neighboring irradiated cell and behave as though it had been irradiated which leads to genomic instability and cell death (7, 8). Abscopal effect refers to an effect away from the target. It is an immune system rendered response to ionizing radiation by cancer cells that are located distant from the cancer cells with the accumulation of the therapeutic radionuclide or the irradiated site in the case of external beam radiotherapy (9). With the advent of immune checkpoint therapeutics that activate the immune system, therapies combining radionuclide therapy with immunotherapy have the potential to boost the abscopal response rates.

Other theranostic approaches being explored include the use of a single platform strategy such as near-infrared photoimmunotherapy (NIR-PIT) that incorporates therapeutic and diagnostic components in one entity (10). NIR-PIT is a target specific therapy involving an antibody conjugated to a photoabsorber that binds to target cells and causes cellular damage upon subsequent exposure to NIR light. The irradiation with NIR light at 690 nm causes cell membrane damage and necrotic cell death. The specificity of NIR-PIT comes from the specificity of the antibody, injected intravenously for tumor targeting, and the toxicity induced by the photosensitizer after exposure to NIR light (11). NIR-PIT induces phototoxic effects only when NIR irradiation and cell membrane binding are combined. Importantly, NIR-PIT does not require intracellular delivery of the therapeutic agent. The NIR emission of IR700 dye can also be used for non-invasive fluorescence detection to optimize the delivery of the theranostic irradiation.

Another strategy is targeted nanoparticle delivery to the ovarian tumors (12). Nanoparticles make it feasible to deliver multiple imaging and therapeutic components simultaneously to the cancer cells, and enable an on demand or environmentally responsive therapeutic release once a sufficient concentration of payload reaches the tumor.

We will discuss various imaging modalities and targets that could be used for imaging, therapeutic and theranostic agent development to diagnose and treat ovarian cancer, as listed in **Table 1**.

IMAGING TECHNIQUES USED FOR OVARIAN CANCER DETECTION AND DIAGNOSIS

Currently, women with a clinical suspicion of ovarian cancer are assessed with pelvic examination, transvaginal ultrasound (TVUS), and serum biomarkers. However, these techniques have significant limitations in the accuracy of detection and characterization of ovarian malignancy. Staging of ovarian cancer is usually done with histology and computed tomography (CT) to decide treatment and surgical procedures. Ultrasound (US) imaging is frequently used in the diagnosis of ovarian cancer (41, 42). The reported accuracies for distinguishing malignant from benign tumors by US is 65–94%, 35–88%, and 48–99% for gray-scale, color Doppler flow imaging, and Doppler arterial resistance measurements, respectively (43). In a meta analysis Kinkel et al. showed that sonographic techniques combining gray scale morphologic assessment with tumor vascularity imaging information are significantly better in characterizing ovarian lesions compared to individual measurements alone. The Q* point (and 95% CI) for combined techniques was 0.92 (0.87, 0.96) vs. 0.85 (0.83, 0.88), 0.82 (0.78, 0.86), and 0.73 (0.58, 0.87) for morphology, Doppler US and color Doppler flow imaging, respectively (43). Q* values correspond to the point on the summary receiver operating characteristic (ROC) curve where sensitivity and specificity were equal.

To further improve ovarian cancer detection by US, different non-targeted and targeted contrast agents have been

TABLE 1 | Molecules, modalities and applications of ovarian cancer targeted theranostics.

Molecular target	Imaging/Theranostic agent	Imaging method	Potential clinical application	References
CA125	^{89}Zr-DFO-mAb-B43.13	PET	Cancer detection	(13)
	^{99}Tcm-MAb-B43.13	SPECT	Cancer detection	(14)
	Nanobubbles	US	Cancer detection and drug delivery	(15)
Folate receptor	Mirvetuximab soravtansine (IMGN853)	PET	Cancer detection	(16–18)
	^{89}Zr-radiolabeled M9346A (parent mAb of IMGN853)	PET	Pre-screen cancer patients for IMGN853 treatment	(19, 20)
	Folate or folate analog (EC17) conjugated to FITC	Optical	Real-time surgical visualization of tumors for intraoperative staging and surgical resection	(21, 22)
	^{64}Cu-labeled pyropheophorbide-folate conjugate	PET and optical	Detection and intraoperative guidance of cancer resection	(23)
	SPION-CDF-FA-PAMAM	MR	Cancer detection and treatment	(24)
	PLGA-RbCur-gadolinium complex	MR	Combination therapies	(12)
	Microbubbles loaded with paclitaxel and oxygen	US and US targeted MB destruction	Anti-cancer drugs and/or oxygen delivery for combination therapy	(25)
Her2	^{89}Zr-trastuzumab	PET	Cancer detection	(26, 27)
	^{89}Zr-pertuzumab	PET	Cancer detection	(28–30)
	^{177}Lu or ^{212}Pb radiolabeled trastuzumab	Targeted radiotherapy	Cancer therapy	(31–33)
	IR700DX-trastuzumab	NIR-PIT	Cancer detection and treatment	(11)
	EC1-GLuc-liposome	bioluminescence	Cancer detection and treatment	(34)
NaPi2b (SLC34A2)	^{211}At MX35 F(ab')2	Targeted radiotherapy	Cancer therapy	(35)
EGFR	Cetuximab-benzoporphyrin derivate conjugate	NIR-PIT	Cancer detection and treatment	(36)
KDR	Microbubbles	US	Cancer detection	(37)
GSA	GSA-IR700	NIR-PIT	Cancer detection and treatment	(38)
β-galactosidase	HMRef-βGal SPiDER-βGal	Optical	Laparotomic and endoscopic detection of tumor and metastases	(39, 40)

developed and explored. Application of microbubbles (MB) as a contrast agent to improve the detection of early stage ovarian malignancies has been explored in preclinical (44), and clinical studies (45). Intravenous injection of non-targeted perflutren MB contrast agent was used to image 26 benign masses and 10 malignancies, to acquire the following parameters: presence of contrast enhancement, time to peak enhancement, peak contrast enhancement, half wash-out time, and area under the enhancement curve (AUC). The study showed that an AUC $>787\ s^{-1}$ was the most accurate diagnostic criterion for ovarian cancer with high sensitivity (100.0%) and specificity (96.2%). Other values that were found to be useful are the peak contrast enhancement >17.2 dB that showed 90.0% sensitivity and 98.3% specificity, and half wash-out time >41 s that 100.0% sensitivity and 92.3% specificity (45).

Optical imaging is being extensively used in preclinical settings and more recently in the clinic intraoperatively. Intraoperative fluorescence imaging could be applied to improve tumor staging and debulking in the course of cytoreductive surgery to improve prognosis. Multiple tumor-specific intraoperative fluorescence probes have been developed, and applied to ovarian cancer, both in preclinical (39), and clinical (21, 22) studies. Those clinical studies demonstrated the potential benefit of a systemically administered tumor-specific targeted fluorescent agent for intraoperative fluorescence imaging and in staging and debulking surgery for ovarian cancer.

Positron emission tomography (PET) imaging is highly sensitive and provides specific and quantitative information of a disease process given a molecularly targeted imaging agent is available. The most conspicuous radiotracer ^{18}F-Fluorodeoxyglucose reports on upregulated glucose metabolism in tumors and is routinely used in the management of ovarian cancer for diagnosis, staging, and for monitoring tumor response to chemotherapy (46).

Due to cost and availability limitations, Magnetic resonance imaging (MRI) is not frequently used for ovarian cancer diagnosis. MRI and magnetic resonance spectroscopy (MRS) have been applied to describe the feasibility of effective cancer imaging to assess complex ovarian masses indeterminate on either palpation or ultrasonography. MRI diagnostic criteria of ovarian malignancies are usually based on morphology, thick septum, vegetations, ascites, lymphadenopathy, and contrast characteristics. MRI can also be used for functional and metabolic imaging *via* dynamic contrast enhanced (DCE)-MRI, diffusion weighted imaging (DWI) and MRS, in addition to gaining the anatomic information. DCE-MRI is used to characterize ovarian cancer noninvasively (47), and to distinguish benign from malignant lesions on the basis of differences in contrast agent distribution and uptake that are manifested by neoangiogenesis induced microcirculation (48). Carter et al., showed that quantitative parameters from DCE-MRI and T_2 mapping could be used to differentiate benign ($n = 22$) from malignant ($n = 12$) ovarian masses (49). MRS has been proved useful in diagnosis, grading and treatment planning of brain and prostate cancer. However, studies using MRS for female pelvic lesions are limited, due to technical issues that arise from susceptibility to motion artifacts. The few reported clinical studies have shown the feasibility of using single voxel spectroscopy to differentiate benign from malignant lesions by measuring total choline (tCho) levels (50, 51). Booth et al., have shown that MRI at 3T can be used to stage ovarian cancer with an accuracy comparable to that obtained with surgical staging (52). 3D MRSI of ovarian masses can also be performed at 3T to allow an accurate spatially resolved analysis of ovarian cancer (53). There are however some limitations associated with using MRS alone. tCho in primary and metastatic ovarian tumors can be quantified using ^{1}H MRS, although a high rate of failure has been observed (51). Moreover, tCho was detected at 3T in both benign and malignant gynecological neoplasms (52), highlighting the importance of combining multiple MR techniques in order to improve tumor detection and staging.

MOLECULAR TARGETS USED FOR OVARIAN CANCER DETECTION AND THERAPY

CA125

The overexpression of MUC16/cancer antigen 125 (CA125) is one of the hallmarks of high-grade serous ovarian cancer (HGSOC) (54). CA125, a mucin-type-*O*-linked glycoprotein, is expressed as a membrane bound protein at the ovarian cancer cell surface. It is also released in soluble form in bodily fluids. CA125 level in serum, quantified *via* immunoassays, is one of the most extensively studied biomarker for ovarian cancer. CA125 measurements are applied in clinical management of ovarian cancer in different situations including early detection, disease monitoring, early prediction of outcome, tumor status after completion of chemotherapy, and early detection of recurrence (55, 56).

Lymph node involvement is observed in 75% of ovarian cancer cases of late stage disease. Serum-based biomarkers, such as CA125, despite their routine use and low cost, fail to accurately pinpoint the lymph nodes involved and the site of recurrence. PET probes targeting CA125 could be valuable tools in the management of ovarian cancer for whole body visualization and quantification of CA125. Antibodies that bind to CA125 have been reported and can be readily converted into PET imaging agents by conjugating imaging radionuclides with suitable half-life such as zirconium-89 (3.27 days). Taking advantage of the available antibodies, Sharma et al., have demonstrated that a Zr-89 labeled anti-CA125 murine antibody B43.13 (57) (or ^{89}Zr-DFO-mAb-B43.13) could be used for clear delineation of CA125 positive human tumor xenografts from negative tumors in mouse models (13) (**Figure 1**). CA125 positive tumors were detected as early as 24 h after radiotracer injection. In mouse models with lymph node involvement, the authors also observed high levels of ^{89}Zr-DFO-mAb-B43.13 concentrations in lymph nodes by PET imaging. That increased uptake observed was cancer specific and confirmed by pathological validation of metastatic disease in excised samples. PET negative lymph nodes were found to be free of metastatic disease further validating the specificity of the radiotracer. Collectively, these data show the potential for development of a theranostic variant for detecting and targeting CA125 positive ovarian cancer as one could readily generate a radiotherapeutic version of the antibody. The pharmacokinetics and radiation dosimetry of B43.13 labeled with ^{99m}Tc, a SPECT radionuclide, have been reported previously (14). Additional clinical studies with B43.13 as an imaging agent have not yet been reported but B43.13 is being tested in combination with other therapeutics in several clinical trials (58).

CA125 has also been shown as a potential target for contrast enhanced ultrasound imaging. CA125-targeted echogenic lipid and surfactant-stabilized nanobubbles were used in a mouse model to image CA125 positive OVCAR3 tumor with a standard clinical contrast harmonic ultrasound (15). An enhanced tumor accumulation of nanobubbles, higher peak ultrasound signal intensity and slower wash out rates were observed in OVCAR3 tumors compared to CA125 negative SKOV3 tumors. The CA125 binding nanobubbles also showed increased tumor retention and prolonged echogenicity compared to untargeted nanobubbles. The study results suggest that CA125 antibody-conjugated nanobubble-based ultrasound molecular imaging could potentially improve diagnosis of CA125 positive ovarian cancer (15).

Folate Receptor

Another target that is of significant interest in ovarian cancer is folate receptor-α (FRα), a glycosylphosphatidylinositol (GPI)-anchored membrane glycoprotein with a high affinity to folic

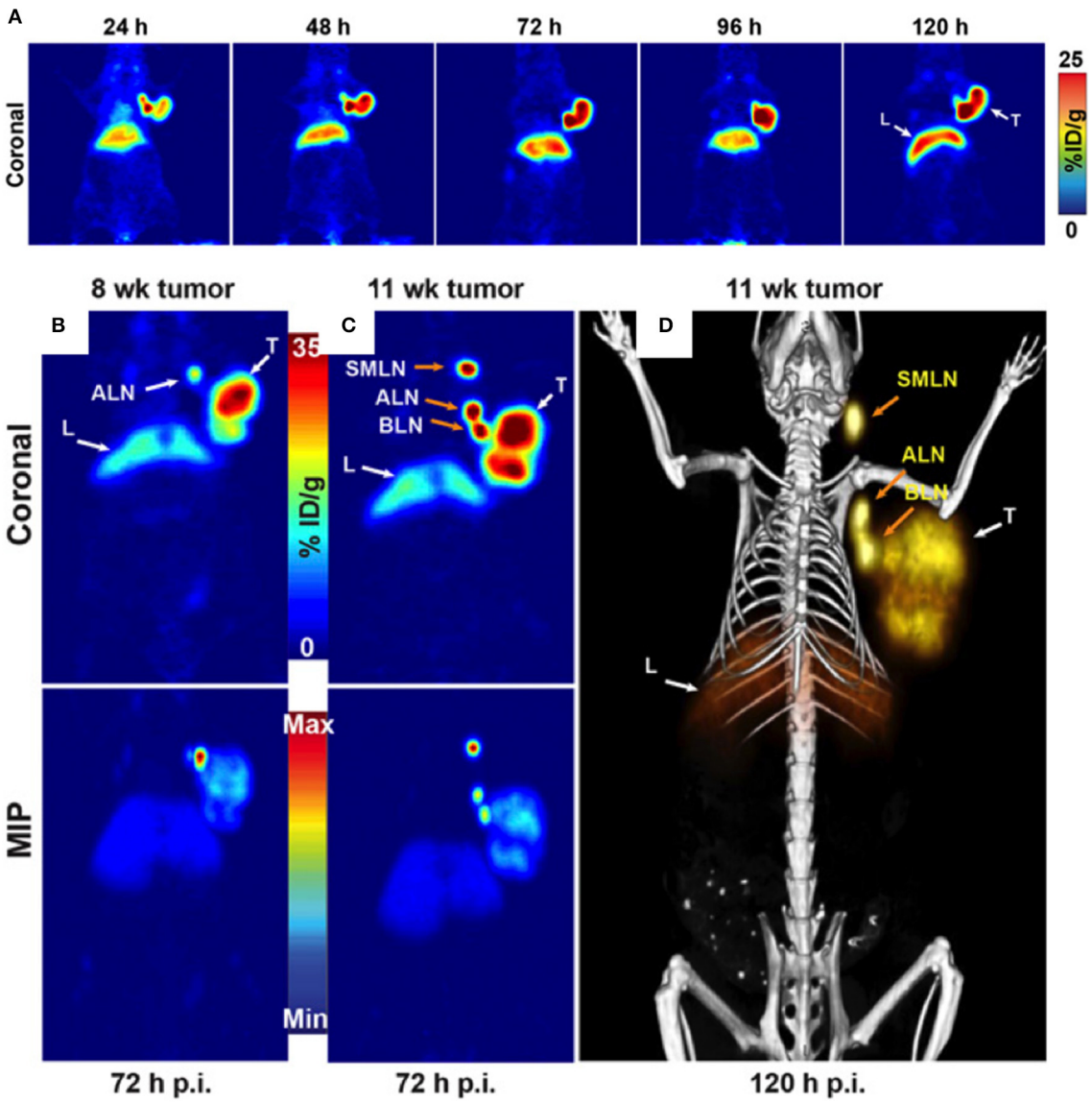

FIGURE 1 | (A) Serial PET images of an athymic nude mouse bearing a CA125-positive OVCAR3 xenograft after tail vein injection of ^{89}Zr-DFO-mAb-B43.13 after (10.2–12.0 MBq). Coronal planar images intersect the middle of the tumor. **(B)** Coronal (top) and maximum-intensity projection (MIP; bottom) PET image obtained 72 h after administration of ^{89}Zr-DFO-mAb-B43.13 to a mouse 8 week post implantation of an OVCAR3 xenograft on the right shoulder. **(C)** Coronal (top) and MIP (bottom) PET images obtained 72 h after administration of ^{89}Zr-DFO-mAb-B43.13 to the same mouse 11 week post tumor implantation. **(D)** PET/CT image obtained 120 h after administration of ^{89}Zr-DFO-mAb-B43.13 to the same mouse 11 week post tumor implantation. ALN, axillary LNs; BLN, brachial LN; L, liver; p.i., post-injection; SML, submandibular LN; T, tumor. Adapted with permission from Sharma et al. (13).

acid. Nearly 90% of HGSOC overexpress FRα (59). Expression of FRα in normal tissues is negligible, thus providing an opportunity for FRα specific delivery of theranostics to the tumor. Folic acid binding results in internalization and sequestration of the bound conjugates. Taking advantage of that phenomenon, folate has been used to develop PET, SPECT, and fluorescence-based imaging agents that yield highly resolved images of FRα positive tumors in preclinical models (60).

A variety of folate-derived conjugates have been developed as PET imaging agents incorporating most clinically used radionuclides F-18 and Ga-68 (16). The overexpression of FRα in cancer has also led to the development of a variety of FR targeted therapeutics including antibody drug conjugates. One such agent is mirvetuximab soravtansine (IMGN853), an FRα-targeting humanized monoclonal antibody-drug conjugate. IMGN853 is being tested in several clinical trials in cancer patients, including platinum resistant ovarian cancer patients (17, 18). Selection of patients for those therapies currently relies on immunohistochemistry (IHC) analysis of archived biopsies. To improve patient selection and therapeutic intervention, two

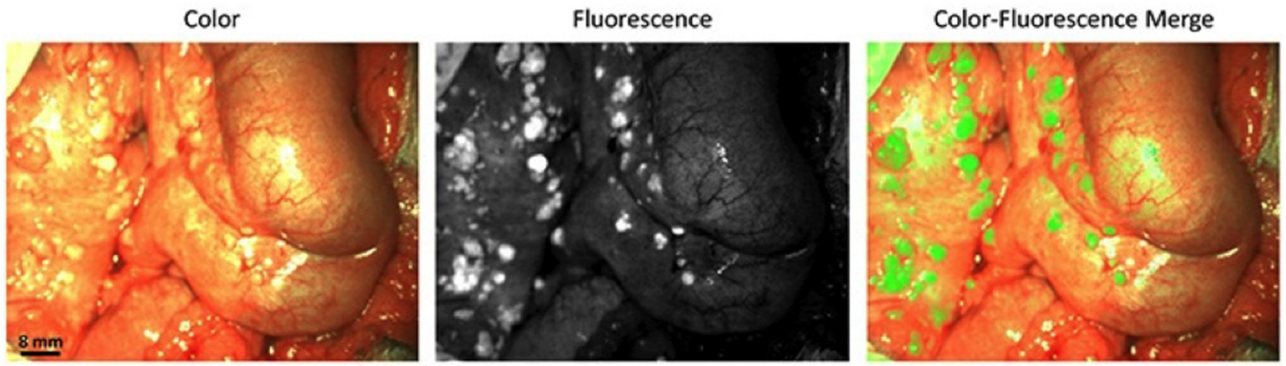

FIGURE 2 | Biopsies of lesions found histologically to be metastases of serous adenocarcinoma. In total, 57 fluorescent lesions that were identified during surgery were resected. Of these resected lesions 44 (77%) appeared to be malignant on histopathology. Seven (16%) of these 44 lesions were not detected by visual inspection with the naked eye or palpation either because they appeared benign or because they were missed during inspection due to small size (<10 mm) and flat nature. Adapted with permission from Tummers et al. (22).

studies developed a ^{89}Zr-radiolabeled version of M9346A as a radiotracer for FRα detection. M9346A is the parent antibody of IMGN853 (19, 20). Evaluation of ^{89}Zr-M9346A uptake in patient derived xenograft models of triple negative breast cancer and ovarian cancer with graded expression levels of FRα showed target specificity, sensitivity and correlated with treatment response to antibody drug conjugate. Those studies portend the potential of ^{89}Zr-M9346A PET as a theranostic tool to pre-screen ovarian or other cancer patients for IMGN853 treatment.

FRα can also be used as a target for optical imaging. Folate conjugated with fluorescein isothiocyanate was used for real-time visualization of tumors in patients for suspected ovarian cancer and undergoing laparotomy. In that study, fluorescence was detected intraoperatively in all patients with FRα positive malignant tumors but not in FRα negative malignant tumors or benign tumors, facilitating fluorescence guided surgical resection of tumor deposits (21). Such agents could have direct impact on patient survival by facilitating improved intraoperative staging and surgical resection, as targeted probes improve specificity and sensitivity of cancer detection during surgery. These results were later confirmed in another study (22) where an FRα-targeting agent, EC17, was intravenously injected to ovarian cancer patients 2–3 h before surgery. EC17 consisted of a folate analog conjugated to 5-fluorescein isothiocyanate (FITC). Using fluorescence imaging ovarian cancer metastases located on the intestine and mesentery could be visualized in those patients **(Figure 2)**. As a next step, the number of lesions and positive margins detected with fluorescence were measured, following which correlation was assessed between the fluorescent signal, the presence of a malignant lesion, and the FRα status. Fluorescence imaging detected 77% of lesions that appeared malignant on histopathology in ovarian cancer patients and 16% of those were not detected with inspection/palpation. A correlation between fluorescence and FRα- and tumor status was demonstrated by histopathology. In spite of a clear fluorescent signal produced by EC17 in ovarian cancer tissue, false-positives were observed due to the normal tissue expression of FRα, or auto-fluorescence signal from collagen and false negatives were linked to inadequate penetration depth of the fluorescence technology.

Those advances have also lead to the development of dual- and multi-modality agents. Liu et al., developed a multimodal PET and optical FRα-targeted agent for ovarian cancer imaging. The agent, ^{64}Cu-labeled pyropheophorbide-folate conjugate, showed selective uptake in metastatic ovarian cancer deposits of <1 mm size that could assist in non-invasive tumor detection as well as in intraoperative guidance of cancer resection (23).

MRI has also the potential to be used to visualize delivery of FR targeting theranostic agent. Luong et al. developed a polyvalent theranostic nanocarrier consisting of a superparamagnetic iron oxide nanoparticle (SPION) core, loaded with a highly potent anticancer agent, 3,4-difluorobenzylidene-curcumin (CDF) and decorated with folic acid-polyamidoamine dendrimers (FA-PAMAM) (24). *In vitro*, those nanoparticles exhibited a high MR contrast and anticancer activity in ovarian (SKOV3) and cervical (HeLa) cancer cells that are known to overexpress FR. The intracellular accumulation and therapeutic effects were more pronounced with targeted particles compared to non-targeted ones. These studies showed the ability of multivalent theranostic nanoparticles for simultaneous imaging and therapy in cancer cells and will have to be confirmed *in vivo*.

Combination therapies can improve treatment efficacy. Novel dual therapy nanoparticles such as poly (lactic-co-glycolic acid) (PLGA) nanoparticles that simultaneously deliver a boron-curcumin complex (RbCur) and an amphiphilic gadolinium complex into tumor cells are being developed (12). Those nanoparticles combined boron and gadolinium neutron capture therapy with anti-proliferative effects of curcumin. The presence of gadolinium makes the nanoparticles visible to MRI. These nanoparticles were tested *in vitro* on ovarian cancer IGROV-1 cells with FR targeting. In those studies, an effective synergic activity was described when neutron treatment was combined with and curcumin cytotoxicity (12). The authors showed that the presence of curcumin before and during neutron exposure leads to increased cell mortality and significantly decreased

proliferation of the surviving cells resulting in improved treatment outcome compared to gadolinium neutron capture therapy used alone (12).

Microbubbles (MBs) have the potential to deliver anti-cancer drugs and/or oxygen for combination therapy in addition to being used as contrast enhancement agents for ultrasound imaging (25). MBs have a core-shell structure and can effectively encapsulate anti-cancer drugs. The US targeted MB destruction (UTMD) technique has been applied to increase drug delivery to the tumors to improve therapeutic effect. Under ultrasound pulses, MBs undergo stable and inertial acoustic cavitations that induce a variety of dynamic processes leading to cell membrane disruption and facilitating intracellular uptake of drugs (25). When MBs are exposed to an US field, the mechanical wave causes them to cavitate. Cavitation is a broad term for US-induced oscillation, and collapse of bubbles (61). For drug delivery, the US parameters induce mechanical effects that also have the potential of enhancing the antitumor efficacy of drugs by increasing microvessel permeability, enhancing drug penetration through the interstitial space, and increasing tumor cell drug uptake (61). Enhanced therapeutic efficacy was demonstrated *in vitro* using US-targeted MB destruction with delivery of paclitaxel and oxygen (25). Ligands can be conjugated to the surface of the drug-loaded MBs to enhance cancer cell selectivity, as shown by Luo et al. who developed oxygen-paclitaxel loaded lipid MBs specifically targeted to FR expressing cells, demonstrating therapeutic efficiency in ovarian cancer xenograft models (62).

HER2

The EGF receptor (EGFR) (or HER) proto-oncogene family consists of four transmembrane tyrosine kinase receptors (i.e., EGFR, ErbB2, ErbB3, and ErbB4) that play a role in cancer pathogenesis and has been described as key therapeutic target in many types of cancer, including ovarian cancer (63).

HER2 (or Erbb2) is a 185 KDa transmembrane glycoprotein known to be overexpressed in a variety of cancers including breast, ovarian, cervical, colon, endometrial, esophageal, lung, and pancreatic cancers (64). HER2 overexpression may confer a selective growth advantage to the tumor cells making it one of the most important biomarkers for guiding therapy. HER2 status determined by IHC and fluorescence *in situ* hybridization has been used to guide and predict the efficacy of anti-HER2 therapy (65). In ovarian cancer, HER2 overexpression has been reported as highly variable. A broad range of HER2 expression frequencies has been found based on IHC results, from 0 to 100% with an average frequency equal to 40% among malignant ovarian tumors across all studies (63). HER2 overexpression contributes to poor survival, and patients with HER2 positive tumors are treated with trastuzumab, a monoclonal antibody targeting HER2 that received FDA approval.

Because of the significant interest in quantifying changes in HER2 expression non-invasively, several antibodies and antibody fragments including affibodies and nanobodies have been developed as imaging agents. Those agents were then used to quantify HER2 expression non-invasively and to assess HER2 positive tumor response to therapy. Radiolabeled trastuzumab, ^{89}Zr-trastuzumab, has demonstrated HER2 specific uptake in patients with metastatic breast cancer (26). Similarly, ^{89}Zr-pertuzumab, another HER2 targeted antibody that inhibits dimerization of HER2, has shown promise in detecting HER2 positive tumors in preclinical models and in patients with metastatic disease (28–30). The optimal image contrast times for those intact antibodies are in days, which could potentially limit their routine use in the clinic. Therefore, varieties of agents that would allow image acquisition within hours after injection have been investigated to improve clinical use. For example, affibody and nanobody molecules labeled with a variety of radionuclides including ^{18}F, ^{68}Ga, and ^{111}In have shown promise in detecting HER2 positive ovarian tumors within hours after the radiotracer injection (66, 67). Such agents could be used to pre-screen patients for HER2 targeted therapies and for real-time assessment of tumor response to therapy.

Imaging is also uniquely positioned to inform on the drug activity in real-time in the tumor. In patients, multiple mechanisms contribute to trastuzumab resistance and imaging has the potential to relate drug exposure at the tumor to response to therapy. In a study by Gebhart et al. radiolabeled trastuzumab was investigated in patients for non-invasive quantification of HER2 expression (27). Nearly one third of the breast cancer patients with tumors expressing HER2, as confirmed by IHC, showed little or no uptake of ^{89}Zr-trastuzumab across their metastases. Those data suggest that penetration of a drug, in this case ^{89}Zr-trastuzumab, into tumor tissue does not solely rely on target presence and that molecular imaging could provide insights into tumor response to therapy. Although those data were acquired in breast cancer patients, the results could have implications for all solid tumors, including ovarian cancers.

Ovarian cancer spreads through the intraperitoneal cavity contributing to significant morbidity and mortality. Low toxicity treatments for intraperitoneal disease are few and an unmet medical need. Intraperitoneal chemotherapy has improved survival but it is not a standard option and carries life-threatening toxicity (68). Targeted radiopharmaceutical therapy delivers the radiation directly to the target expressing cancer cells thus enhancing efficacy and limiting toxicity. Such radiopharmaceutical therapies are often delivered using α- and β-emitting radionuclides. Those radiotherapeutics provide multiple advantages including cross-fire effect and abscopal response that is not generally observed with conventional systemic therapies (9). The overexpression of HER2 and high selectivity of trastuzumab have been exploited to develop radioimmunotherapy. Trastuzumab radiolabeled with α- and β-emitting radionuclides have been investigated for the treatment of disseminated peritoneal disease and tumors with HER2 expression (31). The β-emitting ^{177}Lu radiolabeled transtuzumab is being investigated in patients providing a theranostic approach to HER2 overexpressing cancers (32). Similarly, initial studies with β-emitting radioimmunotherapeutics of TAG-72, tumor-associated glycoprotein 72, for treating ovarian cancer have shown promise (69–71). However, the failure of anti-MUC1 HMFG1 antibodies conjugated with ^{90}Y, a β-emitter, to improve survival in patients with intraperitoneal disease in Phase-III trials have prompted

further investigation of α-particle therapies in ovarian cancer patients (72).

α-emitter therapy has been gaining attention for treating ovarian cancer with intraperitoneal dissemination. α-particles are highly suited for targeting single cells or small tumor clusters as they have a short range in tissues ($< 100\,\mu M$) with high linear energy transfer that deposits a localized irradiation generating highly cytotoxic double strand breaks in the DNA (73). Intraperitoneal radioimmunotherapy using ^{212}Pb conjugated to trastuzumab, an α-emitter, in a first-in-human study was found to be safe with patients showing a trend of decreasing tumor growth and blood-based biomarkers with increasing administered radioactivity (33). In another study Hallqvist et al., investigated intraperitoneal α-particle therapy using MX35, the antigen-binding fragments-F(ab′)2-of a mouse monoclonal antibody, conjugated with α-emitter ^{211}At in epithelial ovarian cancer patients (35). MX35 F(ab′)2 fragment targets the cell surface glycoprotein NaPi2b (SLC34A2) that is expressed on more than 90% of human epithelial ovarian cancers (74). Long-term follow up of those patients showed no apparent signs of radiotoxicity and no decreased tolerance to relapse therapy, thus paving the way for the use of α-particle therapy in ovarian cancers.

Ovarian cancer is a great candidate for NIR-PIT as the light can be applied during cytoreductive surgery. NIR-PIT has been shown to induce effective cell killing of HER2 expressing SKOV3 cells, in subcutaneous and disseminated peritoneal ovarian cancer preclinical models (11). The antibody-photosensitizer conjugate consisted of trastuzumab and IR700DX. The antitumor effect was observed in both models after repeated light exposure, highlighting the potential role of NIR-PIT to treat disseminated peritoneal tumors (11).

Liposomes have been described in multiple studies as effective targeted drug delivery systems for cancer therapy. In the context of ovarian cancer, Han et al., have developed a liposome conjugated with a recombinant protein, EC1-GLuc, fusion of EC1 peptide, an artificial ligand of HER2, with *Gaussia* luciferase (GLuc) for bioluminescent imaging (34). This EC1-GLuc-liposome could be an effective theranostic system for HER2-overexpressing metastatic ovarian carcinoma by combining targeted imaging to drug delivery. *In vitro* experiments revealed selective targeting and internalization of the EC1-GLuc-liposome into HER2-overexpressing SKOV3 cells. To assess the intracellular delivery, a cell-impermeable fluorescence dye (HPTS) was encapsulated in EC1-GLuc-liposome and delivered into SKOV3 cells. *In vivo*, EC1-GLuc-liposomes targeted and delivered HPTS to metastatic SKOV3 tumors, as shown by bioluminescence imaging (34).

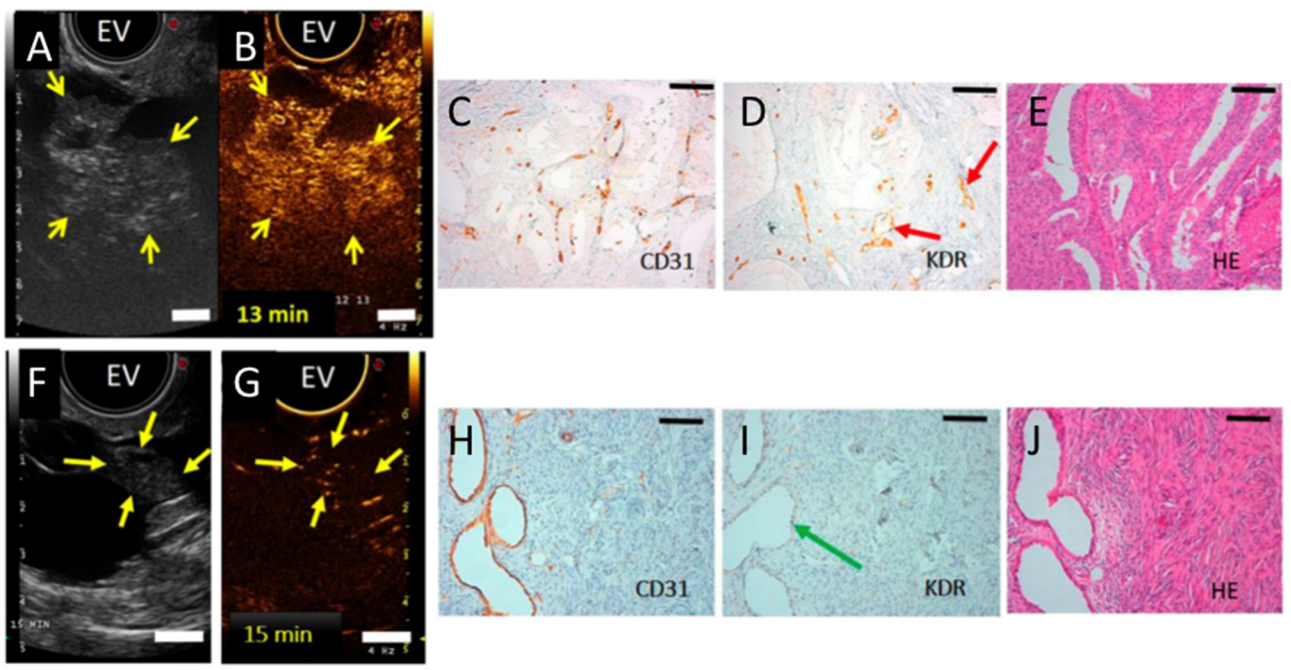

FIGURE 3 | (A) Transverse endovaginal (EV) low mechanical index reference B-mode ultrasound image of the right ovary in a 50-year-old woman showing a 5.2-cm cystic and solid lesion (yellow arrows point to solid portion). **(B)** 13 min post iv injection of KDR-targeted contrast MBs (MBKDR), strong imaging signal is seen in the solid portion of the lesion (yellow arrows) on contrast mode ultrasound molecular image. **(C,D)** IHC performed on adjacent tissue sections demonstrating strong KDR expression on tumor-associated neovasculature (CD31+) (red arrows). **(E)** Histology showing endometrioid carcinoma. **(F)** Transverse endovaginal low mechanical index reference B-mode ultrasound image of right ovary showing a 4.8-cm cystic and solid ovarian lesion (yellow arrows point to solid portion) in a 65-year-old woman. **(G)** 15 min post iv injection of MBKDR, only minimal background signal is seen in 1.3-cm solid part of the lesion (yellow arrows) on contrast mode ultrasound molecular imaging. **(H,I)** IHC demonstrating minimal KDR expression (green arrow) on CD31+ vasculature. **(J)** Histology showing benign serous cystadenofibroma. Adapted with permission from Willmann et al. (37).

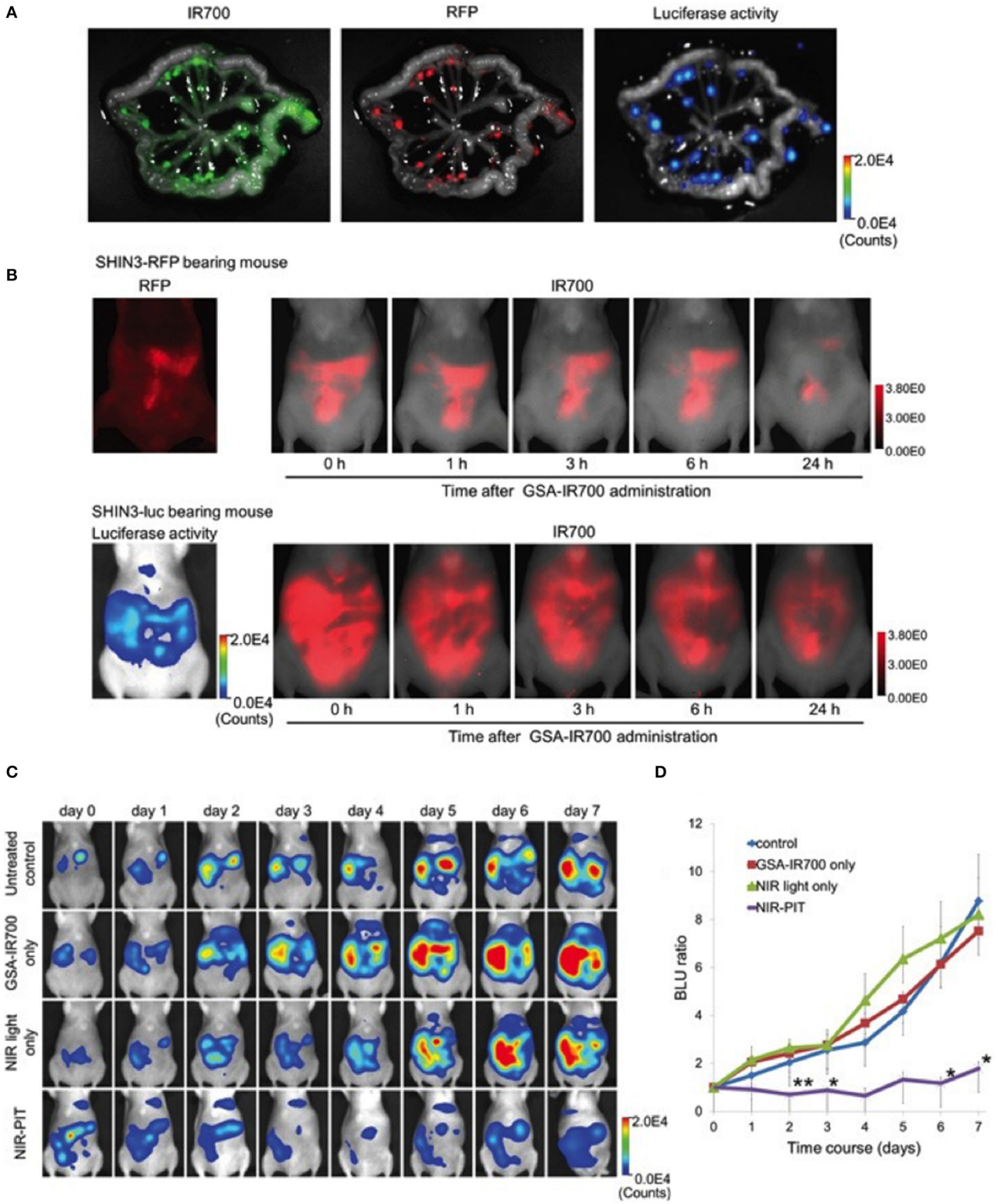

FIGURE 4 | (A) IR700, RFP fluorescence, and luciferase activity in extracted mesentery from a SHIN3-luc-RFP tumor bearing mouse 3 h after i.p. injection of GSA-IR700. IR700 fluorescent signal and luciferase activity were mostly coincident with RFP positive foci. **(B)** *in vivo* serial IR700 fluorescence images of SHIN3-RFP (upper row) and SHIN3-luc (lower row) of tumor-bearing mice after administration of GSA-IR700. The distribution of GSA-IR700 correlated with the fluorescence of

(Continued)

FIGURE 4 | RFP or luciferase activity without evident accumulation in other organs up to 6 h after GSA-IR700 administration. **(C)** BLI of SHIN3-luc tumor bearing mice was obtained every day up to day 7. Luciferase activity decreased only in the NIR-PIT group. **(D)** Quantitative analysis of BLU ratio. Significant suppression of increment of BLU ratio was seen in the NIR-PIT group compared to other groups. Adapted with permission from Harada et al. (38).

EGFR

Epidermal growth factor receptor (EGFR, ErbB1, HER1) has been described as overexpressed in ovarian epithelial cancer of all histologic subtypes. IHC studies reported highly variable levels of EGFR expression among malignant ovarian tumors with results ranging from 4 to 100% of ovarian carcinomas expressing EGFR, and an average frequency of 48% across all studies (63). Leveraging that expression, NIR-PIT targeting EGFR has been applied to treat primary tumors as well as to target metastases. Residual micrometastases are difficult to detect by current imaging techniques and escape standard treatments. Ovarian cancer metastases spread by hematogenous and lymphatic routes and also through peritoneal dissemination. Removal of peritoneal metastases have been shown to improve overall survival in ovarian cancer patients, however, diffuse peritoneal dissemination often consists of a large number of unresectable sub-millimeter lesions that contribute to disease recurrence. To monitor and treat disseminated micrometastases, Spring et al., developed an EGFR targeting dual function activatable immunoconjugate (36) and demonstrated the efficacy of activatable PIT in an OVCAR5 peritoneal micrometastases model (36). That strategy allowed enhanced contrast imaging and selective delivery of therapy to micrometastases while decreasing background fluorescence and toxicity to vital tissues (36). In those studies, a benzoporphyrin derivate (BPD) was used as NIR photoactivatable cytotoxic chromophore. To achieve optimized tumor specificity and quenching, seven BPD conjugates were combined to EGFR targeting cetuximab antibody (Cet-BPD). Cet-BPD conjugates were trafficked to lysosomes through EGFR internalization, and degradation pathway. Intracellular release and dequenching of BPD led to activation of fluorescence emission resulting in phototoxicity. Furthermore, use of a fluorescence micro-endoscope allowed quantification of *in vivo* pharmacokinetics of the immunoconjugate and monitoring of metastatic burden reduction without the need of surgery and with a reduced non-specific phototoxicity, demonstrating the potential impact of the approach for metastatic disease.

New Directions

Several new targets and approaches are being evaluated for ovarian cancer targeting with an emphasis on improving detection and applications in image-guided surgery. A first-in-human clinical trial using ultrasound molecular imaging in patients with breast and ovarian lesions was recently performed (37). In that study, a kinase insert domain receptor [KDR] targeted clinical-grade microbubble contrast agent [MBKDR] was used. KDR is one of the key regulators of neoangiogenesis in cancer and angiogenesis plays a crucial role in the progression of ovarian cancer and metastases (75). As a phase I, the aim of the study was to assess safety and quantify KDR expression using the gold standard IHC. Patients with focal ovarian or breast lesions were intravenously injected with MBKDR, followed with ultrasound molecular imaging and then underwent surgical resection of the lesions. Those resected tissues were immunostained for CD31 and KDR. Results from those studies showed that MBKDR was well tolerated, and that KDR expression on IHC correlated with US imaging signal in 85% of malignant ovarian lesions, as shown in **Figure 3**. A robust KDR-targeted signal was observed in 77% of malignant ovarian lesions and absence of signal was noted in 78% of benign lesions (37).

NIR-PIT studies often use antibody as targeting moiety. A non-antibody derived NIR-PIT agent was developed by Harada et al., and tested in a disseminated ovarian cancer model (38). Galactosyl serum albumin (GSA) that is composed of galactose molecule conjugated to albumin *via* carboxyl groups was used. This construct can bind to beta-D-galactose receptor, a surface lectin, which is overexpressed in many cancers, including ovarian cancers. beta-D-galactose receptor is quickly internalized after binding to ligands. The agent was tested using SHIN3 cells that overexpress galactose receptor and produces diffuse peritoneal dissemination (38). GSA-IR700 probe accumulated specifically in the tumor, and repeated regimens of NIR-PIT improved the treatment efficacy by increasing the depth of GSA-IR700 delivery into tumor nodules **(Figure 4)**. The study showed specific delivery of GSA-IR700 to the tumor (**Figures 4A,B**), and reduction of the metastatic burden after NIR-PIT (**Figures 4C,D**).

Nearly 50% of primary ovarian cancers show enhanced enzymatic activities of β-galactosidase compared to normal ovaries (76) and has been a focus of enzymatically activated fluorescence probe development to visualize ovarian cancer metastases (39, 40). Asanuma et al., developed a membrane-permeable HMRef-βGal allowing visualization of metastases of $<$1 mm in diameter in the peritoneal cavity after intraperitoneal administration of the fluorescence probe (40). More recently, a topically-sprayable and activatable fluorescent probe was developed to detect cancer, that would eliminate the need for an iv injection pre-surgery. After activation by the enzyme β-galactosidase, SPiDER-βGal can be retained within cells by anchoring to intracellular proteins. SPiDER-βGal was tested *in vitro* on different cancer cell lines and *ex vivo* on tumor tissues (39). SPiDER-βGal when compared to γGlu-HMRG, a probe activated by γ-glutamyltranspeptidase, demonstrated high sensitivity for detection of ovarian cancer metastases in the peritonium in a mouse model (39). SPiDER-βGal presented higher signal retention, and improved contrast of the tumor margin, as compared to γGlu-HMRG. Additionally, SPiDER-βGal resulted in a high target-to-background ratio due to an intense enhancement within the tumor and those signals lasted up to 60 min after activation (39). These results demonstrated the potential applications of SPiDER-βGal targeted probes

for laparotomic and endoscopic detection of primary tumors and metastases.

CONCLUSION

The increasing use of genomic and epigenomic information from cancerous tissue is providing new insights into the genetic abnormalities, pathway alterations and target expression, allowing for improved understanding and classification of ovarian cancers. Assimilation of those advances combined with the availability of highly specific probes, chemistry and radiochemistry methods are likely to enhance the potential of theranostic approaches that are already showing promise. Ovarian cancer is also highly suitable for optical imaging applications for surgical guidance. Both preclinical and clinical studies have demonstrated the utility of fluorescent probes for tumor detection during cytoreductive surgery and the development of handheld devices will further increase their use. Although MRI-based studies of ovarian cancer are limited in their scope at this time, the integration of PET/MR scanners could allow for characterization of tumor molecular and metabolic features thus paving the way for imaging and therapeutic guidance by taking advantage of both modalities. These advances on multiple fronts, we believe, are likely to transform our ability to detect, treat and hopefully eradicate ovarian cancer.

AUTHOR CONTRIBUTIONS

SN and M-FP wrote the review, and provided approval for publication of the content.

FUNDING

SN was supported by NIH 1R01CA236616, NIH P41EB024495, and Allegheny Health Network-Johns Hopkins Cancer Research Fund. M-FP was supported by Emerson Collective and Hopkins Catalyst Award.

REFERENCES

1. Miller KD, Siegel RL, Lin CC, Mariotto AB, Kramer JL, Rowland JH, et al. Cancer treatment and survivorship statistics, 2016. *CA Cancer J Clin*. (2016) 66:271–89. doi: 10.3322/caac.21349
2. Gadducci A, Guarneri V, Peccatori FA, Ronzino G, Scandurra G, Zamagni C, et al. Current strategies for the targeted treatment of high-grade serous epithelial ovarian cancer and relevance of BRCA mutational status. *J Ovarian Res*. (2019) 12:9. doi: 10.1186/s13048-019-0484-6
3. Herhaus P, Habringer S, Philipp-Abbrederis K, Vag T, Gerngross C, Schottelius M, et al. Targeted positron emission tomography imaging of CXCR4 expression in patients with acute myeloid leukemia. *Haematologica*. (2016) 101:932–40. doi: 10.3324/haematol.2016.142976
4. Werner RA, Weich A, Kircher M, Solnes LB, Javadi MS, Higuchi T, et al. The theranostic promise for Neuroendocrine Tumors in the late 2010s - where do we stand, where do we go? *Theranostics*. (2018) 8:6088–100. doi: 10.7150/thno.30357
5. Barber TW, Singh A, Kulkarni HR, Niepsch K, Billah B, Baum RP. Clinical outcomes of (177)Lu-PSMA radioligand therapy in earlier and later phases of metastatic castration-resistant prostate cancer grouped by previous taxane chemotherapy. *J Nucl Med*. (2019) 60:955–62. doi: 10.2967/jnumed.118.216820
6. Langbein T, Weber WA, Eiber M. Future of theranostics: an outlook on precision oncology in nuclear medicine. *J Nucl Med*. (2019) 60(Suppl 2):13S–19S. doi: 10.2967/jnumed.118.220566
7. Mothersill C, Seymour CB. Radiation-induced bystander effects–implications for cancer. *Nat Rev Cancer*. (2004) 4:158–64. doi: 10.1038/nrc1277
8. Brady D, O'Sullivan JM, Prise KM. What is the role of the bystander response in radionuclide therapies? *Front Oncol*. (2013) 3:215. doi: 10.3389/fonc.2013.00215
9. Ngwa W, Irabor OC, Schoenfeld JD, Hesser J, Demaria S, Formenti SC. Using immunotherapy to boost the abscopal effect. *Nat Rev Cancer*. (2018) 18:313–22. doi: 10.1038/nrc.2018.6
10. Kobayashi H, Choyke PL. Near-infrared photoimmunotherapy of cancer. *Acc Chem Res*. (2019) 52:2332–9. doi: 10.1021/acs.accounts.9b00273
11. Sato K, Hanaoka H, Watanabe R, Nakajima T, Choyke PL, Kobayashi H. Near infrared photoimmunotherapy in the treatment of disseminated peritoneal ovarian cancer. *Mol Cancer Ther*. (2015) 14:141–50. doi: 10.1158/1535-7163.MCT-14-0658
12. Alberti D, Protti N, Franck M, Stefania R, Bortolussi S, Altieri S, et al. Theranostic nanoparticles loaded with imaging probes and rubrocurcumin for combined cancer therapy by folate receptor targeting. *ChemMedChem*. (2017) 12:502–9. doi: 10.1002/cmdc.201700039
13. Sharma SK, Sevak KK, Monette S, Carlin SD, Knight JC, Wuest FR, et al. Preclinical 89Zr immuno-PET of high-grade serous ovarian cancer and lymph node metastasis. *J Nucl Med*. (2016) 57:771–6. doi: 10.2967/jnumed.115.167072
14. McQuarrie SA, Baum RP, Niesen A, Madiyalakan R, Korz W, Sykes TR, et al. Pharmacokinetics and radiation dosimetry of 99Tcm-labelled monoclonal antibody B43.13 in ovarian cancer patients. *Nucl Med Commun*. (1997) 18:878–86. doi: 10.1097/00006231-199709000-00013
15. Gao Y, Hernandez C, Yuan HX, Lilly J, Kota P, Zhou H, et al. Ultrasound molecular imaging of ovarian cancer with CA-125 targeted nanobubble contrast agents. *Nanomedicine*. (2017) 13:2159–68. doi: 10.1016/j.nano.2017.06.001
16. Boss SD, Muller C, Siwowska K, Buchel JI, Schmid RM, Groehn V, et al. Reduced (18)F-folate conjugates as a new class of PET tracers for folate receptor imaging. *Bioconjug Chem*. (2018) 29:1119–30. doi: 10.1021/acs.bioconjchem.7b00775
17. Ponte JF, Ab O, Lanieri L, Lee J, Coccia J, Bartle LM, et al. Mirvetuximab soravtansine (IMGN853), a folate receptor alpha-targeting antibody-drug conjugate, potentiates the activity of standard of care therapeutics in ovarian cancer models. *Neoplasia*. (2016) 18:775–84. doi: 10.1016/j.neo.2016.11.002
18. Moore KN, Martin LP, O'Malley DM, Matulonis UA, Konner JA, Perez RP, et al. Safety and activity of mirvetuximab soravtansine (IMGN853), a folate receptor alpha-targeting antibody-drug conjugate, in platinum-resistant ovarian, fallopian tube, or primary peritoneal cancer: a phase I expansion study. *J Clin Oncol*. (2017) 35:1112–8. doi: 10.1200/JCO.2016.69.9538
19. Brand C, Sadique A, Houghton JL, Gangangari K, Ponte JF, Lewis JS, et al. Leveraging PET to image folate receptor alpha therapy of an antibody-drug conjugate. *EJNMMI Res*. (2018) 8:87. doi: 10.1186/s13550-018-0437-x
20. Heo GS, Detering L, Luehmann HP, Primeau T, Lee YS, Laforest R, et al. Folate receptor alpha targeted 89Zr-M9346A immuno-PET for image-guided intervention with mirvetuximab soravtansine in triple negative breast cancer. *Mol Pharm*. (2019) 16:3996–4006. doi: 10.1021/acs.molpharmaceut.9b00653
21. van Dam GM, Themelis G, Crane LM, Harlaar NJ, Pleijhuis RG, Kelder W, et al. Intraoperative tumor-specific fluorescence imaging in ovarian cancer by folate receptor-alpha targeting: first in-human results. *Nat Med*. (2011) 17:1315–9. doi: 10.1038/nm.2472
22. Tummers QR, Hoogstins CE, Gaarenstroom KN, de Kroon CD, van Poelgeest MI, Vuyk J, et al. Intraoperative imaging of folate receptor alpha positive ovarian and breast cancer using the tumor specific agent EC17. *Oncotarget*. (2016) 7:32144–55. doi: 10.18632/oncotarget.8282

23. Liu TW, Stewart JM, Macdonald TD, Chen J, Clarke B, Shi J, et al. Biologically-targeted detection of primary and micro-metastatic ovarian cancer. *Theranostics*. (2013) 3:420–7. doi: 10.7150/thno.6413
24. Luong D, Sau S, Kesharwani P, Iyer AK. Polyvalent folate-dendrimer-coated iron oxide theranostic nanoparticles for simultaneous magnetic resonance imaging and precise cancer cell targeting. *Biomacromolecules*. (2017) 18:1197–209. doi: 10.1021/acs.biomac.6b01885
25. Sun J, Yin M, Zhu S, Liu L, Zhu Y, Wang Z, et al. Ultrasound-mediated destruction of oxygen and paclitaxel loaded lipid microbubbles for combination therapy in hypoxic ovarian cancer cells. *Ultrason Sonochem*. (2016) 28:319–26. doi: 10.1016/j.ultsonch.2015.08.009
26. Dijkers EC, Oude Munnink TH, Kosterink JG, Brouwers AH, Jager PL, de Jong JR, et al. Biodistribution of 89Zr-trastuzumab and PET imaging of HER2-positive lesions in patients with metastatic breast cancer. *Clin Pharmacol Ther*. (2010) 87:586–92. doi: 10.1038/clpt.2010.12
27. Gebhart G, Lamberts LE, Wimana Z, Garcia C, Emonts P, Ameye L, et al. Molecular imaging as a tool to investigate heterogeneity of advanced HER2-positive breast cancer and to predict patient outcome under trastuzumab emtansine (T-DM1): the ZEPHIR trial. *Ann Oncol*. (2016) 27:619–24. doi: 10.1093/annonc/mdv577
28. Marquez BV, Ikotun OF, Zheleznyak A, Wright B, Hari-Raj A, Pierce RA, et al. Evaluation of (89)Zr-pertuzumab in Breast cancer xenografts. *Mol Pharm*. (2014) 11:3988–95. doi: 10.1021/mp500323d
29. Jiang D, Im HJ, Sun H, Valdovinos HF, England CG, Ehlerding EB, et al. Radiolabeled pertuzumab for imaging of human epidermal growth factor receptor 2 expression in ovarian cancer. *Eur J Nucl Med Mol Imaging*. (2017) 44:1296–305. doi: 10.1007/s00259-017-3663-y
30. Ulaner GA, Lyashchenko SK, Riedl C, Ruan S, Zanzonico PB, Lake D, et al. First-in-human human epidermal growth factor receptor 2-targeted imaging using (89)Zr-pertuzumab PET/CT: dosimetry and clinical application in patients with breast cancer. *J Nucl Med*. (2018) 59:900–6. doi: 10.2967/jnumed.117.202010
31. Milenic DE, Garmestani K, Brady ED, Albert PS, Ma D, Abdulla A, et al. Targeting of HER2 antigen for the treatment of disseminated peritoneal disease. *Clin Cancer Res*. (2004) 10:7834–41. doi: 10.1158/1078-0432.CCR-04-1226
32. Bhusari P, Vatsa R, Singh G, Parmar M, Bal A, Dhawan DK, et al. Development of Lu-177-trastuzumab for radioimmunotherapy of HER2 expressing breast cancer and its feasibility assessment in breast cancer patients. *Int J Cancer*. (2017) 140:938–47. doi: 10.1002/ijc.30500
33. Meredith RF, Torgue JJ, Rozgaja TA, Banaga EP, Bunch PW, Alvarez RD, et al. Safety and outcome measures of first-in-human intraperitoneal alpha radioimmunotherapy with 212Pb-TCMC-trastuzumab. *Am J Clin Oncol*. (2018) 41:716–21. doi: 10.1097/COC.0000000000000353
34. Han XJ, Wei YF, Wan YY, Jiang LP, Zhang JF, Xin HB. Development of a novel liposomal nanodelivery system for bioluminescence imaging and targeted drug delivery in ErbB2-overexpressing metastatic ovarian carcinoma. *Int J Mol Med*. (2014) 34:1225–32. doi: 10.3892/ijmm.2014.1922
35. Hallqvist A, Bergmark K, Back T, Andersson H, Dahm-Kahler P, Johansson M, et al. Intraperitoneal alpha-emitting radioimmunotherapy with (211)At in relapsed ovarian cancer: long-term follow-up with individual absorbed dose estimations. *J Nucl Med*. (2019) 60:1073–9. doi: 10.2967/jnumed.118.220384
36. Spring BQ, Abu-Yousif AO, Palanisami A, Rizvi I, Zheng X, Mai Z, et al. Selective treatment and monitoring of disseminated cancer micrometastases *in vivo* using dual-function, activatable immunoconjugates. *Proc Natl Acad Sci USA*. (2014) 111:E933–942. doi: 10.1073/pnas.1319493111
37. Willmann JK, Bonomo L, Carla Testa A, Rinaldi P, Rindi G, Valluru KS, et al. Ultrasound molecular imaging with BR55 in patients with breast and ovarian lesions: first-in-human results. *J Clin Oncol*. (2017) 35: 2133–40. doi: 10.1200/JCO.2016.70.8594
38. Harada T, Nakamura Y, Sato K, Nagaya T, Okuyama S, Ogata F, et al. Near-infrared photoimmunotherapy with galactosyl serum albumin in a model of diffuse peritoneal disseminated ovarian cancer. *Oncotarget*. (2016) 7:79408–16. doi: 10.18632/oncotarget.12710
39. Nakamura Y, Mochida A, Nagaya T, Okuyama S, Ogata F, Choyke PL, et al. A topically-sprayable, activatable fluorescent and retaining probe, SPiDER-betaGal for detecting cancer: advantages of anchoring to cellular proteins after activation. *Oncotarget*. (2017) 8:39512–21. doi: 10.18632/oncotarget.17080
40. Asanuma D, Sakabe M, Kamiya M, Yamamoto K, Hiratake J, Ogawa M, et al. Sensitive beta-galactosidase-targeting fluorescence probe for visualizing small peritoneal metastatic tumours *in vivo*. *Nat Commun*. (2015) 6:6463. doi: 10.1038/ncomms7463
41. Fleischer AC. Transabdominal and transvaginal sonography of ovarian masses. *Clin Obstet Gynecol*. (1991) 34:433–42. doi: 10.1097/00003081-199106000-00027
42. Fleischer AC, Lyshchik A, Jones HW Jr, Crispens M, Loveless M, Andreotti RF, et al. Contrast-enhanced transvaginal sonography of benign versus malignant ovarian masses: preliminary findings. *J Ultrasound Med*. (2008) 27:1011–8; quiz 1019–21. doi: 10.7863/jum.2008.27.7.1011
43. Kinkel K, Hricak H, Lu Y, Tsuda K, Filly RA. US characterization of ovarian masses: a meta-analysis. *Radiology*. (2000) 217:803–11. doi: 10.1148/radiology.217.3.r00dc20803
44. Niermann KJ, Fleischer AC, Huamani J, Yankeelov TE, Kim DW, Wilson WD, et al. Measuring tumor perfusion in control and treated murine tumors: correlation of microbubble contrast-enhanced sonography to dynamic contrast-enhanced magnetic resonance imaging and fluorodeoxyglucose positron emission tomography. *J Ultrasound Med*. (2007) 26:749–56. doi: 10.7863/jum.2007.26.6.749
45. Fleischer AC, Lyshchik A, Jones HW III, Crispens MA, Andreotti RF, Williams PK, et al. Diagnostic parameters to differentiate benign from malignant ovarian masses with contrast-enhanced transvaginal sonography. *J Ultrasound Med*. (2009) 28:1273–80. doi: 10.7863/jum.2009.28.10.1273
46. Marzola MC, Chondrogiannis S, Rubello D. Fludeoxyglucose F 18 PET/CT assessment of ovarian cancer. *PET Clin*. (2018) 13:179–202. doi: 10.1016/j.cpet.2017.11.005
47. Mitchell CL, O'Connor JP, Jackson A, Parker GJ, Roberts C, Watson Y, et al. Identification of early predictive imaging biomarkers and their relationship to serological angiogenic markers in patients with ovarian cancer with residual disease following cytotoxic therapy. *Ann Oncol*. (2010) 21:1982–9. doi: 10.1093/annonc/mdq079
48. Thomassin-Naggara I, Bazot M, Darai E, Callard P, Thomassin J, Cuenod CA. Epithelial ovarian tumors: value of dynamic contrast-enhanced MR imaging and correlation with tumor angiogenesis. *Radiology*. (2008) 248:148–59. doi: 10.1148/radiol.2481071120
49. Carter JS, Koopmeiners JS, Kuehn-Hajder JE, Metzger GJ, Lakkadi N, Downs LS Jr, et al. Quantitative multiparametric MRI of ovarian cancer. *J Magn Reson Imaging*. (2013) 38:1501–9. doi: 10.1002/jmri.24119
50. Stanwell P, Russell P, Carter J, Pather S, Heintze S, Mountford C. Evaluation of ovarian tumors by proton magnetic resonance spectroscopy at three Tesla. *Investigat Radiol*. (2008) 43:745–51. doi: 10.1097/RLI.0b013e31817e9104
51. McLean MA, Priest AN, Joubert I, Lomas DJ, Kataoka MY, Earl H, et al. Metabolic characterization of primary and metastatic ovarian cancer by 1H-MRS *in vivo* at 3T. *Magnetic Reson Med*. (2009) 62:855–61. doi: 10.1002/mrm.22067
52. Booth SJ, Pickles MD, Turnbull LW. *In vivo* magnetic resonance spectroscopy of gynaecological tumours at 3.0 Tesla. *BJOG*. (2009) 116:300–3. doi: 10.1111/j.1471-0528.2008.02007.x
53. Esseridou A, Di Leo G, Sconfienza LM, Caldiera V, Raspagliesi F, Grijuela B, et al. *in vivo* detection of choline in ovarian tumors using 3D magnetic resonance spectroscopy. *Invest. Radiol*. (2011) 46:377–82. doi: 10.1097/RLI.0b013e31821690ef
54. Scholler N, Urban N. CA125 in ovarian cancer. *Biomark Med*. (2007) 1:513–23. doi: 10.2217/17520363.1.4.513
55. Jacobs I, Bast RC Jr. The CA 125 tumour-associated antigen: a review of the literature. *Hum Reprod*. (1989) 4:1–12. doi: 10.1093/oxfordjournals.humrep.a136832
56. Jelovac D, Armstrong DK. Recent progress in the diagnosis and treatment of ovarian cancer. *CA Cancer J Clin*. (2011) 61:183–203. doi: 10.3322/caac.20113
57. Berek JS. Immunotherapy of ovarian cancer with antibodies: a focus on oregovomab. *Expert Opin Biol Ther*. (2004) 4:1159–65. doi: 10.1517/14712598.4.7.1159
58. Tse BW, Collins A, Oehler MK, Zippelius A, Heinzelmann-Schwarz VA. Antibody-based immunotherapy for ovarian cancer: where are we at? *Ann Oncol*. (2014) 25:322–31. doi: 10.1093/annonc/mdt405

59. Kalli KR, Oberg AL, Keeney GL, Christianson TJ, Low PS, Knutson KL, et al. Folate receptor alpha as a tumor target in epithelial ovarian cancer. *Gynecol Oncol*. (2008) 108:619–26. doi: 10.1016/j.ygyno.2007.11.020
60. Ke CY, Mathias CJ, Green MA. Folate-receptor-targeted radionuclide imaging agents. *Adv Drug Deliv Rev*. (2004) 56:1143–60. doi: 10.1016/j.addr.2004.01.004
61. Chen H, Hwang JH. Ultrasound-targeted microbubble destruction for chemotherapeutic drug delivery to solid tumors. *J Ther Ultrasound*. (2013) 1:10. doi: 10.1186/2050-5736-1-10
62. Luo T, Sun J, Zhu S, He J, Hao L, Xiao L, et al. Ultrasound-mediated destruction of oxygen and paclitaxel loaded dual-targeting microbubbles for intraperitoneal treatment of ovarian cancer xenografts. *Cancer Lett*. (2017) 391:1–11. doi: 10.1016/j.canlet.2016.12.032
63. Lafky JM, Wilken JA, Baron AT, Maihle NJ. Clinical implications of the ErbB/epidermal growth factor (EGF) receptor family and its ligands in ovarian cancer. *Biochim Biophys Acta*. (2008) 1785:232–65. doi: 10.1016/j.bbcan.2008.01.001
64. Iqbal N, Iqbal N. Human epidermal growth factor receptor 2 (HER2) in cancers: overexpression and therapeutic implications. *Mol Biol Int*. (2014) 2014:852748. doi: 10.1155/2014/852748
65. Serrano-Olvera A, Duenas-Gonzalez A, Gallardo-Rincon D, Candelaria M, De la Garza-Salazar J. Prognostic, predictive and therapeutic implications of HER2 in invasive epithelial ovarian cancer. *Cancer Treat Rev*. (2006) 32:180–90. doi: 10.1016/j.ctrv.2006.01.001
66. Ren G, Zhang R, Liu Z, Webster JM, Miao Z, Gambhir SS, et al. A 2-helix small protein labeled with 68Ga for PET imaging of HER2 expression. *J Nucl Med*. (2009) 50:1492–9. doi: 10.2967/jnumed.109.064287
67. Heskamp S, Laverman P, Rosik D, Boschetti F, van der Graaf WT, Oyen WJ, et al. Imaging of human epidermal growth factor receptor type 2 expression with 18F-labeled affibody molecule ZHER2:2395 in a mouse model for ovarian cancer. *J Nucl Med*. (2012) 53:146–53. doi: 10.2967/jnumed.111.093047
68. Tewari D, Java JJ, Salani R, Armstrong DK, Markman M, Herzog T, et al. Long-term survival advantage and prognostic factors associated with intraperitoneal chemotherapy treatment in advanced ovarian cancer: a gynecologic oncology group study. *J Clin Oncol*. (2015) 33:1460–6. doi: 10.1200/JCO.2014.55.9898
69. Meredith RF, Partridge EE, Alvarez RD, Khazaeli MB, Plott G, Russell CD, et al. Intraperitoneal radioimmunotherapy of ovarian cancer with lutetium-177-CC49. *J Nucl Med*. (1996) 37:1491–6.
70. Rosenblum MG, Verschraegen CF, Murray JL, Kudelka AP, Gano J, Cheung L, et al. Phase I study of 90Y-labeled B72.3 intraperitoneal administration in patients with ovarian cancer: effect of dose and EDTA coadministration on pharmacokinetics and toxicity. *Clin Cancer Res*. (1999) 5:953–61.
71. Alvarez RD, Huh WK, Khazaeli MB, Meredith RF, Partridge EE, Kilgore LC, et al. A phase I study of combined modality (90)Yttrium-CC49 intraperitoneal radioimmunotherapy for ovarian cancer. *Clin Cancer Res*. (2002) 8:2806–11.
72. Verheijen RH, Massuger LF, Benigno BB, Epenetos AA, Lopes A, Soper JT, et al. Phase III trial of intraperitoneal therapy with yttrium-90-labeled HMFG1 murine monoclonal antibody in patients with epithelial ovarian cancer after a surgically defined complete remission. *J Clin Oncol*. (2006) 24:571–8. doi: 10.1200/JCO.2005.02.5973
73. McDevitt MR, Sgouros G, Sofou S. Targeted and nontargeted α-particle therapies. *Annu Rev Biomed Eng*. (2018) 20:73–93. doi: 10.1146/annurev-bioeng-062117-120931
74. Yin BW, Kiyamova R, Chua R, Caballero OL, Gout I, Gryshkova V, et al. Monoclonal antibody MX35 detects the membrane transporter NaPi2b (SLC34A2) in human carcinomas. *Cancer Immun*. (2008) 8:3.
75. Bamberger ES, Perrett CW. Angiogenesis in epithelian ovarian cancer. *Mol Pathol*. (2002) 55:348–59. doi: 10.1136/mp.55.6.348
76. Chatterjee SK, Bhattacharya M, Barlow JJ. Glycosyltransferase and glycosidase activities in ovarian cancer patients. *Cancer Res*. (1979) 39(6 Pt 1):1943–51.

Conflict of Interest: The authors declare that the research was conducted in the absence of any commercial or financial relationships that could be construed as a potential conflict of interest.

frontiers in Oncology

ORIGINAL RESEARCH
published: 28 February 2020
doi: 10.3389/fonc.2020.00266

Gonadotropin-Releasing Hormone Receptor-Targeted Near-Infrared Fluorescence Probe for Specific Recognition and Localization of Peritoneal Metastases of Ovarian Cancer

Qiyu Liu [1,2,3†], Xiaobo Zhou [4†], Wei Feng [4], Tao Pu [1,2,3], Xiaoping Li [5], Fuyou Li [4], Yu Kang [1,2,3], Xiaoyan Zhang [1,2,3] and Congjian Xu [1,2,3*]*

[1] Obstetrics and Gynecology Hospital, Fudan University, Shanghai, China, [2] Department of Obstetrics and Gynecology of Shanghai Medical School, Fudan University, Shanghai, China, [3] Shanghai Key Laboratory of Female Reproductive Endocrine Related Diseases, Shanghai, China, [4] Department of Chemistry, Fudan University, Shanghai, China, [5] Department of Obstetrics and Gynecology, Peking University People's Hospital, Beijing, China

OPEN ACCESS

Edited by:
Zaver Bhujwalla,
Johns Hopkins University,
United States

Reviewed by:
Aslam Khan,
University of Missouri, United States
Arturo Aguilar-Rojas,
Mexican Social Security Institute, Mexico
Andrew Douglas Newton,
Hospital of the University of Pennsylvania, United States

***Correspondence:**
Xiaoyan Zhang
zhxy@fudan.edu.cn
Congjian Xu
xucongjian@fudan.edu.cn

[†] These authors have contributed equally to this work

Specialty section:
This article was submitted to Cancer Imaging and Image-directed Interventions, a section of the journal Frontiers in Oncology

Received: 14 October 2019
Accepted: 17 February 2020
Published: 28 February 2020

Citation:
Liu Q, Zhou X, Feng W, Pu T, Li X, Li F, Kang Y, Zhang X and Xu C (2020) Gonadotropin-Releasing Hormone Receptor-Targeted Near-Infrared Fluorescence Probe for Specific Recognition and Localization of Peritoneal Metastases of Ovarian Cancer. Front. Oncol. 10:266. doi: 10.3389/fonc.2020.00266

Background: Peritoneal dissemination is common in advanced ovarian cancer. The completeness of cytoreduction is an independent prognostic factor. The intraoperative fluorescence imaging via tumor-specific near-infrared fluorophore might improve staging and surgical completeness. A promising target for ovarian cancer is the gonadotropin-releasing hormone receptor (GnRHR). This study aimed to develop a GnRHR-targeted near-infrared imaging probe for the detection of peritoneal metastases of ovarian cancer.

Methods: Indocyanine green (ICG) was conjugated with GnRH antagonist peptide to develop an ovarian cancer-selective fluorescence probe GnRHa-ICG. GnRHR expression was detected in ovarian cancer tissues. The binding capacity of GnRHa-ICG and ICG was detected in both cancer cell lines and mouse models of peritoneal metastatic ovarian cancer using fluorescence microscopy, flow cytometry, and near-infrared fluorescence imaging.

Results: Tissue microarray analysis revealed the overexpression of GnRHR in ovarian cancer. GnRH-ICG exhibited the binding capacity in a panel of cancer cell lines with different expression levels of GnRHR. In ovarian cancer mouse models, GnRHa-ICG signals were detected in peritoneal tumor lesions rather than normal peritoneal and intestines tissues. ICG showed intensive fluorescence signals in intestines. The tumor-to-muscle ratio and tumor-to-intestine ratio of GnRHa-ICG was 7.41 ± 2.82 and 4.37 ± 1.66, higher than that of ICG (4.60 ± 0.50 and 0.57 ± 0.06) at 2 h post administration. The fluorescence signal of peritoneal metastases peaked in intensity at 2 h and maintained for up to 48 h. ICG also showed a weak signal in the tumor lesions due to the enhanced permeability and retention effect, but the intensity decreased quickly within 48 h.

Conclusions: The developed GnRHR-targeted imaging agent GnRHa-ICG could specifically detected peritoneal tumor lesions from normal peritoneal and intestines

tissues because of the modification of GnRHa to ICG. The plateau period of GnRHa-ICG accumulation may be feasible for clinical applications in fluorescence-guided surgery. Our GnRHR imaging concept may be effective in other hormone-related tumors with upregulated GnRHR expression.

Keywords: targeted imaging, near-infrared fluorescence, gonadotropin-releasing hormone receptor, indocyanine green, ovarian cancer

INTRODUCTION

Among all gynecologic malignancies, ovarian cancer is the most common cause of death worldwide (1). The 10-year survival rate is only 15% for patients diagnosed with stage III-IV disease (2). Unfortunately, over 80% of cases are diagnosed at advanced stages. Currently, cytoreductive surgery remains the cornerstone of treatment for advanced ovarian cancer. The completeness of cytoreduction is associated with local recurrence rates and clinical outcomes (3). The median survival time of patients who undergo complete resection of all visible disease (R0) is 99.1 months, and the corresponding durations for patients with residuals of 0.1–1 cm or >1 cm are 36.2 or 29.6 months, respectively (4). Patients with R0 resection seem to have the best overall outcomes (5). However, the R0 resection rate is only 8.1% in patients with stage IV epithelial ovarian cancer and 51.2% in patients with stage IIIC or IV ovarian cancer after neoadjuvant chemotherapy (6, 7). Successful cytoreduction relies on the accurate localization of cancerous lesions, especially minimal residual diseases, followed by their complete resection.

Traditional imaging approaches, such as ultrasound, CT, and MRI, are more suitable for pre- and post-operative assessment. The combination of real-time fluorescence imaging and tumor-targeted fluorophores can transform the paradigm of surgery through the accurate intraoperative differentiation of cancer from adjacent normal tissue (8). Such an approach might improve staging and survival rates.

Over the past two decades, researchers have attempted to improve the fluorescence imaging system, identify potential targetable biomarkers, and develop tumor-specific fluorophores for clinical applications (9–11). In particular, near-infrared fluorescence (NIRF) imaging is advantageous for clinical use owing to its improved penetration depth and limited autofluorescence compared with visible-light fluorescence imaging (12). Indocyanine green (ICG) is the first FDA-approved near-infrared fluorophore and has been widely used in clinical angiography and lymphography. Through binding with serum proteins, ICG has also been used to nonspecifically detect cancers as a result of an enhanced permeability and retention (EPR) effect (13). The EPR effect for large particles (proteins, macromolecules, and liposomes) has been widely observed in solid tumors, mainly because of extensive angiogenesis, leaky vasculature, and impaired lymphatic drainage (14). However, this may not be ideal for the detection of ovarian cancer metastasis, owing to nonspecific signals (for example, inflammation) (15). The need for tumor-specific near-infrared agents remains.

A promising target for ovarian cancer is the gonadotropin-releasing hormone receptor (GnRHR). High-affinity GnRHR binding spots have been reported in 78% of ovarian cancers as well as in other hormone-related cancers (85% of endometrial cancers, 50% of breast cancers, and 86% of prostate cancers) (16, 17). Hence, GnRHR may be a good target for imaging purposes. As a ligand of GnRHR, GnRH peptide has already been conjugated to cytotoxic drugs or nanoparticles for targeted therapy and has shown strong antitumor activities.

In this study, we report the use of a molecular imaging probe using GnRH peptide, a specific and high-affinity GnRHR ligand, conjugated to the near-infrared fluorophore ICG. GnRHa-ICG showed specific binding capacities to GnRHR-positive cancer cells and effectively distinguished peritoneal metastases from adjacent normal tissue in ovarian cancer mouse models.

MATERIALS AND METHODS

Analysis of the Cancer Genome Atlas (TCGA) Data

Transcriptome profiling data related to samples of ovarian cancer, breast cancer, endometrial cancer, and prostate cancer were downloaded from the TCGA data portal (2019). The GnRHR mRNA expression level is presented as FPKM-UQ (Upper Quartile normalized Fragments Per Kilobase to transcript per Million mapped reads).

Cell Culture

A total of six cell lines were used for the experiments, including human ovarian cancer cell lines (A2780, CAOV-3, ES-2, and HeyA8), immortalized human normal ovarian surface epithelial (OSE) cells, and the human lung cancer cell line H1299. All cell lines were archived in our laboratory. Cells were cultured in RPMI-1640 medium containing 10% fetal bovine serum.

Histology

Tissue microarrays comprising 56 high-grade serous ovarian cancer tissue samples were obtained from the tissue bank of the Obstetrics and Gynecology Hospital of Fudan University after Ethical Committee approval. The slides were stained with standard hematoxylin-eosin (HE) and immunohistochemistry (IHC) staining using a 1:100 dilution of GnRHR antibody (ab183079, Abcam). The GnRHR expression level was categorized as low, medium, or high.

Western Blot

Protein lysates were obtained using cell lysis buffer supplemented with protease inhibitor. Proteins were separated by SDS-PAGE and transferred onto nitrocellulose filter membranes (Millipore). The membrane was incubated with the following primary antibodies: GnRHR antibody (Abcam, ab183079) and β-tubulin (Absin, abs830032). Proteins were visualized by chemiluminescence using the ImageQuant LAS4000 system (GE).

Synthesis of GnRHa-ICG

The peptide sequence of GnRH antagonist Cetrorelix (D-2-Nal-D-4-Cl-Phe-D-3-Pal-Ser-Tyr-D-Cit-Leu-Arg-Pro-D-Ala-NH_2) was adopted as the GnRHa peptide. GnRHa peptide (>95% purity) was synthesized using standard solid-phase methods (GL Biochem Ltd., Shanghai, China). Fluorescein isothiocyanate (FITC) was labeled on the N-terminus of the peptide by an Acp (amino caproic acid) linker. For the synthesis of GnRHa-ICG, GnRHa peptide (3 mg) and 20 μL of N, N-diisopropylethylamine were added into 0.5 mL of ultra-dry DMF and reacted for 10 min under nitrogen protection. ICG-NHS (1 mg) was added into the solution and continued reacted for 12 h at room temperature. The mixture was precipitated using 5 mL of ether. The obtained solid was dissolved with methanol and subjected to high performance liquid chromatography (HPLC) purification (Eluent: water/methanol) to obtain the green solid (2 mg). The final products of GnRHa-FITC and GnRHa-ICG were identified by analytical HPLC and MALDI mass spectroscopy.

Fluorescence Microscopy

The cells were placed in an 8-well chamber slide (Ibidi) and grown to ∼60% confluence. A2780, CAOV-3, ES-2, and HeyA8 cells were incubated with 100 μmol/L GnRHa-FITC, and A2780, OSE, and H1299 cells were incubated with 20 μmol/L GnRHa-ICG or ICG (Sigma-Aldrich) for 60 min at 37°C. After incubation, the cells were washed with PBS, fixed in 4% paraformaldehyde, labeled with WGA Alexa Fluor 594 conjugate or WGA Alexa Fluor 488 conjugate (Invitrogen), and mounted with DAPI. These samples were analyzed using TCS SP5 confocal microscopy (Leica). For quantitative analysis, the mean fluorescence intensity was calculated using ImageJ software (version 1.50 g).

Flow Cytometry

A2780 and OSE cells were placed in 6-well plates, grown to ∼70% confluence, and then incubated with GnRHa-FITC (20 μmol/L) or GnRHa-ICG/ICG (10 μmol/L) for 30 min at 37°C. For the blocking experiments, cells were pretreated with 100 μmol/L GnRHa peptide for 10 min and then incubated with 2 μmol/L GnRHa-ICG for 30 min at 37°C. Samples were measured on a CytoFLEX flow cytometer (Beckman Coulter) or a FACSAria flow cytometer (BD Biosciences). All samples were examined in triplicate. Data were analyzed using FlowJo software (version X 10.0.7).

Cell Viability Assay

A2780 cells were seeded in 96-well plate and grown to ∼40% confluence. Cells were incubated with GnRHa-ICG at different concentrations: 0, 1, 10, and 100 μmol/L. Each group had 4 sub-wells. After exposure for 48 h, cell viabilities were assessed by Cell Counting Kit-8 assay (Dojindo). The absorbance at 450 nm (reference wavelength: 630 nm) was measured with a microplate reader.

Animal Model

The xenograft model for metastatic ovarian cancer was previously described (18). Female Balb/c nude mice (5–6 weeks old) were intraperitoneally injected with 1×10^7 A2780 cells. Tumors were allowed to grow for 2–3 weeks. The Institutional Animal Care and Use Committee of Fudan University approved all protocols presented in these studies.

Near-Infrared Fluorescence Imaging

For *ex vivo* GnRHa-ICG and ICG (0, 1, 10, and 20 μmol/L) imaging, fluorescence signals were taken using the IVIS Lumina K imaging system (PerkinElmer) and the clinically used Fluorescence Navigation system (the FloNavi, Optomedic Technique Inc., Guangdong, China). For intraperitoneal metastasis imaging, 0.72 μmol/kg of GnRHa-ICG or ICG was injected intraperitoneally in mice. Mice were sacrificed at the indicated times (n = 3 per group), and the abdominal cavities were exposed. Fluorescence images were obtained using the IVIS Lumina K imaging system (PerkinElmer) with a 780 nm excitation filter and an 845 nm emission filter. For *ex vivo* imaging, xenografts and organs were immediately dissected and analyzed after sacrifice.

Fluorescence signals were quantified as the average radiant efficiency ([p/s/cm²/sr]/[μW/cm²]) using the Living Image software. The fluorescence intensity was measured by drawing a region of interest (ROI) around the area. The tumor-to-background ratio (TBR) was calculated as the average fluorescence intensity of the tumor divided by that of the skeletal muscle or intestine.

In vivo Toxicity Test

The toxicity of GnRHa-ICG was determined in Balb/c nude mice ($n = 4$). Two groups received intraperitoneal injections of 1.5 mg/kg GnRHa-ICG and were followed for 2 and 96 h. The control group received vehicle alone. Blood draws were done to assess alanine transaminase (ALT), aspartate transaminase (AST), blood urea nitrogen (BUN), creatinine (CREA), white blood cells (WBC), and red blood cells (RBC). Tissues of the heart, lung, liver, spleen and kidney were harvested for HE staining.

Statistical Analysis

Student's t-tests were used to compare the intensities. Values of $P < 0.05$ were considered significant and reported as mean ± SD.

RESULTS

GnRHR Is Overexpressed in Human Ovarian Cancer

To evaluate the relevance of GnRHR as an imaging target in human ovarian cancer, we first analyzed 373 cases of serous ovarian cancer from TCGA datasets. GnRHR mRNA expression was found in 89.5% of these samples (**Figure 1A**). In addition, 97.5% of breast cancers, 79.1% of endometrial cancers, and 97.1% of prostate cancers in the TCGA datasets also expressed GnRHR (**Figure 1B**), suggesting that GnRHR targeting may be effective in other hormone-related tumors. In addition, we analyzed GnRHR expression in various normal tissues from the Genotype-Tissue Expression (GTEx) Portal database. Higher expression of GnRHR mRNA was observed in ovaries than in other tissues in the abdominal and pelvic cavities (**Figure 1C**). GnRHR expression was confirmed by IHC analysis of 56 high-grade serous ovarian carcinomas from our tissue bank. Moderate (10 cases, 18%) and high (43 cases, 77%) expression of GnRHR was observed in 95% of these tumors (**Figure 1D**), consistent with previous studies (17, 19). Collectively, these data suggested that GnRHR could be a potential imaging target for the detection of ovarian cancer.

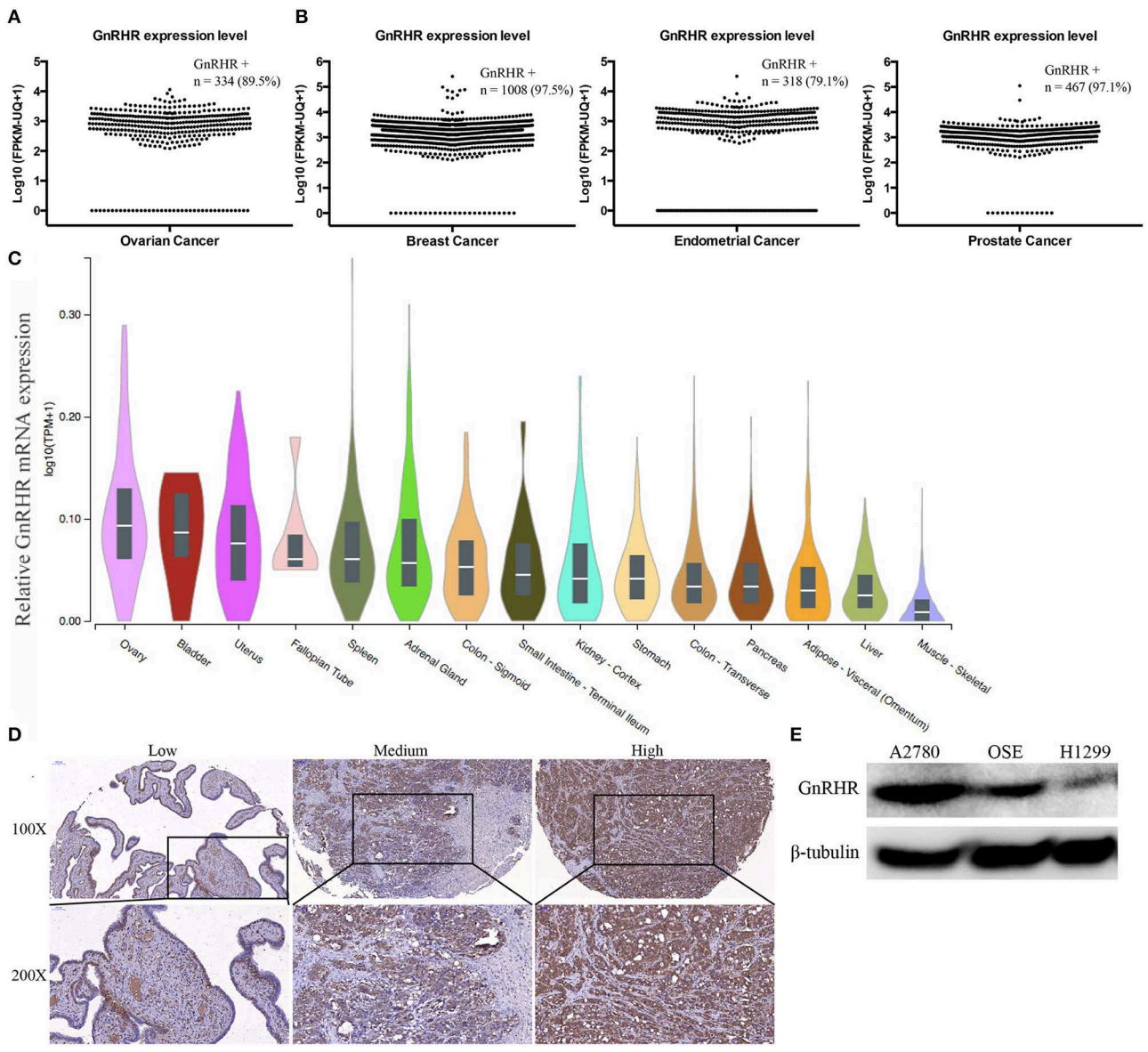

FIGURE 1 | Gonadotropin-releasing hormone receptor is overexpressed in human ovarian cancer. Scatter plot of the GnRHR mRNA expression level in **(A)** serous ovarian cancer, **(B)** breast cancer, endometrial cancer, and prostate cancer from the TCGA dataset. **(C)** Relative GnRHR mRNA expression in human normal tissues. **(D)** Representative IHC staining for GnRHR in high-grade serous ovarian cancer. **(E)** Western blot showing GnRHR expression in different cell lines.

GnRHR expression in cancer cell lines was evaluated by western blot. The ovarian cancer cell line A2780 and immortalized normal OSE cells showed high expression levels; the lung cancer cell line H1299 showed low expression levels (**Figure 1E**). Therefore, we selected A2780 and OSE as the positive controls and H1299 as the negative control for further studies.

Synthesis and Characterization of GnRHa-ICG

ICG was conjugated to the GnRHa peptide (D-2-Nal-D-4-Cl-Phe-D-3-Pal-Ser-Tyr-D-Cit-Leu-Arg-Pro-D-Ala-NH_2). We chose the peptide sequence of Cetrorelix, a widely used GnRHR antagonist, which has several amino acids modified from the natural hypothalamic hormone (20). A schematic diagram of the molecular structure is shown in **Figure 2A**. The final product was identified by analytical HPLC (**Figure 2B**). The molecular weight of GnRHa-ICG was 2082 Da. The conjugated near-infrared fluorophore had an excitation wavelength of 795 nm and emitted light at 810 nm (**Figures 2C,D**). *Ex vivo* fluorescence imaging of GnRHa-ICG and ICG was obtained using the IVIS Lumina K imaging system (**Figure S1A**) and clinically used Fluorescence Navigation System (**Figure S1B**).

The Enhanced Cell Binding Capacity of GnRHa-ICG

To test whether GnRHa peptide was taken up by ovarian cancer cells, we incubated GnRHa-FITC with different cell lines. Fluorescence signals were detected in different ovarian cancer cell lines (**Figure 3A**). Flow cytometry analysis confirmed the accumulation of GnRHa-FITC in A2780 and OSE cells (**Figure 3B**).

Next, we incubated GnRHa-ICG with cancer cell lines with different GnRHR expression levels. A significant difference

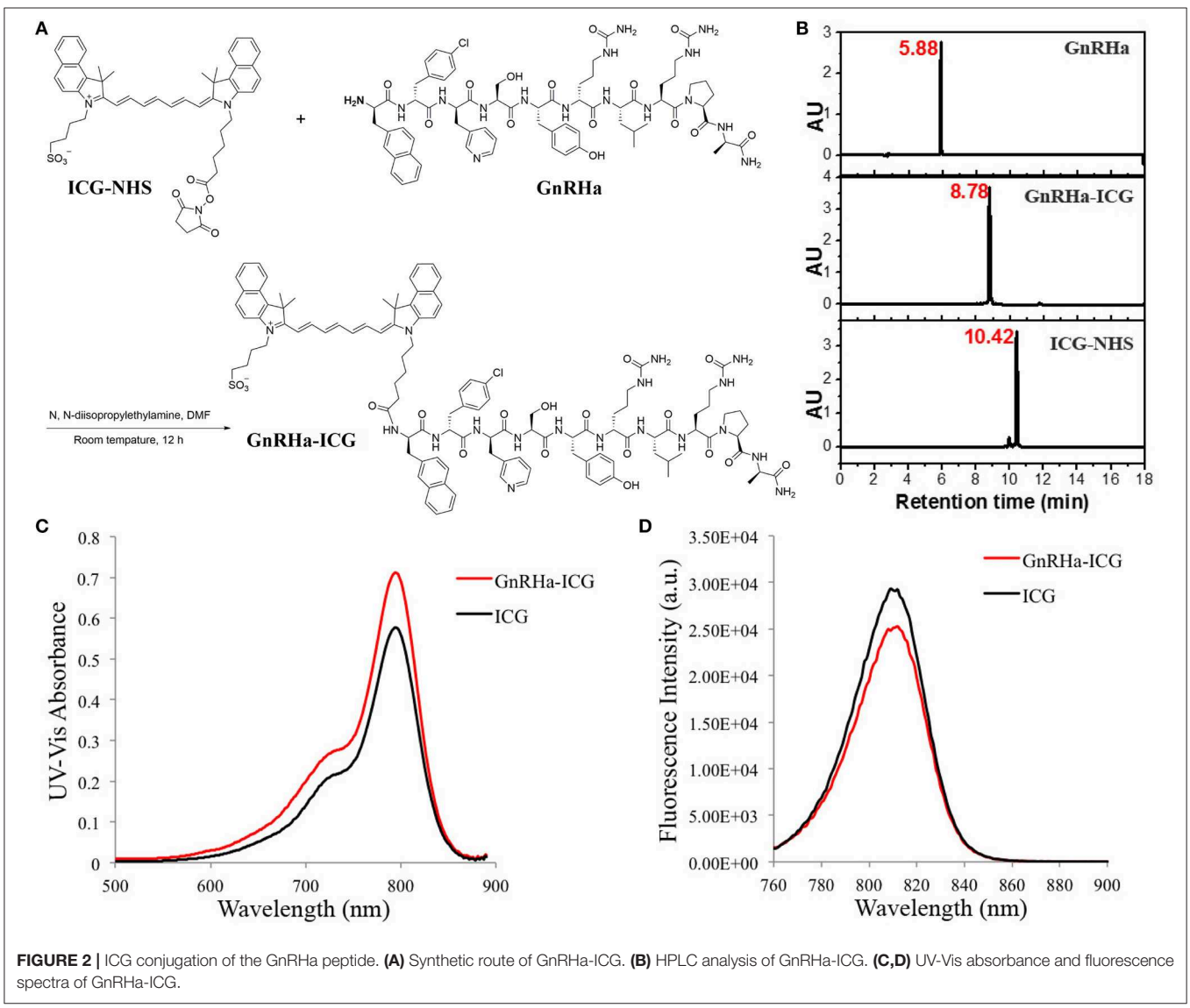

FIGURE 2 | ICG conjugation of the GnRHa peptide. **(A)** Synthetic route of GnRHa-ICG. **(B)** HPLC analysis of GnRHa-ICG. **(C,D)** UV-Vis absorbance and fluorescence spectra of GnRHa-ICG.

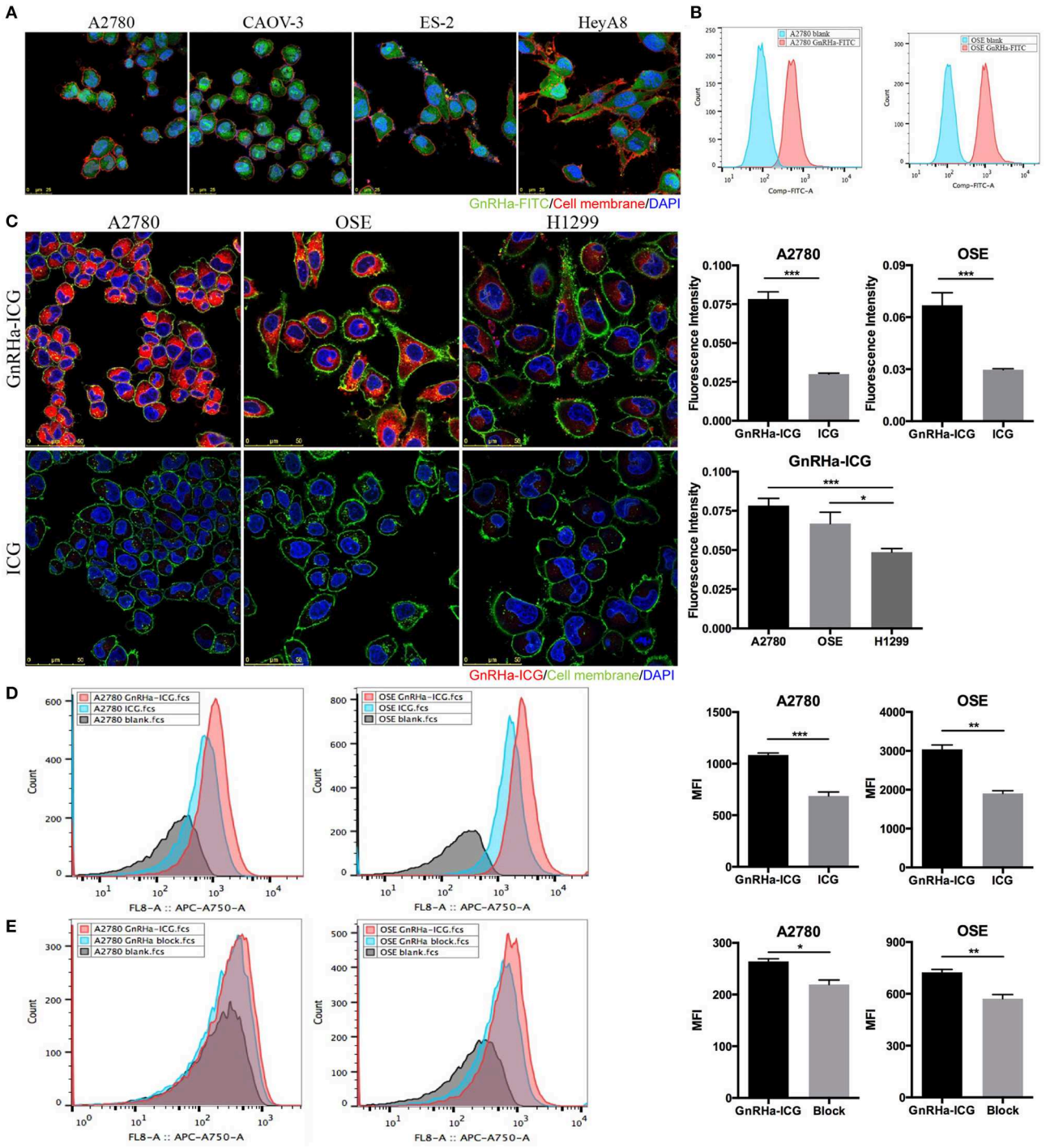

FIGURE 3 | Cell binding study of GnRHa-ICG. **(A)** Representative fluorescence microscopy images of ovarian cancer cells after incubation with GnRHa-FITC. **(B)** Flow cytometry analysis of A2780 and OSE cells after incubation with GnRHa-FITC. **(C)** Comparison between GnRHa-ICG and ICG in A2780, OSE, and H1299 cells. **(D)** Flow cytometry analysis of A2780 and OSE cells after incubation with GnRHa-ICG and ICG. **(E)** Flow cytometry analysis of A2780 and OSE cells after the GnRHa block (*$P < 0.01$; **$P < 0.001$; ***$P < 0.0001$).

in fluorescence intensity was detected between the GnRHR-positive cell lines (A2780 and OSE) and the GnRHR-negative cell line (H1299) (**Figure 3C**). The fluorescence intensity in the A2780 and OSE cells was 1.56- and 1.34-fold higher, respectively, than that in the H1299 cells. To control for nonspecific binding, incubation with ICG alone was performed.

A significant difference in the fluorescence signal was observed between ICG (20 μM) and GnRHa-ICG (20 μM) (**Figure 3C**). The fluorescence signal was 2.61 and 2.25 times lower than that with the incubation of GnRHa-ICG in A2780 and OSE cells, respectively. We further confirmed the accumulation of GnRHa-ICG in GnRHR-positive cells by flow cytometry analysis (**Figure 3D**). In addition, competition of GnRHa-ICG with unlabeled GnRHa resulted in a partial reduction in fluorescence intensity (**Figure 3E**). To address concerns of possible side effects caused by GnRHa-ICG, we assessed the tumorigenic potential of GnRHa-ICG exposure by assessing the cell viability of GnRHR positive A2780 cells. Our results indicated that a 48-h exposure does not increase cell viability (**Figure S2**). Taken together, these results demonstrated the GnRHR-specific binding capacity of GnRHa-ICG.

GnRHa-ICG Specifically Recognized Peritoneal Metastases of Ovarian Cancer

Common metastasis sites of ovarian cancer include the omentum, mesentery, and intestine. To evaluate its specificity for *in vivo* cancer imaging, we injected GnRHa-ICG and ICG intraperitoneally into a mice model of metastatic ovarian cancer and control mice. Mice were sacrificed 2 h after injection, and fluorescence images were obtained and NIRF signals analyzed using the IVIS Lumina K imaging system (**Figure 4A**). Separate fluorescence intensities of the tumor and background (muscle and intestine) per dose group are shown in **Figure S3**. A dose of 1.5 mg/kg was considered for the following experiments because of the higher TBR. In tumor-bearing mice, GnRHa-ICG specifically localized to peritoneal tumors, while accumulation of ICG was observed not only at the tumor site but also in the intestine. Control mice injected with GnRHa-ICG did not show fluorescence signals, which indicated a low background in normal tissues. In contrast, the intestine exhibited high fluorescence signals in normal mice injected with ICG. The corresponding *ex vivo* imaging of the intestine with mesenteric metastasis is shown in **Figure 4B**. Tiny tumor nodules (∼1 mm) on the mesentery could also be visualized while the intestine exhibited few fluorescence signals after GnRHa-ICG administration. The intraperitoneal lesions were also confirmed

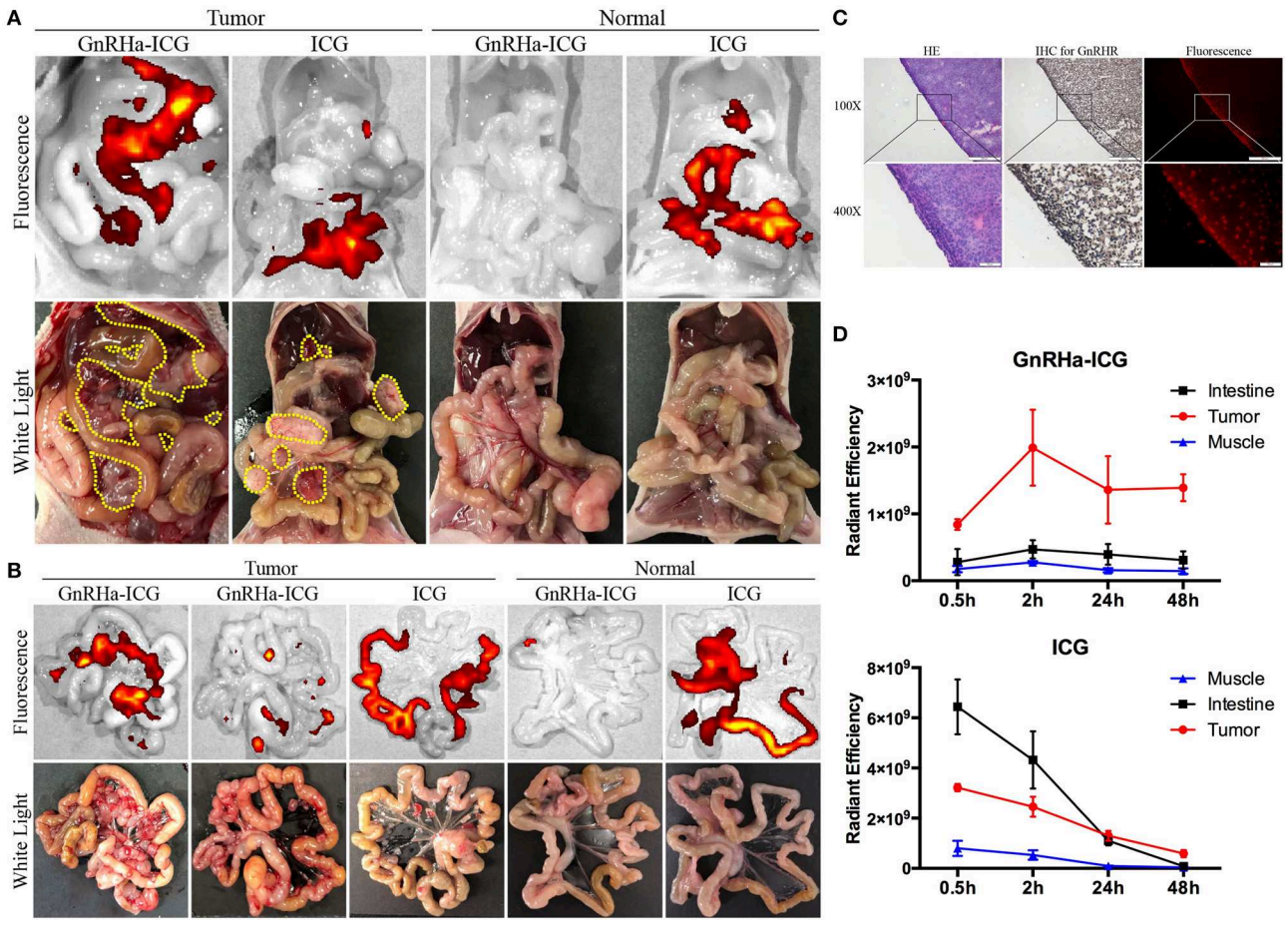

FIGURE 4 | GnRHa-ICG localizes to GnRHR expression in peritoneal ovarian cancer. Representative images of the **(A)** peritoneal cavity and **(B)** mesentery 2 h after the injection of GnRHa-ICG and ICG. Yellow dotted lines indicate the tumor location. **(C)** Histopathological analysis of a tumor slice showing the colocalization of tumor cells, GnRHR expression, and GnRHa-ICG fluorescence. **(D)** Comparison of fluorescence intensities between the tumor, muscle, and intestine.

by pathology and exhibited GnRHR overexpression and the accumulation of GnRHa-ICG (**Figure 4C**).

Metastases of ovarian cancer are widely spread in the pelvic and abdominal cavities, and both the intestine and muscle were considered as the background. To further evaluate the capacity of GnRHa-ICG for distinguishing peritoneal metastases from background tissues, the fluorescence intensities of the tumor, intestine, and muscle were collected at 0.5, 2, 24, and 48 h (**Figure 4D**). GnRHa-ICG exhibited few fluorescence signals in the intestine and muscle tissues at any time point. ICG exhibited higher fluorescence signals in the intestine tissues than in tumors before 24 h and similar fluorescence signals in both tissues after 24 h. The TBR is shown in **Figure S4**. The TBR of GnRHa-ICG was stable between 2 and 48 h. Although the TBR of ICG increased after 24 h because of the EPR effect and fast clearance, the fluorescence intensities of the tumor decreased quickly and might have influenced the detection of tumor signals. Furthermore, according to a previous study, the clinical use of ICG based on the EPR effect was not viable owing to a high false-positive rate, especially in lymph node and inflammatory tissues (15). In the present study, *ex vivo* imaging of the brain did not show fluorescence signals compared to the tumor and ovarian tissues, which indicated limited binding of GnRHa-ICG to the hypothalamic GnRHR receptor (**Figures S5A,C**). In addition, fewer fluorescence signals were detected in the benign retroperitoneal lymph nodes than in the tumor (**Figures S5B–C**).

These data suggested that GnRHa-ICG could specifically recognize metastatic lesions from peritoneal normal tissues and intestine tissues, and the modification of GnRHa improved the capacity of ICG for tumor imaging.

Dynamics and Biodistribution of GnRHa-ICG

To evaluate the biodistribution of probes, the fluorescence signals of *ex vivo* tumor and organs were collected at 2 h post administration. Confocal imaging of A2780 xenograft

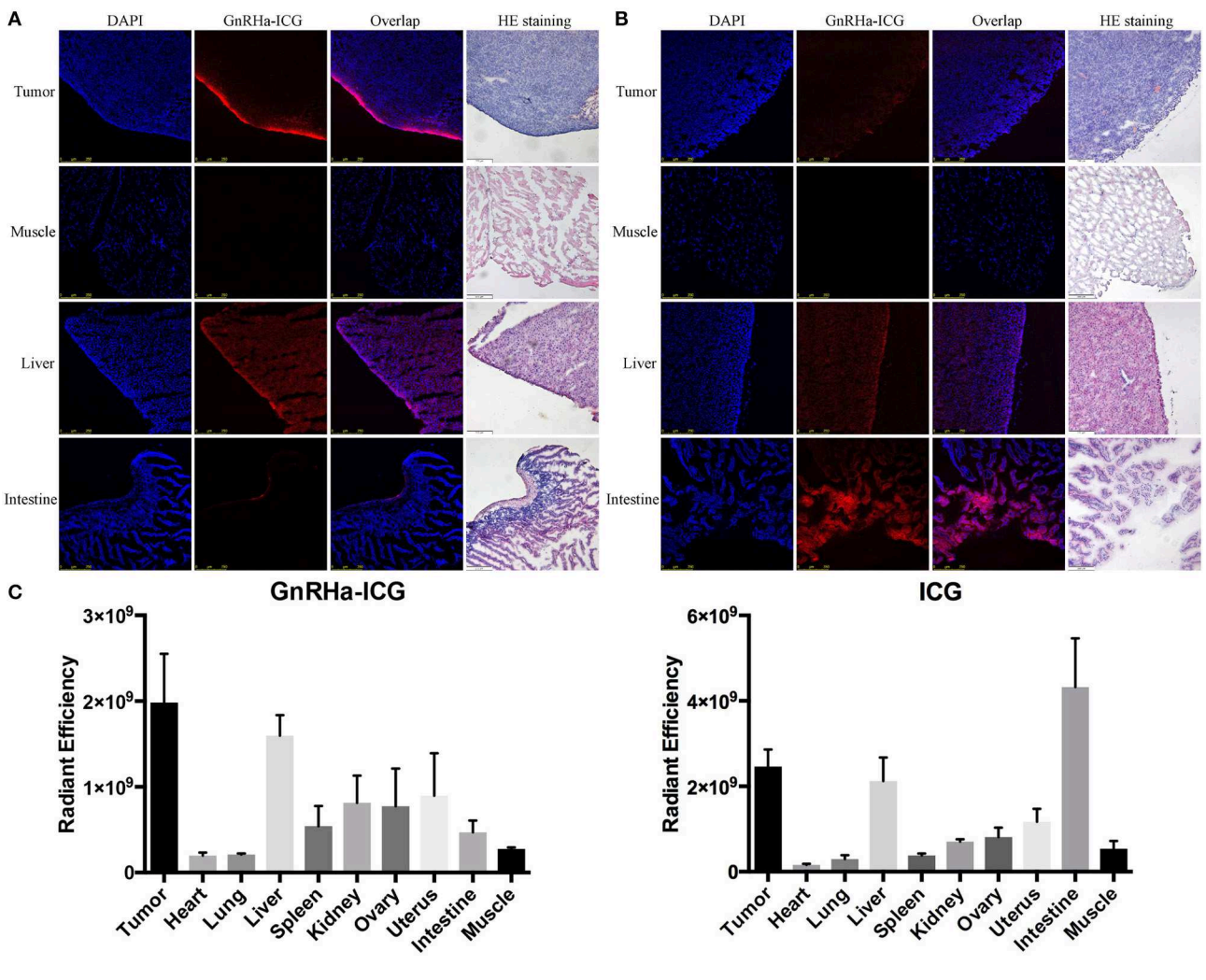

FIGURE 5 | Comparison of biodistribution between GnRHa-ICG and ICG. Confocal microscopy of frozen sections of tumors and other organs in mice injected with **(A)** GnRHa-ICG and **(B)** ICG. **(C)** Biodistribution of GnRHa-ICG and ICG 2 h after injection.

confirmed the high accumulation of GnRHa-ICG, while ICG also demonstrated a weak signal in the tumor, mainly because of leaky vasculature and impaired lymphatic drainage in the tumor tissues (EPR effect) (**Figures 5A,B**). Additionally, ICG showed strong fluorescence signals in the liver and intestine. These results were consistent with the *in vivo* fluorescence signal. As shown in **Figure 5C**, a biodistribution assay of ICG also showed high fluorescence in the liver and intestine, indicating liver-intestine clearance, while GnRHa-ICG showed low fluorescence in the intestine.

The metabolism of GnRHa-ICG in A2780 tumor-bearing mice was further evaluated. Mice were injected intraperitoneally with GnRHa-ICG and monitored for 96 h. Representative *ex vivo* NIRF images of different time points are presented (**Figure 6A**). The mean fluorescence intensities of the xenografts and organs of different time points are shown (**Figure 6B**). GnRHa-ICG was cleared mainly through the liver pathway and reached the highest fluorescence density in the liver at 24 h post administration. The fluorescence signal of the A2780 xenografts peaked in intensity at 2 h. The tumor fluorescence intensities were maintained for up to 48 h and decreased slightly after that. The plateau period (from 2 to 48 h) of GnRHa-ICG specific accumulation may be feasible for clinical applications in cytoreductive surgery. Although normal uterus and ovary tissues also showed a slight increase in fluorescence signals, indicating GnRHR-specific binding of the probe, the intensities of malignant lesions were high enough to differentiate them from those of normal reproductive tissues. Few fluorescence signals were detected in the intestine, kidney, and other normal tissues.

Toxicity of GnRHa-ICG

Toxicity of GnRHa-ICG was determined in Balb/c nude mice ($n = 4$) by measurement of blood panels and hematology. There was no significant difference observed in ALT, AST, CREA, WBC, and RBC between the control and test groups. A slight decrease in BUN was observed 96 h after GnRHa-ICG injection, which may be attributable to dietary factors (**Figure 7A**). Histological observation of different main organs did not present any obvious damage (**Figure 7B**).

DISCUSSION

Herein, we report a novel targeted imaging probe, near-infrared fluorophore GnRHa-ICG, and its successful use to target peritoneal metastases of ovarian cancer in mice models, suggesting a strong potential for the application of fluorescence-guided surgery.

Over the past decade, several studies have demonstrated the potential use of fluorescence-guided surgery in ovarian cancer. Although studies have shown the capacity to detect ovarian cancer in real time, existing probes still have some deficiencies, including poor specificity, insufficient penetration depth, and side effects. Van Dam reported the first human trial of folate receptor α-targeted imaging in ovarian cancer (9). Although this study showed the real-time intraoperative detection of tumor deposits, the imaging agent FITC has a limited penetration depth due to its non-NIR fluorescence spectrum. Vahrmeijer replaced FITC with the NIRF dye Cy7 (OTL38), which improved the penetration depth, but the agent showed nonspecific binding in noncancerous lymph nodes (express folate receptor β) (10). False-positive lymph nodes were also observed in a phase II trial of OTL38 in ovarian cancer (21). Sundaram reported a prolactin receptor-specific probe using placental lactogen (hPL) conjugated to MRI and NIRF imaging agents and showed improved specificity over currently used contrast agents (11). However, continuous exposure (16 days)

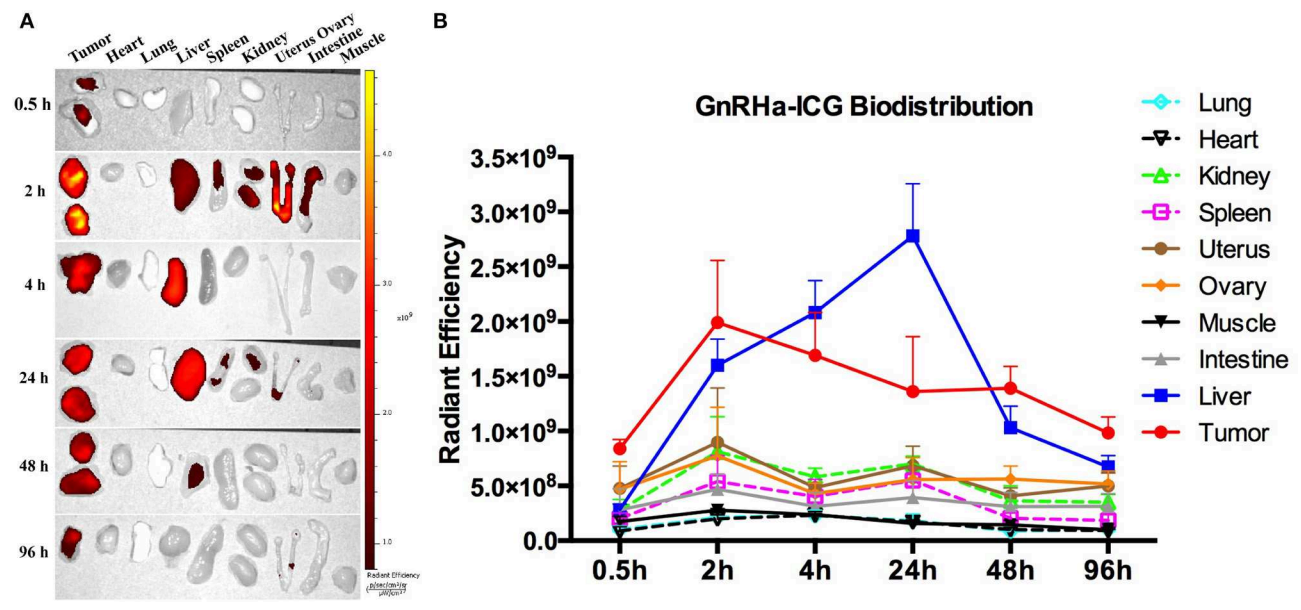

FIGURE 6 | Dynamics and biodistribution of GnRHa-ICG. **(A)** Representative *ex vivo* fluorescence images of A2780 xenografts and mouse organs. **(B)** Biodistribution of GnRHa-ICG.

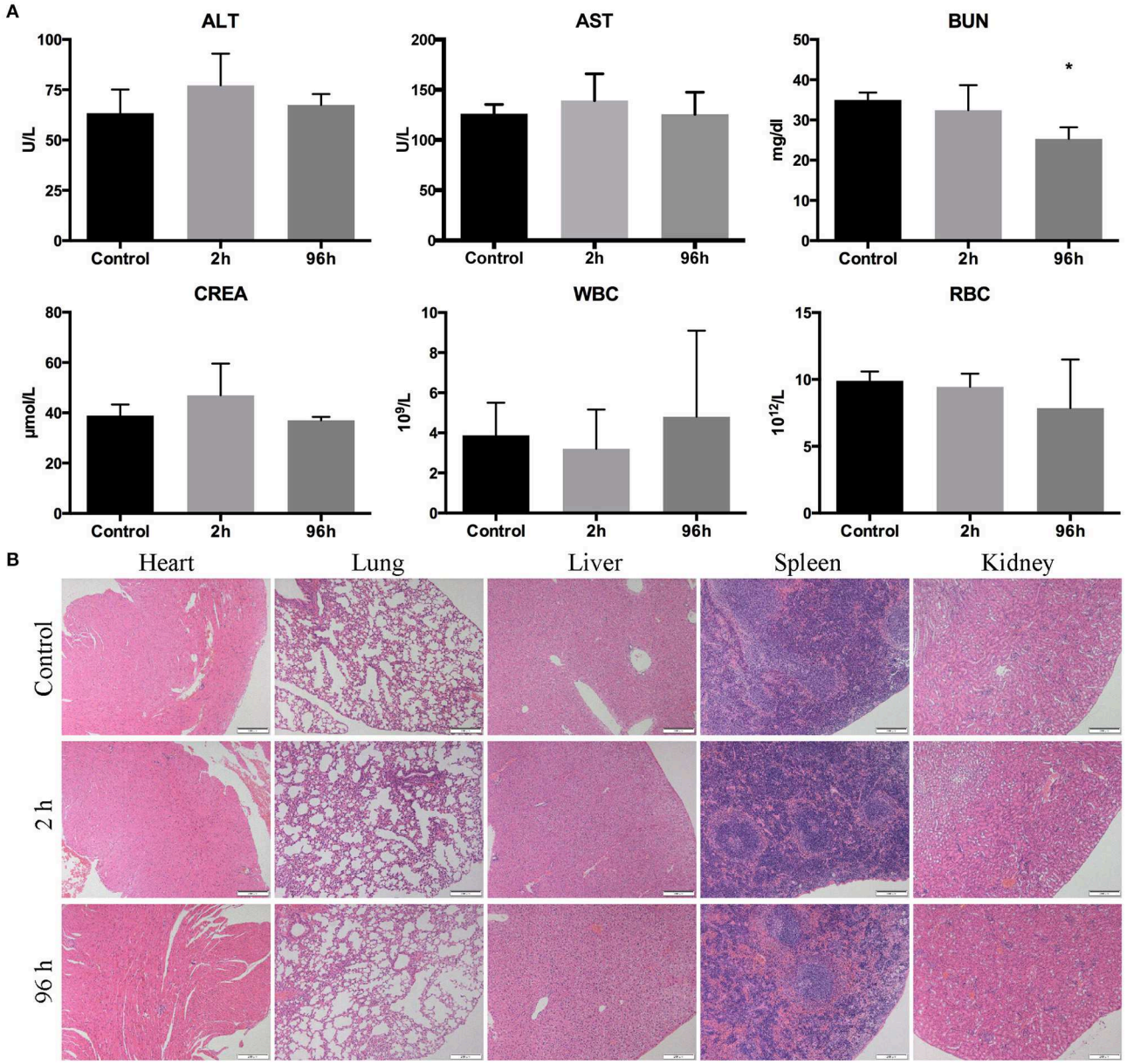

FIGURE 7 | Toxicity of GnRHa-ICG in Balb/c nude mice. **(A)** Assessment of the liver panel, kidney panel, and blood cells. **(B)** HE staining of the heart, lung, liver, spleen, and kidney (*$P < 0.05$).

to hPL conjugates caused increased activity in ovarian cancer cells. Thus, the demand for ovarian cancer-specific near-infrared probes remains.

A significant number of studies on GnRHR-based therapy have substantiated its applicability, specificity, and safety in cancer targeting (16). In this study, we introduced GnRHR as the target for the molecular imaging of ovarian cancer. It is well established that GnRHR is overexpressed in ovarian cancer and other hormone-related cancers, even in some hormone-unrelated cancers (pancreatic cancer, lung cancer, melanoma, and glioblastoma) (17). The expression of GnRHR in ovarian cancer tissue is higher than that in normal ovarian tissue (22). In addition, GnRHR expression is also detected in lymph node metastasis (23). Consistent with previous studies, our own analysis confirmed that the majority (95%) of high-grade serous ovarian cancers express moderate to high levels of GnRHR. Having demonstrated the specific binding capacity of GnRHa-ICG in ovarian cancer, we speculate that our GnRHR imaging concept might also be effective in other tumors with upregulated GnRHR expression.

Currently, a few viable targets, including the folate receptor and prolactin receptor, have emerged for optical imaging in

ovarian cancer. To compare the specificity of these targets, we analyzed the expression of different receptors in normal tissues within the abdominal and pelvic cavities, which may be involved in debulking surgery (GTEx Portal database, data not shown). Higher expression of GnRHR was observed in reproductive tissues than in other tissues. However, higher expression of the folate receptor and prolactin receptor was observed in the gastrointestinal tract. These results suggested that GnRHR might have better specificity than the folate or prolactin receptors. The Lymphadenectomy in Ovarian Neoplasms (LION) trial reported that the removal of clinically negative lymph nodes was not associated with longer survival and may cause excess morbidity and mortality (24). Thus, non-specific binding of noncancerous lymph nodes should be avoided. Compared to the previously reported folate receptor α-targeted probe OTL38 (10, 21) or the clinically used non-specific imaging agent ICG (15), non-specific binding to benign retroperitoneal lymph nodes was not observed using GnRHR-ICG in our mice model of metastatic ovarian cancer.

As the binding ligands of GnRHR, GnRH analogs (both agonists and antagonists) have been conjugated to various cytotoxic drugs and shown a high affinity for cancer cells. Few studies have employed GnRH analogs to achieve targeted delivery of optical imaging agents (25–27). Existing GnRHR-targeted agents use GnRH agonists as the binding moiety and have not been validated in peritoneal metastasis models. Although many studies have demonstrated the antitumor activity of GnRH agonists, contrasting results also exist. Schally's group reported that a [D-Trp^6] GnRH agonist stimulated the proliferation of ovarian cancer cells at a low dose (28). Unlike agonists, antagonists competitively bind to GnRHR without activating the downstream signaling cascade. Several GnRH antagonists are already commercially available and have various clinical applications. Thus, we adopted the peptide sequence of Cetrorelix, a third-generation antagonist, as the targeting sequence of the imaging agent. Cetrorelix has been reported to inhibit the growth of ovarian, endometrial, breast, and prostate cancer, suggesting a potential therapeutic effect as the targeting moiety (17). In the current study, no obvious tumorigenic potential caused by GnRHa-ICG exposure was observed in the *ex vivo* experiments. In terms of the concern of potential binding with the hypothalamic GnRHR, fluorescence imaging of brain indicated limited binding of GnRHa-ICG in the hypothalamus, which may be due to the peritoneal administration of the drugs performed in this study. Further animal studies are warranted to assess the tumorigenic or endocrine potential of GnRHa-ICG.

NIRF imaging is an emerging biomedical imaging modality for fluorescence-guided surgery because of its significant penetration depth, light absorption, real-time capabilities, and absence of ionizing radiation. The first FDA-approved NIRF dye, ICG, has been in clinical use for more than half a century and has proven to be safe and feasible. GnRHa-ICG had the same excitation and emission wavelength as ICG, which made its clinical application possible. Owing to the EPR effect, ICG has been used for the intraoperative identification of cancers, including ovarian, pancreatic, and colorectal cancer (8). However, the ICG detection of ovarian cancer and metastasis is not satisfactory because of nonspecific binding. Tummers reported that despite the successful detection of all metastatic lesions, 13 nonmalignant lesions also exhibited fluorescence, resulting in a high false-positive rate of 62% (15). A recent pilot study revealed that ICG could detect peritoneal metastasis but was unable to distinguish between benign and malignant nodules after neoadjuvant chemotherapy (29). Previous studies have highlighted the need for the development of more specific probes to detect metastatic ovarian cancer.

In this study, we developed a tumor-specific probe, GnRHa-ICG, by conjugating ICG with a GnRH antagonist peptide. Both ICG and the GnRH antagonist (Cetrorelix) were already proven to be safe in clinical use. GnRHa-ICG showed specific binding to peritoneal metastases in ovarian cancer mouse models, whereas ICG was mainly localized to the liver and intestine, consistent with its liver-intestine clearance. ICG also exhibited a weak signal in tumors due to the EPR effect, but the intensity decreased quickly within 48 h. In contrast, the plateau period of GnRHa-ICG accumulation in metastases lasted for nearly 2 days and allowed for flexibility in terms of surgery time, which may be practical for clinical applications. Both ICG and Cetrorelix were cleared through the liver-intestine pathway. The conjugation of GnRHa (the peptide sequence of Cetrorelix) to ICG may have affected the pharmacokinetic and biodistribution properties of the ICG. Liver metabolism of GnRHa-ICG was significantly decreased compare to that of ICG. A slight increase in intestinal signals within the subsequent 96 h indicated that the drug might be cleared through biliary excretion. Whether there are other metabolic pathways remains to be investigated. The toxicity of GnRHa-ICG was assessed, and no obvious hepatotoxicity was observed in the current study.

Previous preclinical studies have developed several ICG-based targeted imaging agents. BLZ-100 is a tumor-targeted imaging agent composed of ICG and the modified CTX peptide, which targets Annexin A2 on cancer cells (30). BLZ-100 was successfully validated in canine tumor models and is being evaluated in phase I clinical trials. Furthermore, Ogawa conjugated ICG to three FDA-approved monoclonal antibodies (daclizumab, trastuzumab, and panitumumab) (31), and a prostate-specific membrane antigen (PSMA)-specific imaging probe was synthesized by linking ICG to the anti-PSMA antibody J591 (32). In contrast to previous studies, we utilized peritoneal rather than systemic administration of the imaging agent. Since ovarian cancer has a peritoneal dissemination pattern, imaging agents can bind to malignant lesions more directly through peritoneal injection. Several studies have testified the viability of the peritoneal administration of imaging agents for detecting peritoneal metastasis (11, 33, 34). Nonetheless, systemic administration of the probe will be attempted to detect distant metastasis or deep lesions in further studies.

Several limitations exist in this study. Further assessment of the tumorigenic or endocrine potential of GnRHa-ICG is needed in molecular levels. The metabolic pathways of GnRHa-ICG remain unclear. The specificity and sensitivity of GnRHa-ICG imaging for ovarian cancer lesions should be investigated in a pilot study.

In summary, the developed GnRHR-targeting imaging agent binds selectively to ovarian cancer. The GnRHa-ICG probe has the potential to aid surgeons in staging and debulking surgery via intraoperative tumor-specific fluorescence imaging. Our GnRHR imaging concept may also be effective in other hormone-related tumors with upregulated GnRHR expression.

DATA AVAILABILITY STATEMENT

The datasets used in this study are available at: TCGA: https://portal.gdc.cancer.gov.

Selection criteria: Primary site: Ovary/Breast/Prostate gland/Corpus uteri; Workflow Type: HTSeq-FPKM-UQ; Data Category: Transcriptome Profiling; Experimental Strategy: RNA-Seq.

GTEx Portal: https://gtexportal.org/home/.

Gene symbol: GnRHR ENSG00000109163; FSHR ENSG00000170820.

ETHICS STATEMENT

The Institutional Animal Care and Use Committee of Fudan University approved all protocols presented in these studies.

AUTHOR CONTRIBUTIONS

QL: experimental studies, data analysis, and writing—original draft. XZho: experimental studies and data analysis. WF, TP, XL, FL, and YK: experimental studies and methodology. XZha and CX: study design and writing—review and editing.

FUNDING

This work was supported by National Key R&D Program of China (2016YFC1303100), National Natural Sciences Foundation of China (81472424), Shanghai Sailing Program (19YF1404400), Shanghai Medical Center of Key Programs for Female Reproductive Diseases (2017ZZ01016), and Shanghai Commission of Science and Technology planning (1494212663).

ACKNOWLEDGMENTS

We express our thanks to Guangdong OptoMedic Technologies Inc. for their assistance in fluorescence imaging using the Fluorescence Navigation system (the FloNavi). We are grateful to Ms. Shengru Pang and Ms. Xiao Guo in the Joint Live Small Animal Imaging Laboratory of Fudan University Shanghai Medical College - PerkinElmer Company, for their technical support in the use of IVIS Lumina K imaging system.

SUPPLEMENTARY MATERIAL

The Supplementary Material for this article can be found online at: https://www.frontiersin.org/articles/10.3389/fonc.2020.00266/full#supplementary-material

Figure S1 | *Ex vivo* fluorescence imaging of GnRHa-ICG and ICG (0, 1, 10, and 20 μmol/L) using the IVIS Lumina K imaging system and clinically used Fluorescence Navigation system. **(A)** Fluorescence images of the IVIS Lumina K imaging system. **(B)** Fluorescence images of the Fluorescence Navigation system.

Figure S2 | Cell viability of A2780 cells treated with GnRHa-ICG. Samples include no exposure to GnRHa-ICG (control) and a 48-h exposure to different concentrations of GnRHa-ICG.

Figure S3 | Dose-escalation cohort of GnRHa-ICG. **(A)** Mean fluorescence intensities of the tumor and background tissues. **(B)** Tumor-to-background ratio per dose group.

Figure S4 | Tumor-to-background ratio of GnRHa-ICG and ICG at different time points. **(A)** Tumor-to-intestine ratio. **(B)** Tumor-to-muscle ratio.

Figure S5 | Limited binding of GnRHa-ICG in the brain and lymph node tissues. **(A)** *Ex vivo* imaging of the hypothalamus (yellow arrow). **(B)** *Ex vivo* imaging of lymph node tissues (yellow arrow). **(C)** Histopathological analysis of the hypothalamus and lymph node tissues. Liver tissue was used as a positive control.

REFERENCES

1. Bray F, Ferlay J, Soerjomataram I, Siegel RL, Torre LA, Jemal A. Global cancer statistics 2018: GLOBOCAN estimates of incidence and mortality worldwide for 36 cancers in 185 countries. *CA Cancer J Clin.* (2018) 68:394–424. doi: 10.3322/caac.21492
2. Narod S. Can advanced-stage ovarian cancer be cured? *Nat Rev Clin Oncol.* (2016) 13:255–261. doi: 10.1038/nrclinonc.2015.224
3. Horowitz NS, Miller A, Rungruang B, Richard SD, Rodriguez N, Bookman MA, et al. Does aggressive surgery improve outcomes? Interaction between preoperative disease burden and complex surgery in patients with advanced-stage ovarian cancer: an analysis of GOG 182. *J Clin Oncol.* (2015) 33:937–43. doi: 10.1200/JCO.2014.56.3106
4. du Bois A, Reuss A, Pujade-Lauraine E, Harter P, Ray-Coquard I, Pfisterer J. Role of surgical outcome as prognostic factor in advanced epithelial ovarian cancer: a combined exploratory analysis of 3 prospectively randomized phase 3 multicenter trials: by the Arbeitsgemeinschaft Gynaekologische Onkologie Studiengruppe Ovarialkarzinom (AGO-OVAR) and the Groupe d'Investigateurs Nationaux Pour les Etudes des Cancers de l'Ovaire (GINECO). *Cancer.* (2009) 115:1234–44. doi: 10.1002/cncr.24149
5. Nick AM, Coleman RL, Ramirez PT, Sood AK. A framework for a personalized surgical approach to ovarian cancer. *Nat Rev Clin Oncol.* (2015) 12:239–45. doi: 10.1038/nrclinonc.2015.26
6. Winter WE III, Maxwell GL, Tian C, Sundborg MJ, Rose GS, Rose PG, et al. Tumor residual after surgical cytoreduction in prediction of clinical outcome in stage IV epithelial ovarian cancer: a Gynecologic Oncology Group Study. *J Clin Oncol.* (2008) 26:83–9. doi: 10.1200/JCO.2007.13.1953
7. Vergote I, Trope CG, Amant F, Kristensen GB, Ehlen T, Johnson N, et al. Neoadjuvant chemotherapy or primary surgery in stage IIIC or IV ovarian cancer. *N Engl J Med.* (2010) 363:943–53. doi: 10.1056/NEJMoa0908806
8. Zhang RR, Schroeder AB, Grudzinski JJ, Rosenthal EL, Warram JM, Pinchuk AN, et al. Beyond the margins: real-time detection of cancer using targeted fluorophores. *Nat Rev Clin Oncol.* (2017) 14:347–64. doi: 10.1038/nrclinonc.2016.212
9. van Dam GM, Themelis G, Crane LM, Harlaar NJ, Pleijhuis RG, Kelder W, et al. Intraoperative tumor-specific fluorescence imaging in ovarian cancer by folate receptor-alpha targeting: first in-human results. *Nat Med.* (2011) 17:1315–9. doi: 10.1038/nm.2472
10. Hoogstins CE, Tummers QR, Gaarenstroom KN, de Kroon CD, Trimbos JB, Bosse T, et al. A novel tumor-specific agent for intraoperative near-infrared fluorescence imaging: a translational study in healthy volunteers

and patients with Ovarian cancer. *Clin Cancer Res.* (2016) 22:2929–38. doi: 10.1158/1078-0432.CCR-15-2640
11. Sundaram KM, Zhang Y, Mitra AK, Kouadio JK, Gwin K, Kossiakoff AA, et al. Prolactin receptor-mediated internalization of imaging agents detects epithelial ovarian cancer with enhanced sensitivity and specificity. *Cancer Res.* (2017) 77:1684–96. doi: 10.1158/0008-5472.CAN-16-1454
12. Haque A, Faizi MSH, Rather JA, Khan MS. Next generation NIR fluorophores for tumor imaging and fluorescence-guided surgery: a review. *Bioorg Med Chem.* (2017) 25:2017–34. doi: 10.1016/j.bmc.2017.02.061
13. Kosaka N, Mitsunaga M, Longmire MR, Choyke PL, Kobayashi H. Near infrared fluorescence-guided real-time endoscopic detection of peritoneal ovarian cancer nodules using intravenously injected indocyanine green. *Int J Cancer.* (2011) 129:1671–7. doi: 10.1002/ijc.26113
14. Maeda H, Wu J, Sawa T, Matsumura Y, Hori K. Tumor vascular permeability and the EPR effect in macromolecular therapeutics: a review. *J Control Rel.* (2000) 65:271–84. doi: 10.1016/S0168-3659(99)00248-5
15. Tummers QR, Hoogstins CE, Peters AA, de Kroon CD, Trimbos JB, van de Velde CJ, et al. The value of intraoperative near-infrared fluorescence imaging based on enhanced permeability and retention of indocyanine green: feasibility and false-positives in ovarian cancer. *PLoS ONE.* (2015) 10:e0129766. doi: 10.1371/journal.pone.0129766
16. Ghanghoria R, Kesharwani P, Tekade RK, Jain NK. Targeting luteinizing hormone-releasing hormone: A potential therapeutics to treat gynecological and other cancers. *J Control Rel.* (2018) 269:277–301. doi: 10.1016/j.jconrel.2016.11.002
17. Limonta P, Montagnani Marelli M, Mai S, Motta M, Martini L, Moretti RM. GnRH receptors in cancer: from cell biology to novel targeted therapeutic strategies. *Endocr Rev.* (2012) 33:784–811. doi: 10.1210/er.2012-1014
18. Lengyel E, Burdette JE, Kenny HA, Matei D, Pilrose J, Haluska P, et al. Epithelial ovarian cancer experimental models. *Oncogene.* (2014) 33:3619–33. doi: 10.1038/onc.2013.321
19. Feng Z, Wen H, Bi R, Ju X, Chen X, Yang W, et al. A clinically applicable molecular classification for high-grade serous ovarian cancer based on hormone receptor expression. *Sci Rep.* (2016) 6:25408. doi: 10.1038/srep25408
20. Reissmann T, Schally AV, Bouchard P, Riethmiiller H, Engel J. The LHRH antagonist cetrorelix: a review. *Hum Reprod Update.* (2000) 6:322–31. doi: 10.1093/humupd/6.4.322
21. Randall LM, Wenham RM, Low PS, Dowdy SC, Tanyi JL. A phase II. Multicenter, open-label trial of OTL38 injection for the intra-operative imaging of folate receptor-alpha positive ovarian cancer. *Gynecol Oncol.* (2019) 155:63–8. doi: 10.1016/j.ygyno.2019.07.010
22. Dharap SS, Wang Y, Chandna P, Khandare JJ, Qiu B, Gunaseelan S, et al. Tumor-specific targeting of an anticancer drug delivery system by LHRH peptide. *Proc Natl Acad Sci USA.* (2005) 102:12962–7. doi: 10.1073/pnas.0504274102
23. Liu SV, Schally AV, Hawes D, Xiong S, Fazli L, Gleave M, et al. Expression of receptors for luteinizing hormone-releasing hormone (LH-RH) in prostate cancers following therapy with LH-RH agonists. *Clin Cancer Res.* (2010) 16:4675–80. doi: 10.1158/1078-0432.CCR-10-1113
24. Harter P, Sehouli J, Lorusso D, Reuss A, Vergote I, Marth C, et al. A Randomized trial of lymphadenectomy in patients with advanced ovarian neoplasms. *N Engl J Med.* (2019) 380:822–32. doi: 10.1056/NEJMoa1808424
25. Taratula O, Patel M, Schumann C, Naleway MA, Pang AJ, He H, et al. Phthalocyanine-loaded graphene nanoplatform for imaging-guided combinatorial phototherapy. *Int J Nanomed.* (2015) 10:2347–62. doi: 10.2147/IJN.S81097
26. Taratula O, Garbuzenko OB, Kirkpatrick P, Pandya I, Savla R, Pozharov VP, et al. Surface-engineered targeted PPI dendrimer for efficient intracellular and intratumoral siRNA delivery. *J Control Rel.* (2009) 140:284–93. doi: 10.1016/j.jconrel.2009.06.019
27. Saad M, Garbuzenko OB, Ber E, Chandna P, Khandare JJ, Pozharov VP, et al. Receptor targeted polymers, dendrimers, liposomes: which nanocarrier is the most efficient for tumor-specific treatment and imaging? *J Control Rel.* (2008) 130:107–14. doi: 10.1016/j.jconrel.2008.05.024
28. Arencibia JM, Schally AV. Luteinizing hormone-releasing hormone as an autocrine growth factor in ES-2 ovarian cancer cell line. *Int J Oncol.* (2000) 16:1009–13. doi: 10.3892/ijo.16.5.1009
29. Veys I, Pop FC, Vankerckhove S, Barbieux R, Chintinne M, Moreau M, et al. ICG-fluorescence imaging for detection of peritoneal metastases and residual tumoral scars in locally advanced ovarian cancer: A pilot study. *J Surg Oncol.* (2018) 117:228–35. doi: 10.1002/jso.24807
30. Fidel J, Kennedy KC, Dernell WS, Hansen S, Wiss V, Stroud MR, et al. Preclinical validation of the utility of BLZ-100 in providing fluorescence contrast for imaging spontaneous solid tumors. *Cancer Res.* (2015) 75:4283–91. doi: 10.1158/0008-5472.CAN-15-0471
31. Ogawa M, Kosaka N, Choyke PL, Kobayashi H. *In vivo* molecular imaging of cancer with a quenching near-infrared fluorescent probe using conjugates of monoclonal antibodies and indocyanine green. *Cancer Res.* (2009) 69:1268–72. doi: 10.1158/0008-5472.CAN-08-3116
32. Nakajima T, Mitsunaga M, Bander NH, Heston WD, Choyke PL, Kobayashi H. Targeted, activatable, *in vivo* fluorescence imaging of prostate-specific membrane antigen (PSMA) positive tumors using the quenched humanized J591 antibody-indocyanine green (ICG) conjugate. *Bioconjug Chem.* (2011) 22:1700–5. doi: 10.1021/bc2002715
33. Urano Y, Sakabe M, Kosaka N, Ogawa M, Mitsunaga M, Asanuma D, et al. Rapid cancer detection by topically spraying a gamma-glutamyltranspeptidase-activated fluorescent probe. *Sci Transl Med.* (2011) 3:110ra119. doi: 10.1126/scitranslmed.3002823
34. Asanuma D, Sakabe M, Kamiya M, Yamamoto K, Hiratake J, Ogawa M, et al. Sensitive beta-galactosidase-targeting fluorescence probe for visualizing small peritoneal metastatic tumours *in vivo*. *Nat Commun.* (2015) 6:6463. doi: 10.1038/ncomms7463

Conflict of Interest: The authors declare that the research was conducted in the absence of any commercial or financial relationships that could be construed as a potential conflict of interest.

frontiers in Oncology

REVIEW
published: 05 June 2020
doi: 10.3389/fonc.2020.00884

Prostate Cancer Theranostics - An Overview

Diane Abou[1,2,3]*, *Nadia Benabdallah*[1,2], *Wen Jiang*[2,4], *Lu Peng*[1,2,5], *Hanwen Zhang*[1,2], *Alexandria Villmer*[1,2], *Mark S. Longtine*[1] *and Daniel L. J. Thorek*[1,2,5,6]*

[1] Department of Radiology, Mallinckrodt Institute of Radiology, Washington University School of Medicine, St. Louis, MO, United States, [2] Program in Quantitative Molecular Therapeutics, Washington University School of Medicine, St. Louis, MO, United States, [3] Radiology Cyclotron Facility, Mallinckrodt Institute of Radiology, Washington University in St. Louis, St. Louis, MO, United States, [4] Department of Biomedical Engineering, Johns Hopkins University, Baltimore, MD, United States, [5] Department of Biomedical Engineering, Washington University in St. Louis, St. Louis, MO, United States, [6] Oncologic Imaging Program, Siteman Cancer Center, Washington University School of Medicine, St. Louis, MO, United States

Metastatic prostate cancer is incurable, and novel methods to detect the disease earlier and to direct definitive treatment are needed. Molecularly specific tools to localize diagnostic and cytotoxic radionuclide payloads to cancer cells and the surrounding microenvironment are recognized as a critical component of new approaches to combat this disease. The implementation of theranostic approaches to characterize and personalize patient management is beginning to be realized for prostate cancer patients. This review article summarized clinically translated approaches to detect, characterize, and treat disease in this rapidly expanding field.

Keywords: peptide, radionuclide, radiotherapy, alpha particle, prostate cancer

OPEN ACCESS

Edited by:
Georgios S. Limouris, National and Kapodistrian University of Athens, Greece

Reviewed by:
Di Dong, Institute of Automation (CAS), China
Caroline Rousseau, Institut de Cancérologie de l'Ouest (ICO), France

***Correspondence:**
Diane Abou
dabou1@wustl.edu
Daniel L. J. Thorek
thorek.lab@wustl.edu

Specialty section:
This article was submitted to Cancer Imaging and Image-directed Interventions, a section of the journal Frontiers in Oncology

Received: *16 October 2019*
Accepted: *05 May 2020*
Published: *05 June 2020*

Citation:
Abou D, Benabdallah N, Jiang W, Peng L, Zhang H, Villmer A, Longtine MS and Thorek DLJ (2020) Prostate Cancer Theranostics - An Overview. Front. Oncol. 10:884. doi: 10.3389/fonc.2020.00884

INTRODUCTION

Prostate cancer (PCa) is the most common malignancy in men. In 2019 there were ∼175,000 new cases of PC with >30,000 deaths, yielding enormous personal, societal, and economic costs (1). For many low-risk patients with primary PCa, "active surveillance" to monitor indolent disease by serial biopsy and prostate specific antigen (PSA) measures is an appropriate option. If treatment is desired for primary PCa, standards of care may involve surgical resection, external beam or proton radiotherapy, and brachytherapy and often are curative. For patients diagnosed with primary PCa, 5-year survival rates exceed 90%. However, for patients with advanced prostate cancer with tumor cells present at distant sites outside of the prostate there are severe impacts on quality of life and a low (<30%) 5-year survival rate. Upon metastasis to the bone, the most common site of PCa metastasis, the 5-year survival rate falls to a dismal 3–5%, making the disease essentially incurable and the second leading cause of cancer death in men (2–6). Conventional treatments for later-stage and metastatic disease can involve anti-hormonal therapies, chemotherapies, further use of radiation, and the use of bone-targeted agents.

An emerging area with significant potential to combat this lethal disease is the use of theranostic agents that detect PCa with exquisite sensitivity and can precisely ablate these sites. The implementation of an expanding array of nuclear medicine approaches to accurately characterize disease status enabling personalized patient management for prostate cancer patients is beginning to be realized. Advances in radionuclide production and availability, chemical synthesis, and clinical trial implementation are rapid and ongoing, and new tools and approaches will undoubtedly emerge in the near future.

In this review, we concisely present molecular imaging and theranostic tools that have been developed to better delineate, monitor, and treat prostate cancer, with a focus on clinically implemented radionuclide theranostics. There have been numerous changes in the management

for prostate cancer patients and the options for treatment in the previous decade. In **Figure 1A**, a general schematic for the progression of disease in a patient is presented, by following their hypothetical disease burden as measured by their secreted PSA (prostate specific antigen) values. Focal treatment options are available for primary disease sites, followed by different systemic treatments at different disease states (**Figure 1B**). Recent approvals of several different pharmacological and radiological entities by the FDA/EMA, often for the same indications, underline the value for molecularly targeted imaging and therapeutics to guide and enhance patient outcomes.

The present review helps provide context and an overview of the new options and methods leveraged to detect, characterize, and combat disease in this evolving clinical landscape. First, we describe methods using molecular imaging tools for the central oncological driver of the disease, the androgen receptor, to read out pharmacological properties of candidate hormonal therapy. Next, we describe efforts to target radiopharmaceuticals to receptors overexpressed on the surface of prostate cancer cells. Finally, we discuss efforts to target imaging and to direct treatment to the microenvironment of the bone-tropic metastases of this disease.

ANDROGEN RECEPTOR IMAGING WITH [^{18}F]-FDHT

The androgen receptor (AR), an intracellular DNA-binding, hormone-responsive transcription factor, is the key molecular

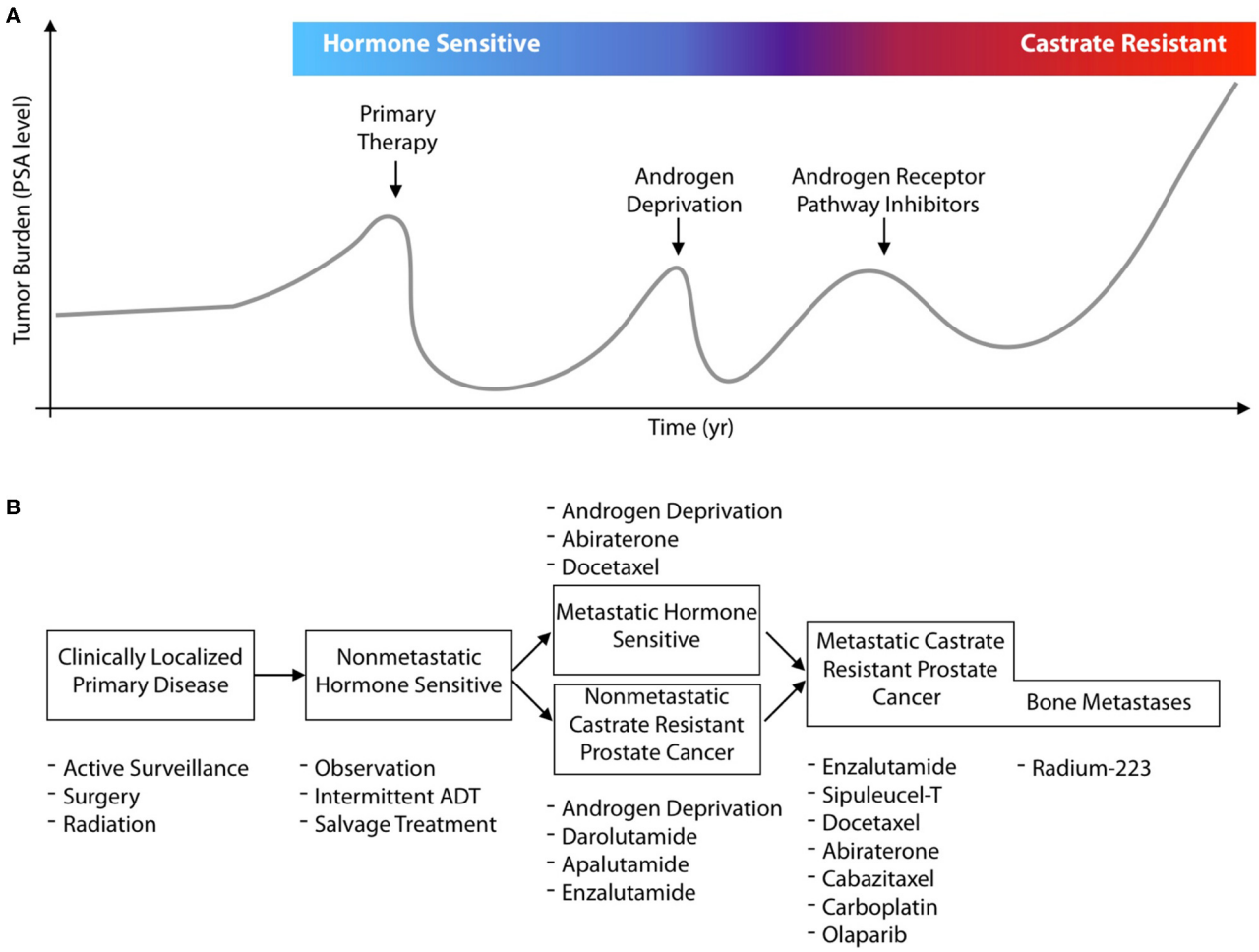

FIGURE 1 | Contemporary prostate cancer states and systemic treatments. **(A)** Adenocarcinoma arising in the prostate gland is the second most common cancer in males, and can be cured with local intervention if detected when still localized to the organ. Disease is often detected by serum PSA measures which also enable tracking of disease recurrence should initial therapy and subsequent lines of treatment fail. Most commonly, disease control is attempted with hormonal control of the androgen receptor signaling access through (chemical) castration and the use of androgen receptor inhibitors. **(B)** The last decade has seen the approval of 8 new agents for prostate cancer across different disease states. These approvals result from significant survival benefits for patients at multiple lines of treatment. However, the eventual progression on novel antiandrogens, Radium-223, and chemotherapies leave considerable room for improvement. Despite the number of existing treatment options, efforts with molecularly targeted radiotherapies are under intense, global, evaluation; as well as to use new imaging agents to better guide drug development and more accurately characterize disease.

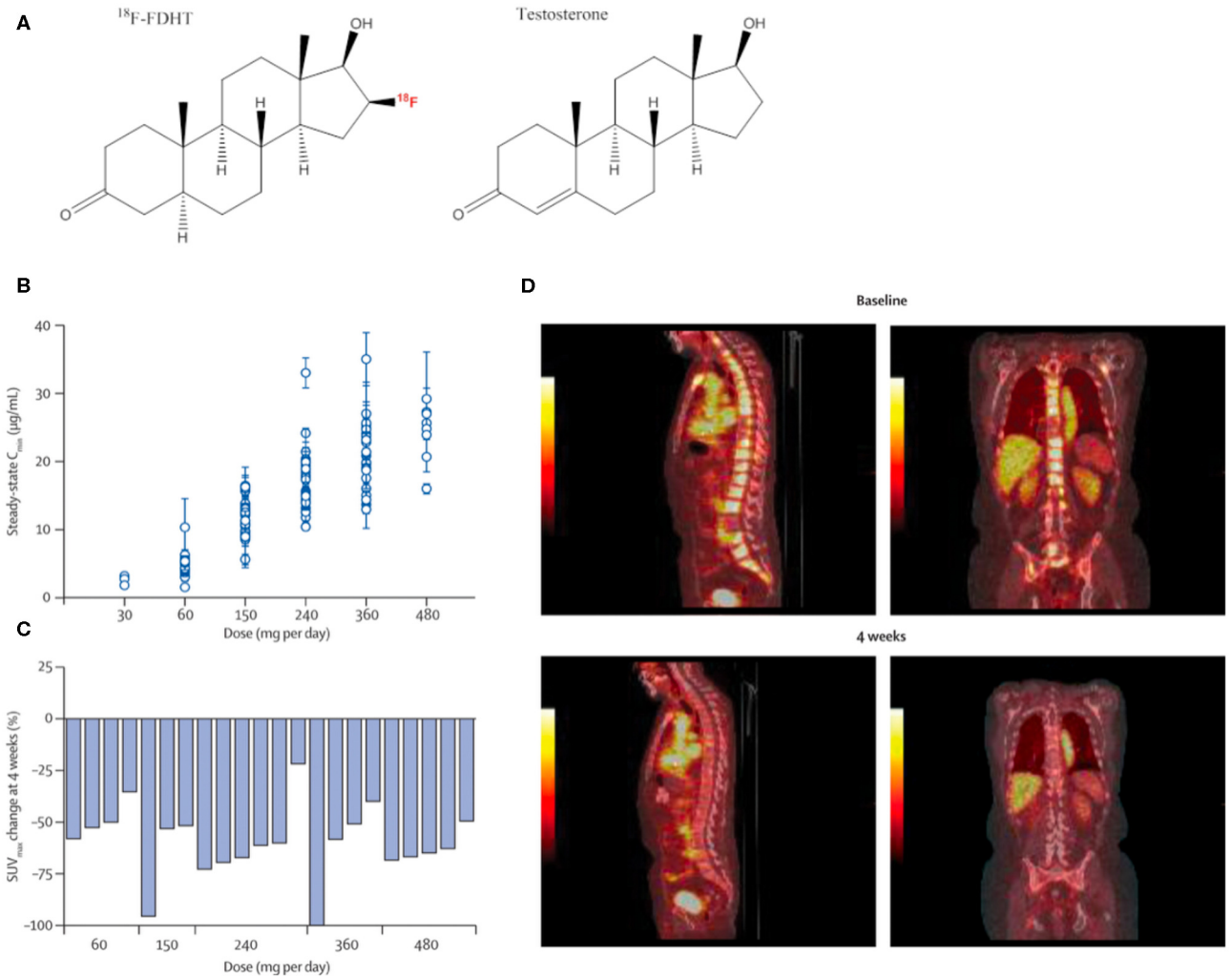

FIGURE 2 | Quantitative imaging of the androgen receptor. [^{18}F]-FDHT, which annotates the AR, the central molecular driver of prostate cancer development and progression, is an effective imaging tool to evaluate pharmacodynamic features of candidate therapies. MDV3100 treatment, a second-generation orally bioavailable anti-androgen, was tested in men with castrate-resistant prostate cancer. **(A)** Chemical structure of positron-emitting ^{18}F-FDHT and testosterone. **(B)** MDV3100 serum concentration by dose level. **(C)** Representative baseline and treatment scans showing marked decrease in radio-androgen uptake in skeletal metastases. Reproduced from Scher et al. (16) **(D)** Change in standardized uptake value of [^{18}F]-FDHT PET for men at baseline compared to 4 weeks of treatment.

driver for male organ development and is the oncological driver of PCa (7). Activated by binding androgens such as testosterone in the cytoplasm, the AR then translocates to the nucleus and stimulates the expression of genes involved in differentiation and proliferation (8). The effectiveness of repressing this central AR pathway by androgen-deprivation therapy was discovered by Huggins over 70-years ago (9, 10), and remains a mainstay of PCa treatment. However, after an initial response, AR pathway reactivation inevitably occurs, leading to disease progression. Recently developed, highly potent anti-androgen molecules can be employed to some effect, even in late-stage, castrate-resistant PCa [CRPC (11)]. This demonstrates that AR-signaling maintains its central role over the entire course of disease progression (9, 12), rather than CRPC becoming AR-signaling independent. Mechanisms of resistance to anti-androgen therapy in CRPC include AR-receptor gene amplification, AR-upregulation, local hormone production, and/or constitutively active AR-mutations (13–15). Counter intuitively, the term "castrate-resistant" most often reflects continued androgen dependence, rather than evolved AR-pathway independence. Thus, even in CRPC disease, the AR pathway thus remains an appropriate therapeutic and imaging target.

16β-[^{18}F]-fluoro-5α-dihydrotestosterone ([^{18}F]-FDHT) is a positron-emitting analog of the native AR-binding dihydrotestosterone with a conjugated positron-emitting radionuclide ([^{18}F]; **Figure 2A**) and has been used in small animals studies (17, 18) and in clinical studies to evaluate AR-expression levels and occupancy (19–21). [^{18}F]-FDHT positron emission tomography (PET) enables detection of metastatic

lesions, as indicated by increased concentrations of AR, and is being evaluated for its capacity to phenotype lesions in concert with other conventional imaging modalities (22).

The majority of CRPC escape anti-androgen therapy by AR-signaling amplification, and hormonal therapies that can inhibit AR-signaling are a mainstay of treatment for CRPC. Thus, imaging the expression levels of AR is a viable strategy to measure receptor density and the pharmacological response to these anti-androgen therapies (22, 23) (**Figures 2B–D**). These features have been exploited in the clinical evaluation of next generation anti-androgens in early clinical trial to directly quantitate AR-blockade. Reduction in [^{18}F]-FDHT uptake and a plateau, consistent with saturation of AR binding, can be quantitated directly on a lesional or patient basis (16, 24).

PROSTATE SPECIFIC MEMBRANE ANTIGEN IMAGING

Prostate Specific Membrane Antigen (PSMA) has emerged as the pre-eminent prostate cancer target for diagnostic imaging, assisting efforts to detect disease earlier, monitor recurrence, and track the progression of disease. PSMA is a robust target for PCa, with numerous pathological studies reporting elevated PSMA expression on 85–100% of prostate cancers (25–28). The number of clinical trials that use PSMA-targeted agents for diagnostic or therapeutic purposes is large and continues to expand: in the clinicaltrials.gov database, there are currently over 100 clinical trials that utilize PSMA for imaging or therapy.

PSMA is a type II transmembrane protein present on the cell surface, and, interestingly, PSMA contains an extracellular domain with glutamate carboxypeptidase activity (29). Although neither the exact physiological role of PSMA nor the reason for its overexpression on PCa cells is known, it has been used utilized in the targeting of multiple PSMA-binding small molecules, many of which are urea based and bind to the enzymatic site. We note that the use of PSMA as nomenclature to refer to this protein can be confusing, as this receptor is expressed in multiple non-prostate-derived tissues including the brain, peripheral nerves, salivary glands, gut, and kidney. Due to its independent discovery in multiple tissues, this protein, which we will refer to as PSMA, is also identified in the literature as glutamate carboxypeptidase II (GCPII) in the gut and as N-acetyl-L-aspartyl-L-glutamate peptidase I of NAAG peptidase I (NAALADase I) in the brain.

An array of agents have been developed that target PSMA with high affinity, including antibodies and small molecules. PSMA imaging agents for use in PET imaging and single-photon emitting computed tomography (SPECT) have been evaluated in preclinical and clinical settings, using an array of positron emitting radionuclides such as Fluorine-18, Gallium-68, Scandium-44 and Zirconium-89, or single-photon emitting radionuclides such as Technetium-99m and Iodine-125. Examples of widely tested structures and antibodies are found in **Figure 3**. Multiple PSMA imaging agents have been tested in humans and several have been evaluated in late stage, multicenter, clinical trials (**Table 1**).

The first effort to target and image PSMA involved the 7E11-C5.3 murine antibody, which targets an intracellular epitope of PSMA (30, 31). Labeled with Indium-111, permitting imaging by SPECT, this agent was known as capromab pendetide or ProstaScint and was approved in 1996 for the detection of PCa lesions (32, 33). This initial PSMA-targeting agent found limited clinical implementation due to low contrast imaging, likely resulting from low accessibility *in vivo* to the intracellular PSMA epitope, concerns over human anti-murine immune responses, and competing conventional imaging methods.

A substantial improvement in PSMA imaging was achieved with the generation of J591, a humanized antibody targeting an epitope on the extracellular region of PSMA. J591 has been labeled with radionuclides for both PET and SPECT imaging of PCa lesions in humans (34–36). However, as antibody and antibody-fragment derived agents require administration of the radiolabeled agent several days before effective PSMA/tumor imaging can be performed, as this time is required for clearance of the tracer and optimal tumor/background signal. This relatively longer time frame from administration to imaging, which requires a return visit of the patient, has reduced enthusiasm for J591-based PSMA imaging.

Instead, much of the current intense interest in PCa-lesion imaging using PSMA revolves around PSMA-targeting small molecules (37). Small molecules can have exquisite targeting sensitivity and specificity, and they allow a much more rapid turnaround from agent injection to imaging (minutes to hours) than do antibodies (days). Also, small molecule agents that rapidly target PSMA allow the use of short-lived PET radionuclides, permitting high resolution, and sensitive detection with a reduced radiation dosed compared to antibody-based PET imaging methods (38, 39).

A large number of PSMA-targeted small molecules have been tested for PCa imaging in preclinical models and in humans. An example of a patient scan with the high affinity fluorinated agent is shown in **Figure 4A**. Multiple prospective clinical trials with targeted small-molecule PSMA imaging agents are underway, with encouraging results on the sensitivity of detection and the utility of these tracers in clinical settings (42–44). The most widely reported clinical imaging has been performed with PET imaging using radiometal-labeled [^{68}Ga]PSMA 617 or [^{68}Ga]PSMA-11 or using fluorinated [^{18}F]-DCFPyL (45). There are currently many options for radionuclide and PSMA-targeting ligand, and several studies to compare imaging features have been undertaken. Optimal uptake time, magnitude of tumor and background organ uptake, and imaging resolution are dependent on ligand and radionuclide. Logistical and cost issues are also a consideration. Multiple doses of Fluorine-18 radiolabeled inhibitor are available at institutions with a medical cyclotron, with the ability to ship agent at greater distances. Lower upfront costs are required for Gallium-68 isolation on a ^{68}Ge/^{68}Ga generator system, however fewer doses are produced with lower specific activity, and decreased resolution (46–49).

The capacity to perform highly sensitive molecular imaging of PSMA to detect minute foci of metastatic disease, led by PET-isotope labeled, PSMA-targeted small molecules, is motivating a paradigm shift in prostate cancer patient management. For

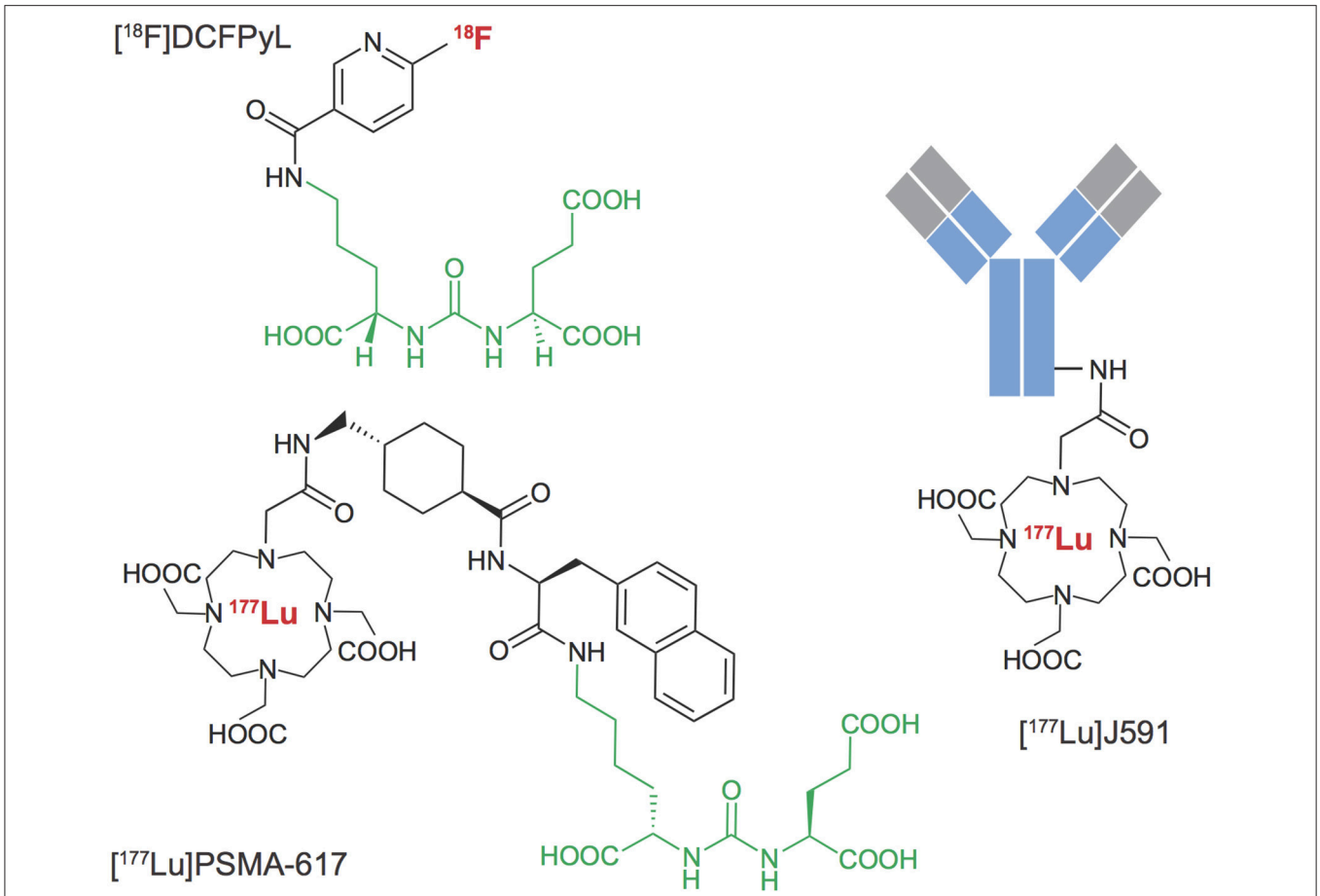

FIGURE 3 | PSMA Targeted radiopharmaceuticals. Examples of diagnostic and therapeutic agents targeting Prostate Specific Membrane Antigen. A common urea-based motif (green) has been widely derivatized for localization at sites of prostate cancer metastases that over-express the membrane-localized PSMA metalloenzyme. Antibody targeting vectors with high affinity for PSMA have also been labeled with positron, beta-particle and alpha-particle emitting radionuclides.

TABLE 1 | Selected prostate cancer trials for disease detection and radiotherapy treatment of metastatic disease.

CTID	Abbreviated titles	Purpose	Phase	Compound	Patients	Status
NCT02981368	18F-DCFPyL PET/CT imaging in patients with prostate cancer (OSPREY)	Diagnostic	II/III	[18F]-DCFPyL	385	Completed
NCT03739684	18F-DCFPyL PET/CT imaging in patients with suspected recurrence of prostate cancer (CONDOR)	Diagnostic	III	[18F]-DCFPyL	200	Active
NCT03392428	177Lu-PSMA617 theranostic Vs. cabazitaxel in progressive metastatic CRPC (TheraP)	Therapy	III	[177Lu]-PSMA-617	201	Active
NCT03511664	177Lu-PSMA-617 in metastatic castrate-resistant prostate cancer (VISION)	Therapy	III	[177Lu]-PSMA-617	750	Active
NCT03276572	225Ac–J591 in patients with mCRPC	Therapy	Ib	[225Ac]-J591	42	Recruiting
NCT03939689	I-131-1095 radiotherapy in combination with enzalutamide in patients with mCRPC (ARROW)	Therapy	II	[131I]-MIP-1095	175	Recruiting
NCT02552394	Radioimmunotheraspy in prostate cancer using 177Lu-J5912 antibody	Therapy	I	[177Lu]-J591	54	Recruiting

example, the ability to rapidly determine lesion response on a given treatment regimen (41, 50, 51), as shown in **Figures 4B,C**, or to target external beam radiotherapy to sites of oligometastatic disease (52, 53), are means of precise disease control not previously possible. Of course, it should be noted that rigorous, prospective, controlled and multi-center trials, and statistical analyses are required before we can be confident that these new tools provide real-world benefit for patients.

PROSTATE SPECIFIC MEMBRANE ANTIGEN TARGETED RADIOTHERAPY

Concurrent with the development of the PSMA-targeted diagnostic agents described above, the application of PSMA-directed targeted radiotherapy of PCa is an ongoing area of great potential. Here, PSMA-binding ligands are labeled with radionuclides that produce potent cytotoxic decay products,

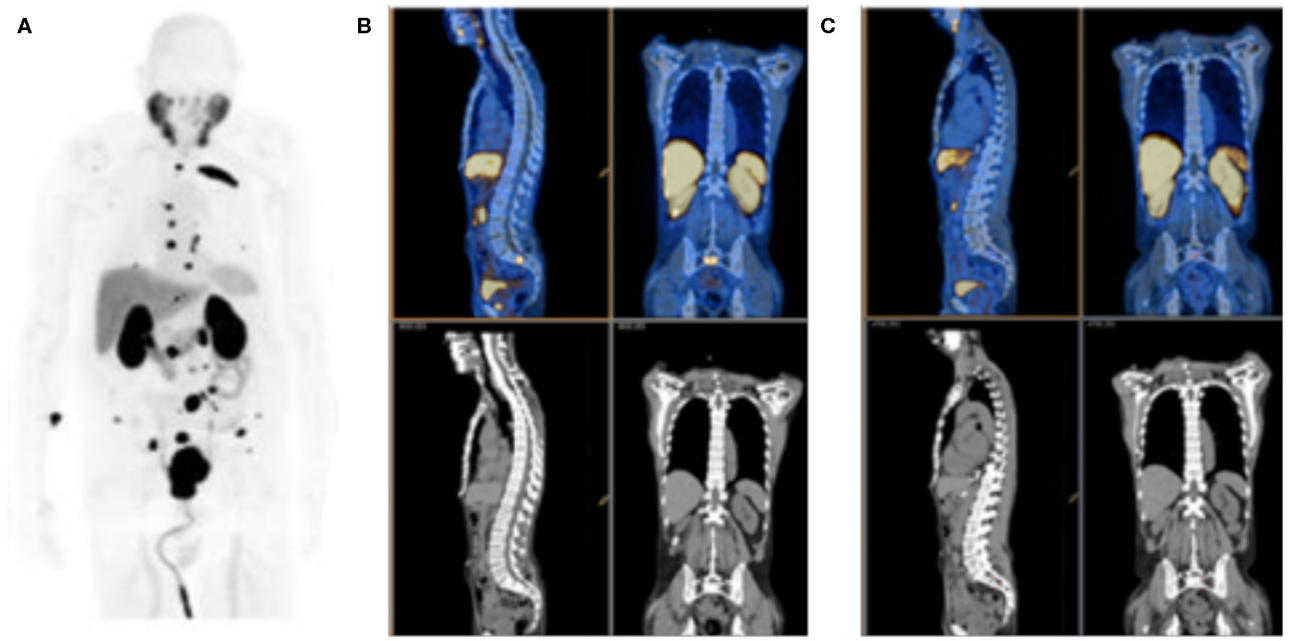

FIGURE 4 | PSMA PET Imaging. **(A)** Detection of prostate cancer lesions with [^{18}F]DCFPyL, along with uptake in kidneys, salivary gland and liver. **(B)** Pre-treatment [^{68}Ga]PSMA-11 and **(C)** post-treatment PET/CT, top, and CT, bottom, scans obtained on day 9 after initiating combined anti-androgen hormone therapy. Reproduced from **(A)**(40) and **(B,C)** (41).

without or with the co-emission of imageable photons. Both beta-particle (Lutetium-177, Copper-67, Iodine-131) and alpha-particle (Bismuth-213 and Actinium-225) emitting PSMA-targeted agents are at various stages of drug development (54–58). It is noteworthy that PSMA-ligands are internalized by endocytosis after PSMA binding, allowing increased intracellular levels of residualizing therapeutic radionuclides and improved potential for tumor-cell killing. Several PSMA-targeted radiotherapeutic agents have begun to be applied in late stage metastatic prostate cancer (PCa) patients (58–62); **Table 1**.

The most developed agent in the PSMA-targeted radiotherapeutic class is [^{177}Lu]PSMA-617. [^{177}Lu]PSMA-617 is inherently theranostic in that the decay pathway of ^{177}Lu emits both tumor-cell-killing beta particles and imageable photons, detectable by planar scintography, and SPECT imaging. Thus, [^{177}Lu]PSMA-617 allows both therapy and imaging of agent distribution and uptake with the same agent. The majority of response data for this agent have been accrued from retrospective trials that have shown efficacy in reducing PSA levels with manageable hematological, renal, and salivary gland toxicity (63–69). Patient characteristics varied to a large degree with respect to previous treatment, disease stage, and radiographic and biochemical features (70). Thus, these results are encouraging as they indicate that there may be a benefit for patients along the spectrum of disease burden and stage, but also present a problem as informing to how these agents can be wielded most effectively. To aid in answering these questions, well-powered prospective trials with [^{177}Lu]PSMA-617 are now underway.

Great interest has also been generated by the application of PSMA-617 labeled with ^{225}Ac, which emits four cell-killing alpha particles. This agent has been studied in small cohorts of men in Germany and in South Africa and clinical findings have generated great interest, **Figure 5** (58, 71, 72). Alpha particles emitted from heavy isotopes, such as Actinium-225 and Radium-223 (described below), have high energies, in the 5-8 MeV range, that produce extremely cytotoxic genomic damage. Alpha particles also exhibit a much shorter path length than β-particles, such as those emitted by Lutetium-177. Together, the radiobiological properties of alpha-particle emitting agents mean that even small deposits of cancer cells could be eradicated with appropriate uptake (57), while largely sparing adjacent and distant tissues because of their short path length. Investigations with additional alpha-particle emitting theranostics, including with generator-produced [^{213}Bi]PSMA-617 and [^{212}Pb]PSMA-617 (57, 73), are also being evaluated, which may alleviate sourcing issues regarding ^{225}Ac.

However, the expression of PSMA on non-prostate-derived cells as noted above leads to a major concern in the application of PSMA-targeted therapies: the on-target but off-tumor localization. Dosimetric evaluation of the distribution of the diagnostic and theranostic ligands provides a means to predict absorbed doses to sites of both healthy and diseased tissue uptake. Radiosensitive organs, such as the hematopoietic niche of the bone marrow, kidneys, nerves, and intestine often account for the dose-limiting activity that can safely be administered to a patient (74, 75). The major side-effect producing sites of undesired localization of PSMA-targeted agents identified at

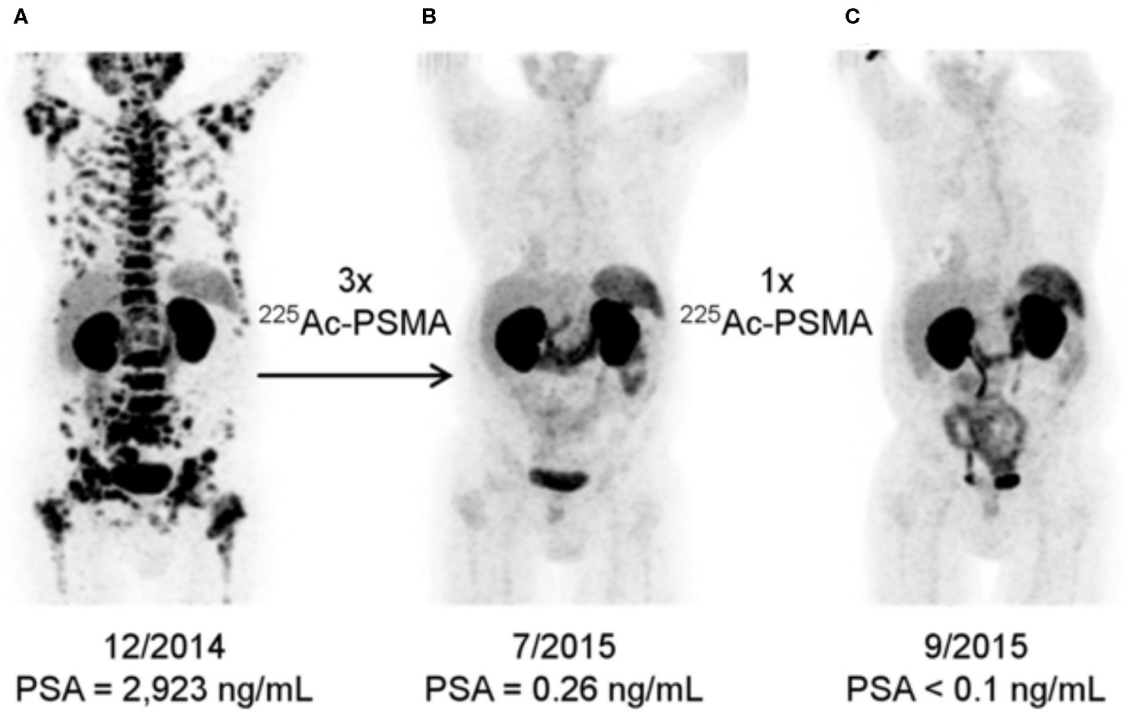

FIGURE 5 | [^{68}Ga]PSMA-11 Imaging Response to [^{225}Ac]PSMA-617. Alpha-particle emitting Ac-225 bound to the DOTA chelator-bearing PSMA-617 scaffold was used to treat a patient following disease progression after several lines of conventional treatment and [^{177}Lu]PSMA-617. Serial images during the treatment course reveal significantly less PSMA expression and potential lesion eradication. A decrease in salivary gland uptake is also noted, as it is a site of PSMA expression inadvertently treated by these agents. Reproduced from (71).

this time include the salivary glands and kidney, which highly express PSMA, are radiosensitive and are critical for survival and quality of life. Xerostomia from non-repairable damage to the salivary glands has been reported with ^{225}Ac-PSMA-617, with varying degrees of glandular damage observed with ^{177}Lu-PSMA-617. Interestingly, biological targeting vectors such as ^{177}Lu-J591 which do not apparently accumulate in the salivary glands may have additional utility with the potential for a favoragle therapeutic window (76, 77). The much longer-onset effect of severe kidney toxicity has not yet been clinically noted (63). However, studies to date generally lack rigorous patient enrollment and follow-up criteria and have not followed patients for long periods of time. Prospective and randomized trials will be needed to compare patient benefit against conventional treatments and the effectiveness of means to reduce these off-tumor toxicities.

GRPR BOMBESIN

The gastrin-releasing peptide receptor (GRPR) is expressed on a wide range of cell types in higher mammals, especially in the nervous system and gastrointesinal tract (78, 79). Small peptides interact with GPRP to modulate a wide range of cell and organ functions (80). GRPR is aberrantly overexpressed on the cell surface of many cancers, including lung, breast, and prostate cancer (81, 82). The bombesin subfamily is the best studied GRPR, and a large number of mammalian and amphibian bombesin peptide analogs have been radiolabeled for cancer imaging and therapy (82).

Because of the frequent overexpression of GRPR in prostate cancer, several bombesin radiopharmaceuticals have been tested in humans for PCa disease detection, including [^{68}Ga]RM2, [^{68}Ga]BAY86-7548, and [^{64}Cu]-CB-TE2A-AR06, among others. Studies reveal high-contrast detection of disseminated and primary disease (83–86). While GRPR expression may not be as ubiquitous on prostate cancer cells as PSMA, there is no background target expression in the kidneys or salivary glands. Thus, there may be utility for other prostate cancer targeted theranostics in addition to PSMA (87), especially in the GRPR class.

THERANOSTICS FOR THE BONE METASTASIC MICROENVIRONMENT

The skeletal compartment is the most frequent site of metastases in prostate cancer patients. These lesions are often painful, and may also further degrade quality of life through fracture, spinal cord compression, hypercalcemia, and impaired mobility (3, 88). Bone metastases occupy a nutrient-rich niche that enhances the treatment-resistant nature of disseminated tumor cells (89). Early

detection and specific localized treatment of these disseminated sites are recognized as necessary components of a successful strategy to combat bone metastatic prostate cancer.

Conventional imaging modalities for PCa bone metastases include magnetic resonance and X-ray computed tomography, which are commonly applied in concert with nuclear medicine scans for accurate bone lesion detection. [^{99m}Tc]-bisphosphonates and [^{18}F]-NaF are both bone-seeking agents that are incorporated at sites of active bone remodeling adjacent to metastatic foci and are used for imaging. Approved beta particle-emitting agents for bone pain palliation are [^{89}Sr]chloride and [^{153}Sm]EDTMP, an ion and phosphonic acid ligand, respectively, which are taken up at or near sites of bone metastasis. Both produce imageable emissions for planar imaging in order to evaluate uptake. Unfortunately, the long path length of these energetic beta particle emissions result in irradiation of the bone marrow, a dose limiting organ, and these agents have not produce survival improvements when evaluated in clinical trial.

The first bone-targeted radionuclide that aids in pain palliation and also achieves an overall survival benefit over standard of care is the alpha-particle emitting [^{223}Ra]Cl_2 citrate, tradename Xofigo (90). Radium-223 is a calcium-mimetic and localizes to sites of active bone turnover, where it subsequently decays, irradiating nearby prostate cancer cells. The short path lengths of the alpha particles do not result in anemic responses and the drug is well-tolerated. While difficult to image, efforts are underway to provide quantitative assessment of $^{223}RaCl_2$ distribution to inform absorbed dose measures at sites of disease and background organs (91–94).

CONCLUSION

Agents that specifically and sensitively target molecular features of prostate cancer are being brought to bear to detect, guide, and deliver treatments for men with advanced prostate cancer. The underlying initiator of PCa, the androgen receptor, is the driver of prostate adenocarcinoma development, can be visualized with [^{18}F]-FDHT. This imaging tool can evaluate the pharmacological impact of anti-androgens and their efficacy. Cell surface antigen targeted agents, in particular PSMA targeted urea-based ligands and antibodies, have now been assessed in a wide range of scenarios to detect and treat metastatic prostate cancer. Prospective clinical trials that are currently recruiting or underway will provide clearer information on the utility of these new theranostic approaches to improve quality of life and overall survival. These agents have the capacity to deliver ablative doses to sites of disease throughout the body with the potential to overcome this currently incurable disease. Differences in the imaging properties and therapeutic niche for different molecular entities and radionuclides are of continuing research interest to provide optimal patient-specific diagnostic information and therapeutic outcome. These ongoing trials may also shed light on the important question of how these novel imaging and therapy agents will integrate with current treatment modalities and approved imaging methods, including conventional imaging and imaging of prostate cancer cell metabolism with established agents such as [^{11}C/^{18}F]-choline, [^{18}F]-fluorodeoxyglucose and [^{18}F]-fluciclovine.

AUTHOR CONTRIBUTIONS

All authors listed have made a substantial, direct and intellectual contribution to the work, and approved it for publication.

FUNDING

This work was supported in part by NIH NCI R01CA229893, R01CA201035, and R01CA240711 (DT); and the American Cancer Society (HZ).

REFERENCES

1. Siegel RL, Miller KD, Jemal, A. Cancer statistics, 2018. *CA Cancer J Clin*. (2018) 68:7–30. doi: 10.3322/caac.21442
2. Nørgaard M, Jensen AØ, Jacobsen JB, Cetin K, Fryzek JP, Sørensen HT. Skeletal related events, bone metastasis and survival of prostate cancer: a population based cohort study in Denmark (1999 to 2007). *J Urol*. (2010) 184:162–7. doi: 10.1016/j.juro.2010.03.034
3. Bubendorf L, Schöpfer A, Wagner U, Sauter G, Moch H, Willi N, et al. Metastatic patterns of prostate cancer: an autopsy study of 1,589 patients. *Hum Pathol*. (2000) 31:578–83. doi: 10.1053/hp.2000.6698
4. Rajpar S, Fizazi, K. Bone targeted therapies in metastatic castration-resistant prostate cancer. *Cancer J*. (2013) 19:66–70. doi: 10.1097/PPO.0b013e31827f123e
5. Mehra R, Kumar-Sinha C, Shankar S, Lonigro RJ, Jing X, Philips NE, et al. Characterization of bone metastases from rapid autopsies of prostate cancer patients. *Clin Cancer Res*. (2011) 17:3924–32. doi: 10.1158/1078-0432.CCR-10-3120
6. Lilja H, Ulmert D, Vickers AJ. Prostate-specific antigen and prostate cancer: prediction, detection and monitoring. *Nat Rev Cancer*. (2008) 8:268–78. doi: 10.1038/nrc2351
7. Augello MA, Den RB, Knudsen, KE. AR function in promoting metastatic prostate cancer. *Cancer Metastasis Rev*. (2014) 33:399–411. doi: 10.1007/s10555-013-9471-3
8. Carver BS. Strategies for targeting the androgen receptor axis in prostate cancer. *Drug Discov Today*. (2014) 19:1493–97. doi: 10.1016/j.drudis.2014.07.008
9. Huggins C, Hodges CV. Studies on prostatic cancer. I. The effect of castration, of estrogen and of androgen injection on the normal and on the hyperplastic prostate glands of dogs. *Cancer Res*. (1941) 1:293–8.
10. Huggins C, Hodges, CV. Studies on prostatic cancer: I. The effect of castration, of estrogen and of androgen injection on serum phosphatases in metastatic carcinoma of the prostate. 1941. *J Urol*. (2002) 168:9–12. doi: 10.1016/S0022-5347(05)64820-3
11. Teo MY, Rathkopf DE, Kantoff P. Treatment of advanced prostate cancer. *Annu Rev Med*. (2019) 70:479–99. doi: 10.1146/annurev-med-051517-011947
12. Ferraldeschi R, Welti J, Luo J, Attard G, de Bono JS. Targeting the androgen receptor pathway in castration-resistant prostate cancer: progresses and prospects. *Oncogene*. (2015) 34:1745–57. doi: 10.1038/onc.2014.115
13. Pfitzenmaier J, Ellis WJ, Hawley S, Arfman EW, Klein JR, Lange PH, et al. The detection and isolation of viable prostate-specific antigen positive

epithelial cells by enrichment: a comparison to standard prostate-specific antigen reverse transcriptase polymerase chain reaction and its clinical relevance in prostate cancer. In: *Urologic Oncology: Seminars and Original Investigations*. New York, NY: Elsevier (2007). doi: 10.1016/j.urolonc.2006.09.018

14. Koivisto P, Kononen J, Palmberg C, Tammela T, Hyytinen E, Isola J, et al. Androgen receptor gene amplification: a possible molecular mechanism for androgen deprivation therapy failure in prostate cancer. *Cancer Res*. (1997) 57:314–9.
15. Pedersen EA, Shiozawa Y, Pienta KJ, Taichman RS. The prostate cancer bone marrow niche: more than just "fertile soil". *Asian J Androl*. (2012) 14:423–7. doi: 10.1038/aja.2011.164
16. Scher HI, Beer TM, Higano CS, Anand A, Taplin ME, Efstathiou E, et al. Prostate cancer foundation/department of defense prostate cancer clinical trials consortium. antitumour activity of MDV3100 in castration-resistant prostate cancer: a phase 1-2 study. *Lancet*. (2010) 375:1437–46. doi: 10.1016/S0140-6736(10)60172-9
17. Larimer BM, Dubois F, Bloch E, Nesti S, Placzek M, Zadra G, et al. Specific 18F-FDHT accumulation in human prostate cancer xenograft murine models is facilitated by prebinding to sex hormone-binding globulin. *J Nucl Med*. (2018) 59:1538–43. doi: 10.2967/jnumed.118.208785
18. Bonasera TA, O'Neil JP, Xu M, Dobkin JA, Cutler PD, Lich LL, et al. Preclinical evaluation of fluorine-18-labeled androgen receptor ligands in baboons. *J Nucl Med*. (1996) 37:1009–15.
19. Miederer M, McDevitt MR, Sgouros G, Kramer K, Cheung NKV, Scheinberg DA. Pharmacokinetics, dosimetry, and toxicity of the targetable atomic generator, 225Ac-HuM195, in nonhuman primates. *J Nucl Med*. (2004) 45:129–37.
20. Dehdashti F, Picus J, Michalski JM, Dence CS, Siegel BA, Katzenellenbogen JA, et al. Positron tomographic assessment of androgen receptors in prostatic carcinoma. *Eur J Nucl Med Mol Imaging*. (2005) 32:344–50. doi: 10.1007/s00259-005-1764-5
21. Larson SM, Morris M, Gunther I, Beattie B, Humm JL, Akhurst TA, et al. Tumor localization of 16β-18F-fluoro-5α-dihydrotestosterone versus 18F-FDG in patients with progressive, metastatic prostate cancer. *J Nucl Med*. (2004) 45:366–73.
22. Fox JJ, Gavane SC, Blanc-Autran E, Nehmeh S, Gönen M, Beattie B, et al. Positron emission tomography/computed tomography-based assessments of androgen receptor expression and glycolytic activity as a prognostic biomarker for metastatic castration-resistant prostate cancer. *JAMA Oncol*. (2018) 4:217–24. doi: 10.1001/jamaoncol.2017.3588
23. Hoving H, Palthe S, Vallinga M, Dost R, Gietema JA, Antunes I, et al. Early 18F-FDHT PET/CT as a predictor of treatment response in mCRPC treated with enzalutamide. *J Clin Orthod*. (2019) 37:232. doi: 10.1200/JCO.2019.37.7_suppl.232
24. Rathkopf DE, Morris MJ, Fox JJ, Danila DC, Slovin SF, Hager JH, et al. Phase I study of ARN-509, a novel antiandrogen, in the treatment of castration-resistant prostate cancer. *J Clin Oncol*. (2013) 31:3525–30. doi: 10.1200/JCO.2013.50.1684
25. Wright GL Jr, Haley C, Beckett ML, Schellhammer PF. Expression of prostate-specific membrane antigen in normal, benign, and malignant prostate tissues. *Urol Oncol*. (1995) 1:18–28. doi: 10.1016/1078-1439(95)00002-Y
26. Bostwick DG, Pacelli A, Blute M, Roche P, Murphy GP. Prostate specific membrane antigen expression in prostatic intraepithelial neoplasia and adenocarcinoma: a study of 184 cases. *Cancer*. (1998) 82:2256–61. doi: 10.1002/(SICI)1097-0142(19980601)82:11<2256::AID-CNCR22>3.0.CO;2-S
27. Kusumi T, Koie T, Tanaka M, Matsumoto K, Sato F, Kusumi A, et al. Immunohistochemical detection of carcinoma in radical prostatectomy specimens following hormone therapy. *Pathol Int*. (2008) 58:687–94. doi: 10.1111/j.1440-1827.2008.02294.x
28. Mannweiler S, Amersdorfer P, Trajanoski S, Terrett JA, King D, Mehes G. Heterogeneity of prostate-specific membrane antigen (PSMA) expression in prostate carcinoma with distant metastasis. *Pathol Oncol Res*. (2009) 15:167–72. doi: 10.1007/s12253-008-9104-2
29. Barinka C, Rojas C, Slusher B, Pomper M. Glutamate carboxypeptidase II in diagnosis and treatment of neurologic disorders and prostate cancer. *Curr Med Chem*. (2012) 19:856–70. doi: 10.2174/092986712799034888
30. Horoszewicz JS, Kawinski E, Murphy GP. Monoclonal antibodies to a new antigenic marker in epithelial prostatic cells and serum of prostatic cancer patients. *Anticancer Res*. (1987) 7:927–35
31. Wynant GE, Murphy GP, Horoszewicz JS, Neal CE, Collier BD, Mitchell E, et al. Immunoscintigraphy of prostatic cancer: preliminary results with 111In-labeled monoclonal antibody 7E11-C5.3 (CYT-356). *Prostate*. (1991) 18:229–41. doi: 10.1002/pros.2990180305
32. Hinkle GH, Burgers JK, Neal CE, Texter JH, Kahn D, Williams RD, et al. Multicenter radioimmunoscintigraphic evaluation of patients with prostate carcinoma using indium-111 capromab pendetide. *Cancer: Interdiscipl Int J Am Cancer Soc*. (1998) 83:739–47. doi: 10.1002/(SICI)1097-0142(19980815)83:4<739::AID-CNCR16>3.0.CO;2-T
33. Manyak MJ, Hinkle GH, Olsen JO, Chiaccherini RP, Partin AW, Piantadosi S, et al. Immunoscintigraphy with indium-111-capromab pendetide: evaluation before definitive therapy in patients with prostate cancer. *Urology*. (1999) 54:1058–63. doi: 10.1016/S0090-4295(99)00314-3
34. Osborne JR, Green DA, Spratt DE, Lyashchenko S, Fareedy SB, Robinson BD, et al. A Prospective pilot study of 89Zr-J591/prostate specific membrane antigen positron emission tomography in men with localized prostate cancer undergoing radical prostatectomy. *J Urol*. (2014) 191:1439–45. doi: 10.1016/j.juro.2013.10.041
35. Bander NH, Trabulsi EJ, Kostakoglu L, Yao D, Vallabhajosula S, Smith-Jones P, et al. Targeting metastatic prostate cancer with radiolabeled monoclonal antibody J591 to the extracellular domain of prostate specific membrane antigen. *J Urol*. (2003) 170:1717–21. doi: 10.1097/01.ju.0000091655.77601.0c
36. Morris MJ, Divgi CR, Pandit-Taskar N, Batraki M, Warren N, Nacca A, et al. Pilot trial of unlabeled and indium-111-labeled anti-prostate-specific membrane antigen antibody J591 for castrate metastatic prostate cancer. *Clin Cancer Res*. (2005) 11:7454–61. doi: 10.1158/1078-0432.CCR-05-0826
37. Rowe SP, Gorin MA, Pomper MG. Imaging of prostate-specific membrane antigen with small-molecule PET radiotracers: from the bench to advanced clinical applications. *Annu Rev Med*. (2019) 70:461–77. doi: 10.1146/annurev-med-062117-073027
38. Pandit-Taskar N, O'Donoghue JA, Beylergil V, Lyashchenko S, Ruan S, Solomon SB, et al. ^{89}Zr-huJ591 immuno-PET imaging in patients with advanced metastatic prostate cancer. *Eur J Nucl Med Mol Imaging*. (2014) 41:2093–105. doi: 10.1007/s00259-014-2830-7
39. Pandit-Taskar N, O'Donoghue JA, Durack JC, Lyashchenko SK, Cheal SM, Beylergil V, et al. A phase I/II study for analytic validation of 89Zr-J591 immunoPET as a molecular imaging agent for metastatic prostate cancer. *Clin Cancer Res*. (2015) 21:5277–85. doi: 10.1158/1078-0432.CCR-15-0552
40. Szabo Z, Mena E, Rowe SP, Plyku D, Nidal R, Eisenberger MA, et al. Initial evaluation of [(18)F]DCFPyL for prostate-specific membrane antigen (PSMA)-targeted PET imaging of prostate cancer. *Mol Imaging Biol*. (2015) 17:565–74. doi: 10.1007/s11307-015-0850-8
41. Emmett L, Yin C, Crumbaker M, Hruby G, Kneebone A, Epstein R, et al. Rapid modulation of PSMA expression by androgen deprivation: serial 68Ga-PSMA-11 PET in men with hormone-sensitive and castrate-resistant prostate cancer commencing androgen blockade. *J Nucl Med*. (2019) 60:950–4. doi: 10.2967/jnumed.118.223099
42. Rousseau E, Wilson D, Lacroix-Poisson F, Krauze A, Chi K, Gleave M, et al. A prospective study on 18F-DCFPyL PSMA PET/CT imaging in biochemical recurrence of prostate cancer. *J Nucl Med*. (2019) 60:1587–93. doi: 10.2967/jnumed.119.226381
43. Calais J, Czernin J, Fendler WP, Elashoff D, Nickols NG. Randomized prospective phase III trial of 68Ga-PSMA-11 PET/CT molecular imaging for prostate cancer salvage radiotherapy planning [PSMA-SRT]. *BMC Cancer*. (2019) 19:18. doi: 10.1186/s12885-019-5297-x
44. McCarthy M, Francis R, Tang C, Watts J, Campbell A. A multicenter prospective clinical trial of 68gallium PSMA HBED-CC PET-CT restaging in biochemically relapsed prostate carcinoma: oligometastatic rate and distribution compared with standard imaging. *Int J Radiat Oncol Biol Phys*. (2019) 104:801–8. doi: 10.1016/j.ijrobp.2019.03.014
45. Chen Y, Pullambhatla M, Foss CA, Byun Y, Nimmagadda S, Senthamizhchelvan S, et al. 2-(3-{1-Carboxy-5-[(6-[18F]fluoro-pyridine-3-carbonyl)-amino]-pentyl}-ureido)-pentanedioic acid, [18F]DCFPyL, a PSMA-based PET imaging agent for prostate cancer. *Clin Cancer Res*. (2011) 17:7645–53. doi: 10.1158/1078-0432.CCR-11-1357

46. Rosar F, Buchholz HG, Michels S, Hoffmann MA, Piel M, Waldmann CM, et al. Image quality analysis of 44Sc on two preclinical PET scanners: a comparison to 68Ga. *EJNMMI Phys*. (2020) 7:16. doi: 10.1186/s40658-020-0286-3
47. Eppard E, de la Fuente A, Benešová M, Khawar A, Bundschuh RA, Gärtner FC, et al. Clinical translation and first in-human use of [44Sc]Sc-PSMA-617 for PET imaging of metastasized castrate-resistant prostate cancer. *Theranostics*. (2017) 7:4359–69. doi: 10.7150/thno.20586
48. Werner RA, Derlin T, Lapa C, Sheikbahaei S, Higuchi T, Giesel FL, et al. 18F-labeled, PSMA-targeted radiotracers: leveraging the advantages of radiofluorination for prostate cancer molecular imaging. *Theranostics*. (2020) 10:1–16. doi: 10.7150/thno.37894
49. Ferreira G, Iravani A, Hofman MS, Hicks RJ. Intra-individual comparison of 68Ga-PSMA-11 and 18F-DCFPyL normal-organ biodistribution. *Cancer Imaging*. (2019) 19:23. doi: 10.1186/s40644-019-0211-y
50. Siva S, Murphy D, Hofman MS, Tran B. 223P Using PSMA PET/CT to assess response in metastatic prostate cancer (mPC) patients (pts) receiving upfront chemohormonal therapy. *Ann Oncol*. (2018) 29: mdy434–011. doi: 10.1093/annonc/mdy434.011
51. Plouznikoff N, Artigas C, Sideris S, Martinez Chanza N, Gil T, Peltier A, et al. Evaluation of PSMA expression changes on PET/CT before and after initiation of novel antiandrogen drugs (enzalutamide or abiraterone) in metastatic castration-resistant prostate cancer patients. *Ann Nucl Med*. (2019) 33:945–54. doi: 10.1007/s12149-019-01404-2
52. Phillips RM, Gorin MA, Rowe SP, Pomper MG, Pienta KJ, Ross AE, et al. Complete biochemical response after stereotactic ablative radiotherapy of an isolated prostate cancer pelvic soft tissue recurrence detected by 18F-DCFPyL PET/CT. *Urol Case Rep*. (2018) 16:86–8. doi: 10.1016/j.eucr.2017.11.021
53. Phillips R, Lim SJ, Shi WY, Antonarakis ES, Rowe S, Gorin M, et al. Primary outcomes of a phase II randomized trial of observation versus stereotactic ablative radiation for oligometastatic prostate cancer (ORIOLE). *Int J Radiat Oncol Biol Phys*. (2019) 105:681. doi: 10.1016/j.ijrobp.2019.08.031
54. Rahbar K, Ahmadzadehfar H, Kratochwil C, Haberkorn U, Schäfers M, Essler M, et al. German multicenter study investigating 177Lu-PSMA-617 radioligand therapy in advanced prostate cancer patients. *J Nucl Med*. (2017) 58:85–90. doi: 10.2967/jnumed.116.183194
55. Kelly JM, Amor-Coarasa A, Ponnala S, Nikolopoulou A, Williams C Jr, Thiele NA, et al. A single dose of 225Ac-RPS-074 induces a complete tumor response in an LNCaP xenograft model. *J Nucl Med*. (2019) 60:649–55. doi: 10.2967/jnumed.118.219592
56. Zechmann CM, Afshar-Oromieh A, Armor T, Stubbs JB, Mier W, Hadaschik B, et al. Radiation dosimetry and first therapy results with a 124I/131I-labeled small molecule (MIP-1095) targeting PSMA for prostate cancer therapy. *Eur J Nucl Med Mol Imaging*. (2014) 41:1280–92. doi: 10.1007/s00259-014-2713-y
57. Sathekge M, Knoesen O, Meckel M, Modiselle M, Vorster M, Marx S. 213Bi-PSMA-617 targeted alpha-radionuclide therapy in metastatic castration-resistant prostate cancer. *Eur J Nucl Med Mol Imaging*. (2017) 44:1099–100. doi: 10.1007/s00259-017-3657-9
58. Kratochwil C, Bruchertseifer F, Rathke H, Hohenfellner M, Giesel FL, Haberkorn U, et al. Targeted α-therapy of metastatic castration-resistant prostate cancer with 225Ac-PSMA-617: swimmer-plot analysis suggests efficacy regarding duration of tumor control. *J Nucl Med*. (2018) 59:795–802. doi: 10.2967/jnumed.117.203539
59. Tagawa ST, Milowsky MI, Morris M, Vallabhajosula S, Christos P, Akhtar NH, et al. Phase II study of lutetium-177–labeled anti-prostate-specific membrane antigen monoclonal antibody J591 for metastatic castration-resistant prostate cancer. *Clin Cancer Res*. (2013) 19:5182–91. doi: 10.1158/1078-0432.CCR-13-0231
60. Kratochwil C, Giesel FL, Stefanova M, Benešová M, Bronzel M, Afshar-Oromieh A, et al. PSMA-targeted radionuclide therapy of metastatic castration-resistant prostate cancer with 177Lu-labeled PSMA-617. *J Nucl Med*. (2016) 57:1170–6. doi: 10.2967/jnumed.115.171397
61. Bander NH, Milowsky MI, Nanus DM, Kostakoglu L, Vallabhajosula S, Goldsmith SJ. Phase I trial of 177lutetium-labeled J591, a monoclonal antibody to prostate-specific membrane antigen, in patients with androgen-independent prostate cancer. *J Clin Oncol*. (2005) 23:4591–601. doi: 10.1200/JCO.2005.05.160
62. Milowsky MI, Nanus DM, Kostakoglu L, Vallabhajosula S, Goldsmith SJ, Bander NH. Phase I trial of yttrium-90-labeled anti-prostate-specific membrane antigen monoclonal antibody J591 for androgen-independent prostate cancer. *J Clin Oncol*. (2004) 22:2522–31. doi: 10.1200/JCO.2004.09.154
63. Yadav MP, Ballal S, Tripathi M, Damle NA, Sahoo RK, Seth A, et al. 177Lu-DKFZ-PSMA-617 therapy in metastatic castration resistant prostate cancer: safety, efficacy, and quality of life assessment. *Eur J Nucl Med Mol Imaging*. (2017) 44:81–91. doi: 10.1007/s00259-016-3481-7
64. Rahbar K, Schmidt M, Heinzel A, Eppard E, Bode A, Yordanova A, et al. Response and tolerability of a single dose of 177Lu-PSMA-617 in patients with metastatic castration-resistant prostate cancer: a multicenter retrospective analysis. *J Nucl Med*. (2016) 57:1334–8. doi: 10.2967/jnumed.116.173757
65. Rahbar K, Boegemann M, Yordanova A, Eveslage M, Schäfers M, Essler M, et al. PSMA targeted radioligandtherapy in metastatic castration resistant prostate cancer after chemotherapy, abiraterone and/or enzalutamide. a retrospective analysis of overall survival. *Eur J Nucl Med Mol Imaging*. (2018) 45:12–9. doi: 10.1007/s00259-017-3848-4
66. Ferdinandus J, Eppard E, Gaertner FC, Kürpig S, Fimmers R, Yordanova A, et al. Predictors of response to radioligand therapy of metastatic castrate-resistant prostate cancer with 177Lu-PSMA-617. *J Nucl Med*. (2017) 58:312–9. doi: 10.2967/jnumed.116.178228
67. Ahmadzadehfar H, Wegen S, Yordanova A, Fimmers R, Kürpig S, Eppard E, et al. Overall survival and response pattern of castration-resistant metastatic prostate cancer to multiple cycles of radioligand therapy using [177Lu]Lu-PSMA-617. *Eur J Nucl Med Mol Imaging*. (2017) 44:1448–54. doi: 10.1007/s00259-017-3716-2
68. Ahmadzadehfar H, Schlolaut S, Fimmers R, Yordanova A, Hirzebruch S, Schlenkhoff C, et al. Predictors of overall survival in metastatic castration-resistant prostate cancer patients receiving [177Lu]Lu-PSMA-617 radioligand therapy. *Oncotarget*. (2017) 8:103108–16. doi: 10.18632/oncotarget.21600
69. Bräuer A, Grubert LS, Roll W, Schrader AJ, Schäfers M, Bögemann M, et al. 177Lu-PSMA-617 radioligand therapy and outcome in patients with metastasized castration-resistant prostate cancer. *Eur J Nucl Med Mol Imaging*. (2017) 44:1663–70. doi: 10.1007/s00259-017-3751-z
70. Yadav MP, Ballal S, Sahoo RK, Dwivedi SN, Bal C. Radioligand therapy with 177Lu-PSMA for metastatic castration-resistant prostate cancer: a systematic review and meta-analysis. *AJR Am J Roentgenol*. (2019) 213:275–85. doi: 10.2214/AJR.18.20845
71. Kratochwil C, Bruchertseifer F, Giesel FL, Weis M, Verburg FA, Mottaghy F, et al. 225Ac-PSMA-617 for PSMA-targeted α-radiation therapy of metastatic castration-resistant prostate cancer. *J Nucl Med*. (2016) 57:1941–4. doi: 10.2967/jnumed.116.178673
72. Sathekge M, Bruchertseifer F, Knoesen O, Reyneke F, Lawal I, Lengana T, et al. 225Ac-PSMA-617 in chemotherapy-naive patients with advanced prostate cancer: a pilot study. *Eur J Nucl Med Mol Imaging*. (2019) 46:129–38. doi: 10.1007/s00259-018-4167-0
73. dos Santos JC, Schäfer M, Bauder-Wüst U, Lehnert W, Leotta K, Morgenstern A, et al. Development and dosimetry of 203Pb/212Pb-labelled PSMA ligands: bringing "the lead" into PSMA-targeted alpha therapy? *Eur J Nucl Med Mol Imaging*. (2019) 46:1081–91. doi: 10.1007/s00259-018-4220-z
74. Lim A, Joseph KJ. Predicting radiation-adverse effects using three-dimensional dose and fractionation data: radiation dermatitis. *Int J Radiat Oncol Biol Phys*. (2019) 105:E130. doi: 10.1016/j.ijrobp.2019.06.2259
75. Loke KSH, Padhy AK, Ng DCE, Goh ASW, Divgi C. Dosimetric considerations in radioimmunotherapy and systemic radionuclide therapies: a review. *World J Nucl Med*. (2011) 10:122–38. doi: 10.4103/1450-1147.89780
76. Tagawa ST, Vallabhajosula S, Christos PJ, Jhanwar YS, Batra JS, Lam L, et al. Phase 1/2 study of fractionated dose lutetium-177-labeled anti-prostate-specific membrane antigen monoclonal antibody J591 (177 Lu-J591) for metastatic castration-resistant prostate cancer. *Cancer*. (2019) 125:2561–9. doi: 10.1002/cncr.32072
77. Niaz MJ, Batra JS, Walsh RD, Ramirez-Fort MK, Vallabhajosula S, Jhanwar YS, et al. Pilot study of hyperfractionated dosing of lutetium-177-labeled antiprostate-specific membrane antigen monoclonal antibody J591 (177 Lu-J591) for metastatic castration-resistant prostate cancer. *Oncologist*. (2020) 2020–0028. doi: 10.1634/theoncologist.2020-0028

78. Sunday ME, Kaplan LM, Motoyama E, Chin WW, Spindel ER. Gastrin-releasing peptide (mammalian bombesin) gene expression in health and disease. In: *Pathology Reviews*. Totawa, NJ: Humana Press (1989). p. 54–7. doi: 10.1007/978-1-4612-4502-5_4
79. Penman E, Wass JA, Butler MG, Penny ES, Price J, Wu P, et al. Distribution and characterisation of immunoreactive somatostatin in human gastrointestinal tract. *Regul Pept*. (1983) 7:53–65. doi: 10.1016/0167-0115(83)90281-1
80. Jensen RT, Battey JF, Spindel ER, Benya RV. International union of pharmacology. LXVIII. mammalian bombesin receptors: nomenclature, distribution, pharmacology, signaling, and functions in normal and disease states. *Pharmacol Rev*. (2008) 60:1–42. doi: 10.1124/pr.107.07108
81. Cuttitta F, Carney DN, Mulshine J, Moody TW, Fedorko J, Fischler A, et al. Bombesin-like peptides can function as autocrine growth factors in human small-cell lung cancer. *Nature*. (1985) 316:823–6. doi: 10.1038/316823a0
82. Ramos-Álvarez I, Moreno P, Mantey SA, Nakamura T, Nuche-Berenguer B, Moody TW, et al. Insights into bombesin receptors and ligands: highlighting recent advances. *Peptides*. (2015) 72:128–44. doi: 10.1016/j.peptides.2015.04.026
83. Touijer KA, Michaud L, Alvarez HAV, Gopalan A, Kossatz S, Gonen M, et al. Prospective study of the radiolabeled GRPR antagonist BAY86-7548 for positron emission tomography/computed tomography imaging of newly diagnosed prostate cancer. *Eur Urol Oncol*. (2019) 2:166–73. doi: 10.1016/j.euo.2018.08.011
84. Roivainen A, Kahkonen E, Borkowski S, Hofmann B, Lehtio K, Luoto P, et al. Radiometabolism, whole-body distribution and radiation dosimetry of Ga-68-bombesin antagonist BAY86-7548 in healthy men. In: *European Journal Of Nuclear Medicine And Molecular Imaging*. Springer, NY: Spring (2012). p. 10013. doi: 10.2967/jnumed.112.114082
85. Stephens A, Loid I WC, Beheshti M, Jambor I, Kemppainen J, Bostrom P, et al. Detection of prostate cancer with the [68Ga]-labeled bombesin antagonist RM2 in patients undergoing radical prostatectomy. *J Clin Oncol*. (2016) 34 (Suppl. 80):80. doi: 10.1200/jco.2016.34.2_suppl.80
86. Wieser G, Popp I, Rischke HC, Drendel V, Grosu AL, Bartholomä M, et al. Diagnosis of recurrent prostate cancer with PET/CT imaging using the gastrin-releasing peptide receptor antagonist 68 Ga-RM2: Preliminary results in patients with negative or inconclusive [18 F] Fluoroethylcholine-PET/CT. *Eur J Nucl Med Mol Imaging*. (2017) 44:1463–72. doi: 10.1007/s00259-017-3702-8
87. Iagaru A. Will GRPR compete with PSMA as a target in prostate cancer? *J Nucl Med*. (2017) 58:1883–4. doi: 10.2967/jnumed.117.198192
88. Coleman RE. Metastatic bone disease: clinical features, pathophysiology and treatment strategies. *Cancer Treat Rev*. (2001) 27:165–76. doi: 10.1053/ctrv.2000.0210
89. Ren G, Esposito M, Kang Y. Bone metastasis and the metastatic niche. *J Mol Med*. (2015) 93:1203–12. doi: 10.1007/s00109-015-1329-4
90. Parker C, Nilsson S, Heinrich D, Helle SI, O'sullivan JM, Fosså SD, et al. Alpha emitter radium-223 and survival in metastatic prostate cancer. *N Engl J Med*. (2013) 369:213–23. doi: 10.1056/NEJMoa1213755
91. Flux GD. Imaging and dosimetry for radium-223: the potential for personalized treatment. *Br J Radiol*. (2017) 90:20160748. doi: 10.1259/bjr.20160748
92. Abou DS, Rittenbach A, Tomlinson RE, Finley PA, Tsui B, Simons BW, et al. Preclinical single photon emission computed tomography of alpha particle-emitting radium-223. *Cancer Biother Radiopharm*. (2020). doi: 10.1089/cbr.2019.3308. [Epub ahead of print].
93. Benabdallah N, Bernardini M, Bianciardi M, de Labriolle-Vaylet C, Franck D, Desbrée A. 223Ra-dichloride therapy of bone metastasis: optimization of SPECT images for quantification. *EJNMMI Res*. (2019) 9:20. doi: 10.1186/s13550-019-0488-7
94. Umeda T, Koizumi M, Fukai S, Miyaji N, Motegi K, Nakazawa S, et al. Evaluation of bone metastatic burden by bone SPECT/CT in metastatic prostate cancer patients: defining threshold value for total bone uptake and assessment in radium-223 treated patients. *Ann Nucl Med*. (2018) 32:105–13. doi: 10.1007/s12149-017-1224-x

Conflict of Interest: The authors declare that the research was conducted in the absence of any commercial or financial relationships that could be construed as a potential conflict of interest.

frontiers in Oncology

MINI REVIEW
published: 22 July 2020
doi: 10.3389/fonc.2020.01131

Theranostic Pretargeting Drug Delivery and Imaging Platforms in Cancer Precision Medicine

Sudath Hapuarachchige[1]* *and Dmitri Artemov*[1,2]

[1] The Russell H. Morgan Department of Radiology and Radiological Science, The Johns Hopkins University School of Medicine, Baltimore, MD, United States, [2] Department of Oncology, The Sidney Kimmel Comprehensive Cancer Center, The Johns Hopkins University School of Medicine, Baltimore, MD, United States

Theranostics are nano-size or molecular-level agents serving for both diagnosis and therapy. Structurally, they are drug delivery systems integrated with molecular or targeted imaging agents. Theranostics are becoming popular because they are targeted therapeutics and can be used with no or minimal changes for diagnostic imaging to aid in precision medicine. Thus, there is a close relation between theranostics and image-guided therapy (IGT), and theranostics are actually a subclass of IGT in which both therapeutic and imaging functionalities are attributed to a single platform. An important theranostics strategy is biological pretargeting. In pretargeted IGT, first, the target is identified by a target-specific natural or synthetic bioligand followed by a nano-scale or molecular drug delivery component, which form therapeutic clusters by *in situ* conjugation reactions. If pretargeted drug delivery platforms are labeled with multimodal imaging probes, they can be used as theranostics for both diagnostic imaging and therapy. Optical and nuclear imaging techniques have mostly been used in proof-of-concept studies with pretargeted theranostics. The concept of pretargeting in theranostics is comparatively novel and generally requires a confirmed overexpression of surface receptors on targeted cells/tissue. In addition, the receptors should have natural or synthetic bioligands to be used as pretargeting components. Therefore, applications of pretargeting theranostics are still limited to several cancer types, which overexpress cell-surface markers on the target cancer cells. In this review, recent discoveries of pretargeting theranostics in breast, ovarian, prostate, and colorectal cancers are discussed to highlight main strengths and potential limitations the strategy.

Keywords: theranostics, cancer therapy, pretargeted therapy, drug delivery, nanomedicine, bioorthogonal click chemistry

OPEN ACCESS

Edited by:
Marie-France Penet, Johns Hopkins University, United States

Reviewed by:
M. Carmen Martinez-Bisbal, University of Valencia, Spain
Giulio Fracasso, University of Verona, Italy

***Correspondence:**
Sudath Hapuarachchige
shapuar1@jh.edu

Specialty section:
This article was submitted to Cancer Imaging and Image-directed Interventions, a section of the journal Frontiers in Oncology

Received: *09 December 2019*
Accepted: *05 June 2020*
Published: *22 July 2020*

Citation:
Hapuarachchige S and Artemov D (2020) Theranostic Pretargeting Drug Delivery and Imaging Platforms in Cancer Precision Medicine. Front. Oncol. 10:1131. doi: 10.3389/fonc.2020.01131

INTRODUCTION

Theranostics is a rapidly developing field that combines the unique opportunities offered by nanotechnology with personalized medicine to provide significantly improved treatment efficacy with reduced off-target effects through the specific delivery of therapy to targeted tissues. Theranostic approaches combine imaging that uses one of the non-invasive imaging modalities, with specific delivery of therapeutic components, which can be based on different biophysical and biological principles. Theranostics can be synthesized to have optimal delivery properties, low renal clearance, reduced immunogenicity and antigenicity (for example by PEGylating the surface of

theranostic nanoparticles), and high capacity for therapeutic agents, which is required given the limited concentrations of specific molecular markers expressed on cancer cells.

Theranostics

Theranostic probes can be used for both diagnostic imaging and therapy (1). For a truly theranostic application, imaging and therapeutic molecules should be parts of a single platform functionalized with various moieties for specific recognition of molecular targets, imaging markers, and therapeutic compounds. One of the major problems in achieving efficient treatment in this strategy is the uniform delivery and distribution of theranostics with therapeutic cargo in the tumor or sufficiently strong bystander effects of therapy (such as for hyperthermia). As the distribution of nano-scale drug delivery platforms is primarily driven by the passive diffusion facilitated by the enhanced-permeability-retention (EPR) effect, which is present in some solid tumors, optimization of the molecular size, and circulation time of nanoplatforms is of paramount importance for the success of treatment. However, there are additional biological delivery barriers, such as the desmoplastic tumor microenvironment (2) and increased interstitial pressure due to dysfunctional lymphatics in solid tumors (3), which can modulate the delivery. The presence of a functional blood-brain barrier in brain tumors presents an entirely new set of problems with delivery, which is beyond the scope of the current review. Imaging can help to evaluate the uniformity of delivery, but, to achieve high efficacy, the design of a therapeutic system must ensure the effective delivery and distribution of theranostics to all malignant cells within the cancer.

While the initial distribution of theranostics in tumors is driven by passive processes and needs to be optimized based on the intrinsic physicochemical properties of platform, specific retention and cell delivery is typically controlled by active targeting of theranostic to specific molecular targets present on cancer cells using high-affinity molecules, such as antibodies, antibody fragments, affibodies, peptides, etc. It is important to note that, while unique, highly specific molecular targets are preferable for the application of highly cytotoxic theranostics, the initial delivery of theranostics rely on the tumor-specific EPR effect. The "binding site barrier" is a critical factor in targeted drug delivery (4, 5). This issue can be circumvented in theranostic design using biomolecules as platforms and keeping the size of components in subnano level (6).

Pretargeting Theranostic Approach

Important criteria that should be fulfilled for a truly theranostic platform is that the imaging data must provide meaningful information, which can be used to make critical decisions regarding the therapeutic procedure. In pretargeting therapy, the first component is typically used for labeling the target and obtaining the location and size (perhaps tumor stage) of the tumor. Since the pretargeting component is not cytotoxic, its long circulation (and possible weak non-specific binding) does not generate side effects, while providing improved distribution in the tumor. After the target is confirmed, the second therapeutic components can be administered chemoselectively cross-linking the first pretargeting component on cell surface.

Contemporary targeted drug delivery vehicle such as ADCs, with an imaging marker may provide imaging information about the delivery and distribution of the platform in the tumor. Micro-dosing can also be used to track the delivery and image the distribution prior to the administration of the therapeutic dose (**Figure 1**). However, while these approaches can be considered theranostic, in the first case, imaging would only provide secondary information that cannot be used to change and/or optimize the treatment protocol, and, in the latter case, imaging is limited to a significantly reduced dose and the therapeutic dose of nanomedicine is delivered without image guidance.

In situ Conjugation Methods in Pretargeting Theranostics

The conjugation between pretargeting component and the therapeutic delivery component occurs in the biological system in physiological conditions. This *in situ* conjugation method should be fast and proceed at 37°C without releasing toxic byproducts. Avidin-biotin interaction is one of the early stage *in situ* conjugation techniques used for pretargeted imaging and therapy (7). Avidin is a tetrameric protein which binds biotin with high affinity. Since avidin is immunogenic and has a broad non-specific binding, this conjugation method can lead to adverse biological effects and toxicities. Bioorthogonal click chemistry is an alternative conjugation method widely used nowadays for *in situ* conjugation. *Trans*-cyclooctene/tetrazine bioorthogonal click reaction is extremely fast and widely used for pretargeting conjugation compared to other reactions in this category such as, copper-free azide-cyclooctyne click chemistry and Staudinger ligation (8, 9). Specific interaction between peptide nucleic acids, which are non-natural DNA/RNA analogs, can also be used for pretargeting approach (10). These compounds are metabolically stable and show low non-specific binding in healthy tissues.

Imaging Strategy in Theranostic Systems

A wide variety of imaging modalities used for theranostics include optical (fluorescence or bioluminescence), nuclear (PET or SPECT), ultrasound, photoacoustic, magnetic particle, and MR imaging techniques (11, 12). The imaging results pretargeting component can be directly used to (i) verify the expression of surface receptors at the target site and (ii) precisely time the administration of the second, drug-delivery component, based on high specific accumulation of the pretargeting component at the target site and clearance from the rest of the body. Expression of receptors can be variable between the primary tumor and distant metastatic sites and not easily accessible by biopsy. Therefore, images from pretargeting component provide a positive confirmation of the receptor expression and a "go" signal for the administration of the cytotoxic drug carrier. Imaging of the drug carrier is equally important, as it can provide positive confirmation of the successful delivery and retention of the cytotoxic component in

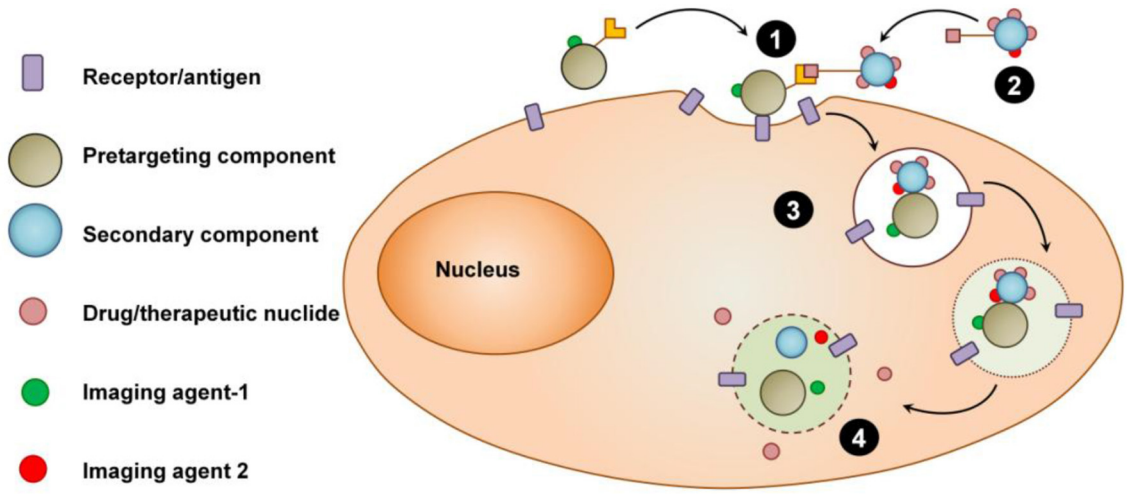

FIGURE 1 | Schematic view of the concept of pretargeting theranostic strategy. (1) Image-guided pretargeting. (2) Therapeutic/radionuclide delivery step. (3) Internalization of the complex of pretargeting-receptor-delivery components. (4) Intracellular release of therapeutics or radionuclides.

the tumor. These imaging results can also be used to correlate the delivery and treatment outcomes and to support their use as imaging markers of response. The optical imaging is widely used in preclinical drug developments because it's fast, convenient, non-invasive, safe, and cost-effective (13). High tissue absorbance and scatter are the major disadvantages in optical imaging in deep locations; however, this issue can be partly overcome in preclinical imaging using near infra-red (NIR) dyes (λ_{ex} in the range of 650–900 nm) (14). In spite of aforementioned problems, NIR optical imaging became a popular imaging technique in pretargeting studies for visualizing the target and the probe and it can provide sufficient information about the target-uptake and biodistribution of the pretargeting component, as well as the tumor dimension and location information in cancer therapy (15).

Nuclear imaging techniques are highly feasible for imaging pretargeting delivery because of excellent sensitivity, quantitative images, and the possibility of using in radiotherapy (16). Nuclear imaging provides sensitivity in the low nM to pM range, but has low spatial resolution and requires an additional anatomical imaging modality, such as CT or MRI, for anatomical reference. PET and SPECT imaging techniques are translational and can be used in both animals and patients. PET provides the highest sensitivity combined with improved spatial resolution; however, it is impossible to differentiate between two tracers with similar half-lives. SPECT provides an intrinsic ability for multi-isotope imaging based on different energy of γ emission (17). However, it is not commonly used for tracking of pretargeting components because of lower sensitivity and spatial resolution. However, it has been used for imaging the second therapeutic component of the system. For instance, in image-guided pretargeting radioimmunotherapy (PRIT), the targeted cells are labeled with antibodies conjugated with TCO groups and treated with SPECT imaging/therapeutic radionuclide conjugated with tetrazine. Pretargeting radiotherapy is one example of combining nuclear imaging to circumvent the use of long-lived radionuclides that is a necessity for sufficient tumor accumulation and target-to-background ratios using conventional approaches (16).

The imaging signals of the second component are mostly used for the biodistribution and pharmacokinetic evaluation and not for detection and evaluation of the tumor, hence the poor contrast and spatial resolution of SPECT imaging can be tolerated. MRI provides high spatial resolution and excellent soft-tissue contrast, but has a moderate sensitivity and requires concentrations of the imaging probe in high micromolar range. Fluorescence optical imaging provides outstanding sensitivity and resolution, but can only be used in superficial locations, such as for image-guided surgical resection, or in optically transparent tissues, such as ocular imaging. Examples of anticancer theranostics applications, which use these multiple imaging modalities are: PET and NIR optical imaging (18); SPECT (19), and MRI (20).

It is important to note that combining a therapeutic platform with short-lived imaging probes presents significant problems because of the short lifetime of the preparation, and consequently, with the logistics of treatment administration and monitoring even if the medication can be formulated in a kit form for rapid radiolabeling (21). Therapeutic modalities used in theranostic nano-platforms include cytotoxic drugs (22–24), radioisotopes (25), optical absorbers for photothermal or photodynamic therapy (26), and phototherapy (27). Specific enzymes can be delivered to activate prodrugs in the context of prodrug therapy (28). Magnetic NPs are therapeutic cargo for magnetic hyperthermia (29), and antibodies, adjuvants, or vaccines can be used for cancer immunotherapy (30). Most often, imaging techniques used in pretargeting theranostics rely on complementary optical and nuclear imaging modalities, such as fluorescence, bioluminescence, PET and SPECT imaging.

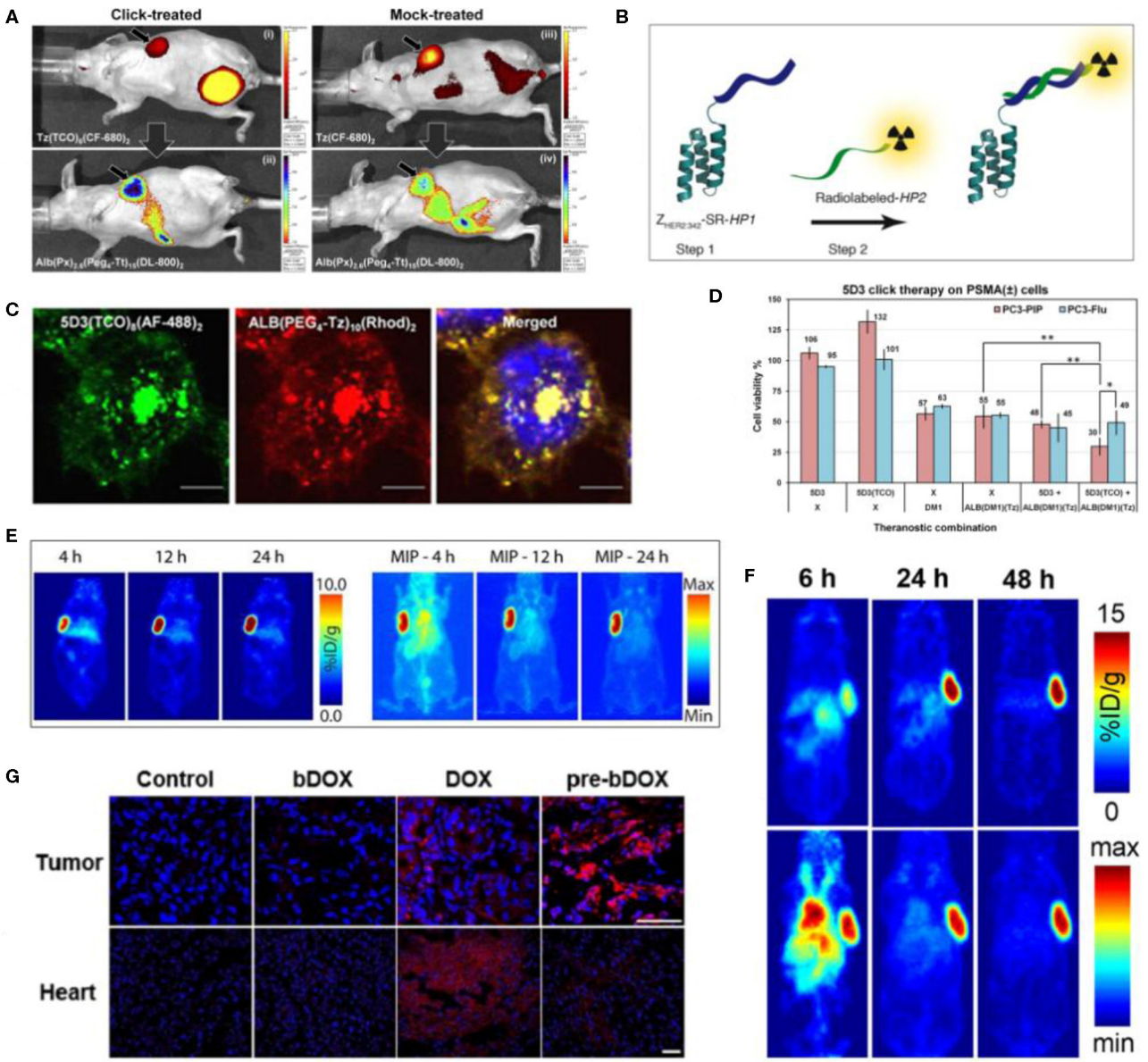

FIGURE 2 | Examples of pretargeted theranostic approaches. **(A)** *In vivo* Xenogen fluorescence images after 8 h post-injection of the secondary component (after 20 h post-injection of pretargeting component). (i) Distribution of pretargeting component $Tz(TCO)_6(CF\text{-}680)_2$ and (ii) tumor uptake of delivery component $Alb(Px)_{2.6}(Peg_4\text{-}Tt)_{15}(DL\text{-}800)_2$. (iii) Distribution of control $Tz(CF\text{-}680)_2$ and (iv) $Alb(Px)_{2.6}(Peg_4\text{-}Tt)_{15}(DL\text{-}800)_2$ in a mock-treated mouse (23). **(B)** Schematic view of the strategy. In step-1 $Z_{HER2:342}$-SR-*HP1* is injected and labeled the HER2(+) tumor cells. Next, the secondary probe *HP2* is injected in step 2. The PNA sequence in *HP2* is matching with *HP1* and hybridized to the pretargeting component bound on cell surface (36). **(C)** Confocal fluorescence microscope images of pretargeted theranostic approach in PSMA(+) PC3-PIP cells. Distribution of $5D3(TCO)_8(AF\text{-}488)_2$ (green), $ALB(PEG_4\text{-}Tz)_{10}(Rhod)_2$ (red), and Hoechst 33342 nuclear counterstaining (blue) (magnification ×100, bar: 30 μm) (22). **(D)** *In vitro* therapeutic study of $5D3(TCO)_8$. The combination of $5D3(TCO)_8$ and $ALB(DM1)_{3.3}(PEG_4\text{-}Tz)_{10}$ exhibited a selective and enhanced toxicity in PSMA(+) PC3-PIP cells compared to the combination of non-functionalized 5D3 and $ALB(DM1)_{3.3}(PEG_4\text{-}Tz)_{10}$ or treatment with a free DM1 or ALB alone. (*$p < 0.05$, **$p < 0.005$) (22). **(E)** Pretargeting PET images of planar and maximum intensity projection (MIP), left and right, respectively in subcutaneous SW1222 tumor bearing nude mice. HuA33-Dye800-TCO was injected (100 μg; 0.66 nmol) and after 48 h, ^{64}Cu-Tz-SarAr was injected. Coronal slices selected from the center of the tumors are shown (37). **(F)** PET images of the athymic nude mice with subcutaneous SW1222 tumor xenografts. The mice were first injected with $huA33(TCO)_{2.4}$, followed after 24 h by the injection of [^{64}Cu]Cu-SarAr-Tz and after 24 h by the injection of [^{177}Lu]Lu-DOTA-PEG_7-Tz. Images are shown at 6, 24, and 48 h after the injection of [^{64}Cu]Cu-SarAr-Tz. Top row: Coronal planar images through center of the tumor. Bottom row: maximum intensity projections (MIP) (38). **(G)** Confonal fluorescence images of frozen sections showing doxorubicin drug uptake in tumor and heart tissues after the administration of PBS, un-pretargeting bDOX, free doxorubicin or pretargeting bDOX. Blue color represents DAPI-stained nuclei, and pseudo-red color represents fluorescence from DOX or bDOX. The scale bar: 50 μm. *$p < 0.05$ (pre-bDOX: pre-targeted bDOX) (39).

EXAMPLES OF PRETARGETED THERANOSTICS

Pretargeted Theranostics in Breast Cancer

Breast cancer is the most prevalent malignancy in women in the United States, and ∼20–30% of human BrCa overexpress HER2 receptors, a molecular marker that correlates with cancer aggressiveness, metastasis, and poor prognosis. HER2-overexpressing BrCa are treated with the humanized anti-HER2 monoclonal antibody, Trastuzumab (Tz), which is highly efficacious, but unfortunately, trastuzumab resistance develops over long-term use (31–33). Trastuzumab-based ADC, T-DM1, was developed for treatment of resistant tumors by directly conjugating the chemotherapeutic drug, mertansine, on the antibody to boost cytotoxicity (34). A potential problem with ADCs is their intrinsically highly toxicity, which can cause non-specific off-target effects in normal tissues due to their long circulation times (35). Hapuarachchige et al. (23, 24) has reported a pretargeting strategy driven by bioorthogonal click chemistry to circumvent this issue. In these studies, HER2(+) cancer cells were prelabeled with a trastuzumab mAb, functionalized with a bioorthogonal, click-reactive, TCO group, and the drug-carrier albumin component with the complementary click-reactive Tt group is delivered after free antibodies have cleared the body, to ensure that the toxic drug component accumulates only at the tumor site (**Figure 2A**). The strategy has been evaluated in human BrCa BT-474 cells and their HER2(+) subcutaneous tumor mouse models. Mice were administered with $Tz(TCO)_6(CF\text{-}680)_2$ image-guided pretargeting component followed by $Alb(Px)_{2.6}(Peg_4\text{-}Tt)_{15}(CF\text{-}750)_2$ drug delivery component. The result revealed that pretargeting approach driven by bioorthogonal click chemistry has higher therapeutic efficacy than the treatment by drug delivery component alone. This therapeutic regimen, when integrated with molecular imaging modalities, can become an effective theranostic tool that will eventually steer the development of cancer regimens toward precision, individuality, and safety.

Pretargeted Theranostics in Ovarian Cancer

Ovarian cancer is the deadliest gynecological cancer in women; hence, the early detection and treatments are vitally important (40). Efforts have been taken to developed drugs to treat ovarian cancers overexpressing estrogen receptor (ER) and HER2. However, long term use of these novel therapies gains drug resistance. Therefore additional therapeutic approaches, such as radioimmunotherapy are needed to be developed for ovarian cancer to overcome the chemo-resistance issues (41). Affibody is a relatively low molecular weight high-affinity protein, which can be used instead of monoclonal antibodies for diagnostic imaging and therapy. Honarvar et al. (36) has developed a HER2 specific affibody conjugate and complementary secondary imaging component and evaluate in HER2(+) ovarian cancer xenografts. They have synthesized $Z_{HER2:342}$-SR-*HP1* and used it as the pretargeting component with 15-mer *HP1* peptide nucleic acid moiety to recognize complementary secondary component, ^{111}In-/^{125}I-*HP2* (**Figure 2B**). The results revealed that the HER2(+) tumor uptake of pretargeting, $Z_{HER2:342}$-SR-*HP1* was significantly higher than HER2 low expressing cells. In the pretargeting approach, accumulation of ^{111}In-*HP2* after the administration of $Z_{HER2:342}$-SR-*HP1* was significantly higher compared to the administration of ^{111}In-*HP2* alone. In regular radioimmunotherapy, the fast clearance of the secondary component, ^{111}In-*HP2*, results in low tumor uptake in bones. Pretargeting strategy enhances the accumulation and retention of the radiotherapeutic agent at the target.

Pretargeted Theranostics in Prostate Cancer

Prostate cancer is one of the most devastating cancer types in men. Yearly more than 150,000 patients are diagnosed with prostate cancer and over 30,000 among them die. Despite existing therapies in prostate cancer management, novel therapeutic approaches and drug delivery strategies are still required to save these patients and eradicate the decease completely (42–44). Prostate-specific membrane antigen (PSMA), a type II membrane protein, is highly expressed in aggressive prostate cancer (PCa) (45–48). In our studies, we have used 5D3 mAb, a novel anti-PSMA mAb which exhibits a 10-fold higher binding affinity on PSMA compared to other known anti-PSMA mAb, such as J591 and 7E11 mAbs (49, 50). 5D3 mAb shows fast internalization after complexing with PSMA; however, this strategy has been successfully applied and proven *in vitro*.

Hapuarachchige et al. (22) has reported a promising pretargeting theranostic approach for treating PSMA-overexpressing prostate cancer using 5D3 mAb. Here, 5D3 conjugated TCO and albumin conjugated with tetrazine have been used as pretargeting and delivery components, respectively. Both components were labeled with fluorophores without spectral profile conflicts to track with optical imaging. PSMA(+) PC3-PIP and PSMA(–) PC3-Flu cells were used to validate the strategy *in vitro*. The pretargeting component, $5D3(TCO)_8(AF\text{-}488)_2$, labeled the PSMA receptors on the targeted cell surface, and was then followed by a second-component, $ALB(DM1)_{2.2}(Peg_4\text{-}Tt)_{10}(Rhod)_2$ (**Figure 2C**). The multiple TCO and Tt groups per component, the high density of PSMA receptors per cell surface, and the fast kinetics of the TCO-Tt click reaction are the driving forces for the formation of nanoclusters on the cell surface. An efficient cross-linking of two components on the targeted cell surface leads to enhanced cellular internalization and results in the highest therapeutic effects in PSMA(+) PC3-PIP cells compared to PSMA(–) PC3-Flu cells (**Figure 2D**). Ideally, the internalization and pharmacokinetics of the pretargeting agent should have similar time scales. After internalization, nanoclusters are hydrolyzed in acidic late endosomes and release cargo drug molecules to the cytoplasm. Eventually, a DM1 anti-tubulin agent blocks the microtubule formation, arresting cell division, and killing targeted cells.

Pretargeted Theranostics in Colorectal Cancer

Colorectal cancer is the most common cancer type in the world after lung and BrCa (51). The surgical approach of managing colorectal cancer is limited for cases with localized

tumors but not feasible in early stage tumors and metastatic tumors. Pretargeting radioimmunotherapy is an optimistic solution to overcome these issues (52). As an initiate, Adumeau et al. (37) has reported a pretargeting multimodal PET/NIRF imaging approach for imaging colorectal cancer. They have used humanized A33 monoclonal antibody (huA33) as the pretargeting platform targeting A33-expressing colorectal cancer. HuA33 was conjugated with TCO and labeled with Dye800 NIR fluorophore and used as the pretargeting component with tetrazine–sarcophagine conjugate labeled with ^{64}Cu radionuclide (^{64}Cu-Tz-SarAr). This strategy has been successfully evaluated in SM1222 colorectal cancer xenograft tumor mouse models overexpressing A33 cell surface antigen (**Figure 2E**). Keinanen et al. (38) from the same group have reported the extension of this study from diagnostic [^{64}Cu]Cu-SarAr-Tz to therapeutic, using [^{177}Lu]Lu-DOTA-PEG$_7$-Tz conjugates, as the secondary component. Both [^{64}Cu]Cu-SarAr-Tz and [^{177}Lu]Lu-DOTA-PEG$_7$-Tz have shown high activity in mice models bearing A33-overexpressing subcutaneous tumors (**Figure 2F**).

The biotin and avidin chemistry has been successfully used for pretargeting imaging of HER2(+) BrCa in preclinical settings (7). Lectin receptors are overexpressed and many cancer types and avidin can bind with lectin as well. Yao et al. (39) have used this phenomenon for pretargeting theranostic approach for image-guided treatment of human colorectal cancer cells, LS180 and HT-29. In their study, avidin without conjugation has been used as the pretargeting component targeting lectin receptors in colorectal cancer cells and tumors in mouse models. Doxorubicin was conjugated with biotic through an acid sensitive hydrazone linker (bDOX). Because of the hydrazone bonding doxorubicin is in prodrug stage. To evaluate the strategy, colorectal cancer LS180 and HT-29 cells were first treated with avidin followed by the administration of bDOX. Avidin is labeled on the lectin receptors of the targeted cell surface. Then biotinylated dDOX will be complexed with avidin followed by rapid internalization by endocytosis. In late endosomes or lysosomes, at low pH acidic condition, hydrazone bond is cleaved releasing free doxorubicin. Compared to doxorubicin alone, pretargeting approach shows higher cellular uptake of the drug. *In vivo* study, LS180 colorectal cancer xenograft mouse models were subsequently administered with avidin and bDOX and significant reduction of tumor growth was observed compared to the mice treated with free doxorubicin (**Figure 2G**). Hence, this strategy is synthetically convenient and exhibits enhanced therapeutic efficacy with minimal systemic toxicities.

CONCLUSIONS

Theranostics can be a highly important tool in the development of precision, highly efficient, and safe therapy for the personalized treatment of cancer using molecular information from a patient's tumors. The pretargeting approach can leverage the inherent strengths of the theranostic strategy; however, it will require a strategy of orthogonal conjugation in physiological conditions. The combination of pretargeting imaging and therapy provided several advantages over single-component theranostics. This strategy significantly reduces the circulatory time and off-target toxicity of the drug-carrier component and provides objective criteria for optimization of the treatment protocol based on the results of non-invasive imaging. The prerequisites for successful applications of a pretargeting theranostic approach are (a) high expression of the target receptor and the use of a high binding affinity pretargeting component, (b) optimal internalization of the pretargeting component-receptor molecular complex, which is a complex parameters that depends on the tumor microenvironment conditions and should allow an adequate time window for *in situ* reactions with a second delivery component, (c) affinity of the binding of two components on the targeted cell surface, and (d) correct combination of imaging agents/imaging modalities and therapeutics on the therapeutic components.

AUTHOR CONTRIBUTIONS

All authors listed have made equal direct and intellectual contribution to the work and preparation of the manuscript and approved the manuscript for publication.

FUNDING

This work was supported in part by NIH R01CA209884, DOD PC150837, and Emersion Collective 128821 grants.

REFERENCES

1. Langbein T, Weber WA, Eiber M. Future of theranostics: an outlook on precision oncology in nuclear medicine. *J Nucl Med.* (2019) 60:13S−9S. doi: 10.2967/jnumed.118.220566
2. Mpekris F, Papageorgis P, Polydorou C, Voutouri C, Kalli M, Pirentis AP, et al. Sonic-hedgehog pathway inhibition normalizes desmoplastic tumor microenvironment to improve chemo- and nanotherapy. *J Control Release.* (2017) 261:105–12. doi: 10.1016/j.jconrel.2017.06.022
3. Jain RK. Delivery of molecular and cellular medicine to solid tumors. *Adv Drug Deliv Rev.* (2012) 64:353–65. doi: 10.1016/j.addr.2012.09.011
4. Weinstein JN, van Osdol W. Early intervention in cancer using monoclonal antibodies and other biological ligands: microphamacology and the "Binding Site Barrier". *Cancer Res.* (1992) 52:2747s−51s.
5. Ruoslahti E, Bhatia SN, Sailor MJ. Targeting of drugs and nanoparticles to tumors. *J Cell Biol.* (2010) 188:759–68. doi: 10.1083/jcb.200910104
6. Rosenblum D, Joshi N, Tao W, Karp JM, Peer D. Progress and challenges towards targeted delivery of cancer therapeutics. *Nat Commun.* (2018) 9:1410. doi: 10.1038/s41467-018-03705-y
7. Zhu W, Okollie B, Bhujwalla ZM, Artemov D. Pamam dendrimer-based contrast agents for Mr imaging of Her-2/Neu Receptors by a three-step pretargeting approach. *Magn Reson Med.* (2008) 59:679–85. doi: 10.1002/mrm.21508
8. Meyer JP, Houghton JL, Kozlowski P, Abdel-Atti D, Reiner T, Pillarsetty NV, Scholz WW, Zeglis BM, Lewis JS. (18)F-Based Pretargeted pet imaging based on bioorthogonal diels-alder click chemistry. *Bioconjug. Chem.* (2016) 27:298-301. doi: 10.1021/acs.bioconjchem.5b00504
9. Mushtaq S, Yun SJ, Jeon J. Recent advances in bioorthogonal click chemistry for efficient synthesis of radiotracers and radiopharmaceuticals. *Molecules.* (2019) 24:3567. doi: 10.3390/molecules24193567
10. Saarbach J, Sabale PM, Winssinger N. Peptide nucleic acid (Pna) and its applications in chemical biology, diagnostics, and therapeutics.

Curr Opin Chem Biol. (2019) 52:112–24. doi: 10.1016/j.cbpa.2019.06.006
11. Penet MF, Chen Z, Kakkad S, Pomper MG, Bhujwalla ZM. Theranostic imaging of cancer. *Eur J Radiol.* (2012) 81(Suppl 1):S124–6. doi: 10.1016/S0720-048X(12)70051-7
12. Yordanova A, Eppard E, Kurpig S, Bundschuh RA, Schonberger S, Gonzalez-Carmona M, et al. Theranostics in nuclear medicine practice. *Onco Targets Ther.* (2017) 10:4821–8. doi: 10.2147/OTT.S140671
13. Arranz A, Ripoll J. Advances in optical imaging for pharmacological studies. *Front Pharmacol.* (2015) 6:189. doi: 10.3389/fphar.2015.00189
14. Dang X, Bardhan NM, Qi J, Gu L, Eze NA, Lin CW, et al. Deep-tissue optical imaging of near cellular-sized features. *Sci Rep.* (2019) 9:3873. doi: 10.1038/s41598-019-39502-w
15. De Grand AM, Lomnes SJ, Lee DS, Pietrzykowski M, Ohnishi S, Morgan TG, et al. Tissue-like phantoms for near-infrared fluorescence imaging system assessment and the training of surgeons. *J Biomed Opt.* (2006) 11:014007. doi: 10.1117/1.2170579
16. Steen EJL, Edem PE, Norregaard K, Jorgensen JT, Shalgunov V, Kjaer A, et al. Pretargeting in nuclear imaging and radionuclide therapy: improving efficacy of theranostics and nanomedicines. *Biomaterials.* (2018) 179:209–45. doi: 10.1016/j.biomaterials.2018.06.021
17. Du Y, Links JM, Becker L, DiPaula AF, Frank T, Schuleri KH, et al. Evaluation of simultaneous 201tl/99mtc dual-isotope cardiac spect imaging with model-based crosstalk compensation using canine studies. *J Nucl Cardiol.* (2014) 21:329–40. doi: 10.1007/s12350-013-9842-8
18. Lee HJ, Ehlerding EB, Jiang D, Barnhart TE, Cao T, Wei W, et al. Dual-labeled pertuzumab for multimodality image-guided ovarian tumor resection. *Am J Cancer Res.* (2019) 9:1454–68.
19. Spa SJ, Welling MM, van Oosterom MN, Rietbergen DDD, Burgmans MC, Verboom W, et al. A supramolecular approach for liver radioembolization. *Theranostics.* (2018) 8:2377–86. doi: 10.7150/thno.23567
20. Hu X, Tang Y, Hu Y, Lu F, Lu X, Wang Y, et al. Gadolinium-chelated conjugated polymer-based nanotheranostics for photoacoustic/magnetic resonance/Nir-Ii fluorescence imaging-guided cancer photothermal therapy. *Theranostics.* (2019) 9:4168–81. doi: 10.7150/thno.34390
21. Ebenhan T, Vorster M, Marjanovic-Painter B, Wagener J, Suthiram J, Modiselle M, et al. Development of a single vial kit solution for radiolabeling of 68ga-Dkfz-Psma-11 and its performance in prostate cancer patients. *Molecules.* (2015) 20:14860–78. doi: 10.3390/molecules200814860
22. Hapuarachchige S, Huang CT, Donnelly MC, Barinka C, Lupold SE, Pomper MG, et al. Cellular Delivery of bioorthogonal pretargeting therapeutics in Psma-positive prostate cancer. *Mol Pharm.* (2020) 17:98–108. doi: 10.1021/acs.molpharmaceut.9b00788
23. Hapuarachchige S, Kato Y, Artemov D. Bioorthogonal, Two-component drug delivery in Her2(+) breast cancer mouse models. *Sci Rep.* (2016) 6:24298. doi: 10.1038/srep24298
24. Hapuarachchige S, Zhu W, Kato Y, Artemov D. Bioorthogonal, Two-component delivery systems based on antibody and drug-loaded nanocarriers for enhanced internalization of nanotherapeutics. *Biomaterials.* (2014) 35:2346–54. doi: 10.1016/j.biomaterials.2013.11.075
25. Pandit-Taskar N. Targeted radioimmunotherapy and theranostics with alpha emitters. *J Med Imaging Radiat Sci.* (2019) 50(4 Suppl 1):S41–4. doi: 10.1016/j.jmir.2019.07.006
26. Yang L, Wang J, Yang S, Lu Q, Li P, Li N. Rod-shape Msn@Mos2 nanoplatform for Fl/Msot/Ct imaging-guided photothermal and photodynamic therapy. *Theranostics.* (2019) 9:3992–4005. doi: 10.7150/thno.32715
27. Chen Y, Chatterjee S, Lisok A, Minn I, Pullambhatla M, Wharram B, et al. A Psma-targeted theranostic agent for photodynamic therapy. *J Photochem Photobiol B.* (2017) 167:111–6. doi: 10.1016/j.jphotobiol.2016.12.018
28. Chen Z, Penet MF, Krishnamachary B, Banerjee SR, Pomper MG, Bhujwalla ZM. Psma-specific theranostic nanoplex for combination of trail gene and 5-Fc prodrug therapy of prostate cancer. *Biomaterials.* (2016) 80:57–67. doi: 10.1016/j.biomaterials.2015.11.048
29. Du Y, Liu X, Liang Q, Liang XJ, Tian J. Optimization and design of magnetic ferrite nanoparticles with uniform tumor distribution for highly sensitive Mri/Mpi performance and improved magnetic hyperthermia therapy. *Nano Lett.* (2019) 19:3618–26. doi: 10.1021/acs.nanolett.9b00630
30. Liu Y, Wang X, Hussain M, Lv M, Dong X, Wang T, et al. Theranostics Applications of nanoparticles in cancer immunotherapy. *Med Sci (Basel).* (2018) 6:100. doi: 10.3390/medsci6040100
31. Luque-Cabal M, Garcia-Teijido P, Fernandez-Perez Y, Sanchez-Lorenzo L, Palacio-Vazquez I. Mechanisms Behind the resistance to trastuzumab in Her2-amplified breast cancer and strategies to overcome it. *Clin Med Insights Oncol.* (2016) 10:21–30. doi: 10.4137/CMO.S34537
32. Pohlmann PR, Mayer IA, Mernaugh R. Resistance to trastuzumab in breast cancer. *Clin Cancer Res.* (2009) 15:7479–91. doi: 10.1158/1078-0432.CCR-09-0636
33. Wang C, Wang L, Yu X, Zhang Y, Meng Y, Wang H, et al. Combating acquired resistance to trastuzumab by an anti-Erbb2 fully human antibody. *Oncotarget.* (2017) 8:42742–51. doi: 10.18632/oncotarget.17451
34. Girish S, Gupta M, Wang B, Lu D, Krop IE, Vogel CL, et al. Clinical pharmacology of trastuzumab emtansine (T-Dm1): an antibody-drug conjugate in development for the treatment of Her2-positive cancer. *Cancer Chemother Pharmacol.* (2012) 69:1229–40. doi: 10.1007/s00280-011-1817-3
35. Mahalingaiah PK, Ciurlionis R, Durbin KR, Yeager RL, Philip BK, Bawa B, et al. Potential mechanisms of target-independent uptake and toxicity of antibody-drug conjugates. *Pharmacol Ther.* (2019) 200:110–25. doi: 10.1016/j.pharmthera.2019.04.008
36. Honarvar H, Westerlund K, Altai M, Sandstrom M, Orlova A, Tolmachev V, et al. Feasibility of affibody molecule-based pna-mediated radionuclide pretargeting of malignant tumors. *Theranostics.* (2016) 6:93–103. doi: 10.7150/thno.12766
37. Adumeau P, Carnazza KE, Brand C, Carlin SD, Reiner T, Agnew BJ, et al. A Pretargeted approach for the multimodal Pet/Nirf imaging of colorectal cancer. *Theranostics.* (2016) 6:2267–77. doi: 10.7150/thno.16744
38. Keinanen O, Brennan JM, Membreno R, Fung K, Gangangari K, Dayts EJ, et al. Dual radionuclide theranostic pretargeting. *Mol Pharm.* (2019) 16:4416–21. doi: 10.1021/acs.molpharmaceut.9b00746
39. Yao M, Ma X, Zhang X, Shi L, Liu T, Liang X, et al. Lectin-mediated pH-sensitive doxorubicin prodrug for pre-targeted chemotherapy of colorectal cancer with enhanced efficacy and reduced side effects. *Theranostics.* (2019) 9:747–60. doi: 10.7150/thno.29989
40. Maeda K, Sasaki H, Ueda S, Miyamoto S, Terada S, Konishi H, et al. Serum exosomal Microrna-34a as a potential biomarker in epithelial ovarian cancer. *J Ovarian Res.* (2020) 13:47. doi: 10.1186/s13048-020-00648-1
41. Kasten BB, Arend RC, Katre AA, Kim H, Fan J, Ferrone S, et al. B7-H3-targeted (212)Pb radioimmunotherapy of ovarian cancer in preclinical models. *Nucl Med Biol.* (2017) 47:23–30. doi: 10.1016/j.nucmedbio.2017.01.003
42. Osanto S, Van Poppel H. Emerging novel therapies for advanced prostate cancer. *Ther Adv Urol.* (2012) 4:3–12. doi: 10.1177/1756287211432777
43. Clarke JM, Armstrong AJ. Novel therapies for the treatment of advanced prostate cancer. *Curr Treat Options Oncol.* (2013) 14:109–26. doi: 10.1007/s11864-012-0222-4
44. Poon DM, Ng J, Chan K. Importance of cycles of chemotherapy and postdocetaxel novel therapies in metastatic castration-resistant prostate cancer. *Prostate Int.* (2015) 3:51–5. doi: 10.1016/j.prnil.2015.03.002
45. Bouchelouche K, Choyke PL, Capala J. Prostate specific membrane antigen - a target for imaging and therapy with radionuclides. *Discov Med.* (2010) 9:55–61.
46. Bravaccini S, Puccetti M, Bocchini M, Ravaioli S, Celli M, Scarpi E, et al. Psma expression: a potential ally for the pathologist in prostate cancer diagnosis. *Sci Rep.* (2018) 8:4254. doi: 10.1038/s41598-018-22594-1
47. Mease RC, Foss CA, Pomper MG. Pet Imaging in prostate cancer: focus on prostate-specific membrane antigen. *Curr Top Med Chem.* (2013) 13:951–62. doi: 10.2174/1568026611313080008
48. Chatalic KL, Veldhoven-Zweistra J, Bolkestein M, Hoeben S, Koning GA, Boerman OC, et al. A novel (1)(1)(1)in-Labeled anti-prostate-specific membrane antigen nanobody for targeted spect/Ct imaging of prostate cancer. *J Nucl Med.* (2015) 56:1094–9. doi: 10.2967/jnumed.115.156729
49. Novakova Z, Foss CA, Copeland BT, Morath V, Baranova P, Havlinova B, et al. Novel Monoclonal antibodies recognizing human prostate-specific membrane antigen (Psma) as research and theranostic tools. *Prostate.* (2017) 77:749–64. doi: 10.1002/pros.23311

50. Banerjee SR, Kumar V, Lisok A, Plyku D, Novakova Z, Brummet M, et al. Evaluation of (111)in-Dota-5d3, a surrogate spect imaging agent for radioimmunotherapy of prostate-specific membrane antigen. *J Nucl Med.* (2019) 60:400–6. doi: 10.2967/jnumed.118.214403
51. McGettigan M, Cardwell CR, Cantwell MM, Tully MA. Physical activity interventions for disease-related physical and mental health during and following treatment in people with non-advanced colorectal cancer. *Cochrane Database Syst Rev*. (2020) 5:CD012864. doi: 10.1002/14651858.CD012864.pub2
52. van de Watering FC, Rijpkema M, Robillard M, Oyen WJ, Boerman OC. Pretargeted imaging and radioimmunotherapy of cancer using antibodies and bioorthogonal chemistry. *Front Med (Lausanne)*. (2014) 1:44. doi: 10.3389/fmed.2014.00044

Conflict of Interest: The authors declare that the research was conducted in the absence of any commercial or financial relationships that could be construed as a potential conflict of interest.

The handling editor declared a past co-authorship with the authors.

Advantages of publishing in Frontiers

OPEN ACCESS
Articles are free to read for greatest visibility and readership

FAST PUBLICATION
Around 90 days from submission to decision

HIGH QUALITY PEER-REVIEW
Rigorous, collaborative, and constructive peer-review

TRANSPARENT PEER-REVIEW
Editors and reviewers acknowledged by name on published articles

Frontiers
Avenue du Tribunal-Fédéral 34
1005 Lausanne | Switzerland

Visit us: www.frontiersin.org
Contact us: frontiersin.org/about/contact

REPRODUCIBILITY OF RESEARCH
Support open data and methods to enhance research reproducibility

DIGITAL PUBLISHING
Articles designed for optimal readership across devices

FOLLOW US
@frontiersin

IMPACT METRICS
Advanced article metrics track visibility across digital media

EXTENSIVE PROMOTION
Marketing and promotion of impactful research

LOOP RESEARCH NETWORK
Our network increases your article's readership